Reduced mode coupling and nonlinear interaction in optical fibres

Aamir Gulistan

Supervisor: Prof. Azizur Rahman

School of Mathematics, Computer Science & Engineering

City, University of London

This dissertation is submitted for the degree of

Doctor of Philosophy

July 2019

Declaration

I, Aamir Gulistan, hereby declare that except where specific reference is made to the work of others, the contents of this dissertation are original and have not been submitted in whole or in part for consideration for any other degree or qualification in this, or any other university. This dissertation is my own work and contains nothing which is the outcome of work done in collaboration with others, except as specified in the text and Acknowledgements.

Aamir Gulistan

July 2019

Acknowledgements

I am thankful to Almighty ALLAH for giving me strength and ability to understand, learn and complete this thesis. I would like to thanks my supervisor, Professor B. M. A. Rahman, for having me as a student and providing me with all the opportunities. I am also very grateful to my parents, siblings and friends for their never ending support and encouragement throughout my studies. I am also very thankful of the Erasmus Mundus Leaders scholarship program from the European Commission for awarding me PhD scholarship.

Abstract

One of the main objectives of this dissertation is to understand the nonlinear effects in optical fibres caused by stimulated Brillouin scattering (SBS). SBS is a nonlinear process, where, a sound wave is generated due to electrostriction effect that creates a travelling Bragg gratings and prevents delivery of high optical power beyond the SBS threshold. An improved full-vectorial numerically efficient Finite Element Method (FEM) based computer code is developed to study complex light-sound interaction in optical waveguides. An improved polar meshing technique is used to efficiently discretised the computational domain consisting of circular boundaries such as optical fibres. The existing structural symmetry of the optical waveguide is also exploited in both optical and acoustic modal solutions and only a half or quarter structure is simulated, as needed. This allows a more efficient element distribution on a smaller region compared to full structure with similar computational resources that result in the improved modal solution accuracy and reduced modal degeneration. The existence of spurious (non-physical) modes in full-vectorial acoustic modal solution and their elimination using the penalty method is also proposed and tested in this thesis. Penalty term consisting of the curl-curl section of the acoustic formulation enforces the acoustic field to suppress the rotational energy of the propagating acoustic wave. As a result of the penalty method, a significant improvement in the solution accuracy and quality of acoustic modes is demonstrated in both low and high index contrast optical waveguides.

A standard single mode Germanium doped Silica fibre is used to study light sound interaction, and overlap of 93 % between fundamental optical and acoustic modes has been

calculated. This acoustic-optic overlap is directly related to the calculation of the SBS threshold. A lower SBS overlap results in an increased SBS threshold and allows more power to be transferred in the optical fibre. Through rigorous numerical simulations, the fibre geometry and refractive index profile are modified, and a layer of a high acoustic index is introduced in the cladding such that the acoustic mode propagates in the cladding. The optical refractive indices of core and cladding are kept same while the acoustic index of 2^{nd} layer is increased by doping it with Boron and Germanium (3.394% B_2O_3 + 2% GeO_2). The acoustic mode completely shifts in the 2^{nd} layer and as a result of this technique, an extremely low overlap of 2.5 % is calculated between optical and acoustic modes.

Another objective of this research was to reduce the nonlinear effects in optical fibres is the use of large mode area (LMA) fibres such as few mode and multimode fibres. LMA fibres provide large effective area resulting in less nonlinear effects for a given power compared to single mode fibres. However, the existence of more than one mode may result in the inter-mode mixing and energy may transfer from one mode to its neighbouring propagating mode. Higher order modes of a MMF has twofold advantage as these modes provide a large effective area and also exhibit a weaker coupling with other modes. To mitigate this, we have proposed two novel techniques to increase the modal stability between higher order modes of a multimode step-index fibre. The modal stability is directly related to the effective index difference (Δn_{eff}) between a given mode of propagation and its neighbouring antisymmetric modes. One of the technique involves the use of strategically located low or high index doped strips along the circumference of MMF such that the modal stability between $LP_{0,n}$, a higher order mode and its neighbouring antisymmetric $LP_{1,n-1}$ and $LP_{1,n+1}$ modes can be increased. We have shown that the modal stability of LP_{09} mode and its neighbouring antisymmetric LP_{18} and LP_{19} modes increases more than 35 % from its original value. In the second technique, we have used an array of strategically located air-holes to increase the modal stability of LP_{06} mode and its neighbouring antisymmetric LP_{15} and LP_{16} modes up to

54 %. Similarly, an air-hole array is also used to increase the modal stability of a few-mode fibre. The Δn_{eff} between first four (LP_{01}, LP_{11}, LP_{21} and LP_{02}) modes of a four-mode fibre is increased more than 30 %. In both the methods we have shown the effect on the effective index difference due to change in the strips width or central location and holes width or central location, respectively. Moreover, it is also shown that both proposed techniques are scalable and can be used to increase the modal stability of other higher order modes.

Table of contents

List of Symbols and Acronyms

Symbols

c	Light velocity in free-space
λ	Wavelength
n_{eff}	Effective refractive index
Δn_{eff}	Effective index difference
k_0	Wavenumber
χ	Susceptibility
α	Attenuation constant
β	Phase constant
v_p	Phase velocity
A_{eff}	Mode effective area
ε_0	Permittivity of free-space
ε_r	Relative permittivity
μ_r	Relative permeability
ω	Angular frequency
σ_x	Spot size
$\vec{E}$	Electric field vector
$\vec{H}$	Magnetic field vector

$\vec{D}$	Electric flux density
$\vec{B}$	Magnetic flux density
α	Penalty term
Si	Silicon
SiO_2	Silicon dioxide
Al_2O_3	Aluminium dioxide
B_2O_3	Boron dioxide
GeO_2	Germanium dioxide

Acronyms

RI	Refractive index
EM	Electromagnetic
TIR	Total internal reflection
SMF	Single mode fibre
MMF	Multimode fibre
FMF	Few mode fibre
LMA	Large mode area
NA	Numerical aperture
SBS	Stimulated Brillouin scattering
SPM	Self phase modulation
FWM	Four wave mixing
CPM	Cross phase modulation
SRS	Stimulated Raman scattering
LD	Laser diode
WiMAX	Worldwide Interoperability for Microwave Access
WLAN	Wireless local area network
MIMO	Multiple-input-multiple-output
WLAN	Wireless local area Network
FTTH	Fibre to the home
PCF	Photonic crystal fibre
FV-FEM	Full-vectorial finite element method
FDM	Finite difference method
FDTD	Finite difference time domain method
TE	Transverse electric
TM	Transverse magnetic
SDM	Space division multiplexing
MCF	Multi-core fibre

List of tables

List of figures

List of Publication

Journal Papers

1. **Aamir Gulistan**, M. M. Rahman, Souvik Ghosh, and B. M. A. Rahman, “Elimination of spurious modes in full-vectorial finite element method based acoustic modal solution,” *Optics Express* 27, 10900–10911 (2019).

2. **Aamir Gulistan**, Souvik Ghosh and B. M. A. Rahman, “Enhancement of modal stability through reduced mode coupling in a few-mode fiber for mode division multiplexing", *OSA Continuum* 1, 309–319 (2018).

3. **Aamir Gulistan**, Souvik Ghosh, S. Ramachandran, and B.M.A. Rahman, “Efficient strategy to increase higher order inter-modal stability of a step index multimode fiber", *Optics Express* 25, 29714–29723 (2017).

4. **Aamir Gulistan**, Souvik Ghosh and B. M. A. Rahman, “A Scalable Technique to increase the Effective index difference between higher order modes of a Step-index Multimode fiber", *Optical Fibre Technology*, Aug (2019).(Under Review)

Conference Papers

1. **Aamir Gulistan**, S. Ghosh, S. Ramachandran, and B. M. A Rahman, “Enhancing mode stability of higher order modes in a multimode fiber,” in *Advanced Photonics 2018 (BGPP, IPR, NP, NOMA, Sensors, Networks, SPPCom, SOF), OSA Technical Digest (Optical Society of America, 2018)*, paper SoW2H.7, Zurich Switzerland, 2–5 July 2018.

2. **Aamir Gulistan**, M. M. Rahman, Souvik Ghosh, and B. M. A. Rahman, "Tailoring light-sound interactions in a single mode fiber for the high-power transmission or sensing applications", *Third International Conference on Photonic Solutions*, In Proc. of SPIE 10714, Thailand, 8-10 Nov 2017.

Chapter 1

Introduction

The unprecedented increase in the growth and popularity of Internet applications and services is becoming a constant challenge for optical networks. Due to this rapid growth and demand for higher bandwidth and better quality services, the current infrastructure is under pressure. The number of devices per user is increasing, and it is predicted that by the year 2020 these devices can be three times the world population [1]. Back in the 1980s, when the optical fibres were deployed, it was considered that optical fibres have unlimited transmission bandwidth, at least for any foreseeable data rate requirement. However, after thirty years, optical fibre transmission experiments have shown clear signs of saturation. This saturation is mainly due to the nonlinear effects that limit reliable data transmission. This data rate exhaust, also known as capacity crunch, has been the main argument underpinning research efforts on optical fibre transmission systems in recent years [2, 3].

High power lasers and amplifiers are also an integral part of optical communication along with the many other industrial applications. Since the first demonstration of fibre lasers in 1964 by Snitzer [4], there is a considerable volume of research and development work for the improvement of fibre lasers. Optical fibre based lasers have received significant attention that generates high optical power with excellent flexibility and high beam quality [5, 6]. The rapid development of high power pump laser diodes (LD) and use of rare-earth

materials in the development of fibre lasers have significantly increased their penetration in different industrial applications [7–9]. Compared to other types of lasers, the long lengths of fibre lasers make them attractive as they provide large single pass gain for effective power scaling. Over the past few years, the performance of fibre lasers has improved significantly with the development of the latest fibre materials, high-brightness pumping diodes and improved drawing techniques. Compared to solid-state lasers, fibre lasers are also more compact, lightweight, flexible and provide immunity to electromagnetic interference [10, 11]. However, due to the fibre geometry, high-intensity light travels under tight confinement for considerably a longer distance that results in increased nonlinear effects [12, 13].

Among the other nonlinear effects, stimulated Brillouin scattering (SBS) have a lower threshold and often considered as one of the main limitations for high power transmission applications [14, 15]. To overcome this limitation the SBS threshold level is required to be increased, which can be achieved by using different techniques, such as the modification of the fibre geometry in order to push the acoustic modes into cladding [16], use of a large mode area fibre such as multimode fibres [17, 18], or doping fibre with anti-acoustic material to suppress SBS [19]. On the other hand, SBS can be exploited for many useful applications such as temperature, pressure and strain sensors. Most recently, the SBS is being exploited for several innovative applications, such as slow and fast light and Brillouin cooling [20–24]. Transverse mode instability (TMI) is also considered as one of the main limitations in power scaling in large mode area fibres or multimode fibres. TMI is a result of refractive index grating formation due to transverse mode beating and coupling between the amplified fundamental mode and higher order modes [25]. Above a certain threshold, TMI deteriorates the output beam quality rapidly. For a single fundamental-mode excitation, large content and strong competition with higher order mode such as LP_{11} is take place after a certain threshold [5]. However, in single mode fibres where light is confined in a small

area, stimulated Brillouin scattering (SBS) is considered as one of the main limitations for high power transmission applications.

Various approaches have been presented to reduce or mitigate these non-linear effects in optical fibres. One of the methods is to reduce the numerical aperture (NA) while increasing the core diameter and maintaining single mode operation [26]. Recently some of the research demonstrated a lower value of NA with a diameter ranging from 35 μm to 52 μm [27, 28] and $NA \sim 0.04$, where, the transmission of three KW power is demonstrated [29]. However, lowering NA value weakens the guidance of fundamental mode and make it more sensitive to bending or other mechanical perturbations [14]. Similarly, photonic crystal fibres (PCF) also falls into a similar category that consists of a solid silica-based core surrounded by periodically arranged air-holes in the cladding. Introduction of air-holes reduces the number of modes effectively, supported by PCF fibre as the higher order modes leak away through the gaps between the air-holes and the modal filtering is an endless single-mode (ESM) PCF is controlled by the geometry [30]. Initially, photonic crystal fibres were proposed with a smaller core size but later on large mode area, photonic crystal fibres are also developed for fibre laser applications [31].

One of the approaches to reduce the nonlinear effects is to use large mode area fibres such as multimode fibres. Multimode fibres (MMF) provides a much higher effective area, but the existence of many modes may result in the random mode mixing and energy may transfer from a desired mode of propagation to its neighbouring modes. The identification and excitation of a selective mode are very important in multimode fibres for lasers and amplifiers related applications. There are different techniques proposed for the efficient excitation of a particular higher order mode, such as the use of the self-imaging property of multimode interference, prism-coupling and use of Single mode-Multimode-Multimode fibre structure etc. [32–34]. Recently, higher order modes (HOM) of MMF are used for high power fibre lasers as they can provide a more stable single mode operation along with the natural

resistance to area reduction due to bending as compared with fundamental mode [35]. Higher order modes of MMF are also more resistant to the mode coupling as the modal stability between HOMs of a given MMF increases with the increase in modal order (m). However, external perturbations such as bending or fabrication imperfections can cause energy transfer from a desired higher order LP_{0m} mode to its neighbouring antisymmetric $LP_{1,m\pm1}$ modes [36, 17]. Here, the term modal stability is used to describe the effective index difference (Δn_{eff}) between a desired mode of propagation and its neighbouring antisymmetric modes. The larger fibre dimensions allow fundamental mode along with other higher order modes to propagate with different effective indices (n_{eff}). A lower value of Δn_{eff} between the adjacent modes may result in the inter-mode mixing and can cause interference effects. However, increasing the Δn_{eff} between these modes can significantly reduce this inter-mode mixing and any possible interference effects between them.

1.1 Aim and objectives

The aim of the research is to develop a full-vectorial finite element method (FEM) based numerical method to study optical and acoustic modes and their interaction in optical waveguides. The acoustic-optic interaction is directly related to the understanding of stimulated Brillouin scattering, a well known nonlinear effect in optical waveguides. The fibre geometry is modified in order to decrease the SBS overlap that increases the SBS threshold and allow more power scaling. Similarly, fibre geometry is also modified to increase the SBS overlap that can be exploited for different sensing applications. Large mode area (LMA) fibres such as few-mode fibres (FMF) and multimode fibres (MMF) provides a higher effective area that also reduces the nonlinear effects. Another aim of the research is to study these optical modes in FMF & MMF and increase the effective index difference between these modes to reduce modal coupling.

These aims and objectives are listed below,

- To study the primary parameters that are associated with optical and acoustic wave propagation and understand the spatial variations and identify different optical and acoustic mode patterns.
- To study the physical properties linked with acoustic wave propagation such as stress, strain, elasticity, particle displacement and acoustic velocity etc.
- Development of a full-vectorial finite element method based computer simulation code for rigorous characterisation and study of the fundamental and higher-order acoustic modes in both low and high index contrast optical waveguides.
- Introduction of penalty term to remove the spurious modes in acoustic modal solution and exploit the symmetry boundary conditions to improve the modal solution accuracy and remove the modal degeneration.
- To investigate the acoustic-optic overlap in a single mode fibre and modifying fibre geometry to reduce the SBS overlap for increased power transmission and to increase the SBS overlap for sensing applications.
- Study of large mode area fibres such as multimode fibres and few-mode fibres as an alternative approach to reduce the nonlinear effects.
- To increase the modal stability between the higher order modes of a MMF by increasing the effective index difference between the mode of propagation and neighbouring antisymmetric modes using low and high index contrast doped strips.
- Introduction of air-holes along the radius of MMF such that the resultant effective index difference is enhanced between the modes of FMF and higher order modes of MMF.

1.2 Structure of the Thesis

This thesis comprises of eight chapters, including the current introduction chapter and two appendices. The chapter contents are briefly described as follows,

- **Chapter 2:**

  Chapter 2, presents the fundamentals of optical waveguides and basic principle of optical fibre guidance. The basic concepts related to optical fibre such as phase & group velocity and dispersion are discussed in the chapter. Nonlinearity is an important effect in the optical waveguides that occur due to refractive index changes in the material or scattering process. These nonlinear effects such as self-phase modulation, cross-phase modulation and four-wave mixing due to refractive index changes are discussed in the chapter. Similarly, nonlinear effects such as Raman scattering and Brillouin scattering that occurs due to nonlinear scattering in the material are also discussed. Chapter 2 also presents a brief description of different computational methods such as the finite element method, finite difference time domain method and frequency difference frequency domain method for the solution of electromagnetic waveguides.

- **Chapter 3:**

  Chapter 3 discusses the basics of light scattering, primarily focusing on the Brillouin scattering. Basic concepts of Brillouin scattering and its different applications such as radio over fibre technology, optical sensing, slow light and optical delay lines etc. are discussed. Chapter 3 also discusses the propagation of the acoustic wave through the optical medium by displacement of particles that depends on the density and elasticity of the material. Detail discussion of the physical quantities related to the acoustic wave propagation is provided. Later in Chapter 3, the propagation of acoustic modes in a 2D acoustic waveguide is also discussed.

- **Chapter 4:**

Chapter 4, explain the variational approach based finite element method (FEM) in details. A step by step process of computational domain discretisation, selection of interpolation function and formation of a global sparse matrix to obtain the modal solution is discussed. Chapter 4, also discusses the newly introduced polar meshing in the FEM code that results in a more accurate solution for circular waveguides. Implementation of full-vectorial FEM in both optical and acoustic modal analysis and introduction of symmetry boundary conditions to avoid the modal degeneration and to improve modal accuracy are discussed.

- **Chapter 5:**

  Chapter 5, discusses the light sound interaction in a standard single mode fibre. Mode profiles of the fundamental optical and acoustic (longitudinal and shear) modes are presented. Effect of penalty term to remove the spurious modes in the acoustic formulation is also discussed in chapter 5. The basic acoustic-optic overlap is calculated without any modification in the optical and acoustic index. Later on, two techniques are suggested to increase the acoustic-optic overlap for fibre optic based sensing applications and to reduce the overlap to increase the SBS threshold for high power transmission applications are presented. Moreover, effect of the penalty method on modal solution is shown in both low and high index contrast acoustic waveguides.

- **Chapter 6:**

  Chapter 6 discusses the modal stability enhancement in higher order modes of multi-mode fibre using doped strips. Multimode fibres provide a higher effective area that reduces the nonlinear effects, however, the existence of many modes may result in the inter mode mixing. A newly proposed technique using high and low index doped strips to increase the effective index difference between the higher order modes is proposed in chapter 6. Numerical results presented have shown significant improvement in the

modal stability of LP_{09} mode and its neighbouring antisymmetric LP_{18} and LP_{19} modes. Moreover, in order to show the scalability of the proposed technique the modal stability between LP_{08} mode and it's neighbouring antisymmetric LP_{17} and LP_{18} modes are also shown. In addition to this, chapter 6 also discusses the possible fabrication tolerances that may occur due to the change in the strip width and strip location from a central position.

- **Chapter 7:**

  Chapter 7 discusses the modal stability enhancement in higher order modes of MMF using air-holes. These air-holes are introduced on specified locations along the circumference of the MMF such that the resultant effective index difference between the mode of propagation and its neighbouring antisymmetric modes is increased. With the introduction of air-holes, the effective index of modes decreases and the magnitude of decrease depends on the field magnitude at that particular location.

  The similar technique is applied to increase the effective index difference between the modes of a few-mode fibre that is useful for the transmission capacity enhancement using mode division multiplexing technique. The enhanced mode spacing reduces the cross talk between the propagating modes and reduces the complexity caused due to MIMO based methods. Chapter 7 also discusses the bending effect in a few-mode fibre before and after the introduction of air-holes.

- **Chapter 8:**

  This chapter summarises the importance of the full-vectorial FEM formulation for the optical and acoustic modal solution. The summary of the stimulated Brillouin scattering and its applications along with some possible future work is also presented in this chapter. Similarly, the modal stability techniques proposed in chapter 6 and

chapter 7 are also summarised and some possible future work in order to enhance the modal stability of higher order modes are also suggested.

Chapter 2

Fundamentals of Optical Waveguides

2.1 Fundamentals of fibre optics

Fast transmission of information from one place to another place was considered a challenging task until 1966 when Kao *et al.* presented glass optical fibre as a potential waveguide for optical communication [37]. Since then properties of optical fibre were explored that included power handling, power losses, number of modes and fabrication process both theoretically and experimentally. The light guiding principle in optical fibre was quite promising for future optical communication but the high loss of available materials at that time was the main limitation. However, after few years Kapron, *et al.* invented a process of chemical vapour deposition that facilitated the fabrication of single mode fibre with the attenuation of 16 dB/km at 633 *nm* wavelength [38]. Within next 10 years, a significant improvement was noticed and optical fibre loss was reduced to a remarkably low value of 0.2 dB/km at 1550 nm along with the ability to be spliced and connect [39, 40]. Later on, with the further improvements in optical fibres together with the invention of lasers and optical fibres, telecommunication industry witnessed revolutionary advancements and optical fibres became the physical layer of today's fast Internet. Besides being the foundation of fast Internet,

optical fibres have also become a core part of many other technologies ranging from sensing, high power industrial applications, biomedical imaging and fibre lasers.

2.1.1 Basic principles of optical fibre guidance

Optical fibres are transparent, flexible and thin like human hair size fibres made by drawing glass (silica) or plastic. Optical fibres mainly consist of a high refractive index core surrounded by a low refractive index cladding. Light propagates inside optical fibre through the phenomenon of total internal reflection as shown in Fig. 2.1.

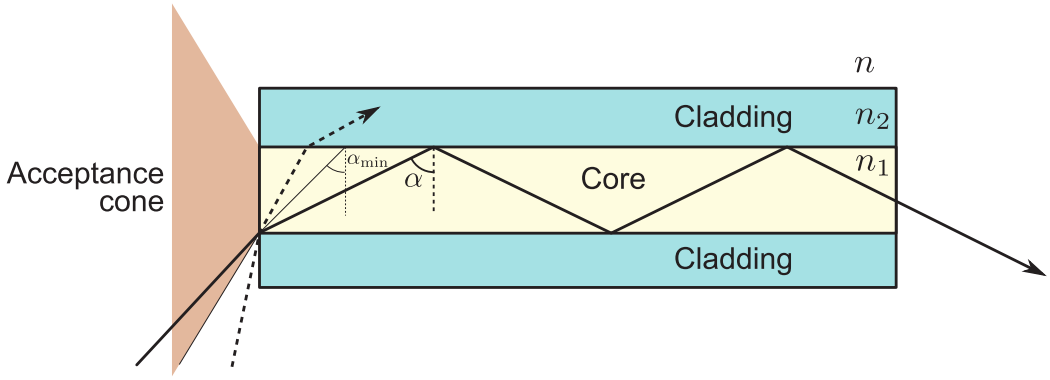

Fig. 2.1 Transmission of optical wave inside a step-index single mode fibre based on total internal reflection (TIR) [41].

Here, n_1 and n_2 are the core and cladding refractive indices where, $n_1 > n_2$ and the refractive index difference is often very small: $(n_1 - n_2)/n_1 << 1$. Generally, optical fibres are made of fused silica (SiO2), and the core refractive index is increased by chemical doping. However, in traditional submarine cables, this can also be achieved by doping cladding with Fluorine which reduces the cladding refractive index resulting core index being higher than that of the cladding [42]. According to Snell's law, the incidence angle required for total internal reflection is calculated as $\alpha > \alpha_{min} = sin^{-1}(n_2/n_1)$. The acceptance cone is shown in Fig. 2.1 is the acceptable angle for incidence wave to follow the TIR principle and for light to propagate inside optical fibre the incident angle should be inside the acceptance cone. Outside of the acceptance cone, the light follows the refraction principle and it escapes into

the cladding. Using Snell's law, the numerical aperture (NA) that is the sine of the maximum angle of the incident optical wave with respect to the fibre axis can be calculated as,

$$NA = n\,sin\left(\frac{\pi}{2} - \alpha_{min}\right) = \sqrt{\left(n_1^2 - n_2^2\right)} \tag{2.1}$$

Here, n is the refractive index of outside medium such as air. From the above description and Fig. 2.1 it can be assumed that any incident ray inside the acceptance cone defined by *NA* can be propagated inside the optical fibre. However, considering the interference effects, only a discrete number of incident rays can be transmitted through the optical fibre at the same time, where each ray corresponds to a mode. Figure 2.2 (a) shows a multimode step-index fibre where more than one mode can propagate at the same time and core diameter varies from 50 μm to 200 μm. Multimode fibres are used for relatively short distance communication because the modes tend to disperse over long lengths. Figure 2.2 (b) shows schematic of a multimode graded index fibre, where the refractive index continuously decreases from the centre of the core to the cladding. The multimode graded index fibre has considerably less dispersion compared to multimode step index fibre. In contrast to multimode fibre (MMF), single mode fibres (SMF) have a smaller core diameter (8-12 μm) and allow only one mode of propagation as shown in Fig. 2.2. The existence of single mode reduces the light reflections and results in lower attenuation which makes SMF more appropriate for long distance communication.

2.1.2 Mode theory of cylindrical waveguides

In order to understand the light propagation along the main axis (z-axis) of the fibre, an important parameter propagation constant β is to be considered. Propagation constant is used to determine the change in the amplitude and phase of a propagating light along the z-axis. In a lossless medium, the propagation constant is purely imaginary and considered as an

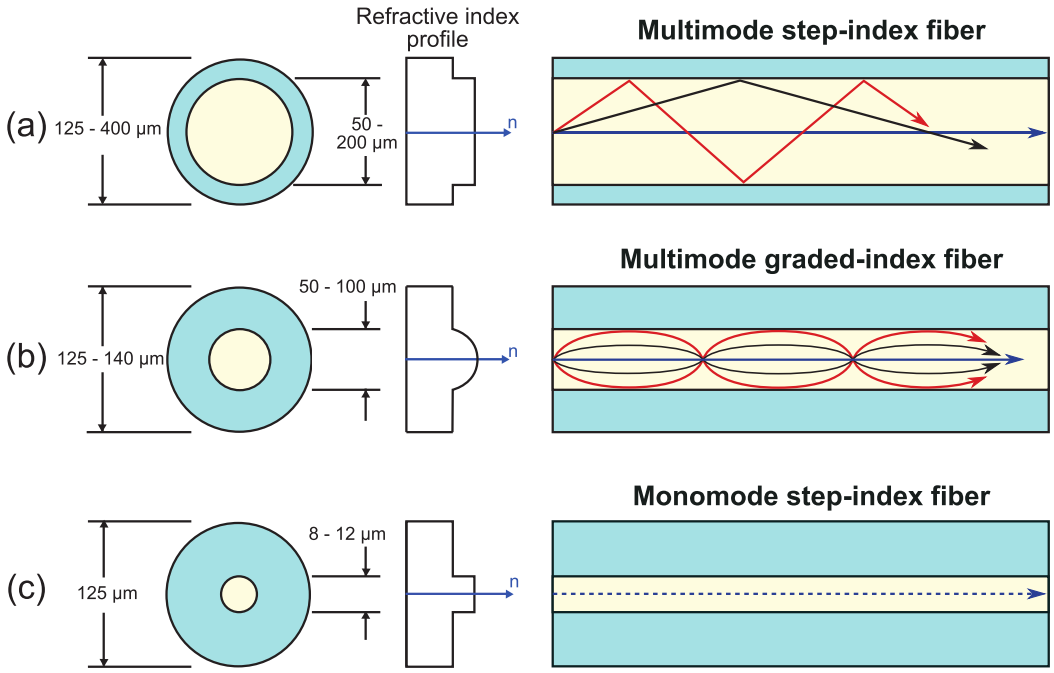

Fig. 2.2 Refractive index profiles, typical dimensions and rays paths in (a) multimode step-index fibre, (b) multimode graded-index fibre and (c) monomode step-index fibre [41].

axial component of wavevector $\vec{k}$. The magnitude of wavevector is given by $|\vec{k}| = k = 2\pi/\lambda$, where, λ is the wavelength.

There are different kinds of modes that propagate inside optical fibres. The guided modes are trapped in the core and have different electric field patterns along the cross-section of the fibre. The cladding modes originate when the light is transmitted on an angle outside of the acceptance cone and it gets trapped in cladding after refraction. The leaky modes partially confine in the core and tend to attenuate more than the guided modes with the propagation. Leaky and guided modes are differentiated by the cutoff condition.

$$n_2 k < \beta < n_1 k \tag{2.2}$$

Equation 2.2 shows the condition for a mode to remain guided in the fibre core. Whereas, if $\beta < n_2 k$, the mode is leaky and this corresponds to TIR limit, explained earlier. The maximum value of propagation constant (β) as a projection of $n_1\vec{k}$ on z-axis is $n_1 k$. The maximum

angle to allow TIR is calculated by Snell's law ($sin(\alpha) = n_2/n_1$) and correspondingly the minimum value of propagation constant is $\beta = n_2 k$.

Equation 2.3 represents the V number or the normalised frequency that is a dimensionless parameter used to determine the number of modes in an optical fibre depending on the refractive index contrast and core radius (a).

$$V = \frac{2\pi a}{\lambda} NA = \frac{2\pi a}{\lambda} \sqrt{(n_1^2 - n_2^2)} \tag{2.3}$$

The cutoff condition for the optical modes is $\beta = n_2 k$ and depending on the modes it occurs on different value of V [43]. For a value of $V \leq 2.405$, the fibre has just one mode of propagation and fibre is monomode. For a large V, the number of modes M in a multimode fibre can be calculated as,

$$M \approx \frac{V^2}{2} \tag{2.4}$$

2.2 Characteristics of optical fibres

In this section, we will discuss the important properties that characterise optical fibres. The main focus of our discussion is on single mode fibres (SMF) and multimode fibres (MMF) as per the scope of the work presented in later chapters.

2.2.1 Phase and group velocity

In electromagnetic waves, there are points that are in a constant phase that forms a surface also known as a wavefront. For a monochromatic lightwave travelling in the z-direction these constant phase points travel at a phase velocity v_p that can be written as,

$$v_p = \omega/\beta \tag{2.5}$$

Where, ω is the angular frequency of the wave and β is the propagation constant. In practice producing a perfectly monochromatic lightwave is impossible and light energy is composed of a sum of plane wave components of different frequencies. There are situations where a group of waves propagating with frequencies close to each other resulting in the form of a wave packet. This wave packet travels with a speed of velocity called group velocity v_g given in Eq. 2.6 rather than the individual wave velocity.

$$v_g = \delta\omega/\delta\beta \tag{2.6}$$

In the understanding of transmission characteristics of optical fibres, the group velocity is very important as it relates to the propagation characteristics of light packets. The propagation constant of lightwave travelling in an infinite medium of refractive index n_1 can be written as,

$$\beta = n_1 \frac{2\pi}{\lambda} = \frac{n_1 \omega}{c} \tag{2.7}$$

Using Eq. 2.5 and Eq. 2.7, following relationship for phase velocity can be written as,

$$v_p = \frac{c}{n_1} \tag{2.8}$$

Similarly, employing Eq. 2.6, where in the limit $\delta\omega/\delta\beta$ becomes $d\omega/d\beta$, the group velocity can be written as,

$$v_g = \frac{\mathrm{d}\lambda}{\mathrm{d}\beta}\frac{\mathrm{d}\omega}{\mathrm{d}\lambda} = \frac{\mathrm{d}}{\mathrm{d}\lambda}\left(n_1 \tfrac{2\pi}{\lambda}\right)^{-1}\left(\tfrac{-\omega}{\lambda}\right)$$

$$= \frac{-\omega}{2\pi\lambda}\left(\tfrac{1}{\lambda}\tfrac{dn_1}{d\lambda} - \tfrac{n_1}{\lambda^2}\right)^{-1}$$

$$= \frac{c}{\left(n_1 - \lambda \frac{dn_1}{d\lambda}\right)} = \frac{c}{N_g} \tag{2.9}$$

In Eq. 2.9 the parameter N_g is known as the group index of the waveguide.

2.2.2 Dispersion

Single mode fibres provide higher bandwidth and enable data transmission over longer distances. However, when a light pulse propagates inside an optical fibre, its shape gets distorted with time and the spreading of the pulse is known as dispersion [44]. The broadening of optical pulses creates interference effect with other optical pulses and this interference limits the power carrying capability of fibres. In optical fibres, the dispersion can be of three types, modal dispersion, material dispersion and waveguide dispersion.

1. **Modal Dispersion:**

   Modal dispersion or intermodal dispersion mainly occurs in multimode fibres where transmitted light containing different modes follow different paths inside the optical fibre and consequently arrives at different times. In a multimode fibre, number of these optical modes can be in thousands that travel inside fibre depending on the intensity of light ray and properties. Some of these light rays take a shorter path such as travelling straight through the optical fibre also known as fundamental modes and some of the rays takes the longer path as a result of reflections at the core-cladding interface known as higher order modes. As a result of these different paths taken by these modes, the transmitted light spreads in time and result in the spreading of transmitted pulses.

   Figure 2.3 provides an illustration of slow and fast travelling modes resulting in modal dispersion. In order to reduce the modal dispersion, a smaller diameter core can be used that will allow fewer modes of propagation. Moreover, a graded-index fibre

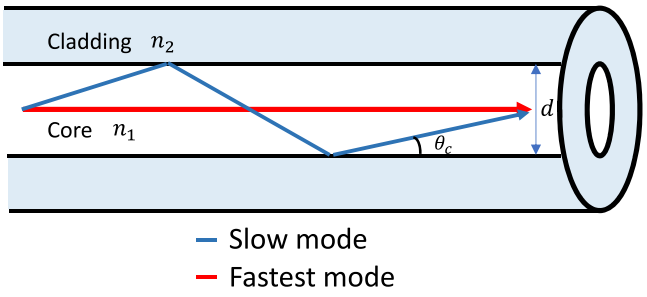

Fig. 2.3 Slow and fast modes travelling at different paths resulting in the modal dispersion.

allows light travelling on longer paths to travel faster and arrive at nearly the same time as rays travelling on shorter paths.

2. **Chromatic Dispersion:**

   Sir Isaac Newton firstly observed chromatic dispersion when he passed sunlight through a prism and saw it diverging into a spectrum of different colours. Optical fibres comprise of core and cladding with different refractive indices causing some wavelengths of light travel slower or faster than others. This result in asynchronous arrival of the optical pulses at the receiving end. For long-haul communication, chromatic dispersion is considered as a serious challenge. Initially, sharped binary pulses (1s and 0s) are affected by the chromatic dispersion and degradation makes more difficult to differentiate these pulses from each other at the far end. This result in the bit error rate (BER) and limits the capacity and effective transmission of the optical systems.

   However, there are techniques used to compensate for the effect of chromatic dispersion such as the use of dispersion compensating fibre (DCF) at receiving end. Another method is to pre-compensate the optical signal to an expected chromatic dispersion in the optical link. Chromatic dispersion is caused by the dispersive properties of the waveguide material known as material dispersion and guidance effects due to fibre structure known as waveguide dispersion.

   - **Material dispersion**

An optical pulse consists of various spectral components that travel with different group velocities and result in material dispersion or pulse broadening. As the refractive index of material depends on the wavelength of light being transmitted, hence, each frequency component travels at a slightly different speed.

The pulse spread due to material dispersion can be calculated by considering group delay τ_g that is reciprocal of group velocity v_g defined in Eqs. 2.6 and 2.9.

Hence, group delay τ_g can be written as,

$$\tau_g = \frac{d\beta}{d\omega} = \frac{1}{c}\left(n_1 - \lambda \frac{dn_1}{d\lambda}\right) \tag{2.10}$$

where, n_1 is refractive index of core. Due to material dispersion the pulse delay τ_m for fibre length (L) can be written as,

$$\tau_m = \frac{L}{c}\left(n_1 - \lambda \frac{dn_1}{d\lambda}\right) \tag{2.11}$$

The rms pulse broadening due to material dispersion σ_m can be written in the form of Taylor series about λ

$$\sigma_m = \sigma_\lambda \frac{d\tau_m}{d\lambda} + \sigma_\lambda \frac{2d^2\tau_m}{d\lambda^2} + ... \tag{2.12}$$

Where, σ_λ is the source rms spectral width and mean wavelength λ. In Eq. 2.12, first term is dominant especially for sources varying 0.8 to 0.9 μm wavelength range, hence:

$$\sigma_m = \sigma_\lambda \frac{d\tau_m}{d\lambda} \tag{2.13}$$

From Eq. 2.11 the pulse spread can be calculated by considering τ_m on λ

$$\frac{d\tau_m}{d\lambda} = \frac{L}{c}\left[\frac{dn_1}{d\lambda} - \frac{\lambda d^2 n_1}{d\lambda^2} - \frac{dn_1}{d\lambda}\right]$$

$$= \frac{-L\lambda}{c}\frac{d^2 n_1}{d\lambda^2} \tag{2.14}$$

Substituting Eq. 2.14 into Eq. 2.13, the rms pulse broadening can be written as,

$$\sigma_m \backsimeq \frac{\sigma_\lambda L}{c}\left|\lambda \frac{d^2 n_1}{d\lambda^2}\right| \tag{2.15}$$

The pulse broadening due to material dispersion can be written in the form of material dispersion parameter M having units $psnm^{-1}km^{-1}$ is defined as [45],

$$M = \frac{1}{L}\frac{d\tau_m}{d\lambda} = \frac{\lambda}{c}\left|\frac{d^2 n_1}{d\lambda^2}\right| \tag{2.16}$$

- **Waveguide Dispersion**

  Waveguide dispersion is also responsible for chromatic dispersion that occurs due to the variation in group velocity with wavelength for a particular mode. Waveguide dispersion is very important in waveguides with small effective mode areas such as photonic crystal fibres and single-mode fibres used in optical fibre communication. To understand the waveguide dispersion ray theory can be considered where the transmission time for the rays varies depending on the angle between the transmitted ray and the fibre axis varying with wavelength. For a single mode with propagation constant β, the fibre shows waveguide dispersion when $d^2\beta/d\lambda^2 \neq 0$. Waveguide dispersion can be minimised using dispersion shifted fibres and using large mode area fibres [46].

2.3 Nonlinear effects in optical waveguides

Any dielectric medium behaves like nonlinear when undergoes high-intensity electromagnetic field. In optical fibres, light is confined in a small region and nonlinear effects may arise due to the intensity dependence of the refractive index in medium or inelastic scattering phenomenon. As a result, even a moderate optical power may create substantial effects particularly in case of fibre amplifier and while transmitting short pulses.

Nonlinearity arises due to the an-harmonic motion of bound electrons under the influence of the applied field. Due to these an-harmonic movements, the polarization P induced by electric dipoles does not follow a linear relation instead satisfies the below-mentioned relation,

$$P = \varepsilon_0 \chi^{(1)} E + \varepsilon_0 \chi^{(2)} E^2 + \varepsilon_0 \chi^{(3)} E^3 + ... \tag{2.17}$$

where, ε_0 is the permittivity of free space, $\chi(k)$ is the k^{th} order susceptibility.

The significant contribution to the total polarization comes from linear susceptibility $\chi^{(1)}$ and the second order susceptibility $\chi^{(2)}$ is responsible for sum-frequency and second harmonic generation. For a medium having a symmetrical molecular structure such as silica, second-order susceptibility is zero. The third order $\chi^{(3)}$ is mainly responsible for the nonlinear effects in the optical fibres [44].

The Kerr effect or Kerr nonlinearity is one of the common and simple nonlinear effect that occurs due to the power dependence of the refractive index.

$$\Delta n = n_2 I \tag{2.18}$$

Here, Δn is the change in the refractive index of the medium, I is the optical intensity and n_2 is the nonlinear refractive index. Based on the input signal, the Kerr-non linearity can cause different effects such as self-phase modulation (SPM), cross-phase modulation (CPM) and four-wave mixing (FWM). Moreover, with the increase in optical intensity, the inelastic

scattering process can induce stimulating effects such as stimulated Raman scattering (SRS) and stimulated Brillouin scattering (SBS). Figure 2.4 shows the summarised form of nonlinear effects in optical fibres.

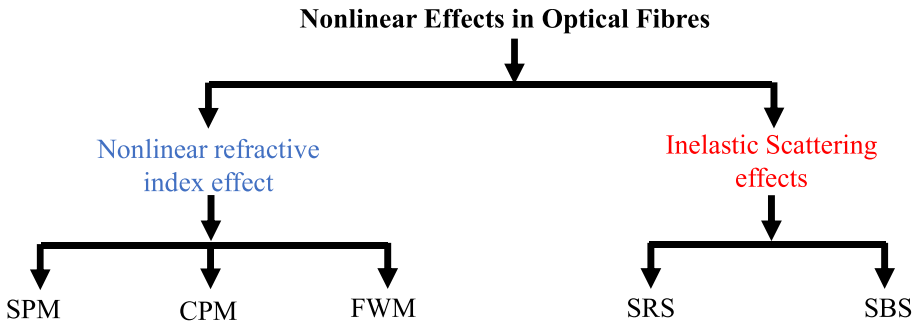

Fig. 2.4 Nonlinear effects in optical fibres

Nonlinear effects except SPM and CPM provides gain to some channel through power depletion from other channels. However, SPM and CPM affect the phase of the signal and result in the spectral broadening that leads to increased dispersion. These nonlinear phenomenons are explained below,

2.3.1 Self-phase modulation (SPM)

Self-phase modulation is a type of non-scattering nonlinearity which is related with the 3^{rd} order susceptibility $\chi^{(3)}$. SPM results from the change in the refractive index of the medium due to the propagation of high-intensity optical wave. Due to the optical Kerr effect, light wave creates a variation in the refractive index that results in the phase change of the propagating pulse. As a result of the phase change, the propagating pulse broadens in the frequency domain. This spectral broadening in of transmitted pulse can be calculated by taking the time-dependent derivative of the nonlinear phase shift as,

$$\Delta\omega_0(z,t) = -\frac{\partial\Phi_{(NL)}(z)}{\partial t} = -n_2\frac{dI_p(t)}{dt}k_0\, z \tag{2.19}$$

Here, $\Delta\omega_0$ is the change in the angular frequency, I_p is the optical intensity and k_0 is the wavenumber. Different parts of transmitted pulse undergo different phase shift due to intensity dependence of phase fluctuations that result in frequency chirping. As a result of the rising and trailing edges of the pulse experience frequency shift in upper and lower sides, respectively. The chirping effect increases with the increase in the transmitted power resulting in more pronounced SPM effect. SPM is different than dispersion as SPM creates spectral broadening while temporal distribution is unchanged. However, SPM is often exploited for two important applications such as solitons and pulse compression.

2.3.2 Cross-phase modulation (CPM)

As discussed above that SPM is a major nonlinear limitation in single channel systems. However, the intensity dependence of the refractive index also gives rise to cross-phase modulation (CPM) when two or more optical pulses propagate simultaneously. CPM also accompany with the SPM as the nonlinear refractive index seen by the optical beam not only depends on the intensity of the beam itself but also the co-propagating beams [47]. The total electric field of co-propagating beams can be written as,s,

$$E(x,y,t) = 1/2[E_1 e^{-j\omega_{01}t} + E_2 e^{-j\omega_{02}t}] + c.c \tag{2.20}$$

here, E_1 and E_2 are the electric fields of first and second optical signals, respectively. ω_{01} and ω_{02} are the angular frequencies of first and second copropagating signals, respectively. The nonlinear phase change can be written as,

$$\Phi_{NL}^{\omega_0 1}(z) = \gamma[|E_1|^2 + 2|E_2|^2] \tag{2.21}$$

In Eq. 2.21 the first term on the right-hand side comes from SPM while the second term is due to CPM. The strength of CPM increases with the increase in the number of channels

and further enhances when the channel spacing is less. There is no energy transfer between the channels due to CPM, which distinguishes it from the crosstalk process. Although, the strength of spectral broadening caused by CPM is twice that of SPM as shown in Eq. 2.21. The strength of CPM also depends on the interaction length of the fibre. The longer interaction length of the fibre result in a stronger CPM effect. Cross-phase modulation can be used in different applications such as optical switching and pulse compression.

2.3.3 Four-wave mixing (FWM)

Four-wave mixing (FWM) also originates due to the nonlinear response of bound electrons with the applied optical field. Like SPM, FWM also originates from third-order nonlinear susceptibility ($\chi^{(3)}$). When three optical fields with carrier frequencies ω_1, ω_2 and ω_3 copropagate simultaneously inside an optical fibre, a fourth field with frequency ω_4 gets generated. The relation between these three frequencies (ω_1, ω_2 and ω_3) and newly generated (ω_4) can be written as $\omega_4 = \omega_1 \pm \omega_2 \pm \omega_3$. In a multichannel system when signals are in phase with each other four-wave mixing can accumulate over long transmission distance and become a prominent effect. Some common applications of four-wave mixing include wavelength conversion, where data and probe signal are inserted in a nonlinear medium, and as a result of FWM, the incoming signal is converted to another wavelength.

Table 2.1 shows the comparison of nonlinear effects such as SPM, CPM and FWM on different characteristics in optical fibre.

2.4 Nonlinear scattering effects

Nonlinear scattering occurs due to inelastic scattering of a photon to a lower energy photon. The scattered optical power transfers from one mode to the same or other modes at a different frequency either in forward or backward direction. Nonlinear scattering depends critically

Table 2.1 Comparison of nonlinear effects in optical fibres [48]

Characteristics	**Nonlinear Phenomenon**		
	SPM	**CPM**	**FWM**
1. Bit-rate	Dependent	Dependent	Independent
2. Origin	Nonlinear susceptibility $\chi^{(3)}$	Nonlinear susceptibility $\chi^{(3)}$	Nonlinear susceptibility $\chi^{(3)}$
3. Effects of $\chi^{(3)}$	Phase shift due to pulse itself only	Phase shift is alone due to copropagating signals	New waves are generated
4. Shape of broadening	Symmetrical	May be a symmetrical	-
5. Energy transfer between medium and optical pulse	No	No	No
6. Channel Spacing	No effect	Increases on decreasing the spacing	Increases on decreasing the spacing

on the intensity of transmitted light and becomes significant above a certain threshold level. Stimulated Raman scattering (SRS) and stimulated Brillouin scattering (SBS) are two common types of nonlinear scattering effects described below,

2.4.1 Stimulated Raman Scattering (SRS)

Stimulated Raman scattering (SRS) is a nonlinear scattering process originates because of a slight modulation of material's refractive index due to incident light [49]. As a result of SRS, one pump photon is converted into a lower energy photon and a new phonon having the difference of energies is generated. The energy difference between pump photon ($\hbar\omega_P$) and slightly reduced energy photon ($\hbar\omega_S$) and resultant optical phonon ($\hbar\omega_V$) can be written as,

$$\hbar\omega_S = \hbar\omega_P - \hbar\omega_V \tag{2.22}$$

Spontaneous Raman scattering occurs at low illumination levels, where material's molecules are vibrating independently, and the scattered light is non-directional. However, when the intensity of incident light is increased the molecules of material can be considered as an array of vibrating oscillators, and the generated photons are coherent in phase. This result in a stronger stimulated Raman scattering process. Raman spectroscopy is an important application of Raman scattering being applied in the life sciences, molecular imaging of cells & tissues and medical diagnosis etc [50]. Raman scattering is also being used for distributed temperature sensing [51]. Moreover, SRS gain can be found at a largely shifted wavelength of the pump (13 THz of 100 nm at 1550 nm in silica); hence, it can also be used for wavelength conversion [52]. Typically SBS has gain bandwidth in GHz compared to SRS that has gain in THz. Agrawal, reported SBS gain spectrum of 40 THz over a large range of frequencies with a broad peak gain near 13 THz [53]. However, Brillouin gain spectrum of 12 GHz with three peaks at 10.0, 10.50, and 11.11 GHz is reported in [54].

2.4.2 Brillouin Scattering

Interaction of light and acoustic phonons is named after Leon Brillouin, who theoretically predicted inelastic scattering of light in 1922 [55]. Brillouin Scattering is an important optical effect that is caused by the nonlinearity of material, specifically related to acoustic phonons. Due to electrostriction, incident light wave when travelling through a medium produces mechanical vibrations in the medium and converts into scattered light and phonons [56]. Scattered light propagates in both forward and backward direction of the fibre, however, forward Brillouin scattering is very weak in comparison with the backward scattering also known as Stokes wave. The scattered light is down-shifted in frequency which is typical of low intensity. However, due to the geometry of fibre, where light can travel tens of kilometres without any significant attenuation, light scattering becomes an unavoidable effect. Detail discussion of Brillouin scattering is presented in Chapter 3.

2.5 Computational electromagnetics

With the development of optical fibres in the late 1960s, several methods were proposed to analyse the propagation of electromagnetic waves in optical waveguides. The propagation of EM waves can be mathematically described using Maxwell's equations that form a system of coupled first-order partial differential equations.

James Clerk Maxwell [1831-1879] was a Scottish physicist who first published the unified theory of electricity and magnetism. It was the first time that he determined the speed of electromagnetic (EM) waves propagation inside a vacuum and found that these waves travel at the speed of $3.00 \times 10^8\ m/s$. Maxwell put together the experimental laws (Ampere's law, Faraday's law) into the form of four equations that are mentioned below. These equations can be represented as both integral or differential form. Differential form of equations is mostly used for solving analytical and numerical problem whereas, the integral form of Maxwell's equation describes the underlying physics laws. Differential form of Maxwell's equation for time-varying electromagnetic fields are:

$$\nabla \cdot \mathbf{D} = \rho \tag{2.23}$$

$$\nabla \cdot \mathbf{B} = 0 \tag{2.24}$$

$$\nabla \times \mathbf{E} = -\frac{\partial \mathbf{B}}{\partial t} \tag{2.25}$$

$$\nabla \times \mathbf{H} = \frac{\partial \mathbf{D}}{\partial t} + \mathbf{J} \tag{2.26}$$

where,

$\mathbf{D}$ = electric flux density (Cm^{-2})

$\mathbf{B}$ = magnetic flux density (Wbm^{-1})

$\mathbf{E}$ = electric field intensity (Vm^{-1})

$\mathbf{H}$ = magnetic field intensity (Am^{-1})

$\mathbf{J}$ = electric current density (Am^{-2})

ρ = electric charge density (Cm^{-3})

Equation 2.23 is the Gauss's law of electrostatics and Eq. 2.24 is the Gauss's law of magnetostatics that are the result of Maxwell's curl equation. Similarly, Eq. 2.25 and Eq. 2.26 are known as the Faraday's law and Ampere's law, respectively.

These Maxwell's equation can be written in a system of four first-order differential equations, a pair of coupled second order differential equations or a fourth order single differential equation by a careful elimination of field components. In 1973, Dil and Blok [57] introduced accurate numerical methods to solve the differential equation that is further expanded by Vassell [58] a year later. With the development of fast digital computers, numerical simulation and modelling have become an essential tool for understanding photonic devices. Based on different numerical methods such as finite-element method [59], finite difference frequency domain method [60], frequency difference time domain method and integral-equation methods different software and in house codes are developed. Some of the well-known numerical methods used to solve the electromagnetic waveguides are:

2.5.1 Finite Element Method (FEM)

Finite element method provides an approximate solution by the discretisation of a larger problem into smaller sub-domain elements. In FEM, instead of solving a large domain in one go, it is divided into sub-domains in a simplistic manner and solution for each element is expressed in terms of values at elements nodes. Then these individual element solution results in the global form of the original domain. A detailed discussion of FEM process is given in Chapter 4.

2.5.2 Finite Difference Frequency Domain (FDFD) Method

The FDFD is a useful numerical method to determine the steady-state time-harmonic solution at a single frequency, as it does not need any time stepping like in case of the FDTD method. FDFD method is beneficial for the waveguide and resonating problems that are associated with the single frequency solution. However, to find out the frequency response with the FDFD method, multiple simulations are required, one for each frequency. Hence, it limits the resolution of spectral response to the limited number of computer simulations.

2.5.3 Finite Difference Time Domain (FDTD)

The FDTD is considered a simple numerical method, both conceptually and in terms of implementation as the derivation of differential equations is considered as straight forward [61]. The FDTD can solve the complicated problem, but it needs more computational resources and memory. In terms of advantages, FDTD needs short development time, it has ease of comprehension due to simple discretisation procedure, and no linear algebra of matrix inversion is needed. However, on the disadvantages side, due to the orthogonal grid structure of the FDTD accuracy is reduced on the curve boundaries.

2.6 Summary

In this chapter, the basic principles of optical fibre guidance and mode theory of cylindrical waveguides are discussed. Some of the characteristics of optical fibres are also presented that includes phase & group velocity and different types of dispersion effects. Moreover, the nonlinear effects due to refractive index change such as self-phase modulation, cross-phase modulation and four-wave mixing are discussed. A short description of two important nonlinear scattering effects Raman scattering and Brillouin scattering is also provided. Later in the chapter, some computational methods such as the finite element method, finite

difference frequency domain method and frequency difference time domain method to solve the electromagnetic wave propagation in optical waveguides are also discussed.

Chapter 3

Light Scattering and Acoustic Wave Theory

3.1 Introduction

In nature, the light we see through our eyes is emitting directly from the source or just a reflection. For example, light from the moon is only a reflected light emitted by the sun and blue sky above us is the scattering of light due to molecules in the atmosphere. Light scattering is also considered as an important phenomenon in optical waveguides that is mainly due to density fluctuations, impurities and thermal particles motion in optical medium [62]. Light scattering can be of two types, linear or nonlinear scattering.

- **Linear Scattering**, where incident optical wave does not affect the medium's optical properties. Linear scattering can be categorised as elastic and inelastic scattering. During elastic scattering such as Rayleigh scattering, the transmitted photon keeps its energy, and no optical frequency shift occurs. In inelastic scattering, an energy exchange occurs between incident optical wave and the material that results in a change

in the frequency of the scattered wave. Raman scattering and spontaneous Brillouin scattering are examples of inelastic linear scattering.

- **Nonlinear Scattering**, When dielectric materials are exposed to an external electric field, a slight displacement in the ions of crystal lattice occurs known as electrostriction. In nonlinear scattering, the properties of the material also change along with the incident optical wave. Stimulated Brillouin scattering is an example of nonlinear scattering that occurs due to electrostriction. Moreover, stimulated Raman scattering is also an example of nonlinear scattering that occurs when molecules of medium absorb pump photon, and as a result, it induces some vibrations or rotational states in it. This result in the emission of a photon having frequency shifted from the molecule frequency.

3.2 Brillouin Scattering

Brillouin scattering can occur even when the intensity of incident light is low, and medium undergoes thermally induced fluctuations known as spontaneous Brillouin scattering [63]. These mechanical vibrations create variation in the medium's density and modulate its refractive index. Effectively, propagating light in medium creates an index grating that scatters light in the backward and forward direction [64]. Above a specific input power the Brillouin scattering process becomes stimulated and optical field generates a substantial amount of phonons through two different mechanisms [65]. One is due to electrostriction, in which medium density increases due to the presence of high optical intensity. The second mechanism is absorption, in which heat is generated and the material expands in the presence of high optical intensity.

SBS is a non-linear process which is directly linked to the input power. Two-way interaction of electromagnetic and mechanical wave results in the generation of the acoustic

wave in the guided material. The input optical power at which the back reflected (Stokes wave) power increases rapidly or became comparable with input power is called the stimulated Brillouin scattering threshold (SBST).

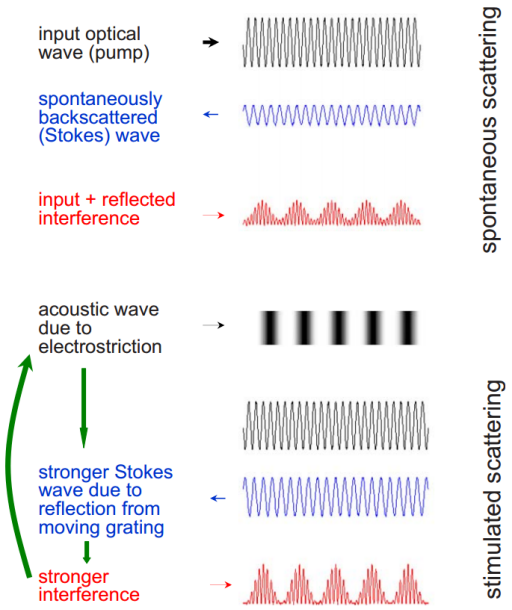

Fig. 3.1 Spontaneous and stimulated Brillouin scattering [66]

Figure 3.1 explains the spontaneous and stimulated Brillouin scattering phenomenon. As it can be seen that, the back-scattered light (shown in blue) interferes with the forward propagating light (pump) wave (shown in black) and creates an interference pattern along the medium length, which is shown in red colour. This back reflected Stokes wave constructively add up with the already back-reflected wave that had started the process of acoustic phonons generation. This process continues until Stokes and acoustic wave gain significant amplitude. Stimulated Brillouin scattering is a more efficient process compared to spontaneous Brillouin scattering and can be exploited for many potential applications.

The physical process of SBS is schematically illustrated in Fig. 3.2. Where the blue arrow shows the forward propagation of pump light and acoustic wave and backward propagation is shown by the red arrow. The amplitudes of incident pump wave, scattered Stokes wave and acoustic vibration are represented by E_p, E_s and U respectively. The law of energy and

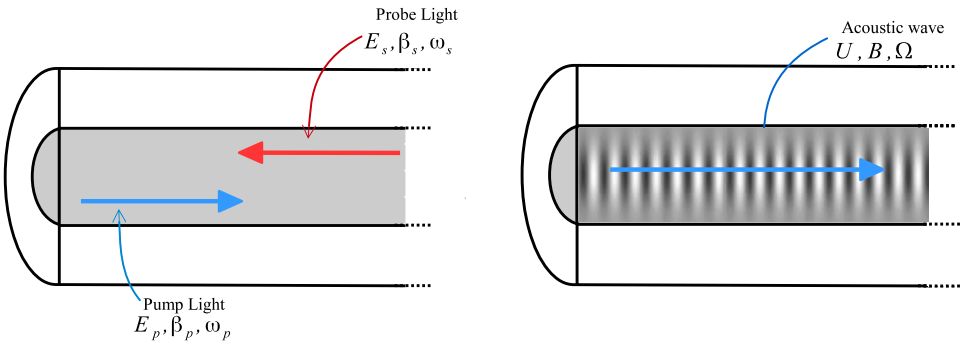

Fig. 3.2 Schematic representation of SBS process showing (a) pump light, probe light and (b) acoustic wave.

momentum conversation must be followed, which results in the relation between angular frequencies of pump photon (ω_p), stokes photon (ω_s) and the acoustic phonon (Ω).

$$\omega_s = \omega_p - \Omega \tag{3.1}$$

Similarly, for the corresponding wave vectors $\vec{\beta}_p$, $\vec{\beta}_s$ and $\vec{B}$, the momentum conservation is required.

$$\vec{\beta}_s = \vec{\beta}_p - \vec{B} \tag{3.2}$$

The respective wavelengths are obtained by

$$\vec{\beta}_p = \frac{2\pi n}{\lambda_p} \qquad \vec{\beta}_s = \frac{2\pi n}{\lambda_s} \qquad \vec{B} = \frac{2\pi}{\lambda_B} = \frac{\Omega}{V_a} \tag{3.3}$$

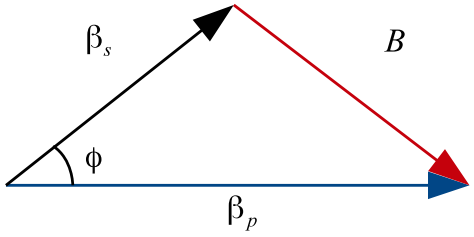

Fig. 3.3 Vector relation between Pump and Stokes waves

From Fig. 3.3 the conservation of momentum with angle ϕ between the pump and the Stokes wave can be written as

$$|\vec{B}| = |\vec{\beta}_p| + |\vec{\beta}_s| - 2|\vec{\beta}_p||\vec{\beta}_s|cos\phi \tag{3.4}$$

From Eqs. 3.3 and 3.4, the relations for the Brillouin frequency shift can be derived as

$$\Omega = \frac{2nV_a}{\lambda_p} sin(\frac{\phi}{2}) \tag{3.5}$$

where $\lambda_p = \frac{c}{\omega_p}$ and Eq. 3.5 can be written as,

$$\Omega = 2V_a \frac{\omega_p n}{c} sin\frac{\phi}{2} \tag{3.6}$$

Here, $\beta_s \approx \beta_p = (\omega_p n)/c$, approximation is used because of the small relative frequency shift of the scattered phonon $\Omega \ll \omega_{p,s}$. As mentioned earlier that the Brillouin frequency shift is highly dependent on the scattering angle ϕ. Hence, from Eq. 3.6 it can be stated that when the angle $\phi = \pi$, Brillouin shift has the maximum value and scattering is in the backward direction. Similarly, when $\phi = 0$, Brillouin shift approaches to zero ($\Omega \to 0$) and has forward propagation direction.

SBS can occur in all states of matter like solids, liquids, gases and plasma. Different factors play an important role in the selection of optimum material for SBS such as acoustic frequency, Brillouin gain coefficient, acoustic wave decay time etc. [67]. Some other factors such as phonon's lifetime light absorption in the medium and pulse duration are also kept in mind for the material selection.

3.2.1 Applications of Brillouin Scattering

SBS is considered an important limitation in the power delivery for amplification and long-haul propagation of optical signals in the fibres. Different methods are used to increase the Brillouin threshold in optical fibres to increase the transmission power. These techniques include reducing the fibre length, doping the fibre with different material that results in Brillouin shift and exploitation of longitudinally varying temperature in high power active devices [68]. Some attempts to reduce the overlap between optical and acoustic wave, or to attenuate the acoustic wave by introducing propagation losses are also presented. However, SBS can be exploited for some key applications such as Brillouin gain amplifiers, fibre ring lasers, temperature and pressure sensors.

3.2.2 Radio-over-Fibre technology

Radio over fibre (RoF) is the transmission of radio signals over an optical fibre, where, data can be transmitted over a longer distance without significant degradation. However, higher transmission power is required for the access networks in which data is usually distributed to many subscribers. Services such as 3G/4G cellular communication, wireless data transmission in WiMAX (Worldwide interoperability for microwave access) or WLAN (Wireless local area network) are becoming high bandwidth demanding applications [69]. Such distributed RoF systems are based on passive optical networks (PON) with many optical splitting ratios (32x to 128x). This large splitting ratio needs high input power such that each subscriber get the optimum power at the receiver end. However, SBS has a significant impact on the optical power enhancement, and it deteriorates the transmitted signal, resulting in a low quality of the received signal. Introduction of high SBS threshold fibre is very beneficial in improving the performance and the cost of the fibre to the home (FTTH) access networks [70, 71]. Error vector magnitude (EVM) is used to check the performance of radio over fibre links. EVM is improved as we increase the input power in an optical link. However, after

a certain level SBS starts to deteriorate the quality of the signal. A significantly improved EVM has been discussed in [66], by using high SBST fibre in a network having 32x splitting ratio and 20 km length with a maximum achieved transmission power of +17 dBm.

3.2.3 SBS based fibre optic sensors

Stimulated Brillouin is a light scattering process that occurs due to the sound waves generated by propagating pressure inside optical fibre also known as density waves [72]. Sound waves have properties of mechanical waves and sensitive to temperature and strain, hence, SBS can be used to design fibre based sensors for the measurement of temperature and strain. The SBS based sensors can work as point sensor, quasi-distributed sensors [73]. Figure 3.4, shows a general configuration of fibre based sensors. The point sensors are used where

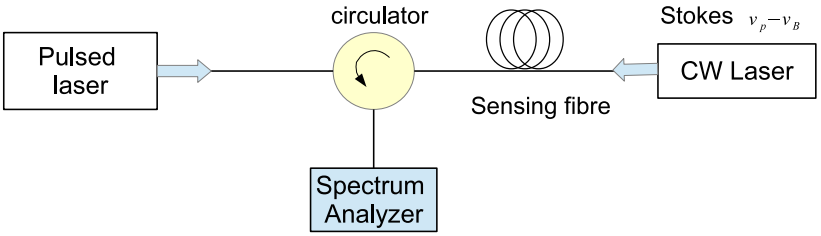

Fig. 3.4 Schematic diagram of SBS-based sensing setup

the point of interest is at one location. To form a point sensor, two similar optical pulses having frequency difference equals to the Brillouin resonance are transmitted in the opposite direction in a fibre. The overlapping regions of both pulses form a transient Brillouin grating (TBG) which depends on the length of pulse. The lifetime of the transient Brillouin grating is very small similar to the phonon lifetime (10 ns). The spectrum of the grating is the resultant of convolution between Brillouin gain spectrum and pulse spectrum. The Brillouin grating can be probed using a 3^{rd} pulse transmitted orthogonal to the fibre axis. The drawback with single point sensors is that it is hard to acquire a series of information. In contrast, distributed sensing provides the measurement along the entire length of the fibre. Distributed sensing using fibre optic is a unique technique compared with other electrical cables because of

flexibility, ruggedness and can be read through time domain reflectometer. Similarly, a single optical fibre is used to measure at many points replacing thousands of single point sensors which reduces calibration and maintenance cost and reduction in installations. Distributed sensing technique involves the analysis of backscattered light signal created at different points along the fibre length. Distributed sensing in the entire fibre is achieved by varying the relative delay between two pump pulses. This result in a large frequency shift having an order of 40-50 GHz that increases the measurement accuracy of strain and temperature compared with the Brillouin gain measurement technique.

Sensing fibre is integrated with the installations (like pipelines, structures or cables). One of the example using SBS based distributed fibre sensors is the monitoring of temperature in a large dam in Switzerland. The distributed sensing fibre was installed during the concrete pouring process [74]. Temperature variations during the chemical process can be used to find out the microcracks and concrete density.

3.2.4 SBS in Raman-Pumped fibres

Raman amplifiers use optical fibre as an active medium and widely used in the communication systems. The distributed nature of the Raman amplifier has a high signal to noise ratio and transmission bandwidth compared with erbium-doped fibre amplifiers (EDFA) [75]. Stimulated Raman scattering (SRS) has a similar phenomenon as of stimulated Brillouin scattering. In Brillouin scattering light interacts with acoustic phonons whereas in Raman scattering, light interacts with photons. It is due to the oscillation frequency of neighbouring crystal planes that lies in the infrared region. In Raman scattering process dispersion curve of the optical photons is flat near the centre [66]. There is a slight dependence of angle between the input wave vector and the scattered light wave vector. Whereas, in the SBS process Brillouin gain has a high dependence on the angle between the pump and scattered light wave. This allows Raman scattering to be equally efficient in both forward and backward

direction. However, the frequency offset of Raman scattering is much higher compared with the Brillouin scattering. A much higher gain (20dB) can be achieved in the Raman amplification process. But the amplified signal can approach to the SBS threshold especially in forward Raman amplification. In Silica fibres, Brillouin gain has intrinsic bandwidth of typically 50-100 MHz and Brillouin frequency shift of 10-20 GHz. The Raman amplifier has a much higher bandwidth compared with the Brillouin frequency shift. This result in the amplification of not only the pump signal but also the Stokes signal. Therefore, the input signal will experience amplification from both stimulated Raman scattering and SBS. Hence gain of Raman amplification become saturated due to SBS threshold [76]. Different techniques are proposed to minimise the effect of SBS on Raman gain. Multimode semiconductor lasers with a linewidth of a few hundred megahertz can be used to reduce the Brillouin gain. The problem with this technique is that semiconductor lasers have limited output power which limits the maximum achievable Raman gain. Another approach could be the use of ultrashort pump pulses in the backward configuration [77]. This will suppress SBS if the pulse duration is much shorter than the inverse Brillouin linewidth. But the problem with this technique is that Raman gain is dependent on the average pump power and pulsed pump mode of operation results in the reduced laser power.

3.2.5 Slow light or optical delay lines using SBS

SBS is one of the important techniques to generate slow light or optical delay lines, that is a major research interest in recent years. Group refractive index of the medium is increased $n_g \gg 1$ by the modification in the dispersion of optical waveguide. This result in the group velocity of the propagating light to be significantly lower than the phase velocity. Narrow Spectral resonance of medium caused by the SBS process modifies the refractive index of the medium. These narrow spectral resonances are responsible for changing the group velocity

of the pulse signal. Equation 3.7 shows the pulse delay ΔT_m due to the m^{th} acoustic mode resonance,

$$\Delta T_m = \frac{\gamma_m P_p L}{2\pi\omega_m} \tag{3.7}$$

Here, a pulse is delayed relative to its propagation time when (γ_m) is positive (gain) and $\Delta T_m > 0$ for Stokes pulse. Similarly, for anti-Stokes pulse above $\gamma_m < 0$, fast light is realised and the pulse is attenuated. The resonant caused by SBS process has the advantage of controlling the pulse duration over other pulse delaying techniques like coherent population oscillation or electromagnetically induced transparency.

Slow light or delay lines using SBS have important applications in telecommunication equipment and moderate pump power sources because of its standard telecom operating windows and room temperature operation [78]. Similarly, optical delay lines can be used for signal processing and synchronisation, jitter compensation and microwave applications. SBS based delay lines that can control pump signal were demonstrated in 2005, where a 2 ns pulses at ($\lambda = 1.55\ \mu m$) was stored for up to 12 ns using a highly non-linear fibre [79]. To introduce the optical delay in an optical signal, a counter-propagating pump signal with a different wavelength is transmitted inside the optical fibre. If the wavelength difference between the pump signal is equal to SBS acoustic frequency, variation in the refractive index is obtained that slows the transmitted light. However, due to SBS gain, the signal strength also gets increased. Later on, many techniques were proposed that includes direct modulation of pump laser with the noise signal that results in the uniform SBS gain spectrum of 325 MHz [80]. Similarly, in [81], SBS spectrum of 12 GHz was achieved through which higher transmission data rate signal ($\sim$10 Gbps) can be delayed. Overall, significant improvements are demonstrated that resulted in an error-free optical delay in high data rate transmission systems.

3.3 Acoustic wave theory

To understand stimulated Brillouin scattering in detail, understanding of acoustic waves is essential. This section provides some theoretical background of acoustic wave propagation and some literature review.

Sound waves are mechanical waves that are generated by the periodic vibrations in the medium. These mechanical vibrations transfer energy from one end to another end of the medium. In a medium, acoustic waves are generated by the time-varying displacement of atoms or particles from their equilibrium position. This change produces a restoring force that introduces the oscillatory motion in the medium. Acoustic waves propagate in a medium by the displacement of particles along the transverse or longitudinal direction.

Acoustic modes in waveguides are of different nature that includes shear, longitudinal, bending, torsional and flexural modes [82]. A waveguide can support these different modes by ensuring one of the velocities either longitudinal or shear in the cladding is higher than that in the core. Acoustic waves undergo different material properties that are defined as elasticity, density, Poisson's ratio and Young's modulus [83]. Acoustic wave propagation is expressed in terms of tensors or their interrelation. As the geometry of most of the solids is not purely symmetric; hence the formulation to represent the acoustic waves get complicated. However, for the sake of simplicity, it can be considered that the acoustic waves are either pure shear or longitudinal type and their corresponding tensor quantities such as stress, strain, elasticity particle velocity and particle displacement can be expressed in one-dimensional form. One dimensional representation of acoustic wave propagation is discussed in this chapter. However, later on, 2D formulation in a uniform waveguide is also presented. It should be noted that the guided wave solutions are assumed to have a dependence on $\exp^{-jkz}$, where z is the direction of wave propagation and k is considered as acoustic propagation constant.

3.4 Acoustic waves in nonpizoelectric materials

Piezoelectric materials have the ability to generate an electric current in response to applied mechanical stress. In order to avoid the current due to stress and strain in the material, nonpiezoelctric materials are used for the study of acoustic wave propagation. Shear and longitudinal are among the most important types of acoustic waves [84]. In the case of shear waves, the motion of the particles is perpendicular (transverse) to the direction of wave propagation as shown in Fig. 3.5 (a). Similarly, in the case of longitudinal waves, the direction of medium particles is in the direction of wave propagation. This motion of particles results in the medium's expansion and contraction in the z-direction. Figure 3.5

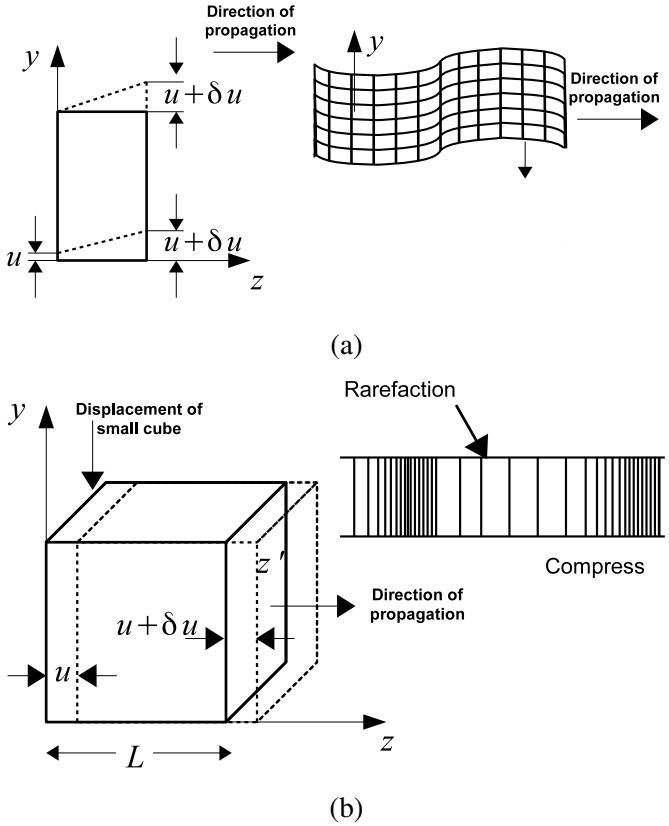

Fig. 3.5 (a) Shear and (b) Longitudinal waves propagation [85]

(b) shows the rarefaction or compression that occurs due to the longitudinal waves. For the shear waves, the particles do not displace equally along the cross-section as in longitudinal

waves, and this results in the density variation in the transverse plane. However, for the sake of simplicity, the density variation in the shear wave propagation is neglected, and it can be considered that there is no density or volume variation.

Generally, an acoustic wave consists of both shear and longitudinal waves while propagating in a medium. Here, propagation is considered only along one axis and formulation for longitudinal waves is derived. Similarly, the formulation for shear waves will have similar results.

3.4.1 One dimensional stress

Stress and strain are highly related to the propagation of acoustic waves. Stress (T) is the applied force per unit area whereas, the strain is the response or the change in the medium with the application of stress. Stress causes medium to deform, and the strain is known as the amount of deformation caused by the applied stress divided by the original dimensions of the medium. In the perspective of acoustic wave propagation, the strain and its effects are considered in the one dimension which can be either in the form of compression or rarefaction. For longitudinal waves in the material of length, L and direction of wave propagation z plane, applied stress on the left-hand side is taken as negative and on the right-hand side it is taken as positive as shown in Fig. 3.6 (a). Similarly, for the transverse wave, the applied stress is taken as positive in the +y direction or +x direction as shown in Fig. 3.6 (b). The change in the length on each side of the slab when the external stress is applied is taken as $L(\frac{\partial T}{\partial z})$. Hence, the force required to move a unit volume of the mass is defined as $\frac{\partial T}{\partial z}$.

3.4.2 One dimensional displacement and strain

Due to applied force in the z-plane as shown in Fig. 3.5 (b) the longitudinal stress introduces a change in the z-direction by an amount of u and in some other direction z' after a distance L, the displacement is change to $u+\delta\ u$. Using Taylor expansion, the first order change in the

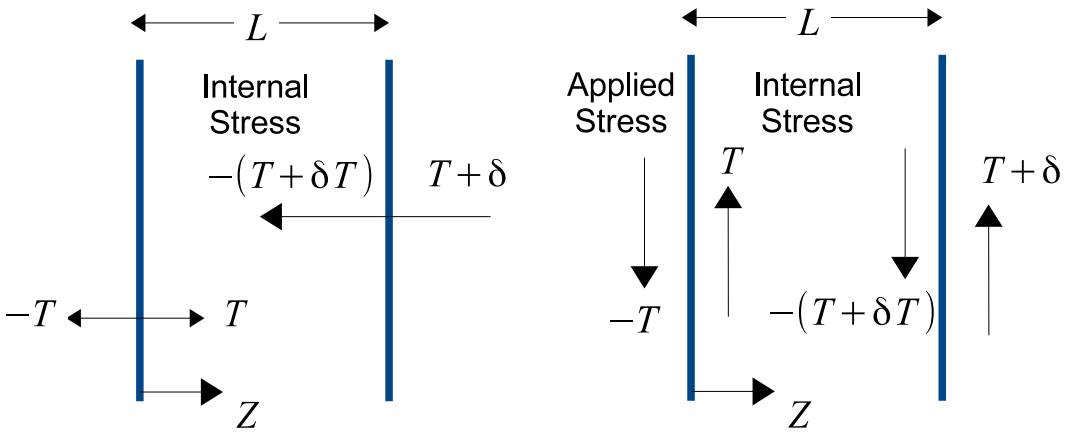

Fig. 3.6 (a) Stress in the longitudinal direction and (b) stress in the transverse direction for a slab of infinite length L [86]

u in a unit length of L can be expressed as

$$\delta u = L\frac{\partial u}{\partial z} = LS \tag{3.8}$$

and the fractional extension also known as strain which can be defined as,

$$S = \frac{\partial u}{\partial z} \tag{3.9}$$

Here, u is the displacement, and it is a function of z. If the material undergoes in a constant displacement u throughout all material then it is known as the bulk translation that is out of the discussion. Similarly, for the transverse displacement, Eq. 3.9 will remain same but u is the transverse displacement (x or y-direction). From the Fig. 3.6 (b) it can be seen that there is no area change occur due to the shear motion of medium particles. Whereas, in case of longitudinal motion shown in Fig. 3.6 (a) the volume change is $A\partial u$ where, A is the area of x, y face. Hence, the relative volume change can be written as $\frac{\partial \forall}{\forall} = \frac{A\partial u}{LA} = \frac{\partial u}{L} = S$. From

the Hook's law, a one-dimensional form of stress and strain relation can be written as,

$$T = CS \tag{3.10}$$

Equation 3.10 represents the one dimensional model for shear and longitudinal wave propagation. Here C is the material elastic constant, T and S are the stress and strain, respectively.

3.4.3 Equation of motion

From the Newton's second law of motion, force applied per unit area of the material $L(\frac{\partial T}{\partial z})$ can be written as,

$$\begin{aligned} F = ma &= \rho \bigvee \dot{v} \\ \Rightarrow \frac{F}{\bigvee} &= \rho \dot{v} \\ \Rightarrow \frac{F}{\partial x \partial y \partial z} &= \rho \dot{v} \end{aligned} \tag{3.11}$$

$$\begin{aligned} \Rightarrow \frac{T}{\partial z} = \rho \dot{v} \qquad & [as \quad T = \frac{F}{\partial x \partial y}] \\ therefore \quad & \frac{\partial T}{\partial z} = \rho \dot{v} = \rho \ddot{u} \end{aligned}$$

Here, v is the velocity, u is the displacement, $\bigvee$ is the volume, m is the mass, ρ is the density, and a is the acceleration and $(\dot{})$ denotes time derivative.

3.5 Tensor notation and constitutive relations

One dimensional shear and longitudinal wave interaction is discussed in this section, where, the wave propagation is considered along a symmetry axis of a crystal. For quantitative calculations, Hook's law, equation of motion and the elastic parameters of the crystal needed to be explained and then reduce them to one-dimensional term. In the subsection, a tensor notation is introduced, and for the simplification of the equations, a reduced subscript notation is also introduced.

3.5.1 Displacement and strain relation

The displacement vector $\boldsymbol{u}$ consists of three u_x, u_y and u_z components. At a given position, these three components may be function of Cartesian components *x, y, z*. Hence, Strain (**S**) is a tensor that consist of nine components with the variation of u_i, where, i is the Cartesian coordinate. For example,

$$S_{xx} = \frac{\partial u_x}{\partial x} \tag{3.12}$$

and

$$S_{xy} = \frac{1}{2}\left[\frac{\partial u_x}{\partial y} + \frac{\partial u_y}{\partial x}\right] \tag{3.13}$$

where, $S_{xy} = S_{yx}$ due to symmetry notation and similar forms can be written for S_{xx}, S_{xy}, S_{xz}, S_{yx}, S_{yz}, S_{zx}, S_{zy} and S_{zz}. Moreover, just one component S_{xx} or S_{zz} to represent longitudinal strain and for the shear strain S_{xy} is sufficient.

3.5.2 Stress in a rectangular cube

$$\textbf{Shear Stress}: \qquad T_{zx} = \frac{F_x}{\delta x \delta y} \tag{3.14}$$

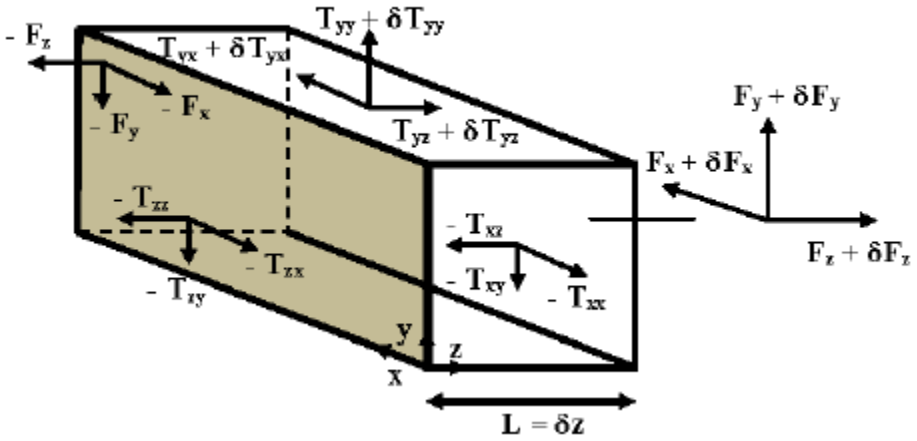

Fig. 3.7 Stress components in a rectangular cube [83].

$$\textbf{Shear Stress}: \qquad T_{zy} = \frac{F_y}{\delta x \delta y} \tag{3.15}$$

and,

$$\textbf{Longitudinal Stress}: \qquad T_{zz} = \frac{F_z}{\delta x \delta y} \tag{3.16}$$

In above tensor **T**, the first subscript shows the coordinate axis perpendicular to the shaded plain and the second subscript shows the axis parallel to the traction force. There are total nine stress components in which three components T_{xx}, T_{yy} and T_{zz} are related to longitudinal stress and other six components $T_{xy} = T_{yx}$, $T_{xz} = T_{zx}$ and $T_{yz} = T_{zy}$ are related to shear stress. These shear stress components are shown in equal in pairs because the internal stresses in the cube does not raise any net rotation. This result in the reduction of nine components into six components as mentioned below,

$$\mathbf{T} = \begin{bmatrix} T_{xx} & T_{xy} & T_{xz} \\ T_{yx} & T_{yy} & T_{yz} \\ T_{zx} & T_{zy} & T_{zz} \end{bmatrix} = \begin{bmatrix} T_1 & T_6 & T_5 \\ T_6 & T_2 & T_4 \\ T_5 & T_4 & T_3 \end{bmatrix} = \begin{bmatrix} T_1 \\ T_2 \\ T_3 \\ T_4 \\ T_5 \\ T_6 \end{bmatrix} \tag{3.17}$$

The net resultant force per unit volume in the z-direction of an infinitesimal cube can be written as,

$$f_z = \frac{\partial T_{zx}}{\partial x} + \frac{\partial T_{zy}}{\partial y} + \frac{\partial T_{zz}}{\partial z} \tag{3.18}$$

Using equation of motion described in Section 3.4.3, Eq. 3.18 can be written as,

$$\rho \ddot{u}_z = \rho \dot{v}_z = \frac{\partial T_{zx}}{\partial x} + \frac{\partial T_{zy}}{\partial y} + \frac{\partial T_{zz}}{\partial z} \tag{3.19}$$

Similarly, equations for other components of u and v can be calculated. The full tensor form of Eq. 3.19 in the z-direction can be written as

$$\rho \frac{\partial^2 u_z}{\partial t^2} = \frac{\partial T_{zx}}{\partial x} + \frac{\partial T_{zy}}{\partial y} + \frac{\partial T_{zz}}{\partial z} \tag{3.20}$$

and in the form of reduced notation Eq. 3.20 can be written as,

$$\rho \frac{\partial^2 u_z}{\partial t^2} = \frac{\partial T_5}{\partial x} + \frac{\partial T_4}{\partial y} + \frac{\partial T_3}{\partial z} \tag{3.21}$$

In a similar way, the relations of equation of motions in the x and y-direction can be derived. Moreover, an often used symbolic notation is also expressed below,

$$\nabla \cdot \mathbf{T} = \hat{x}\left(\frac{\partial T_{xx}}{\partial x} + \frac{\partial T_{xy}}{\partial y} + \frac{\partial T_{xz}}{\partial z}\right) + \hat{y}\left(\frac{\partial T_{yx}}{\partial x} + \frac{\partial T_{yy}}{\partial y} + \frac{\partial T_{yz}}{\partial z}\right) + \hat{z}\left(\frac{\partial T_{zx}}{\partial x} + \frac{\partial T_{zy}}{\partial y} + \frac{\partial T_{zz}}{\partial z}\right) \quad (3.22)$$

and in a compact form Eq. 3.22 can be written as,

$$(\nabla \cdot \mathbf{T})_i = \sum_i \frac{\partial T_{ij}}{\partial u_j} \qquad i, j = x, y, z. \quad (3.23)$$

and using Cartesian coordinates, the translation equation of motion can be written as,

$$\frac{\partial T_{ij}}{\partial u_j} = \rho \frac{\partial^2 u_i}{\partial t^2} - F_i \quad (3.24)$$

where, F_i is the applied external force, which is considered zero for this case.

3.5.3 Elasticity coefficients and Hook's law

Hooks's law states that the stress and strain are proportional to each other when there is a small distortion or displacement occurs. Hook's law states that the stress and strain are proportional to each other when there is a small distortion or displacement occurs and material remains in elastic regime. General representation of Hook's law for a two dimensional structure can be written as,

$$T_{ij} = C_{ijkl} S_{kl} \quad (3.25)$$

Here, T_{ij} and S_{kl} are the stress, and strain tensors and both have nine elements each. Whereas, the C_{ijkl} is the stiffness matrix and consist of 81 (9x9) elements. When symmetry conditions are applied, the above mentioned stiffness matrix can be reduced to 36 elements. Similarly, the independent elements of stress and strain matrix can be reduced to 6 each after exploiting the symmetry conditions. By applying symmetry conditions Equation 3.25 can be expressed

as,

$$[T] = [C][S] \tag{3.26}$$

the subscripts i and j used in Equation 3.25 represents one of the three axes of interest in tensor elements. Whereas, k and l are floating subscripts. Stress T_{ij}, and strain S_{kl} are symmetric in nature that also reflects in the stiffness tensor, C_{ijkl} and results in a symmetric matrix. Stiffness tensor satisfies the two symmetry conditions that are mentioned below,

$$\textbf{Reciprocity}: \qquad C_{ijkl} = C_{klij} \tag{3.27}$$

$$\textbf{Lack of rotation}: \qquad C_{ijkl} = C_{jikl} = C_{ijlk} = C_{jilk} \tag{3.28}$$

These symmetry conditions result in the reduction of 81 independent elements in the fourth order of anisotropic crystal to only 21 independent elements. Similarly, exploiting this symmetry condition, independent constants can be reduced to only 2 in an isotropic crystal. These two independent elements are the Lame constants (λ and μ) [87].

3.5.4 Reduced subscript representation

The reduced subscript notation is used to represent the stress, strain and stiffness notations. The longer notations like S_{kl} and T_{ij} are replaced with the S_R and T_R respectively. Table 3.1 shows the reduced notation used for stress and strain tensor elements.

Similarly, Table 3.2 shows the reduced subscript notation used for stiffness tensor elements.

Based on the reduced stress and strain tensor notation from Table 3.1 and reduced stiffness notation from Table 3.2, Eq. 3.25 can be written as,

$$T_R = C_{IJ} S_R \tag{3.29}$$

Table 3.1 Reduced subscript notation for stress and strain tensor elements [85]

Tensor Element	All Elements	Connotations
Stress: T_R	T_1 (where R=1 = T_{xx})	Longitudinal stress in the x-direction
	T_2 (where R=2 = T_{yy})	Longitudinal stress in the y-direction
	T_3 (where R=3 = T_{zz})	Longitudinal stress in the z-direction
	T_4 (where R=4 = T_{yz})	Transverse stress about the x-axis
	T_5 (where R=5 = T_{zx})	Transverse stress about the y-axis
	T_6 (where R=6 = T_{xy})	Transverse stress about the z-axis
Strain: S_R	S_1 (where R=1 = S_{xx})	Longitudinal strain in the x-direction
	S_2 (where R=2 = S_{yy})	Longitudinal strain in the y-direction
	S_3 (where R=3 = S_{zz})	Longitudinal strain in the z-direction
	S_4 (where R=4 = $2S_{yz}$)	Transverse strain: motion about x-axis, shear in the y and z-direction
	S_5 (where R=5 = $2S_{zx}$)	Transverse strain: motion about y-axis, shear in the x and z-direction
	S_6 (where R=6 = $2S_{xy}$)	Transverse strain: motion about z-axis, shear in the x and y-direction

Table 3.2 Reduced subscript notation for stiffness tensor elements [85]

Standard notation	Reduced notation	Connotations
C_{ijkl}	C_{IJ}	The ratio of the I^{th} stress component to the J^{th} strain component
C_{1111}	C_{11}	The longitudinal elastic constant relating longitudinal stress and strain elements in the x-direction
C_{2323}	C_{44}	The shear elastic constant relating shear stress and strain elements in the 4-direction (motion about x-axis)
$C_{1122} = C_{2211}$	$C_{12} = C_{21}$	$C_{IJ} = C_{JI}$

Similarly, the matrix representation of Equation 3.29 can be written as,

$$\begin{bmatrix} T_1 \\ T_2 \\ T_3 \\ T_4 \\ T_5 \\ T_6 \end{bmatrix} = \begin{bmatrix} C_{11} & C_{12} & C_{13} & C_{14} & C_{15} & C_{16} \\ C_{21} & C_{22} & C_{23} & C_{24} & C_{25} & C_{26} \\ C_{31} & C_{32} & C_{33} & C_{34} & C_{35} & C_{36} \\ C_{41} & C_{42} & C_{43} & C_{44} & C_{45} & C_{46} \\ C_{51} & C_{52} & C_{53} & C_{54} & C_{55} & C_{56} \\ C_{61} & C_{62} & C_{63} & C_{64} & C_{65} & C_{66} \end{bmatrix} \begin{bmatrix} S_1 \\ S_2 \\ S_3 \\ S_4 \\ S_5 \\ S_6 \end{bmatrix} \tag{3.30}$$

By using reduced subscript notation in Equation 3.30 the original stiffness matrix having dimension of 9x9 elements is reduced to 6x6 matrix. Similarly, it can be seen that all elements of stiffness matrix are not independent as, $C_{IJ} = C_{JI}$. This results in only 21 independent elements of [C] matrix. Moreover, due to presence of symmetry in many crystals, we can further reduce independent elements. For example a cubic symmetry crystal have following relationships between its elements in matrix [C],

$$\begin{aligned} C_{11} = C_{22} = C_{33} \\ C_{12} = C_{21} = C_{13} = C_{31} = C_{23} = C_{32} \\ C_{14} = C_{15} = C_{16} = 0 \\ C_{24} = C_{25} = C_{26} = 0 \\ C_{34} = C_{35} = C_{36} = 0 \end{aligned} \tag{3.31}$$

From the set of equations shown in Equation 3.31, it can be observed that the tensor matrix for a cubic symmetry crystal only has three independent components that are C_{11}, C_{12} and C_{44}. The resultant relation between these independent components for an isotropic material is shown in Equation 3.32.

$$C_{11} - C_{12} = 2C_{44} \tag{3.32}$$

3.5.5 Relation between wave velocity and Lame constant in isotropic material

From the Equation 3.32, it can be seen that the number of independent elements in isotropic material are reduced to two. These two elements are known as λ and μ or together as Lame constants. Lame constants are used to determine the total energy stored in a system and can also be related [88] to the elastic constants as,

$$C_{11} = C_{22} = C_{33} = \lambda + \mu \tag{3.33}$$

$$C_{12} = C_{21} = C_{13} = C_{31} = C_{23} = C_{32} = \lambda \tag{3.34}$$

$$C_{44} = C_{55} = C_{66} = \mu = \frac{C_{11} - C_{12}}{2} \tag{3.35}$$

As the other terms in stiffness matrix are zero, so the updated stiffness matrix in terms of lame constants can be written as,

$$\begin{bmatrix} \lambda+2\mu & \lambda & \lambda & 0 & 0 & 0 \\ \lambda & \lambda+2\mu & \lambda & 0 & 0 & 0 \\ \lambda & \lambda & \lambda+2\mu & 0 & 0 & 0 \\ 0 & 0 & 0 & \mu & 0 & 0 \\ 0 & 0 & 0 & 0 & \mu & 0 \\ 0 & 0 & 0 & 0 & 0 & \mu \end{bmatrix} \tag{3.36}$$

Generally, the elastic coefficients and wave velocity have the following relation,

$$V = \sqrt{\frac{C_{ij}}{\rho}} \tag{3.37}$$

here C_{ij}, ρ and V are the material elastic constant, material density and velocity of sound in the material, respectively. Equation 3.37 can have different forms depending upon the type

of wave velocity is to be determined. The relationship between the longitudinal and shear velocities with the lame constants and the elastic coefficients in a medium is written as,

$$\frac{V_L}{V_S} = \sqrt{\frac{C_{11}}{C_{44}}} = \sqrt{2 + \frac{\lambda}{\mu}} \tag{3.38}$$

for longitudinal velocity,

$$V_L = \sqrt{\frac{C_{11}}{\rho}} \tag{3.39}$$

similarly for shear velocity,

$$V_S = \sqrt{\frac{C_{44}}{\rho}} \tag{3.40}$$

Poisson's ratio and Young modulus are used to calculate the longitudinal velocity in a material. Similarly, for the transverse wave velocity shear modulus is used. But for the convenience one can use the lame constants to find these velocities.

- **Poisson's ratio (v):**

  Poisson's ratio is a dimensionless quantity. It is a ratio between shear or radial strain to longitudinal or axial strain.

- **Young's modulus (E):**

  Young's modulus is the measurements of stiffness in an isotropic material. Also known as elastic modulus, Young's modulus gives the relation between the applied stress and corresponding strain in the material. Its unit is Pascal.

- **Bulk modulus (K):** The bulk modulus is the measure of incompressibility of a material under the applied external pressure. Its unit is also Pascal.

3.6 Modes of acoustic wave propagation

As discussed earlier that the acoustic wave travels due to the compression and rarefaction of air molecules. However, in solids, the particles can move in other directions as well. Hence, depending on the particle movements the acoustic waves can be classified in different types. These propagation modes are often described as "wave modes". There are four different types of wave modes that solid medium can support. These acoustic modes are transverse (shear), longitudinal, surface waves and the fourth one is in thin materials called plate waves. The most important for our study are the shear waves or transverse waves and longitudinal waves.

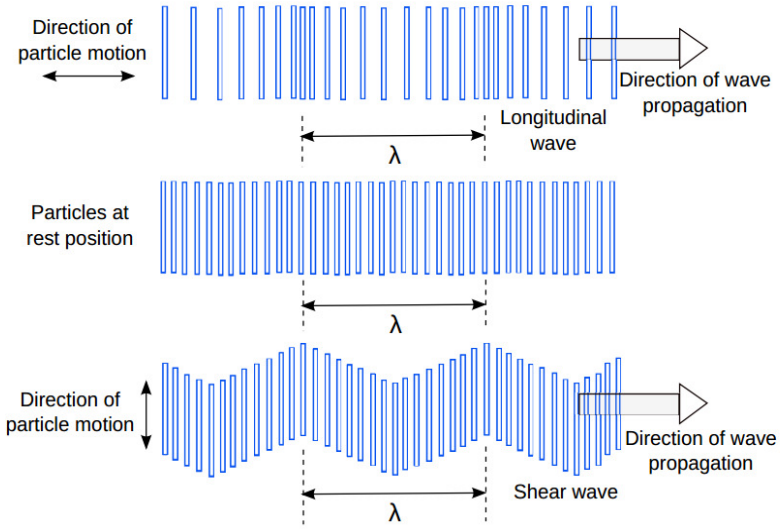

Fig. 3.8 Particles motion and direction for longitudinal and shear waves propagation [85]

The surface waves also known as Rayleigh waves travel along the surface of the thick solid material with a penetration depth of one wavelength [89]. Surface waves are generated by the combination of the shear and longitudinal waves. The movement of surface waves is like elliptical orbit motion, where the major elliptical axis is along the perpendicular to the solid surface. Surface waves are generated when the longitudinal waves intersect a surface around the second critical angle having velocity around 0.87 to 0.95 of the transverse

waves [89]. Surface waves gain importance due to their sensitivity to the surface features and defects. This feature of surface ways results in their use in many applications like ultrasonography that inspects the areas that other waves can not reach. Plate waves are quite similar to a surface wave. The significant difference between plate waves and surface waves is that plate waves can be generated in materials that have a thickness of a few wavelengths. Plate waves are divided into two more types, Lamb and Love waves. Lamb waves propagate parallel to the surface waves throughout the material thickness. Whereas, Love waves have transverse motion (movement is in perpendicular to the direction of travel. As Lamb waves can travel several meters inside the material, so they can be used to scan wires, tubes and plates etc.

3.7 Two dimensional (2D) acoustic waveguide

The main objective is to analyse acoustic-optical interaction in two-dimensional waveguides. This section provides acoustic wave propagation in a two-dimensional optical waveguide. As mentioned earlier, that the propagation of acoustic waves inside a waveguide is pretty complex. The acoustic wave propagation properties can be characterised by the density of the material, Poisson's ratio, elasticity and Young's modulus. During the propagation of an acoustic wave, the material particles displace either in the transverse or in the longitudinal plane, as shown in Fig. 3.8. To guide the acoustic wave in a waveguide at least one of the longitudinal or shear velocities in the cladding must be higher than the core.

In the case of a two-dimensional waveguide, two materials having different acoustic velocities are used in core and cladding. To guide the acoustic wave inside the core it must have a higher acoustic index (lower velocity) in the core than the cladding so that the acoustic wave can be guided. This can be achieved by doping another material such as Germanium oxide (GeO_2) in silica that increases the acoustic index of the core and also ensuring that the

optical refractive index of the core also remains higher. Figure 3.9 shows two different 2D waveguides, where the direction of wave propagation is in the z-direction.

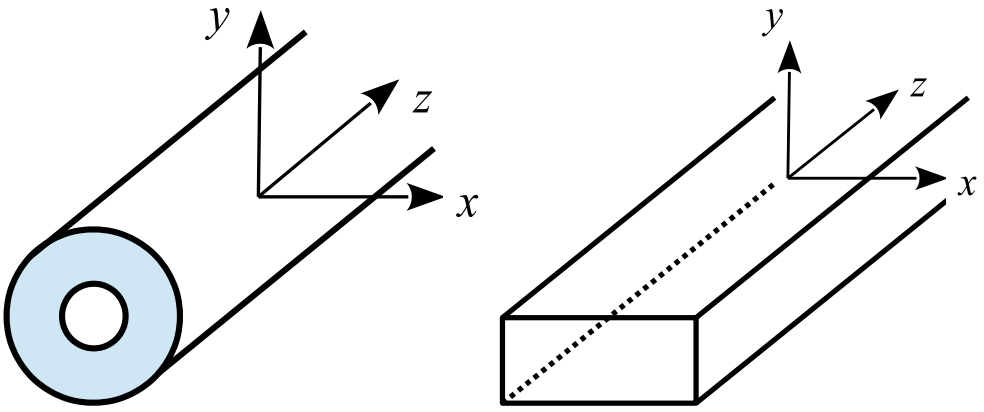

(a) (b)

Fig. 3.9 (a) Circular and (b) rectangular two dimensional optical waveguides with the direction of propagation along z-axis

The acoustic wave propagation along the z-direction is associated with the molecular displacement, and for a time-harmonic acoustic wave the displacement field, $\mathbf{U_i}$ (in *i*=*x, y and z* directions) may be written as in Eq. (3.41) [90];

$$\mathbf{U_i} = \mathbf{u}(u_x, u_y, ju_z)exp^{j(\omega_a t - k_a z)} \tag{3.41}$$

Here, ω_a, is the angular acoustic frequency, k_a, is the acoustic propagation constant and u_x, u_y, u_z are particle displacement vectors along the x, y and z directions, respectively. Similarly, the deformation in an acoustically vibrating body is described by the strain field, **S**, which is related to the partial derivative of the particle displacements, **u** and can be written as in Eq. (3.42) [83];

$$\mathbf{S} = \nabla\mathbf{u} \tag{3.42}$$

The elastic restoring force can be written in terms of stress field and in a freely vibrating medium the inertial elastic restoring forces are related to translation equation of motion and given as [91, 83];

$$\nabla \cdot \mathbf{T} = \rho \frac{\partial^2 \mathbf{u}}{\partial t^2} \tag{3.43}$$

here, ρ is the material density. Solution of the aforementioned equation depends on the accurate implication of the boundary condition,

$$\mathbf{u} \cdot \hat{n} = 0; \qquad \hat{n} \text{ is the unit vector} \tag{3.44}$$

and a constraint equation which describes that the rotational energy of the propagating wave is zero.

$$\nabla \times \mathbf{u} = 0 \tag{3.45}$$

Strain and stress are linearly proportional according to Hooke's Law and can be written as;

$$T_{ij} = c_{ijkl} S_{kl}; \qquad i, j, k, l = x, y, z \tag{3.46}$$

Here, c_{ijkl} are the microscopic spring constants and termed as elastic stiffness constants. The matrix form of the stiffness tensors can be written as

$$[T] = [c][S] \tag{3.47}$$

In finite element method (FEM) [92], a solid structure having displacement field, **u**, can be written with the help of vector nodal values of the displacement field **U** and interpolation shape function [N], and it gives ease to carry out integration and derivation over the elements. This results,

$$\mathbf{u} = [\mathbf{N}]\mathbf{U} \tag{3.48}$$

here [N] is the interpolation matrix of shape function

$$\mathbf{u} = \begin{bmatrix} u_x \\ u_y \\ ju_z \end{bmatrix} = \begin{bmatrix} N_1 & 0 & 0 & N_2 & 0 & 0 & N_3 & 0 & 0 \\ 0 & N_1 & 0 & 0 & N_2 & 0 & 0 & N_3 & 0 \\ 0 & 0 & N_1 & 0 & 0 & N_2 & 0 & 0 & N_3 \end{bmatrix} \begin{bmatrix} u_{x1} \\ u_{y1} \\ ju_{z1} \\ u_{x2} \\ u_{y2} \\ ju_{z2} \\ u_{x3} \\ u_{y3} \\ ju_{z3} \end{bmatrix} \tag{3.49}$$

The general system of equation that is associated with the wave propagation can be written as,

$$([A] - \omega^2[B])\mathbf{U} = \mathbf{F} \tag{3.50}$$

Where [A] and [B] are the stiffness matrix related to strain energy and mass matrix associated with the kinetic energy respectively, these matrices are usually generated for a given propagation constant, k. Similarly, nodal values of the applied forces are represented by the column vectors $\mathbf{F}$. The solution of the above generalised equation results in the eigenvalue as ω^2, where ω is the acoustic angular frequency. Similarly, eigenvector $\mathbf{U}$ is the displacement vector. For a given value of propagation constant, k, and its corresponding output, ω, the phase velocity of the acoustic wave velocity can be calculated by using Eq. 3.51.

$$v = \omega/k \tag{3.51}$$

Using above theoretical study, a numerically efficient computer code has been developed by using the sparse matrix solver along with the versatile mesh generation, that can be used to obtain the acoustic modal solution for the optical waveguides. To implement the FEM for the

two-dimensional analysis, the waveguide is meshed using the first order triangular element. Then the magnetic and acoustics field components of each element are calculated. Chapter 4 discusses the detail implementation of acoustic modal solution using finite element method.

3.8 Summary

In this chapter, the study of Brillouin scattering and its applications are discussed. Basic acoustic theory and reduced form of stress and strain notations are also presented that are used for the governing equations of the acoustic wave propagation. Basic concepts of the acoustically vibrating body like Hook's law and equation of motion are also presented in this chapter. These basic concepts are used to find the governing wave equation, how the particle displacement occurs in a two-dimensional waveguide. Similarly, different types of acoustic waves, mainly, shear and longitudinal waves and their propagation in the waveguides are also discussed.

Chapter 4

Finite Element Method and Variational Approach

4.1 Introduction

Modelling of photonic devices reduces the time and cost in the process of designing, fabrication, testing and possible redesigning. With the availability of advanced computer resources, many computer-based programmes for the modelling of complex photonic devices are being developed. These methods can be classified based on their complexity, processing time and efficiency. However, every method has some pros and cons, and some compromises and assumptions are needed [93].

The Finite Element Method (FEM) is one the most important and accurate numerical methods to solve Maxwell's equation for an electromagnetic wave propagating in photonic devices. A significant advantage of the FEM over other numerical techniques is its ability to solve any complex geometrical shape domain. The finite element method is a step-by-step process that is briefly listed below,

- **Discretisation of the domain:** A large complex domain can be considered as the integration of small and simple sub-domains of different shapes like rectangles and triangles named as finite elements.
- **Interpolation function:** After dividing the large domain into small sub-domains, nodes are assigned to each triangle and the interpolation functions are selected to describe the field variable's variation over the elements.
- **Finding the properties of element:** After the selection of the element shape and the polynomial order for the interpolation function, a system of equations in the matrix form is generated from the individual elements. This results in a global sparse matrix which is further solved to obtain the modal solution.

4.1.1 Discretisation of computational domain

A large computational domain where FEM needs to be applied is subdivided into the smaller domains also known as elements. These elements are chosen such that together they closely match the shape of the entire computational domain. The elements size and shape can be the same or different depending on the structure shape and variation of the electromagnetic field. These elements together construct the mesh that can be regular or irregular as shown in Fig. 4.1.

Irregular mesh has much better accuracy and efficiency in domain discretisation compared to regular mesh as the element size and shape varies in the structure. Moreover, for better utilisation of computational resources, finer elements can be used in the area of interest such as where field changes rapidly, thin and narrow pointed areas and coarse elements in rest of the domain such as far away from the core. Mesh elements can be of different type such as commonly used straight edge, curvilinear elements, infinite and edge elements. The straight edge elements consist of triangles, rectangular and quadrilaterals that are suitable

for geometries having straight boundaries. Curvilinear or iso-parametric elements are more suitable for the geometries having curved surfaces as the elements can match the curved surfaces perfectly as elements have curvature on the edges. Infinite mesh elements are useful for an unbounded or open space problem. In the edge elements, the field is continuous along the edges compared to the nodes in other types of elements.

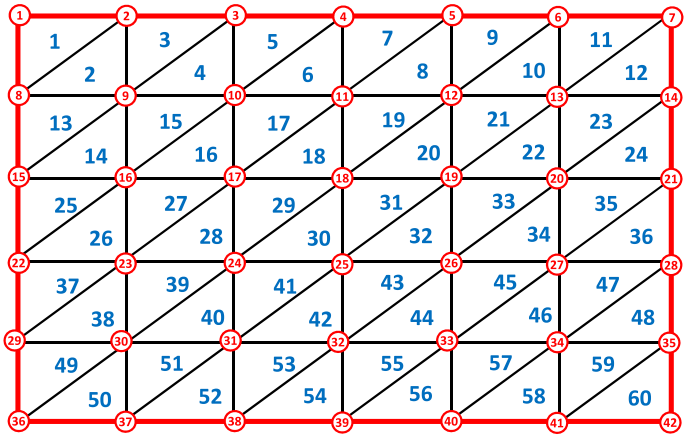

(a)

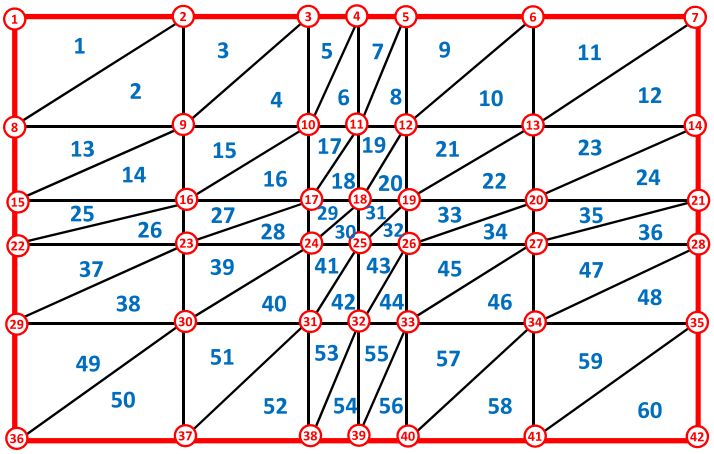

(b)

Fig. 4.1 (a) Regular and (b) irregular mesh used for the discretisation of computational domain [94].

4.1.2 Interpolation or shape function

The interpolation or shape function is used to approximate the unknown field values in the element through its values at the vertices of these elements. Polynomial functions are used as shape functions as they are much easier to solve both algebraically and computationally. Moreover, also a continuous function over the computational domain can also be approximated by polynomial functions. However, the selected polynomial function must have a continuity not only within but also across the boundaries of each element. Otherwise, the polynomial functions cannot be used for variational formulation and electromagnetic field cannot be calculated by the addition of individual element contribution. The shape function of an element must have the same number of terms as the number of nodes in an element. This can also be graphically visualised in Fig. 4.2 by using Pascal triangular structure. The figure shows the relationship between the number of terms and number of nodes in a 2D meshing systems.

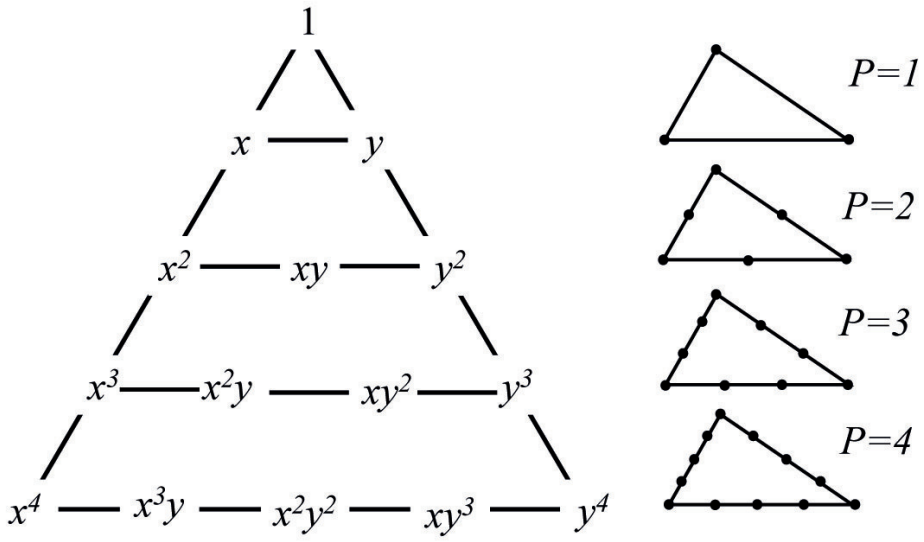

Fig. 4.2 Relation between number of polynomial terms and number of nodes for a shape function in an element represented by Pascal triangle [95]

Lagrange interpolation polynomials are used to construct the polynomial functions for the elements having different shape and size. For a linear 2D triangular element the Lagrange

polynomials L_i^e are given by Eq. 4.1

$$L_i^e = \frac{1}{2A^e}[a_i^e + b_i^e x + c_i^e y] \tag{4.1}$$

Here, A^e is the area of a 2D triangular element, a_i^e, b_i^e and c_i^e are the constants coefficients and subscript i is used to represent the element number.

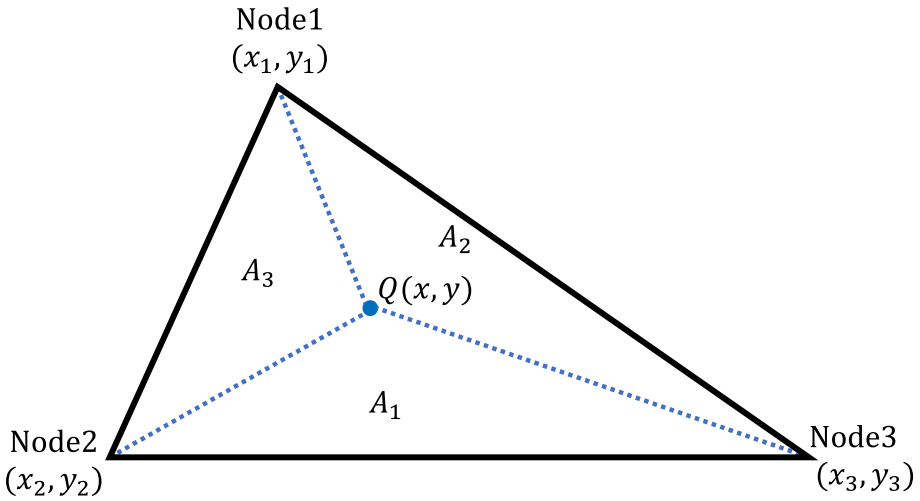

Fig. 4.3 An arbitrary Q point having coordinates (x,y) taken inside the linear triangular element for a two dimensional domain discretisation.

Figure 4.3 shows an arbitrary Q point having coordinates (x, y) inside a 2D triangular element. The Q point divides the triangular element further into three more triangles each having area of A_1, A_2 and A_3

The area of sub triangle A_1 is defined by the points Q(x,y) and node 1 and node 2.

$$A_1 = \frac{1}{2}\begin{vmatrix} 1 & x & y \\ 1 & x_2 & y_2 \\ 1 & x_3 & y_3 \end{vmatrix}$$

$$= \frac{1}{2}[(x_2 y_3 - x_3 y_2) + x(y_3 - y_2) + y(x_3 - x_2)] \tag{4.2}$$

$$\begin{bmatrix} L_1^e \\ L_2^e \\ L_3^e \end{bmatrix} = \frac{1}{A^e} \begin{bmatrix} A_1 \\ A_2 \\ A_3 \end{bmatrix} = \frac{1}{2A^e} \begin{bmatrix} a_1^e & b_1^e & c_1^e \\ a_2^e & b_2^e & c_2^e \\ a_3^e & b_3^e & c_3^e \end{bmatrix} \begin{bmatrix} 1 \\ x \\ y \end{bmatrix} \tag{4.3}$$

Here A_1, A_2 and A_3 is the area of three sub triangular elements as shown in Fig. 4.3. To formulate the shape function, each node of the triangular element is numbered. Figure 4.4 shows the three digits numbering of (a) linear and (b) quadratic 2D element. The number of digits to represent an element depends on the number of Lagrange functions required to define elements. In case of 2D triangular elements, there are three area coordinates, thus the nodes 1, 2 and 3 are represented as (1,0,0), (0,1,0) and (0,0,1), respectively.

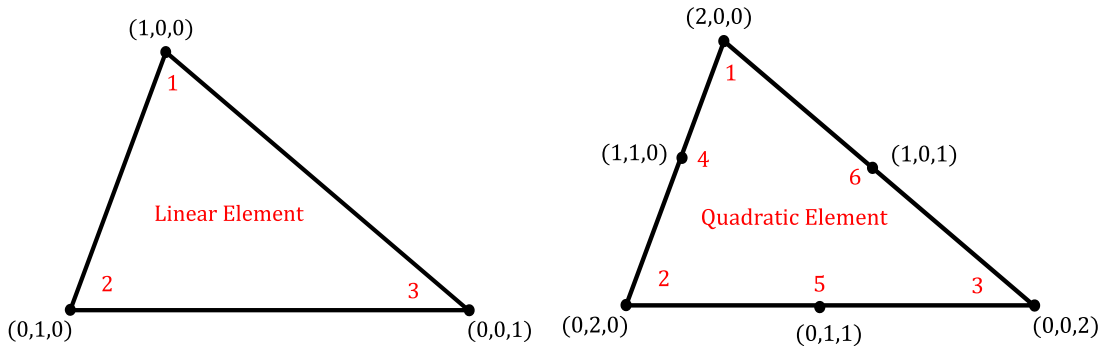

Fig. 4.4 (a) Linear and (b) quadratic 2D elements with the node numbering scheme.

The resultant shape function (N_i^e) for a node (i) can be written as [96]

$$N_i^e = Q_p^{(1)} L_1^e . Q_q^{(1)} L_2^e . Q_r^{(1)} L_3^e \qquad here \quad (p+q+r) = n \tag{4.4}$$

Here, p, q and r are the digits for the element node number and corresponding element order is denoted by n. The element order of (n=1) can be calculated for the digits (1,0,0), (0,1,0) and (0,0,1) of nodes shown in Fig. 4.4 (a).

The generalised form of Eq. 4.4 can be written as

$$Q^{(1)}_{x=p,q,r}L^e_1 = \frac{1}{x!}\prod_{m=1}^{x-1}(L^e_1 - m) \qquad when \quad p > 0 \tag{4.5}$$

Here, $Q^{(1)}_0$ is considered as 1 and the relation between shape functions and the Lagrange polynomials for linear triangular elements can be formed using Eqs. 4.4 and 4.5 can be written as

$$\begin{cases} N^e_1 = Q^{(1)}_{p=1}L^e_1 . Q^{(1)}_{q=0}L^e_2 . Q^{(1)}_{r=0}L^e_3 = L^e_1 \\ N^e_2 = Q^{(1)}_{p=0}L^e_1 . Q^{(1)}_{q=1}L^e_2 . Q^{(1)}_{r=0}L^e_3 = L^e_2 \\ N^e_3 = Q^{(1)}_{p=0}L^e_1 . Q^{(1)}_{q=0}L^e_2 . Q^{(1)}_{r=1}L^e_3 = L^e_3 \end{cases} \tag{4.6}$$

Similarly, for 2D quadratic element shown in Fig. 4.4 (b) the shape functions can be written as

$$\begin{cases} N^e_1 = Q^{(2)}_{p=2}L^e_1 . Q^{(2)}_{q=0}L^e_2 . Q^{(2)}_{r=0}L^e_3 = L^e_1(2L^e_1 - 1) \\ N^e_2 = Q^{(2)}_{p=0}L^e_1 . Q^{(2)}_{q=2}L^e_2 . Q^{(2)}_{r=0}L^e_3 = L^e_2(2L^e_2 - 1) \\ N^e_3 = Q^{(2)}_{p=0}L^e_1 . Q^{(2)}_{q=0}L^e_2 . Q^{(2)}_{r=2}L^e_3 = L^e_3(2L^e_3 - 1) \\ N^e_4 = Q^{(2)}_{p=1}L^e_1 . Q^{(2)}_{q=1}L^e_2 . Q^{(2)}_{r=0}L^e_3 = 4L^e_1L^e_2 \\ N^e_5 = Q^{(2)}_{p=0}L^e_1 . Q^{(2)}_{q=1}L^e_2 . Q^{(2)}_{r=1}L^e_3 = 4L^e_2L^e_3 \\ N^e_6 = Q^{(2)}_{p=1}L^e_1 . Q^{(2)}_{q=0}L^e_2 . Q^{(2)}_{r=1}L^e_3 = 4L^e_3L^e_1 \end{cases} \tag{4.7}$$

After the domain discretisation, the unknown ζ function can be approximated at individual nodes in terms of constant coefficients and node coordinates.

$$\zeta^e_i(x,y) = a^e_i + b^e_i x_i + c^e_i y_i \qquad where\ i = 1,2\ and\ 3 \tag{4.8}$$

After solving the shape function and constant coefficients (a_i^e, b_i^e, and c_i^e) for a specific element, the unknown function (ζ^e) can be interpolated as

$$\zeta^e = \sum_i^n N_i^e \zeta_i^e \tag{4.9}$$

4.2 Polar Mesh discretisation in circular waveguides

The accuracy of the modal solution is highly linked with the density of the mesh being used. However, increasing mesh density requires more computer resources and more simulation time. Regular mesh discussed in Section 4.1.1 is a good option for the waveguides having rectangular or square boundaries. However, for a circular waveguide, the regular triangular mesh may not be a suitable option as the triangular mesh elements do not entirely overlap the circular boundaries.

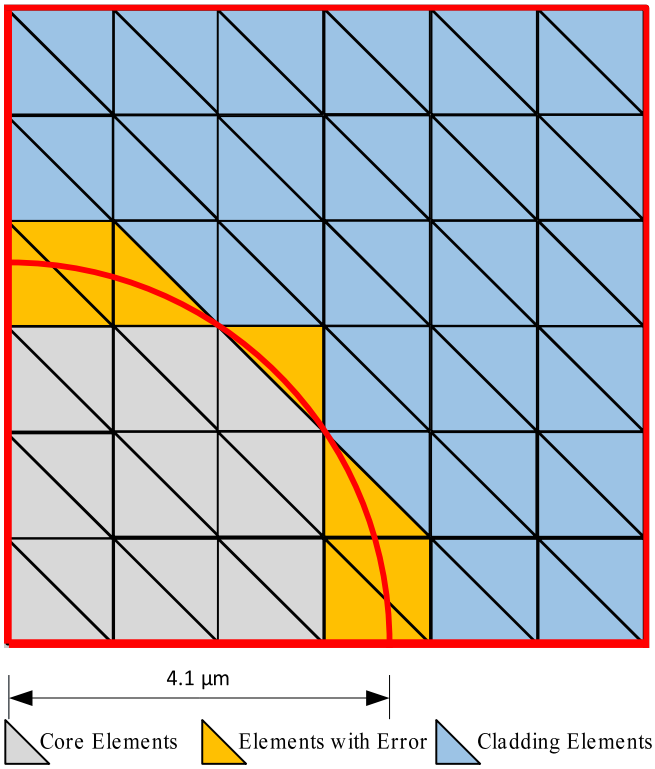

Fig. 4.5 Traditional triangular mesh elements distribution for circular fibre.

In Fig. 4.5 it can be seen that on the circular boundaries, the elements with the yellow colour are partially in core and partly in the cladding. This introduces inaccuracy in the modal solution because the elements are discretized partially in core and partly in the cladding. This error can be minimised by increasing the mesh density, however, as a result, more computational resources and simulation time is needed to obtain an accurate solution.

However, polar mesh distribution may be a good approach to address this problem. In polar mesh, elements are created with the azimuthal angle along the radius of the circle. This gives an accurate distribution of elements at the boundaries of circular waveguides with almost no error due to meshing. Figure 4.6 shows the polar mesh for a circular structure with a two-fold symmetry. Here, *na* is the total azimuthal divisions along the circumference of a circle and *da* is the azimuthal element resolution given as ($da = \frac{\pi}{2*na}$).

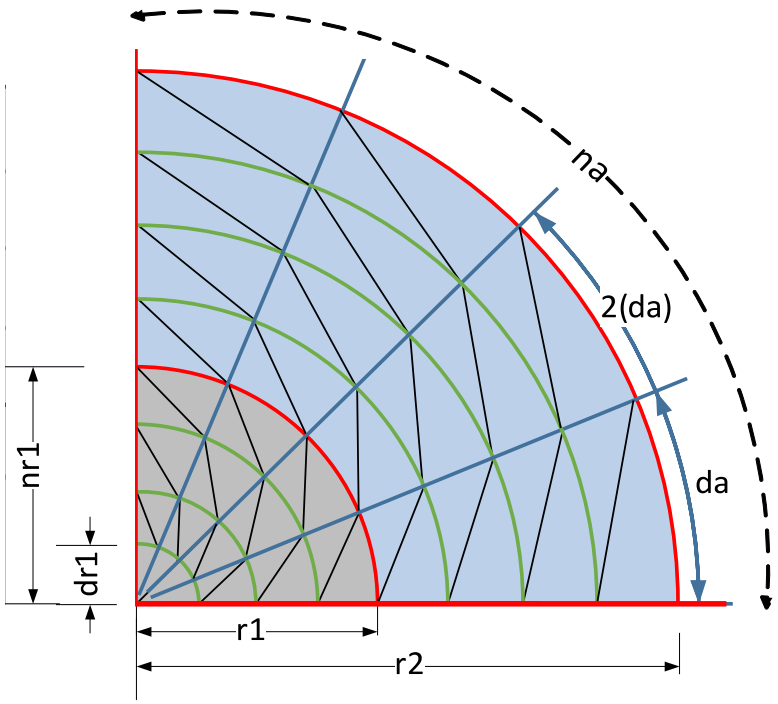

Fig. 4.6 Polar mesh elements distribution for a circular fibre.

Most of the work presented in this thesis is based on the single mode or multimode fibres having a circular structure. Hence, we have used polar mesh distribution for optical and acoustic modal analysis for circular waveguides.

4.3 Variational formulation

The FEM method is based on either a variational or weighted residual approach. The Galerkin method [97] in weighted residual is a more straightforward approach to approximate the solution of an electromagnetic waveguide. However, the variational approach is considered as one of the most powerful methods to solve the electromagnetic field problems where, only one global parameter, propagation constant is required to solve the solution. In this thesis, the variational formulation using FEM is considered. Hence the rest of the discussion will be about the variational approach. Different types of variational approaches have been developed depending on the structural nature of the waveguides [98]. Scalar formulation [91] is known as the simplest variational approach, where the field can be described as predominantly either as Transverse Electric (TE) or Transverse Magnetic (TM). Scalar type formulation is used in solving open boundary problems, homogeneous waveguide problems, analysis of lossy waveguides and anisotropic waveguides [99]. The single scalar formulation provides an approximation for the hybrid mode situation of a two-dimensional in-homogeneous cross-section waveguide problems.

For more accurate modal solution, vector formulation with at least two field components is used. In 1956, Berk proposed different vectorial formulations involving different electromagnetic field components such as $\vec{E}$-field, $\vec{H}$-field or the combinations $E_z + H_z$ and $\vec{E} + \vec{H}$ field [100]. Among the above electromagnetic field components, $\vec{H}$-field formulation is more useful as all the $\vec{H}$-field components are continuous over the material interfaces and external boundary conditions are not required. Vector $\vec{H}$-field formulation has been extensively used for the solution of many optical and microwave waveguides. The $\vec{H}$-field formulation is

more suitable for the dielectric waveguide problem where the magnetic field is continuous across the dielectric interface and the natural boundary conditions are the electric wall. Also, inhomogeneous or anisotropic mediums are also easily solvable. The $\vec{H}$-formulation is given in [100] for the electromagnetic waveguides can be written as,

$$\omega^2 = \frac{\int_A (\vec{\nabla} \times \vec{H})^* . \, \hat{\varepsilon}^{-1} . (\vec{\nabla} \times \vec{H}) \, dA}{\int_A \vec{H}^* . \, \hat{\mu} \, . \vec{H} \, dA} \tag{4.10}$$

where ε and μ are the permittivity and permeability of the lossless medium, respectively. The formulation given in Eq. 4.10 is itself forcing electric wall. Hence, forcing of boundary conditions is not required. Using expressions $k_o = \omega/c$, $\mu = \mu_0 \mu_r$, $\varepsilon = \varepsilon_0 \varepsilon_r$ and $\varepsilon_0 \mu_0 = 1/c^2$, Eq. 4.10 can be modified as

$$k_o^2 = \frac{\int_A (\vec{\nabla} \times \vec{H})^* . \, \hat{\varepsilon_r}^{-1} . (\vec{\nabla} \times \vec{H}) \, dA}{\int_A \vec{H}^* . \, \hat{\mu}_r \, . \vec{H} \, dA} \tag{4.11}$$

here, μ_r is the relative permeability and ε_r is the permittivity of the medium. k_o is the wavenumber of the propagating wave, c is the velocity of light in free space and dA is the area integration ($dA = dxdy$). Equations 4.10 and 4.11 represent the variational formulations used for the analysis of 2D optical waveguides.

4.4 Implementation of Full-Vectorial FEM for optical modal analysis

For 2D full-vectorial formulation, all three $\vec{H}$ field components H_x, H_y and H_z are considered. Equation 4.12 shows the $\vec{H}$ field continuous function of x, y.

$$\vec{H}(x,y) = \begin{bmatrix} H_x(x,y) \\ H_y(x,y) \\ H_z(x,y) \end{bmatrix} \tag{4.12}$$

To calculate the unknown $\vec{H}$ field distribution in a computational domain, an interpolation equation is required to set up for the approximation of $\vec{H}$ field components in an element. The unknown (H_x, H_y and H_z) field components associated with triangular shape functions (N_1, N_2 and N_3) can be written as

$$H_x^e(x,y) = \begin{bmatrix} N_1 & N_2 & N_3 \end{bmatrix} \begin{Bmatrix} H_{x1} \\ H_{x2} \\ H_{x3} \end{Bmatrix}_e \tag{4.13}$$

$$H_y^e(x,y) = \begin{bmatrix} N_1 & N_2 & N_3 \end{bmatrix} \begin{Bmatrix} H_{y1} \\ H_{y2} \\ H_{y3} \end{Bmatrix}_e \tag{4.14}$$

$$H_z^e(x,y) = \begin{bmatrix} N_1 & N_2 & N_3 \end{bmatrix} \begin{Bmatrix} H_{z1} \\ H_{z2} \\ H_{z3} \end{Bmatrix}_e \tag{4.15}$$

Here, letter e in both subscript and superscript represent that the above field components are calculated for particular one triangular element having three shape functions, three nodes and corresponding nine (H_{xi}, H_{yi}, and H_{zi}; where $i = 1,2,3$) field values. From the above mentioned equations the magnetic field vector $[\vec{H}_e]$ can be written as

$$\left[\vec{H}\right]_e = \begin{bmatrix} H_x(x,y) \\ H_y(x,y) \\ H_z(x,y) \end{bmatrix} = \begin{bmatrix} N_1 & N_2 & N_3 & 0 & 0 & 0 & 0 & 0 & 0 \\ 0 & 0 & 0 & N_1 & N_2 & N_3 & 0 & 0 & 0 \\ 0 & 0 & 0 & 0 & 0 & 0 & jN_1 & jN_2 & jN_3 \end{bmatrix} \begin{Bmatrix} H_{x1} \\ H_{x2} \\ H_{x3} \\ H_{y1} \\ H_{y2} \\ H_{y3} \\ H_{z1} \\ H_{z2} \\ H_{z3} \end{Bmatrix}_e \tag{4.16}$$

The imaginary term j in the shape function is considered for a lossless medium where the H_z field component is 90° out of phase with the transverse components H_x and H_y. Equation 4.16 can be simplified as

$$\left[\vec{H}\right]_e = \left[N\right] \left\{\vec{H}\right\}_e \tag{4.17}$$

Here, $[\vec{H}]_e$ is magnetic field component, [N] matrix represents the shape function and $\vec{H}_e$ is the column vector of nodal fields (H_{xi}, H_{yi}, and H_{zi} ; where $i = 1,2,3$) in the triangular element. Substituting Eq. 4.17 in Eq. 4.11 results in the following expression

$$k_o^2 = \frac{\int_A (\vec{\nabla} \times [N]\{\vec{H}\}_e)^* . \hat{\varepsilon}_r^{-1} . (\vec{\nabla} \times [N]\{\vec{H}\}_e)\, dA}{\int_A ([N]\{\vec{H}\}_e)^* . \hat{\mu}_r . [N]\{\vec{H}\}_e\, dA} \tag{4.18}$$

The cross product $(\vec{\nabla} \times \vec{H})$ can be written as

$$\left(\vec{\nabla}\times\vec{H}\right)=\left(\vec{\nabla}\times[N]\{\vec{H}\}_e\right)=\begin{bmatrix}0 & -\frac{\partial}{\partial z} & \frac{\partial}{\partial y}\\ \frac{\partial}{\partial z} & 0 & -\frac{\partial}{\partial x}\\ -\frac{\partial}{\partial y} & \frac{\partial}{\partial x} & 0\end{bmatrix}[N]\{\vec{H}\}_e=\left[Q\right]\left\{\vec{H}_e\right\} \tag{4.19}$$

For simplicity, the product of [$\nabla\times$] and shape function matrix [N] is represented by [Q] matrix. This matrix multiplication has been carried out, and its elements are given in Appendix A. Hence, considering [Q] matrix, Eq. 4.18 can be simplified as

$$k_o^2=\frac{\int_A([Q]\{\vec{H}\}_e)^*.\,\hat{\varepsilon}_r{}^{-1}.([Q]\{\vec{H}\}_e)\,dA}{\int_A([N]\{\vec{H}\}_e)^*.\hat{\mu}_r.[N]\{\vec{H}\}_e\,dA} \tag{4.20}$$

The above equation can be simplified by considering the conjugate transpose properties given as

$$\left([Q]\{\vec{H}\}_e\right)^*=\left(\{\vec{H}\}_e^*[Q]^*\right) \tag{4.21}$$

$$\left([N]\{\vec{H}\}_e\right)^*=\left(\{\vec{H}\}_e^*[N]^*\right) \tag{4.22}$$

Using conjugate transpose properties described in Eqs. 4.21 and 4.22, Eq. 4.20 can be written as

$$k_o^2=\frac{\int_A\{\vec{H}\}_e^*[Q]^*\cdot\,\hat{\varepsilon}_r{}^{-1}\cdot([Q]\{\vec{H}\}_e)\,dA}{\int_A\{\vec{H}\}_e^*[N]^*\cdot\hat{\mu}_r\cdot[N]\{\vec{H}\}_e\,dA} \tag{4.23}$$

Assuming $\vec{H}_e$ and element shape function ([N]) as a real matrix, Eq. 4.23 can be simplified as

$$F_e(\vec{H}) = \int_A \{\vec{H}\}_e^T [Q]^* \cdot \hat{\varepsilon}_r^{-1} \cdot [Q]\{\vec{H}\}_e \, dA - k_o^2 \int_A \{\vec{H}\}_e^T [N]^T \cdot \hat{\mu}_r \cdot [N]\{\vec{H}\}_e \, dA \quad (4.24)$$

Here, T and * denote the transpose and complex conjugate and the $F_e(\vec{H})$ is the numerical error that occurs due to the discretisation of the computational domain. To obtain a stationary solution, minimisation of the variational functional by $\frac{\partial}{\partial\{\vec{H}\}_e} F_e(\vec{H}) = 0$ is carried out

$$\frac{\partial}{\partial\{\vec{H}\}_e} \left[\int_A \{\vec{H}\}_e^T \, [Q]^* \cdot \hat{\varepsilon}_r^{-1} \cdot [Q]\{\vec{H}\}_e \, dA - k_o^2 \int_A \{\vec{H}\}_e^T [N]^T \cdot \hat{\mu}_r \cdot [N]\{\vec{H}\}_e \, dA \right] = 0 \quad (4.25)$$

or,

$$\frac{\partial}{\partial\{\vec{H}\}_e} \left[\{\vec{H}\}_e^T \int_A [Q]^* \cdot \hat{\varepsilon}_r^{-1} \cdot [Q] \, dA \, \{\vec{H}\}_e - k_o^2 \, \{\vec{H}\}_e^T \int_A \{[N]^T \cdot \hat{\mu}_r \cdot [N] \, dA \, \{\vec{H}\}_e \right] = 0 \quad (4.26)$$

or,

$$\frac{\partial}{\partial\{\vec{H}\}_e} \left[\{\vec{H}\}_e^T \underbrace{\int_A [Q]^* \cdot \hat{\varepsilon}_r^{-1} \cdot [Q] \, dA}_{[A]_e} \{\vec{H}\}_e - k_o^2 \, \{\vec{H}\}_e^T \underbrace{\int_A \{[N]^T \cdot \hat{\mu}_r \cdot [N] \, dA}_{[B]_e} \{\vec{H}\}_e \right] = 0 \quad (4.27)$$

The integration parts of the above equation can be represented as two real symmetrical matrix $[A]_e$, $[B]_e$

$$[A]_e = \hat{\varepsilon}_r^{-1} \int_A [Q]^* \cdot [Q] \, dA \quad (4.28)$$

$$[B]_e = \hat{\mu}_r \int_A [N]^T \cdot [N]\, dA \tag{4.29}$$

Equation 4.27 can be simplified as

$$\frac{\partial}{\partial\{\vec{H}_e\}} \left[\{\vec{H}\}_e^T [A]_e \{\vec{H}\}_e - k_o^2 \{\vec{H}\}_e^T [B]_e \{\vec{H}\}_e \right] = 0 \tag{4.30}$$

As the computational domain is divided in a number of elements, hence, the summation of vectorial variational formulation of individual elements result in total contribution and can be expressed as

$$[A]\{\vec{H}\} - k_o^2 [B]\{\vec{H}\} = 0 \tag{4.31}$$

Here, [A] and [B] are the global matrices derived by summing up all the individual element $[A]_e$ and $[B]_e$ matrices. k_o^2 is the eigenvalue and $\{\vec{H}\}$ is a column matrix representing eigenvector of the corresponding eigenvalue k_o^2 global matrices [A] and [B] can be written as

$$[A] = \sum_e [A]_e = \sum_e \hat{\varepsilon}_r^{-1} \int_A [Q]^* \cdot [Q] dA \tag{4.32}$$

and

$$[B] = \sum_e [B]_e = \sum_e \hat{\mu} \int_A [N]^T \cdot [N] dA \tag{4.33}$$

Detailed derivation of $[A]_e$ and $[B]_e$ matrix coefficients are shown in Appendix A.

4.5 Elimination of spurious modes

One of the drawbacks associated with the full-vectorial finite element method is the existence of non-physical spurious solutions. The vector variational formulation is shown in Eq. 4.11 is based on Maxwell's two curl equations shown in Eqs. 2.25 and 2.26. The Euler form of the Eq. 4.11 satisfies the Helmholtz's equation but does not automatically satisfy Maxwell's two

divergence equations. This is considered as the main cause of the existence of the spurious modes. Rahman *et al.* proposed the new formulation by balancing the curl and divergence part with a penalty function approach [101]. In the penalty method, a global weighing factor (p) close to the value of $1/n_{eff}^2$ is considered such that the effect of $div.\vec{B} = 0$ can be incorporated. The value of $(\vec{\nabla} \cdot \vec{H})$ is calculated for each eigenvector over the cross-section of waveguide and solution with low value of $(\vec{\nabla} \cdot \vec{H})$ is considered as real physical mode. This resulted in a major improvement in the modal solution and also spurious modes were totally eliminated. Hence, the new updated FEM equation can be written as,

$$k_o^2 = \frac{\int_A [(\vec{\nabla} \times \vec{H})^* \cdot \hat{\varepsilon}_r^{-1} (\vec{\nabla} \times \vec{H})\, dA + p \int_A (\vec{\nabla} \cdot \vec{H})^* (\vec{\nabla} \cdot \vec{H})]\, dA}{\int_A \vec{H}^* \cdot \hat{\mu}_r \cdot \vec{H}\, dA} \tag{4.34}$$

The solution of Eq. 4.34 consist of eigenvalues and corresponding eigenvectors. With the implementation of 2D full-vectorial FEM, several waveguides such as slot waveguides, single and multimode fibres and nano-wires and plasmonic complex waveguides are designed and optimised accurately. Results and mode profiles for optical waveguides using the full-vectorial FEM are discussed in Chapters 5, 6 and 7.

4.6 Interfaces between two materials and boundary conditions

Optical waveguides may have more than one materials and multiple interfaces between different mediums. This requires continuity of electric and magnetic field across the material interfaces for full-vectorial FEM based model solution. Boundary conditions have a key role in the waveguide solution. The Maxwell's equations cannot completely explain the characteristics of the electromagnetic field as these equations don't consider the boundaries

between two material in an optical waveguide. Hence, boundary conditions are enforced on these equations.

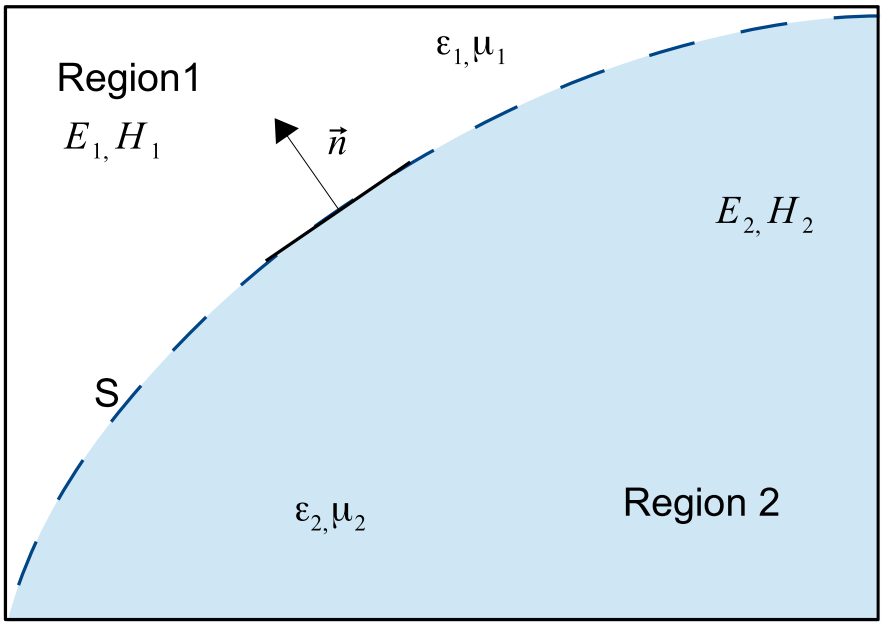

Fig. 4.7 Surface boundary between two different mediums

Figure 4.7 shows two dielectric materials in a waveguide separated by a boundary (S) shown by the blue dashed line. The unit vector $\vec{n}$ is directed from the region 2 to region 1. As the optical waveguides are made up of dielectric materials, the surface charges ($\rho = 0$) and surface current ($\vec{J} = 0$) can be considered not present; hence, the boundary conditions can be written as

1. The tangential component of the electric field and magnetic field must be continuous along the surface boundary (**S**). This means $\hat{n} \times \vec{E}$ and $\hat{n} \times \vec{H}$ must be continuous across the interface.

$$\begin{aligned} \hat{n} \times (\vec{E_1} - \vec{E_2}) = 0 \\ \vec{E_{t1}} = \vec{E_{t2}} \end{aligned} \tag{4.35}$$

$$\begin{aligned} \hat{n} \times (\vec{H}_1 - \vec{H}_2) &= 0 \\ \vec{H}_{t1} &= \vec{H}_{t2} \end{aligned} \tag{4.36}$$

2. Similarly, the normal components of electric and magnetic flux densities must be continuous across the interface.

$$\begin{aligned} \hat{n} \cdot (\vec{D}_1 - \vec{D}_2) &= 0 \\ \varepsilon_1 \vec{E}_{n1} &= \varepsilon_2 \vec{E}_{n2} \end{aligned} \tag{4.37}$$

Here, $\vec{E}_{n1} \neq \vec{E}_{n2}$ as the permittivity ε_1 and ε_2 for medium 1 and 2 are not equal at material boundary, $\varepsilon_1 \neq \varepsilon_2$.

$$\begin{aligned} \hat{n} \cdot (\vec{B}_1 - \vec{B}_2) &= 0 \\ \mu_1 \vec{H}_{n1} &= \mu_2 \vec{H}_{n2} \end{aligned} \tag{4.38}$$

Hence, $\vec{H}_{n1} = \vec{H}_{n2}$, as the μ_1 and μ_2 are the permeability of medium 1 and medium 2, respectively. Here, $\mu_1 = \mu_2 = 1$ is considered as most of the optical materials are non-magnetic.

Apart from above electromagnetic boundary conditions, two types of boundary conditions are commonly applied practically to optical problems. Perfect Electric Wall (PEW) or Perfect Magnetic Wall (PMW), boundary conditions is achieved by the following conditions,

$$\hat{n} \times \vec{E} = 0, \quad or, \quad \hat{n} \cdot \vec{H} = 0 \tag{4.39}$$

In PEW boundary conditions shown in Eq. 4.39, magnetic field vector $\vec{H}$ is forced to zero value, hence the electric field vector $\vec{E}$ remain continuous at the boundary. Similarly,

boundary conditions for perfect magnetic wall or perfect magnetic conductor (PMC) are given as,

$$\hat{n} \times \vec{H} = 0, \quad or, \quad \hat{n} \cdot \vec{E} = 0 \tag{4.40}$$

Here, electric field component, $\vec{E}$ is forced to zero and magnetic field component, $\vec{H}$ remains continuous across the boundary. These boundary conditions are beneficial while exploiting the half or quarter symmetry of the structure.

4.7 Implementation of Full-Vectorial FEM for acoustic modal analysis

The advantage of FEM technique is to solve the complex differential equations into simpler eigenvalue equation matrix, that can be further solved for the required solution using standard methods. In the previous sections, the fundamentals of FEM and its implementation for the modal solution of optical waveguides is discussed. However, to study the acoustic wave propagation, a uniform waveguide having an infinite length in the direction of propagation is considered. For simplicity, the complex problem is reduced to a two-dimensional problem having a cross section in xy plane. An acoustic wave propagating in z-direction having propagation constant k is guided through an optical waveguide. The displacement vector $\mathbf{u}$ of the propagating acoustic wave can be expressed as,

$$\mathbf{u} = \begin{bmatrix} u_x(x,y) \\ u_y(x,y) \\ u_z(x,y) \end{bmatrix} e^{j(\omega t - kz)} \tag{4.41}$$

The problem can be solved by using first order triangular elements and considering specific phase relationship between the nodes of the end surfaces. The acoustic wave

propagation is along the z-direction but the solution can be obtained using bi-dimensional mesh and then reconstitute the entire solution. The standard eigenvalue problem through the FEM given in Eq. 3.50 can be written as

$$[A][U] = \omega^2[B][U] \tag{4.42}$$

Where, [A] and [B] are the stiffness matrix and mass matrix, respectively. The nodal values of externally applied forces are considered to be zero, hence, the resultant modal solution provides **U** and ω^2 as the displacement eigenvector and eigenvalues, respectively.

4.7.1 FEM acoustic wave formulation

The cross-section of the acoustic waveguide is discretised into several triangular elements, and the unknown displacement vector $\mathbf{u_e}$ for each element can be approximated by the following Eq. 4.43

$$\mathbf{u_e} = \sum_{i=1}^{q} N_i U_i^e \tag{4.43}$$

Here, q shows the number of nodes of an element, N_i is a set of interpolation function and U_i^e is the displacement vector at each element node.

For individual element Eq. 3.49 can be written in the matrix form as,

$$\mathbf{u_e} = [N][U]_e \tag{4.44}$$

Similarly, Eq. 4.44 can be represented in the form *x, y* and *z* components of displacement vector as,

$$\mathbf{u_e} = \begin{bmatrix} N_1 & 0 & 0 & N_2 & 0 & 0 & jN_3 & 0 & 0 \\ 0 & N_1 & 0 & 0 & N_2 & 0 & 0 & jN_3 & 0 \\ 0 & 0 & N_1 & 0 & 0 & N_2 & 0 & 0 & jN_3 \end{bmatrix} \begin{bmatrix} U_{x1} \\ U_{y1} \\ U_{z1} \\ U_{x2} \\ U_{y2} \\ U_{z2} \\ U_{x3} \\ U_{y3} \\ U_{z3} \end{bmatrix} \tag{4.45}$$

Here, nodal displacements along the x, y and z direction are represented by U_x, U_y and U_z, respectively. The second subscript (1, 2 and 3) in the nodal displacements indicates the node numbers of element. Whereas, the term j in Eq. 4.45 is used for lossless medium where U_z components are 90° out of phase to the corresponding transverse components. Based on the Hook's law stated in Chapter 3, the stress and strain for small displacements can be related as given in Eq. 3.46. Utilizing this information we can write as,

$$\nabla \cdot \mathbf{T} = \nabla \cdot (C\mathbf{S}) \tag{4.46}$$

Here, **T** and **S** represents the stress and strain, respectively and elastic stiffness coefficient is represented by C. Detailed discussion of elastic stiffness coefficients is presented in sections 3.5.3, 3.5.4, and 3.5.5 of Chapter 3.

The stiffness matrix incorporating strain tensor can be written as [83],

$$\begin{bmatrix} S_1 \\ S_2 \\ S_3 \\ S_4 \\ S_5 \\ S_6 \end{bmatrix} = \begin{bmatrix} \frac{\partial U_x}{\partial x} \\ \frac{\partial U_y}{\partial y} \\ \frac{\partial U_z}{\partial z} \\ \frac{\partial U_y}{\partial z} + \frac{\partial U_z}{\partial y} \\ \frac{\partial U_x}{\partial z} + \frac{\partial U_z}{\partial x} \\ \frac{\partial U_x}{\partial y} + \frac{\partial U_y}{\partial x} \end{bmatrix} = \begin{bmatrix} \frac{\partial}{\partial x} & 0 & 0 \\ 0 & \frac{\partial}{\partial y} & 0 \\ 0 & 0 & \frac{\partial}{\partial z} \\ 0 & \frac{\partial}{\partial z} & \frac{\partial}{\partial y} \\ \frac{\partial}{\partial z} & 0 & \frac{\partial}{\partial x} \\ \frac{\partial}{\partial y} & \frac{\partial}{\partial x} & 0 \end{bmatrix} \begin{bmatrix} u_x^e \\ u_y^e \\ u_z^e \end{bmatrix} \tag{4.47}$$

The element's nodal displacement vectors in the x, y and z directions are represented by u_x^e, u_y^e and u_z^e, respectively. Equation 4.47 can be written as,

$$S_i = \nabla_{ij} u_j^e \tag{4.48}$$

The strain displacement relation can also be written in the symbolic notation as [83], $\mathbf{S} = \nabla_s \mathbf{u}_e$, where, subscript s symbol stands for symmetric. The symmetric gradient operator $\nabla_{ij} = \nabla_s$ in shown in Eq. 4.48 has a matrix form of,

$$\nabla_s \Rightarrow \nabla_{ij} = \begin{bmatrix} \frac{\partial}{\partial x} & 0 & 0 \\ 0 & \frac{\partial}{\partial y} & 0 \\ 0 & 0 & \frac{\partial}{\partial z} \\ 0 & \frac{\partial}{\partial z} & \frac{\partial}{\partial y} \\ \frac{\partial}{\partial z} & 0 & \frac{\partial}{\partial x} \\ \frac{\partial}{\partial y} & \frac{\partial}{\partial x} & 0 \end{bmatrix} = [D] \tag{4.49}$$

For simplicity the symmetric gradient matrix is represented by [D]. The updated Eq. 4.49 can be written as,

$$\mathbf{S} = [D]\mathbf{u_e}$$

$$\Rightarrow \mathbf{S} = [D][N][U]_e \tag{4.50}$$

In Chapter 3, the elastic restoring forces are defined in terms of stress field, $\mathbf{T}(u_j,t)$. As discussed earlier in Section 3.7 the elastic and inertial restoring forces are related through the translational equation of motion shown in Eq. 3.43. Similarly, the stress matrix is considered symmetric as shown in Eq. 3.17, hence, the spatial variation of stress $\mathbf{T}$, can be determined by the divergence of $\mathbf{T}$, as,

$$\nabla\cdot\mathbf{T}=\begin{bmatrix}\frac{\partial}{\partial x}T_{xx}+\frac{\partial}{\partial y}T_{xy}+\frac{\partial}{\partial z}T_{xz}\\ \frac{\partial}{\partial x}T_{yx}+\frac{\partial}{\partial y}T_{yy}+\frac{\partial}{\partial z}T_{yz}\\ \frac{\partial}{\partial x}T_{zx}+\frac{\partial}{\partial y}T_{zy}+\frac{\partial}{\partial z}T_{zz}\end{bmatrix}=\begin{bmatrix}\frac{\partial}{\partial x}&0&0&0&\frac{\partial}{\partial z}&\frac{\partial}{\partial y}\\ 0&\frac{\partial}{\partial y}&0&\frac{\partial}{\partial z}&0&\frac{\partial}{\partial x}\\ 0&0&\frac{\partial}{\partial z}&\frac{\partial}{\partial y}&\frac{\partial}{\partial x}&0\end{bmatrix}\begin{bmatrix}T_1\\T_2\\T_3\\T_4\\T_5\\T_6\end{bmatrix}=[D]^T\begin{bmatrix}T_1\\T_2\\T_3\\T_4\\T_5\\T_6\end{bmatrix} \tag{4.51}$$

For simplicity, the transpose of symmetric gradient matrix is shown by $[D]^T$ in above equation. Using Equations 4.46, 4.50, 4.51 and 3.43 divergence of $\mathbf{T}$ can be written as,

$$\nabla\cdot\mathbf{T}=[D]^T[C][D][N][U]_e=\rho(j\omega)^2[N][U]_e \tag{4.52}$$

Conjugate transpose of nodal displacement vector of element $[N][U]_e$ is multiplied on both sides of Eq. 4.52 and integrated over whole domain of element, Ω_e. Using Equations 4.46, 4.50, 4.51 and 3.43 the above mentioned Eq. 4.52 can be written as,

$$-\int\int_e[N]^*[U]_e^*[D]^T[C][D][N][U]_e d\Omega_e-\omega^2\int\int_e\rho[N^*][U]_e^*[N][U]_e d\Omega_e=0 \tag{4.53}$$

here * shows the conjugate transpose of the matrix. After applying variational principle the generalised form of Eq. 4.53 can be written as,

$$\int\int_e \left(-[N]^*[U]_e^*[D]^T[C][D][N][U]_e - \omega^2\rho[N^*][U]_e^*[N][U]_e \right) d\Omega_e = 0 \tag{4.54}$$

Similar to full-vectorial formulation based on the minimisation of **H**-field for optical modes shown in Eq. 4.10, the fundamental FEM based variational expression used in acoustic modal solution can be written as [102];

$$\omega^2 = \frac{\int\int [(\nabla \cdot \mathbf{U})^* \cdot [C] (\nabla \cdot \mathbf{U})] \, d\Omega_e}{\int\int \mathbf{U}^* \cdot \rho \, \mathbf{U} \, d\Omega_e} \tag{4.55}$$

Here, ω is the acoustic angular frequency, **U** is the displacement eigenvector, ρ and [C] are the density of the material and elastic stiffness tensor, respectively.

For a standard eigenvalue problem, Eq. 4.54 can be rearranged and rewritten in the matrix form as,

$$[A][U] - \omega^2[B][U] = 0 \tag{4.56}$$

here, [U] is the eigenvector, ω^2 is the eigenvalue, [A] is a real symmetric matrix also known as stiffness matrix related to strain whereas, [B] is known as mass matrix that is related to kinetic energy. Both [A] and [B] matrices can be defined as,

$$[A] = -\int\int_e \left([Q]^*[C][Q] \right) d\Omega_e \tag{4.57}$$

$$[B] = \rho \int\int_e [N]^*[N] d\Omega_e \tag{4.58}$$

For simplicity, [Q] matrix is used to replace the multiplication of [D][N] matrices and ρ is known as material density.

These [A] and [B] matrices can be generated for a given value of acoustic propagation constant k. The eigenvalue ω^2 can be calculated by solving the generalised eigenvalue system equation shown in Eq. 4.56 that results in ω, acoustic angular frequency and eigenvector, [U] as the displacement vector. The acoustic velocity v of acoustic modes can be calculated for a given value of acoustic propagation constant, k and generated acoustic frequency ω using Eq. 3.51.

4.8 Summary

This chapter briefly discusses some of the common numerical methods used to find the modal solution for electromagnetic waveguides. Among various available methods, FEM is considered more accurate and provides flexibility to solve the irregular shape structure by dividing a large domain into subdomains (elements). These elements can be of triangular and rectangular shape depending upon the choice. Later on, the individual element solution based on the interpolation function and boundary equations is combined to form a global matrix that results in the modal solution. Variational formulation with the effect of the penalty term is also discussed in this chapter. An improved polar meshing technique is proposed for structures such as SMF and MMF that provides more accurate solution of the waveguides that have curvilinear boundaries.

Chapter 5

Light Sound Interaction in Standard Single Mode Fibre

5.1 Introduction

Light sound interaction also known as stimulated Brillouin scattering (SBS) in optical waveguides attracted considerable large interest over the past years [103, 104]. SBS is a non-linear process, where sound wave is generated due to electrostriction effect that creates a travelling Bragg gratings and prevents delivery of high optical power. Among other non-linear effects like Self Phase Modulation (SPM) or Cross Phase Modulation (CPM), SBS has gained significant attention due to its low threshold that limits the power scaling in photonic devices [105, 52].

Since early 2000's, a large number of research outputs have been reported describing reduction or increase in the overlap between optical and acoustic modes for higher power transmission or for the sensing applications, respectively. These are achieved by incorporating different materials to alter the acoustic properties of the fibre or altering the fibre structure. The SBS gain peaks in a Brillouin spectrum of optical fibre is also calculated by considering the overlap between the acoustic and optical modes. Dasgupta *et al.*[54], used a Finite

Element Method (FEM) based commercially available software, COMSOL Multiphysics®, to investigate the SBS spectrum in a step index Ge-doped fibre where three significant peaks were recorded in the Brillouin spectrum from 9.4 GHz to 11.6 GHz. These SBS gain peaks are the result of high overlap recorded between fundamental optical and dominant longitudinal acoustic LP_{01}, LP_{02} and LP_{03} modes. Shibata *et al*. investigated the effect of different germanium doping concentration in the core of fibres and cladding consisted of either Fluorine or pure Silica for two different fibre designs [106]. For the first design, the acoustic velocity of the cladding was made lower than that in the core of the fibre resulting in an acoustic anti-guide design. Similarly, for a second fibre design where core was doped with germanium and cladding with pure silica, waveguide acts as an acoustic guide and three peaks were reported in Brillouin spectra.

Multimode fibres (MMF) have a higher effective area which results in a high SBS threshold and provides flexibility to enhance maximum transmission power in the fibres. Dragic *et al.* reported the existence of higher order acoustic modes in an acoustic anti-guide by adding an acoustic guide layer around core [107]. They reported two peaks in the Brillouin spectrum of a MMF that has a high acoustic index fluorine doped cladding. A comparison of SBS threshold between SMF and MMF is reported by Iezzi *et al.* [108]. It is demonstrated that due to large mode area of MMF, the pump power threshold is increased to 105 *mW* from the previously calculated 15 *mW* threshold power that is useful for high power applications. However, the existence of more than one mode in MMF may introduce the inter-modal interference that is further discussed in chapter 6.

However, to fully understand the complex light-sound interaction, an accurate analysis of both optical and acoustic modes is required. Various theoretical methods have been reported which can be used for modelling of optical [109] and acoustic [110, 54] waveguides by solving relevant optical and acoustic wave equations. The Finite Element Method (FEM) is a powerful numerical approach, capable of developing modal solutions for both types of

waveguides. With the considerable progress in the field of photonics, optical waveguides are now more intricate or exotic and mostly need a full-vectorial treatment. A scalar formulation may be a simpler approach, but the vector formulations are more accurate. In 1984, it was reported that the vector based FEM formulations are affected by the existence of spurious modes [101]. It was identified that as the proposed **H**-field vector formulation considered only two curl equations but did not consider the divergence-free nature of the field, which allowed spurious modes to appear. As these spurious solutions introduce difficulties to identify physical modes and also deteriorate eigenvector quality, therefore different techniques have been considered to eliminate them. On the other hand, the classification of acoustic modes is even more complex than that of optical modes. There can be different types of acoustic modes, such as longitudinal, transverse, bending, torsional or flexural modes. For a high index contrast waveguide, these acoustic modes are hybrid in nature and need a full vectorial treatment. However, the existence of the spurious solutions associated with vector approaches makes it challenging to recognise the real modes of our interest. Therefore, it is very important to address the appearance of spurious solutions and also to find a way to eliminate them.

We have proposed a penalty term based full-vectorial FEM to eliminate the spurious acoustic modes in both low and high index contrast acoustic waveguides. The introduction of penalty term resulted in not only improved quality of acoustic modes but also eliminated spurious modes without deteriorating the eigenvalues of the desired modes. The proposed penalty approach is tested for both low and high index contrast acoustic waveguides.

5.2 Suppression of spurious modes in full-vectorial models

The FEM is a powerful and versatile numerical method used for solving the electromagnetic field problems in optical waveguides. The existence of spurious solutions in FEM based vector formulations is often considered as a shortcoming of these formulations. These spurious modes are only numerically generated solutions and have no physical significance

and simply considered as wrong solutions [111]. Although the existence of spurious solutions in electromagnetic field problems was identified but little research was carried out in order to eliminate these solutions. Konrad [112] first suggested that rigorous boundary condition can be imposed to eliminate these spurious modes, however, the results were not satisfactory. Rahman and Davies proposed a penalty method [101], used with the full-vectorial **H**-field formulation to eliminate the spurious modes in the optical modal analysis explained in Chapter 4.

This approach has been successful and significant improvement was observed in the quality of optical modes. However, in order to observe the light-sound interaction, the quality of acoustic mode is also very important. In acoustic modal solution, these spurious solutions behave differently and also depends on the type of modes and index contrast. In order to study acoustic wave propagation in liquid, Winkler and Davies proposed an approach similar to Rahman and Davies, where noticeable reduction of the spurious modes was noted [102]. They proposed to restrict the flexibility of the problem by constraining it. Some improvement in the eigenvectors of the physical modes along the reduction of spurious modes were noted. However, a very small mesh size, limited to only 24 triangular elements, was considered. Besides that, no study was presented to observe the effect of penalty value on the modes in acoustic waveguides.

5.3 Introduction of penalty term in acoustic modal solution

The fundamental FEM based variational expression used in acoustic modal solution can be obtained using strain displacement relation, equation of motion and stress strain relation, as given in Eqs. (3.42)-(3.47), and can be written as [102];

$$\omega_a^2 = \frac{\int\int[(\nabla\cdot\mathbf{U})^*\cdot[C](\nabla\cdot\mathbf{U})]\,dxdy}{\int\int\mathbf{U}^*\cdot\rho\,\mathbf{U}\,dxdy} \tag{5.1}$$

Here, ω_a is the acoustic angular frequency, $\mathbf{U}$ is the displacement eigenvector, ρ and [C] are the density of the material and elastic stiffness tensor, respectively. The above mentioned acoustic wave equation can be reduced to a general eigenvalue equation [91]:

$$[A]\mathbf{U} - \omega_a^2[B]\mathbf{U} = 0 \tag{5.2}$$

The [A] matrix is known as the stiffness matrix, related to the strain energy and [B] matrix is the mass matrix related to the kinetic energy. Here, ω_a^2 is the eigenvalue and the eigenvector $\mathbf{U}$ are the unknown values of nodal displacements vectors.

The formulation given by Eq. (5.1) is considered to be sufficient for modelling of acoustic modes in waveguides. However, this formulation also generates spurious solutions which not only effect the desired mode quality but also introduce difficulty in recognising the physical modes. To eliminate these spurious modes, Eq. (5.1) can be modified by adding the two curl equations as a penalty term. The augmented full-vectorial FEM based acoustic formulation is given by Eq. (5.3). Here, the $\nabla\times\mathbf{U} = 0$ constraint on the displacement vector is introduced in a least squares manner by a weighting factor, the penalty term, α, and this is used to control the elimination of spurious solutions.

$$\omega_a^2 = \frac{\int\int[(\nabla\cdot\mathbf{U})^*\cdot[C](\nabla\cdot\mathbf{U}) + \alpha\,(\nabla\times\mathbf{U})^*\cdot(\nabla\times\mathbf{U})]\,dxdy}{\int\int\mathbf{U}^*\cdot\rho\,\mathbf{U}\,dxdy} \tag{5.3}$$

The curl-curl section of the augmented formulation enforces the acoustic field to suppress the rotational energy of the propagating acoustic wave. An increasingly large penalty term makes the Eq. (5.3) overpower to the shear modes. Therefore, the corresponding eigenvectors move towards the longitudinal mode and results in the spurious free longitudinal modes. This formulation can make a considerable improvement in the acoustic modal solutions by reducing or even eliminating spurious modes along with a significant improvement in the

eigenvector quality, as shown in the following sections. The calculations of penalty term $[\alpha(\nabla \times \mathbf{U})^* \cdot (\nabla \times \mathbf{U})]$ in acoustic modal solution is presented in Appendix B.

5.4 Effect of penalty term in low index contrast acoustic waveguides

5.4.1 Elimination of spurious modes

In order to study the effect of penalty term, first we have considered a low-index contrast single mode fibre (SMF) with a core radius of 4.1 μm. The core consists of 6.24 $\%wt$ of GeO_2 and 93.76 $\%wt$ of SiO_2, whereas, cladding is taken as pure SiO_2. The shear and longitudinal acoustic velocities of the core are taken as 3644.85 m/s and 5794.626 m/s, respectively. Similarly for cladding, shear and longitudinal velocities are taken as 3760 m/s and 5970 m/s, respectively [113]. The material density of core and cladding are considered as 2291.25 kg/m^3 and 2201 kg/m^3, respectively. The refractive index and acoustic velocities of 6.24 % GeO_2 doped core are calculated using relation given in reference [114] where the change in the refractive index and acoustic velocities with respect to change in the percentage weight doping of different materials in Silica is provided. For simulations, an equivalent step-index fibre refractive index profile is used where the individual refractive index inside core and cladding are considered smooth without any fluctuations. Table 5.1 summarises the material properties of core and cladding as used for our simulations.

Table 5.1 Core and cladding acoustic velocities and elastic coefficients [114].

SMF	**Materials** ($\%wt$)		**Acoustic Velocities** (m/s)		**Density** (ρ) (kg/m^3)	**Elastic Coefficients**		
	SiO_2	GeO_2	**Shear**	**Longitudinal**		C_{11}	C_{12}	C_{44}
Core	93.76	6.24	3644.85	5794.62	2291.25	76.93488	16.05668	30.43910
Cladding	100	0	3760	5970	2201	78.44562	16.21191	31.11686

Elastic coefficients used in stiffness matrix are derived using shear, longitudinal velocities and material density as given in Eq. 5.4

$$V_L = \sqrt{\frac{C_{11}}{\rho}}; \quad V_S = \sqrt{\frac{C_{44}}{\rho}}; \quad C_{11} - C_{12} = 2C_{44} \tag{5.4}$$

The SBS threshold where the input pump power in optical fibre becomes equal to the back reflected power is considered as a limiting factor and it varies according to relation given in Eq. 5.5

$$P_{th} \propto \frac{KA_{eff}\alpha_j}{G(v_{max}, L)\Gamma_{ij}} \tag{5.5}$$

where K is the polarization factor, A_{eff} is the optical effective area and $G(v_{max}, L)$ is the Brillouin gain at the peak frequency for a fibre of length L [16]. α_j is the acoustic attenuation coefficient for the acoustic mode of order j. The acoustic attenuation coefficient is calculated using phonon lifetime, T_B, and for Silica $T_B = 4.57\ ns$ [115]. Equation 5.6 is used to calculate the acoustic attenuation coefficient for a given acoustic mode having velocity v.

$$T_B = \frac{1}{\alpha_j v} \tag{5.6}$$

The normalised overlap Γ_{ij}, between the j^{th} acoustic mode and i^{th} optical mode can be calculated by the Eq. 5.7.

$$\Gamma_{ij} = \frac{(\int |H_{im}|^2 u_{jn} dxdy)^2}{\int |H_{im}|^4 dxdy \int \left|u_{jn}\right|^2 dxdy}; \quad m, n = x, y, z \tag{5.7}$$

Here, H_{im} is the m^{th} magnetic field component (where, m may be x, y or z) of the i^{th} optical mode and u_{jn} is the n^{th} component of the acoustic displacement profile (where, n may be x, y or z) of the j^{th} acoustic mode [116]. From the SBS threshold equation given in Eq. 5.5, it is understood that the SBS threshold can be increased either by increasing the A_{eff} or reducing the acoustic-optic overlap Γ_{ij}.

In order to calculate the overlap between optical and acoustic modes, both optical and acoustic modal analysis are carried out. For optical modal analysis the refractive indices of core and cladding are taken as n_{core}= 1.44905 and n_{clad}=1.444, respectively at the operating wavelength, $\lambda = 1.55\ \mu m$. The full-vectorial formulation describe in Chapter 4 for the optical modes based on the minimisation of the **H**-field energy functional is used for our modal solution.

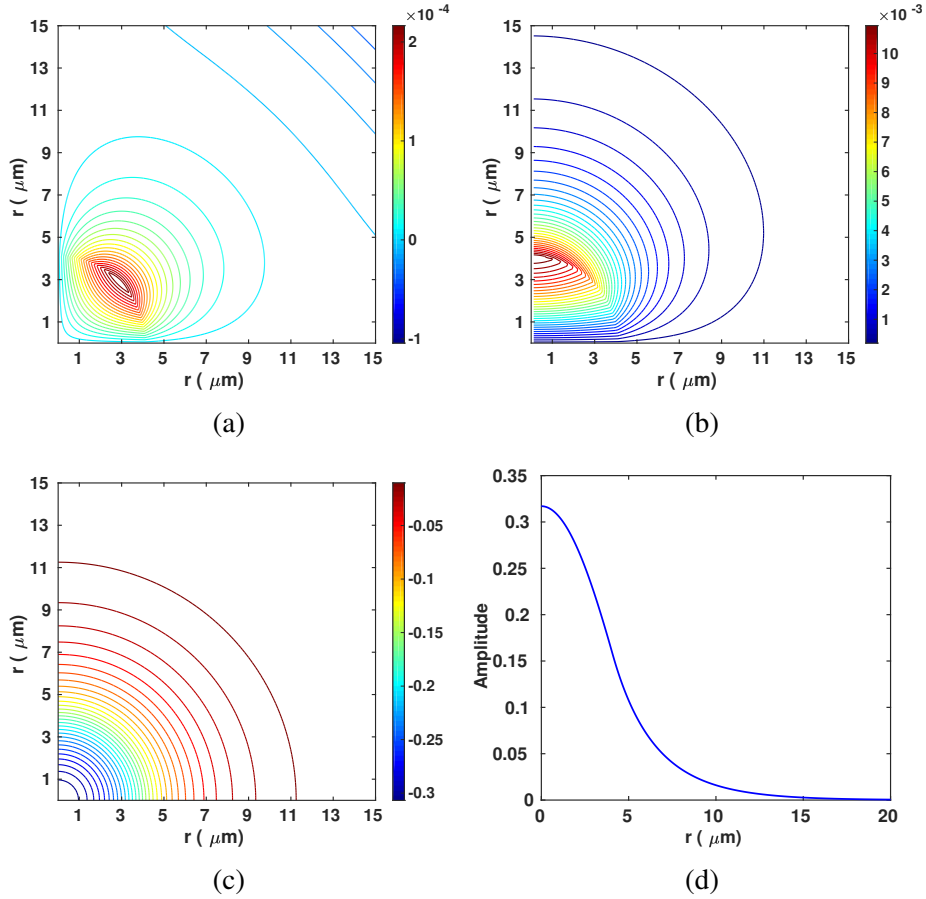

Fig. 5.1 The non-dominant (a) H_x, (b) H_z field profiles of the fundamental optical mode LP_{01}, (c) shows contour field profile of dominant H_y component and (d) shows the H_y field value of the quasi-TE mode along the radius of fibre where the propagation constant is $\beta_{op} = 5.86205\ rad/\mu m$.

Figure 5.1 shows the contours of dominant H_y and non-dominant H_x and H_z fields of the fundamental optical LP_{01} mode. The propagation constant and effective refractive index are

calculated as β_{op} = 5.86205 $(rad/\mu m)$ and n_{eff} = 1.4461163 at the operating wavelength of 1.55 μm. Figures 5.1 (a) and (b) are non-dominant H_x and H_z field profiles of LP_{01} mode, respectively. Figure 5.1 (c) shows the dominant H_y field profile and Fig. 5.1 (d) shows H_y field variation along the radius of the fibre. From the dominant H_y field profile of LP_{01} mode it can be observed that the field is more confined in the core and decreases away from the centre. Whereas, the field profile of non-dominant H_x component is distributed on four quadrants and has zero field at the fibre centre. Similarly, the field profile of non-dominant H_y component is distributed in two upper and lower quadrants as shown in Fig. 5.1 (b). In order to improve the solution accuracy, only a quarter structure is simulated. This allows a much better mesh refinement with given computer resources and also avoid degeneration of modes which have similar eigenvalues [117, 118]. Besides, we have used polar mesh which is more efficient in the distribution of discretized triangular elements along the curved interfaces of a circular waveguide as explained in Section 4.2.

However, in order to observe light sound interaction, the following phase matching condition between optical and acoustic modes should be satisfied.

$$k_a = 2\beta_{op} \tag{5.8}$$

Here, k_a is the wave vector of interacting acoustic mode and, β_{op} is the propagation constant of the optical mode.

A new full-vectorial FEM based computer program for acoustic modal analysis based on the formulation given in Eq. 5.3 has been developed. Similar to optical modal analysis, we have exploited the available two-fold symmetry and only a quarter of the waveguide is simulated. Considering the phase matching condition given in Eq. 5.8 the acoustic propagation constant or wave vector is calculated as k_a=11.7241 rad/μm. Although, this fibre supports only a single mode for either quasi-TE or quasi-TM polarization, however can guide several acoustic modes depending on the acoustic wavenumber. The phase matching

condition can be fulfilled by multiple acoustic modes having different acoustic velocities and frequencies. This results in the interaction of the LP_{01} optical mode with not only the fundamental acoustic mode but also with other higher order acoustic modes. The phase-matched fundamental longitudinal (LP_{01}) mode with dominant U_z vector is found at frequency 10.824 GHz with its corresponding acoustic velocity of 5800.8391 m/s. However, when a computer code using Eq. 5.1 is considered, in addition to this fundamental longitudinal acoustic mode, unfortunately, many other non-physical acoustic modes were also observed in the modal solutions. The existence of these spurious modes resulted in difficulty to identify a particular mode of interest and multiple iterations were carried out in order to find a correct mode. In addition to this, the original mode quality was also significantly affected by the existence of spurious modes when no penalty term is used. Figure 5.2 shows the presence of a single physical LP_{01} mode shown by a square and many other non-physical spurious modes by crosses, respectively. In each simulation run maximum five eigenvalues were obtained. It can be observed that when $\alpha = 0$, there are four spurious modes (shown by crosses) in the vicinity along with only one physical mode (green square), which is the fundamental longitudinal (LP_{01}) acoustic mode in this case. However, when the value of α is more than 1×10^5, the spurious modes vanish completely and the mode quality also improves significantly. Moreover, it can also be observed that the frequency of fundamental longitudinal mode at $\alpha = 1 \times 10^5$ remains almost the same as that is obtained when $\alpha = 0$.

5.4.2 Improvement in the mode quality

Figure 5.3 shows the dominant and non-dominant vector displacement profiles of the fundamental longitudinal acoustic LP_{01} mode when no penalty term was used ($\alpha = 0$). The dominant U_z displacement vector of the LP_{01} mode is slightly affected by the presence of spurious solutions, as shown in Figs. 5.3 (c) and (d), but where a close inspection shows small ripples in the contour lines and displacement vector variation along radius of the fibre,

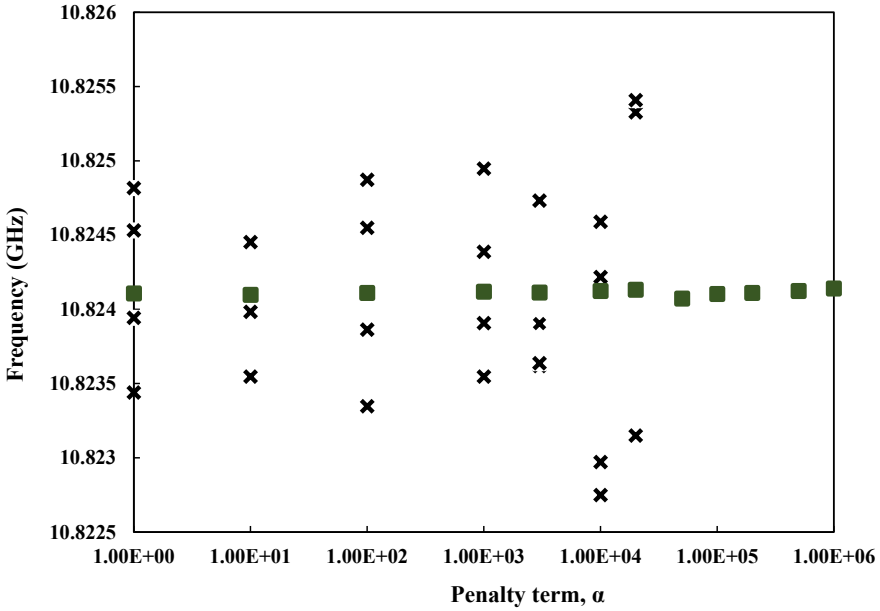

Fig. 5.2 Reduction of spurious solutions with penalty (α) term for the U_z dominant LP_{01} acoustic mode in a SMF.

respectively. However, the non-dominant displacement vectors U_x and U_y profiles shown in Fig. 5.3 (a) and (b), respectively, are more noisy than the dominant U_z vector profile. As in this case, the magnitude of non-dominant displacement vectors U_x and U_y were 40 times smaller than that of the dominant U_z vector, so the smaller non-dominant displacement vectors were more affected by the noise and are of significantly poor quality. As the available two-fold symmetry of the fibre is exploited here, so only a quarter of the structure is shown in Fig. 5.3.

The Gaussian-like displacement vector profile of the dominant U_z vector has the peak value at the centre of the core and monotonically decreases along the radius of the fibre. However, the non-dominant U_x displacement vector has maxima on the x-axis and zero value along the y-axis as shown in Fig. 5.3 (a). Similarly, the non-dominant U_y displacement vector has maxima value along the y-axis and zero along the x-axis as shown in Fig. 5.3 (b). However, quality of these non-dominant components shown here is very poor.

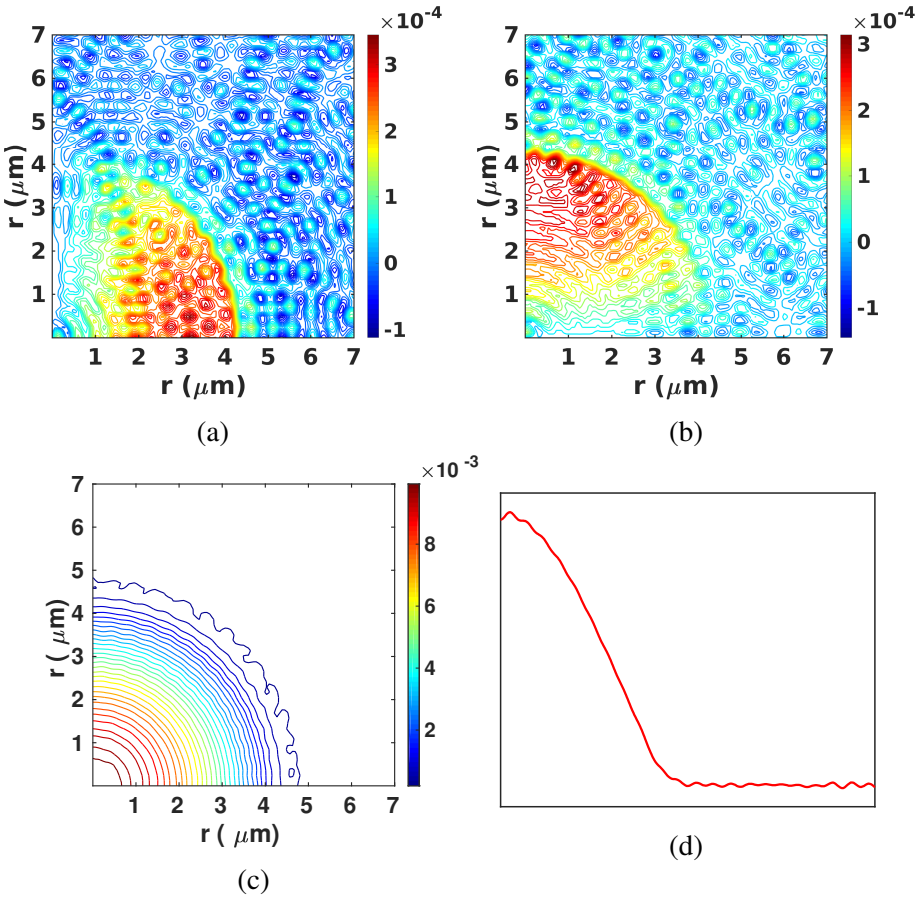

Fig. 5.3 Dominant and non-dominant displacement vector profiles of the fundamental longitudinal LP_{01} acoustic mode for $\alpha = 0$ where, (a) U_x, (b) U_y and (c) U_z contours, respectively. (d) shows the variation of U_z displacement vector along the radius of fibre without penalty term.

The possible reason for noise in the vector displacement profiles of longitudinal acoustic modes is that, for a lower or zero value of α, the spurious modes with eigenvalues close to the desired physical modes, which in this case is LP_{01} mode, perturbed the truly physical mode. When two eigenvalues are close then their eigenvectors can easily get mixed up during numerical simulations. However, after the introduction of the penalty term and choosing $\alpha = 1 \times 10^5$, the eigenvalues of spurious modes are pushed away from the physical mode and results in a clean mode profile, as shown in Fig. 5.4.

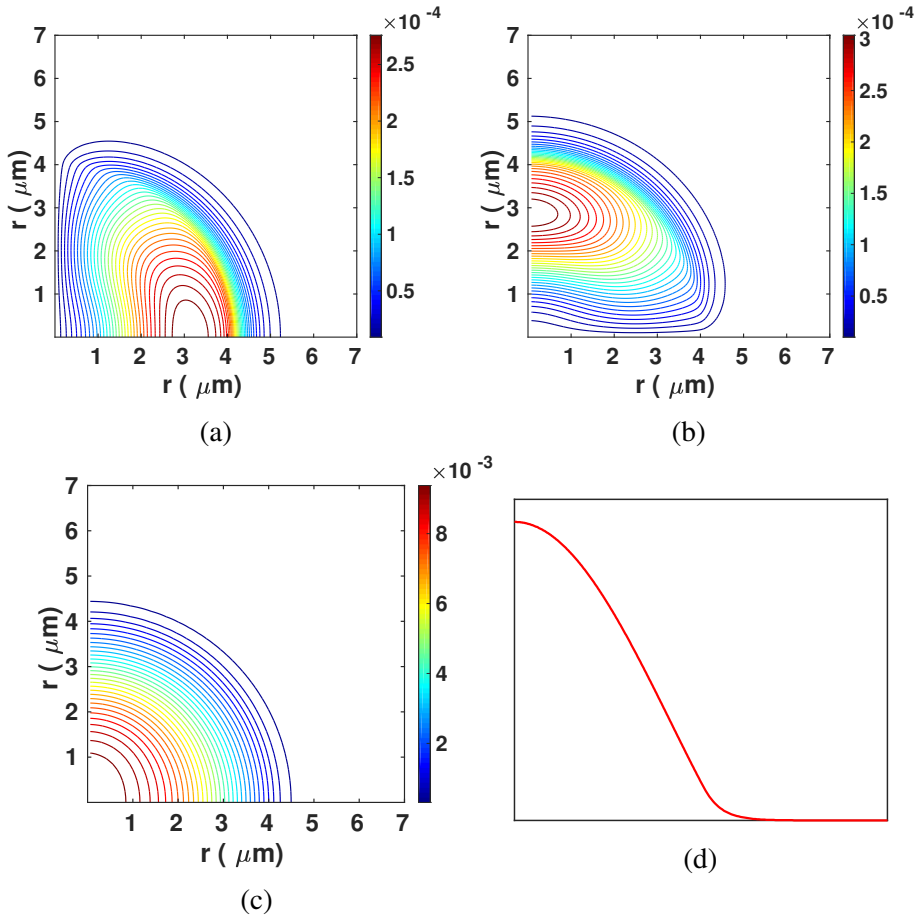

Fig. 5.4 Dominant and non-dominant displacement vector profiles of the fundamental longitudinal LP_{01} acoustic mode for $\alpha = 10^5$, where, (a) U_x, (b) U_y and (c) U_z contours, respectively. (d) shows the variation of U_z displacement vector along the radius of fibre after the penalty term is used, α= 10^5.

It can be observed that the non-dominant U_x and U_y displacement vector of LP_{01} mode shown in Figs. 5.4 (a), (b), respectively, have significantly improved mode profiles compared to the mode profiles shown in Fig. 5.3, without the use of a penalty term. Figures 5.4 (c) the contour plot and (d) variation of displacement vector along the radius of fibre also shows significant improvement in eigenvalues for U_z displacement vector. This significant improvement in the mode quality not only provides a more accurate modal solution but also allows us to understand the full-vectorial nature of these modes and if possible to exploit

them. It also helps to utilise computer resources more efficiently by reducing the multiple iterations often needed to refine individual modes.

5.4.3 Effect of penalty and mesh density on modal solution

It is well known that the solution accuracy of FEM based modal solution is strongly dependent on the discretized mesh elements. Hence, in our simulations, polar mesh is used and mesh density was varied with different values of α. For our analyses we have used three different mesh densities as low, medium, and high with 119800, 479600, and 1439400 first-order triangular elements, respectively, to see the impact on the frequency shift with the penalty factor. The frequency of the fundamental longitudinal mode is calculated as 10.823 GHz, 10.824 GHz, and 10.829 GHz for a low, medium and high mesh densities, respectively, at $\alpha = 10^5$. Although, the variation in the frequency is little, however, we have used a moderate value of α to avoid spurious modes along with a finer mesh for our subsequent simulations to achieve a maximum accuracy.

Figure 5.5 shows the effect on frequency when the penalty term, α increases from 1×10^6 to a very higher value in the order of 1×10^{11}. It can be noted that the acoustic frequency did not change significantly for penalty value up to 1×10^6 and so not shown here. However, when the penalty factor is increased more to observe its behaviour on the frequency, it can be noticed that the acoustic frequency increases. This increase in frequency is also strongly related to the density of mesh distribution used. When a more dense mesh is used, the increase is less as compared to a relatively coarse mesh division. This is due to the fact that a higher mesh distribution is more accurate than a lower mesh. For this reason, we have used a much refined mesh distribution for our modal solutions to achieve a higher accuracy.

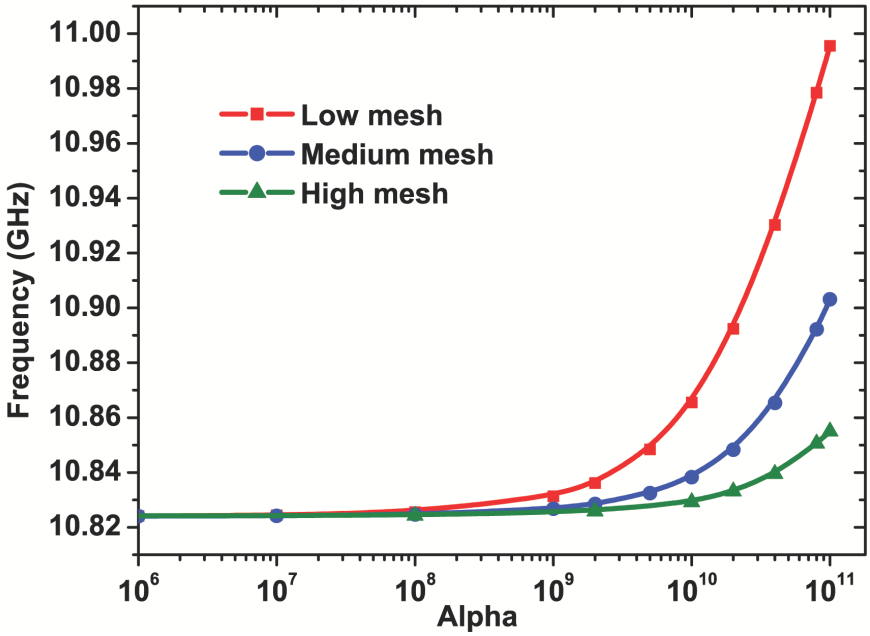

Fig. 5.5 Variation of frequency with respect to change in the value of penalty (α) for the U_z dominant LP_{01} acoustic mode.

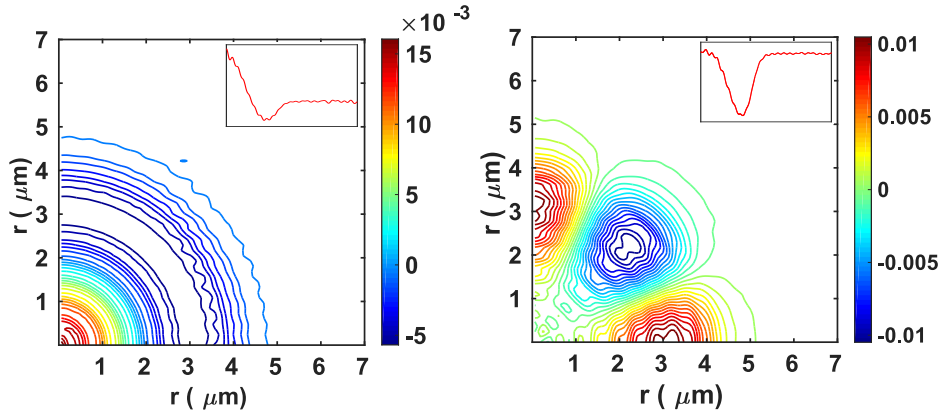

Fig. 5.6 Dominant U_z displacement vector contours of higher order longitudinal acoustic modes with $\alpha = 0$. The variation of U_z displacement vector along the radius (x-axis) of fibre is shown as insets.

Figures 5.6 (a) and (b) show the dominant U_z vector profiles of two higher order LP_{02} and LP_{41} longitudinal acoustic modes, respectively for $\alpha = 0$. Variation of displacement vector profile of these modes along the fibre radius are also shown as insets. The ripples in contour

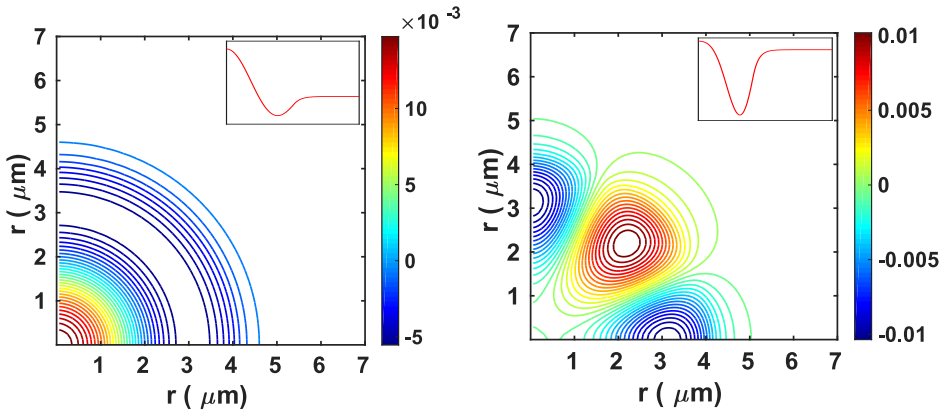

(a) (b)

Fig. 5.7 Dominant U_z displacement vector contours of higher order longitudinal acoustic modes with $\alpha = 10^5$. The variation of Uz displacement vector along the radius (x-axis) of fibre is shown as insets.

plots of the displacement vector clearly show that the higher order mode profiles are also considerably affected by the presence of spurious modes. The quality of their non-dominant displacement vector profiles was even worse than that of LP_{01} mode and not shown here. However, the introduction of penalty term in acoustic formulation resulted in much smooth contour plots of these two higher order LP_{02} and LP_{41} modes and these are as shown in Fig. 5.7. Variations of their displacement vectors along the radius of the fibre are also shown as the insets in Fig. 5.7.

Table 5.2 shows the frequency shift and longitudinal velocities of fundamental and higher order longitudinal modes for $\alpha = 0$ and $\alpha = 10^5$. It can be observed that there is only a small change in these values which indicate the accuracy of the modal solutions are not affected when the penalty term is introduced.

Table 5.2 Effect of α on frequency shift and longitudinal velocities of the fundamental and higher order longitudinal acoustic modes.

Mode	Without penalty (α=0)		With Penalty (α=10^5)	
	Frequency shift (GHz)	Longitudinal velocity (m/s)	Frequency shift (GHz)	Longitudinal velocity (m/s)
LP_{01}	10.824	5800.8391	10.824	5800.8257
LP_{02}	10.873	5827.1568	10.873	5827.059
LP_{41}	10.926	5855.7582	10.927	5856.277
LP_{03}	10.959	5873.2883	10.959	5873.1817

5.5 Effect of penalty term in high index contrast acoustic waveguide

Recently, SBS based nanowire structures are also being considered for many exotic photonic devices, such as microwave photonic filters [119], resonators [120] and on-chip high-performance optical signal processing [121, 122]. Acoustic modes in high index contrast waveguides are even more complex. The magnitudes of their non-dominant displacement vectors are higher and displacement vector profiles often have stronger spatial variations.

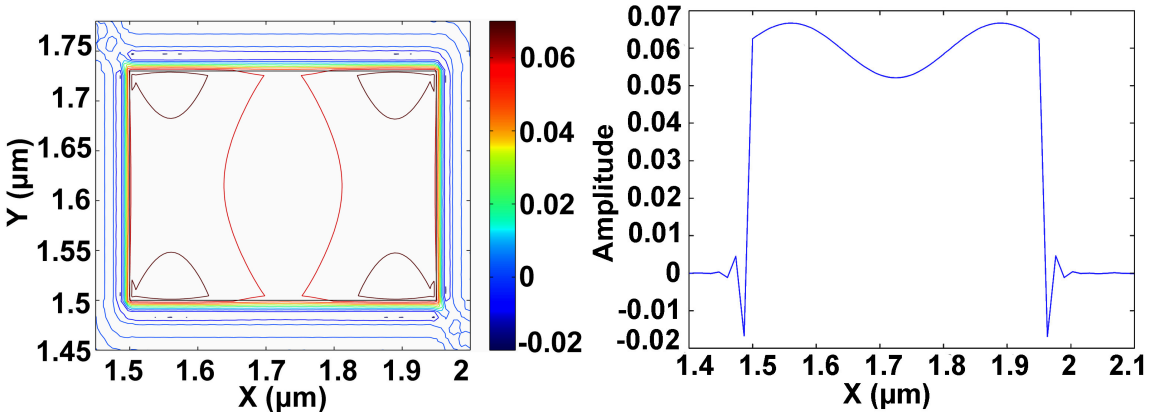

(a) (b)

Fig. 5.8 (a) The dominant U_z vector displacement of a highly hybrid mode and (b) is the variation along the x-axis, when $\alpha = 0$.

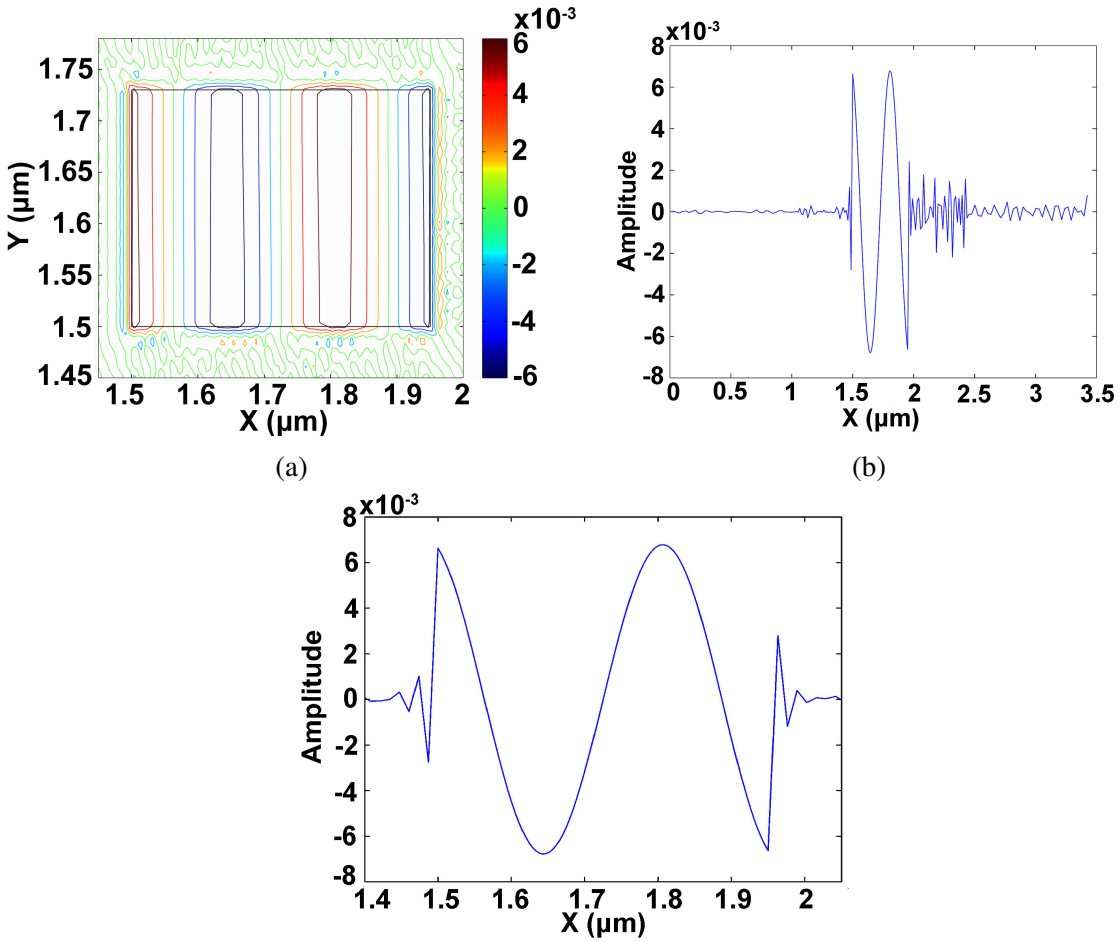

Fig. 5.9 (a) The non-dominant U_x vector displacement profile of a highly hybrid longitudinal mode (b) the variation of U_x displacement vector along the x-axis when $\alpha = 0$, and (c) when $\alpha = 100$.

In order to observe the effect of penalty term in such nano-structures, we have considered a high index contrast air-clad silicon nanowire for modal solutions. Here, we have considered a suspended silicon nanowire with its width and height being 450 nm and 230 nm, respectively. The acoustic shear and longitudinal velocities of silicon are chosen as $V_s = 5840\ m/s$, $V_l = 8433\ m/s$, respectively. Similarly, the longitudinal velocity of air is chosen as 340 m/s while the shear velocity is zero. The material densities of silicon and air are taken as

ρ_{si}=2331 kg/m^3 and ρ_{air}=1.29 kg/m^3, respectively. Moreover, the phase matched acoustic propagation constant is calculated as $k_a = 18.477$.

The contour plot of the dominant U_z displacement vector of a highly hybrid mode at $f = 24.801\ GHz$ and $V = 8433.3184\ m/s$, is shown in Fig. 5.8 (a) and its variation along the x-axis is shown in Fig. 5.8 (b). The dominant U_z displacement vector profile of this longitudinal acoustic mode has a reasonably clean profile without the penalty term. However, still poor quality contour lines can be clearly observed outside the core as shown in Fig. 5.8 (a). From the dominant U_z vector displacement profile along the x-axis, shown in Fig. 5.8 (b), it can be observed that the amplitude increases from the centre of the waveguides along the x-axis towards outer edges of the core and reduces rapidly to zero value with damping oscillations at the core and cladding interfaces.

However, the non-dominant U_x and U_y vector displacement profiles with their small magnitudes are more susceptible to the existence of the spurious modes. Figure 5.9 (a) shows the contour plot of the non-dominant U_x vector displacement profile of this highly hybrid mode without the use of a penalty term. The non-dominant U_x vector has almost constant magnitude along the y-axis, but with two positive and two negative peaks along the x-axis. Its variation along the x-axis is shown in Fig. 5.9 (b). Two positive and two negative peaks are visible but very noisy oscillations outside the core is also clearly visible in Fig. 5.9 (b) when no penalty term is used. However, with the introduction of penalty value ($\alpha = 100$), the vector displacement profiles is improved significantly and damped oscillations at the two interfaces are clearly visible, as shown in Fig. 5.9 (c). It can be noted that for this high-index contrast waveguide, non-dominant vectors are relatively large (about 10%) compared to a low index contrast SMF (about 2.5 %), shown earlier. The magnitude of the optimum value of penalty term is related to the waveguide design, however, as the accuracy of the eigenvalue does not depend much on its value, so its selection is not so critical.

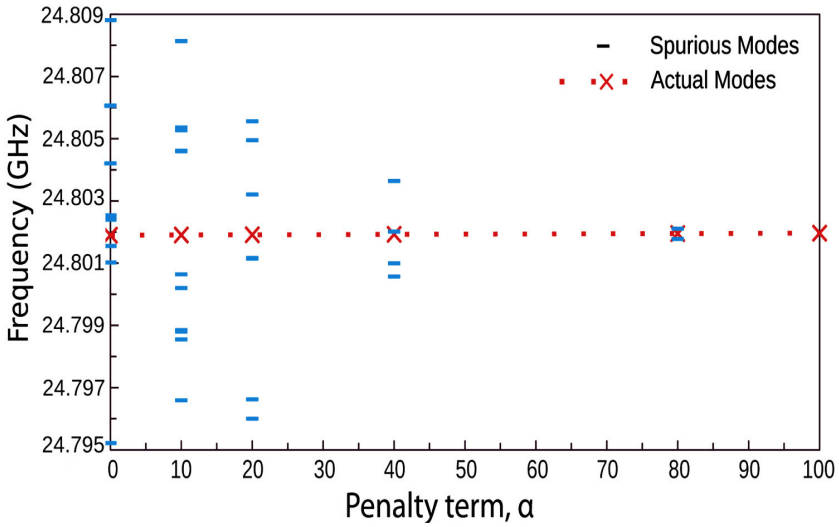

Fig. 5.10 Reduction of spurious modes when tracking a U_z dominant of highly hybrid longitudinal acoustic mode in an air-clad Si nanowire.

In order to observe the effect of α, on the spurious modes and frequency of the desired mode for a high index contrast waveguide numerical simulations were carried out and results are shown in Fig. 5.10. As the α value is increased from zero to higher values, the number of spurious modes start reducing. At $\alpha = 100$, or beyond (not shown here) no spurious mode was observed near the physical eigenvalues and resultant improved quality dominant and non-dominant vector displacement vectors were presented in Fig. 5.9. The spurious modes are shown by the blue dash (-) and the physical modes are shown by the red cross in Fig. 5.10.

It can be noted that for both the structures, the penalty value has a very little effect on the mode's frequency and velocity of propagation. However, the quality of eigenvectors is significantly improved as demonstrated here.

5.6 Acoustic-optic overlap for single mode fibre

The optical and acoustic modal solution of a low index contrast waveguide such as SMF is explained earlier in section 5.4. The propagation constant and effective index of the H_y dominant fundamental optical LP_{01} mode are calculated as $\beta_{op} = 5.86205\ rad/\mu\text{m}$ and $n_{eff} = 1.446116$, respectively, at the operating wavelength of 1.55 μm. Similarly, the frequency and the velocity of phase matched fundamental longitudinal acoustic displacement vector is calculated as 10.824 GHz and 5800.828 m/s, respectively. The resultant overlap of 94.0 % is calculated using Eq. 5.7 between the dominant magnetic field (H_y) of the fundamental optical mode and dominant displacement vector (U_z) of the fundamental longitudinal acoustic mode.

The phase matching condition given in Eq. 5.8 can be satisfied by multiple acoustic modes. For example for a phase matched acoustic wave vector, fundamental and higher order modes exist that have the different frequency shift and propagation velocities. Figure 5.11 shows the dominant displacement vector profiles of the higher order longitudinal acoustic LP_{21}, LP_{02} and LP_{03} modes. Displacement vector variation of higher order longitudinal modes along the fibre radius are also shown in the respective insets of the Fig. 5.11.

The normalised H_y optical field profile of the fundamental LP_{01} optical mode, and U_z vector profiles of the fundamental and higher order longitudinal acoustic modes along the r-axis are shown in Fig. 5.12. It can be observed that the fundamental longitudinal acoustic mode have the similar mode profile as of the fundamental optical mode. However, the acoustic modes are more confined in the core compared to the fundamental optical mode.

Using Eq. 5.7 overlap values of fundamental and higher order longitudinal modes with the fundamental optical mode are calculated. As the displacement vector profile of the dominant U_z of the longitudinal mode and dominant H_y field of optical modes have identical nature hence, an overlap value of 94% is calculated between them. Similar, overlap has been reported in [123], where, the rectangular waveguide of similar dimensions is considered.

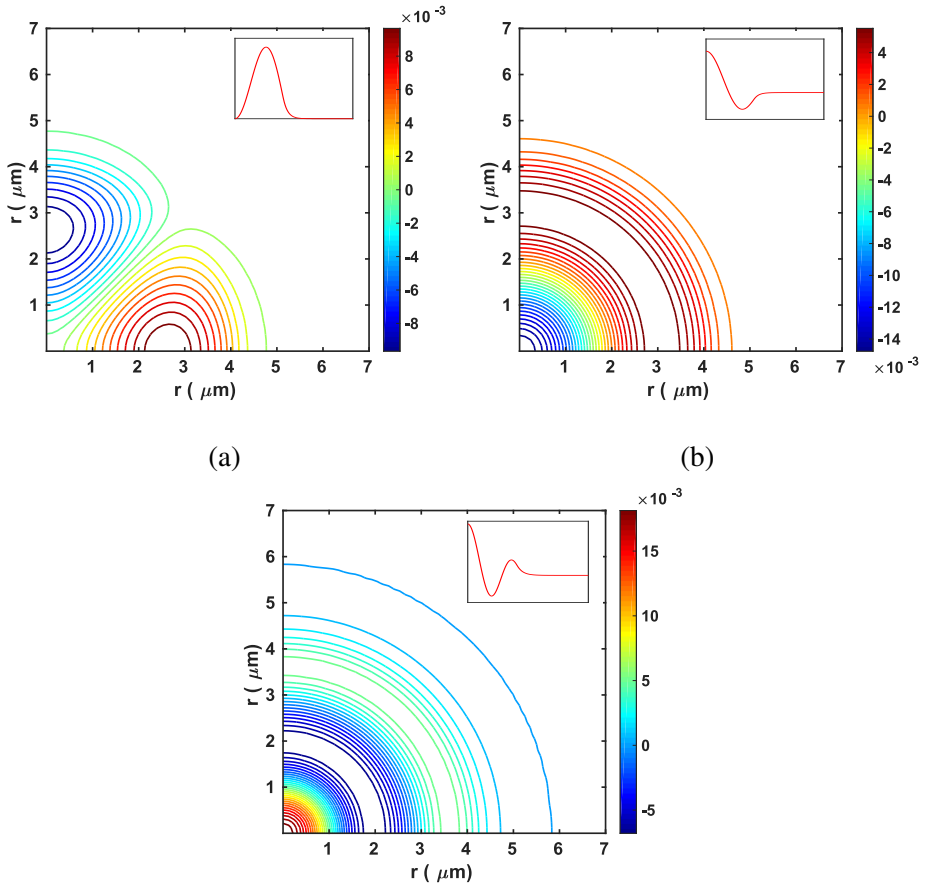

Fig. 5.11 Dominant vector displacement profile U_z of higher order longitudinal modes (a) LP_{21} (b) LP_{02} and (c) LP_{03} phase matched at 10.865 GHz, 10.873 GHz and 10.959 GHz, respectively. The variation of U_z displacement vectors along the radius (x-axis) of fibre are also shown as insets.

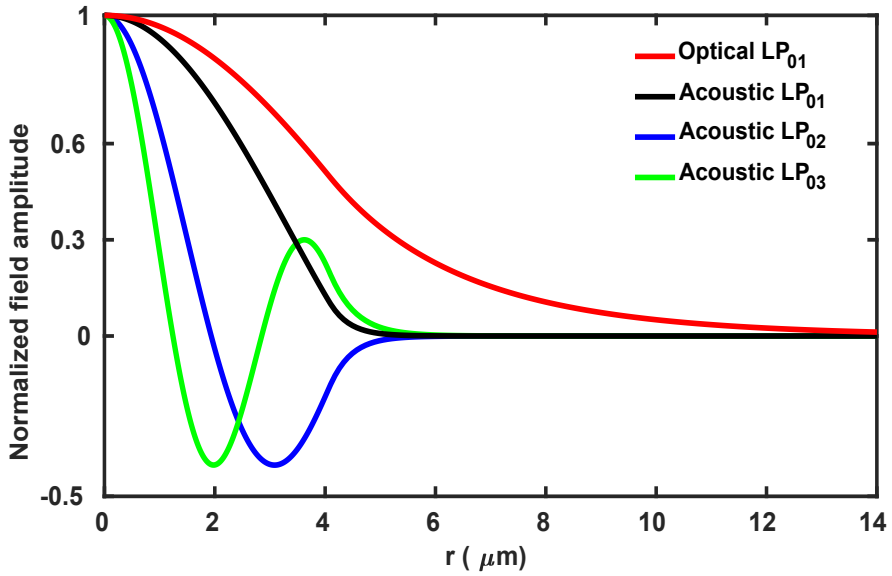

Fig. 5.12 Normalised H_y optical field and U_z longitudinal displacement vector profiles of dominant LP_{01}, LP_{02}, LP_{03} acoustic modes, along the r-axis

Moreover, the overlap between the higher order (LP_{21}, LP_{02}, LP_{03}) modes and the dominant H_y field of the fundamental optical mode are calculated as 0%, 0.91%, 0.77%, respectively. The reason for the 0% overlap between LP_{21} and optical mode is due to the odd symmetrical nature of dominant U_z displacement vector profile of the acoustic mode. However, the overlap between non-dominant U_x and U_y have considerable overlap due to their even symmetry and found as 35.31% and 35.233% respectively.

5.7 Fibre design for sensing applications

5.7.1 Al_2O_3 doped core

Designing an acoustic co- or anti-guide is highly dependent on the choice of the doping materials. The U_z profile for the LP_{01} acoustic mode shows it is more confined in the core than the H_y field profile of the LP_{01} optical mode, as index contrast for the acoustic mode was higher. This index contrast can be adjusted by co-doping an optical fibre by using

two or more dopants. Table 5.3 shows the effect of some commonly used materials for changing the optical and acoustic indices. This table shows the percentage change in the optical refractive index ($\Delta n\%$), shear ($\Delta V_S\%$) and longitudinal ($\Delta V_L\%$) velocities with the percentage weight of dopant. Increase in the acoustic index results in the reduction of shear and longitudinal velocities. As discussed earlier that the acoustic modes are more confined in the core compared with the optical modes. Hence, in order to increase the optical and acoustic overlap, different %wt doping of Al_2O_3 are calculated keeping the optical refractive index n_{core}=1.44905 unchanged. This results in the slightly reduced confinement of the acoustic modes in the core and thus increased overlap with the optical modes.

Table 5.3 Percentage weight change contribution to the optical refractive index and acoustic velocities for different dopants [124, 125].

Doping material	$\frac{\Delta n\%}{Wt\%}$	$\frac{\Delta V_L\%}{Wt\%}$	$\frac{\Delta V_S\%}{Wt\%}$
GeO_2	+0.056	-0.47	-0.49
P_2O_5	+0.02	-0.31	-0.41
F	-0.31	-3.6	-3.1
TiO_2	+0.23	-0.59	-0.45
Al_2O_3	+0.063	+0.42	+0.21
B_2O_3	-0.033	-1.23	-1.18

The effect of Al_2O_3 on the fundamental acoustic mode spot-size and overlap percentage are shown in Table 5.4. The doping concentration of SiO_2, GeO_2 and Al_2O_3 in the core is chosen in way that the optical refractive index remain same as $n_{core} = 1.44905$ and only the acoustic index is modified. The shear and longitudinal velocities for the core are calculated by the relation shown in Table 5.3. It is observed that as the percentage of Al_2O_3 is increased the spot-size or the effective area of the fundamental longitudinal LP_{01} acoustic mode starts increasing. Overlap of 99.76 % is achieved when the core is co-doped with 2.71 %wt of Al_2O_3, 3.20 %wt of GeO_2 and 94.09 %wt of SiO_2. Moreover, Table 5.4 also shows the effect on the spot size (σ_x) of LP_{01} acoustic mode as %wt of Al_2O_3 is increased further. It can be

Table 5.4 Effect of Al_2O_3 doping on the core longitudinal velocity and acoustic-optic overlap

Materials (%wt)			**Fundamental Mode** LP_{01}		**Spot size** σ_x	**Acoustic-optic overlap (%)**
SiO_2	GeO_2	Al_2O_3	**Longitudinal velocity (m/s)**	**Frequency shift (GHz)**		
93.76	6.24	0	5800.8286	10.824	3.208	94.0
93.95	4.5	1.55	5888.4942	10.987	3.341	96.98
94.06	3.5	2.44	5938.2274	11.080	3.546	99.16
94.09	3.2	2.71	5952.8299	11.107	3.751	99.76
94.11	3.0	2.89	5962.2220	11.125	4.059	98.16
94.13	2.90	2.97	5966.5666	11.133	4.396	92.12
94.14	2.85	3.01	5968.4700	11.136	5.087	80.56

observed that as the Al_2O_3 doping is increased from 2.71%wt to higher value, the overlap start reducing as the acoustic power start spreading to a larger effective mode area.

5.7.2 B_2O_3 layer in the inner cladding

Another technique to increase acoustic-optic overlap could be by introducing a high acoustic index layer in cladding. To achieve this, a 4 μm wide annular region layer doped with B_2O_3 is used as shown as region 2 in Fig. 5.13. Figure 5.13 (a) show the schematic of the core, clad and high acoustic index 2^{nd} layer. Whereas, Figs. 5.13 (b) and 5.13 (c) show the optical and acoustic index profiles along the radius, respectively. This high acoustic index layer in the cladding is used to reduce the confinement of the acoustic mode in the core that results in large acoustic mode area.

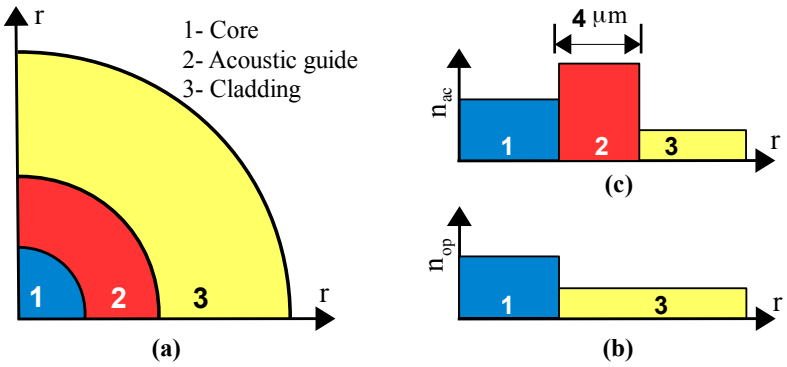

Fig. 5.13 Effect of 2^{nd} layer doping on the optical refractive index and the acoustic index of SMF.

Boron increases the acoustic index in the cladding layer resulting in the acoustic modes shifting towards cladding. The percentage weight doping of B_2O_3 is considered very carefully. If the doping percentage is increased more, the acoustic modes completely shifts in cladding that results the acoustic mode to approach its cutoff. Moreover, due to B_2O_3 doping in the cladding optical refractive index get reduced which is compensated by the addition of GeO_2 doping. The acoustic-optic overlap of 99.69% is achieved with the original core (without Al_2O_3) and high acoustic index cladding layer with doping concentration of (1.697%wt of B_2O_3 + 1%wt of GeO_2 + 97.303%wt of SiO_2).

5.8 Acoustic anti-guide core: for high power transmission

As discussed in the introduction that the SBS is considered as a limiting factor in order to scale the power in the optical fibre lasers and amplifiers. Backward scattering in SBS process reduces the capability of the optical transmission systems by limiting maximum transmission power and introducing the high bit error rate [126]. Many techniques have been proposed in order to reduce the effect of SBS by reducing the acoustic and optical modes overlap [127, 128].

Here, we have proposed a novel idea of the acoustic anti-guide in the core that results in a very low overlap between optical and acoustic modes. The SBS threshold is highly related to the overlap between acoustic and optical modes as mentioned in Eq. 5.7. Hence, increasing the SBS threshold results in the increased optical transmission power and improved data rate performance. For our design, we have introduced a high acoustic index annular layer in the inner cladding named here as a 2^{nd} layer which was used for increasing overlap as discussed in Subsection 5.7.2. However, the difference between high and reduced overlap depends on the doping concentration of B_2O_3 in 2^{nd} layer. Here, we have observed two cases for the doping percentage and the resultant overlap. In first case, where we kept the acoustic and optical properties of the core unchanged and only doped the 2^{nd} layer of cladding with the (3.394%wt of B_2O_3 + 2%wt of GeO_2). The resultant overlap with the fundamental optical mode is observed to be 3.5% with the acoustic mode in 2^{nd} layer. The acoustic mode in the 2^{nd} layer in cladding has the frequency shift and velocity of 10.587 GHz and 5674.08 m/s, respectively. However, it is observed that the fundamental acoustic mode in the core still exists at frequency 10.81768 GHz with velocity 5797.3904 m/s.

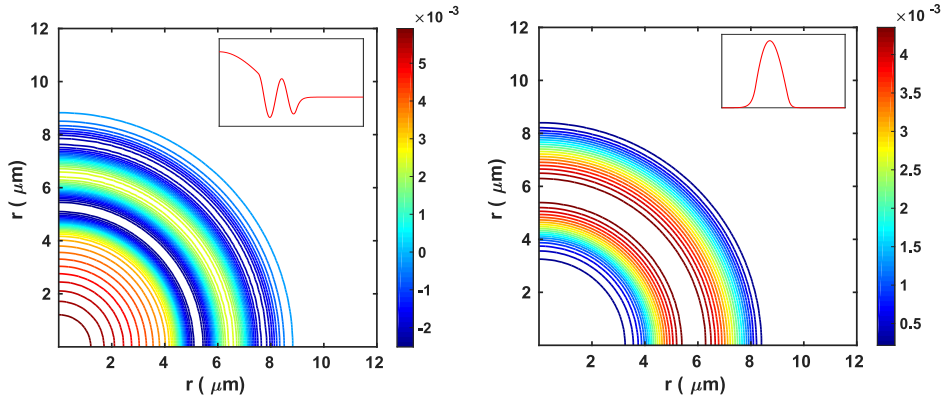

(a) (b)

Fig. 5.14 Dominant U_z displacement vector profile of the fundamental longitudinal LP_{01} modes (a) in the core at f=10.817 GHz and (b) in cladding 2^{nd} layer at f=10.587 GHz. The variation of U_z displacement vectors along the radius (x-axis) of fibre is shown as insets.

Figure 5.14 (a) shows both the acoustic modes in the core at f=10.817 GHz, and in the cladding at f=10.587 GHz. With only B_2O_3 doping in the 2^{nd} layer of cladding and without changing acoustic index in the core it was not possible to make the waveguide completely anti-guide. In order to make the core completely anti-guide, the core is also doped with the aluminium (3.061%wt of Al_2O_3 + 2.8 %wt of GeO_2) to reduce its acoustic index along with the 2^{nd} layer doping to increase its acoustic index as mentioned in the first case. This resulted in the complete shift of acoustic mode in cladding as shown in 5.14 (b) Here we have observed the acoustic-optic overlap of 2.7% for the dominant field of the fundamental optical and longitudinal acoustic modes.

Figure 5.15 (a) shows the contour plot of the dominant (U_Z) vector of the fundamental longitudinal mode (LP_{01}) in the proposed acoustic anti-guide design. Displacement vector profile along the radius of the fibre is also shown in inset of the Fig. 5.15. It can be seen that acoustic mode is shifted outside the core into cladding, however the optical modes still propagates inside the core as the optical refractive index of core and cladding were unchanged. Figures 5.15 (b) and (c) show the contour plots of the dominant U_z displacement vector of LP_{02} and LP_{03} modes, respectively. Higher order longitudinal modes also shifted in the cladding resulting in a very low overlap with the optical mode.

Similarly, Fig. 5.16 shows the field profile of fundamental optical mode, and U_z displacement vector profile of the fundamental and higher order acoustic modes along the radius. It can be observed that the optical mode field is confined in the core while the acoustic modes have shifted towards cladding region resulting in a low overlap. Hence, the proposed design gives a high SBS threshold and it will be very useful for the long haul fibre communication, fibre lasers and amplifiers applications.

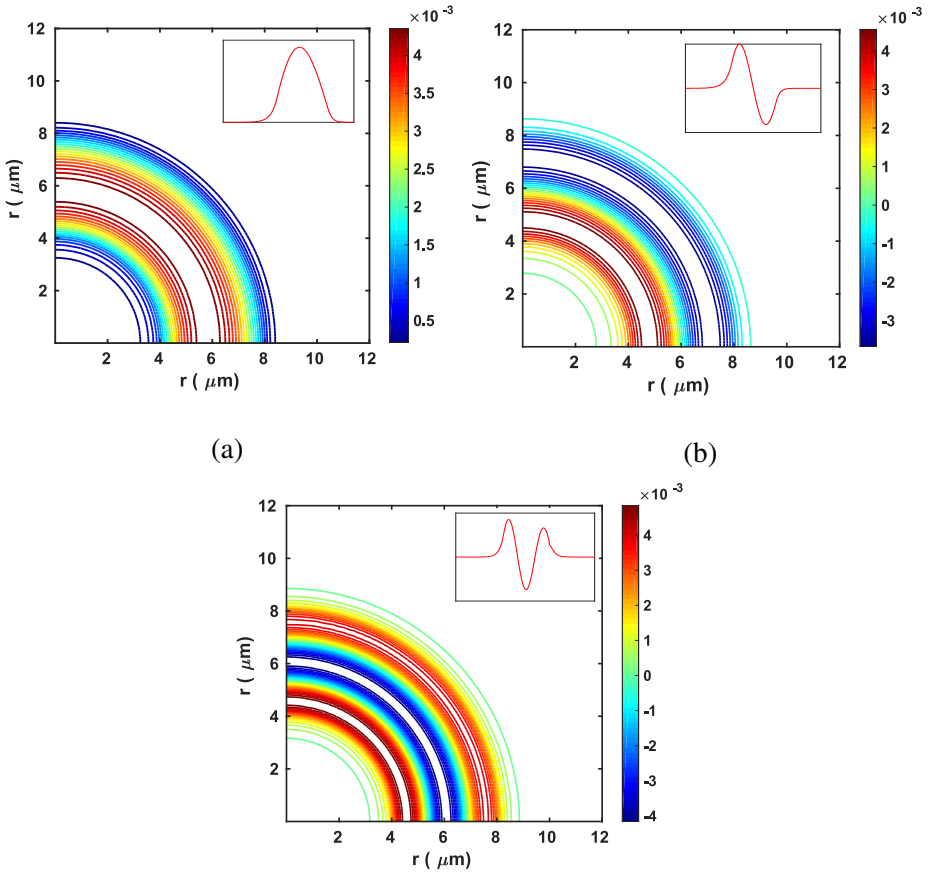

Fig. 5.15 Dominant U_z vector displacement profile of (a) fundamental longitudinal modes LP_{01} mode and higher order (b) LP_{02} mode and (c) LP_{03} mode at f=10.588 GHz, f=10.645 GHz and f=10.737 GHz, respectively. The variation of U_z displacement vectors along the radius (x-axis) of fibre is shown as insets.

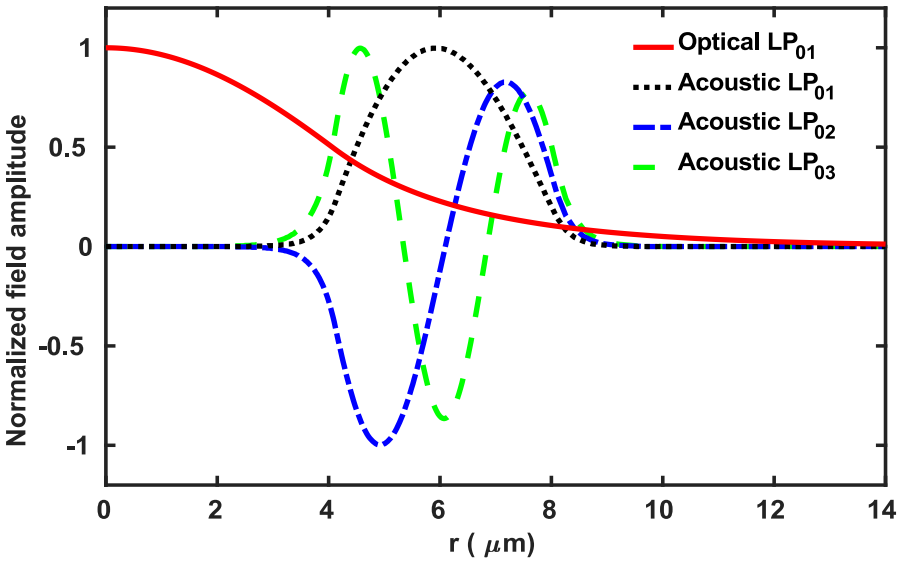

Fig. 5.16 Normalised H_y field of the LP_{01} optical mode and U_z displacement vector profiles of the LP_{01},LP_{02}, LP_{03} acoustic modes along the r-axis

5.9 Summary

A new full-vectorial finite element method based formulation is proposed to analyse the light-sound interaction in acoustic waveguides. The FEM based vector formulation is not only more accurate but essential to study high index contrast waveguides. However, the existence of spurious solutions often deteriorates the quality of physical modes. A penalty function, incorporating additional curl equations is used in order to eliminate these unwanted spurious modes. By introducing penalty term in full-vectorial acoustic formulation the spurious modes are suppressed significantly for both low and high index contrast acoustic waveguides. The proposed penalty method results in improving the mode quality by the elimination of spurious modes without introducing any significant error in the acoustic frequency and velocity of the real modes and thus will be useful to study complex light-sound interaction in optical waveguides for many potential applications and optimise their performances. The proposed full-vectorial acoustic modal solution is also used to analyse the complex light-sound interaction in a SMF. Two designs are proposed, where light-sound

interaction is either increased or reduced for fibre optic sensing or high power transmission applications, respectively. The acoustic-optic overlap is strongly related to the optical and acoustic mode profiles and in this case, it is observed that the acoustic mode is more confined in the core than the optical mode. However, through rigorous numerical simulations, we have identified that, if the percentage (in weight) doping of Al_2O_3 (2.7%) and GeO_2 (3.2%) in the core are chosen then the core optical refractive index remains same as 1.44905 but its acoustic index is reduced. In this case, the acoustic mode profile becomes much closer to the optical mode profile and the overlap increases to 99.7%. On the other hand, an acoustic anti-guide fibre for high-power transmission applications is also designed, where the overlap between acoustic and optical modes is reduced. Here, we have shown that with the aluminium doping in the core and introducing a high acoustic index layer in the cladding (3.394% B_2O_3 +2% GeO_2) results in a very low overlap of 2.7%. This high acoustic index layer in cladding force acoustic modes to completely shifts in the cladding from the core, allowing much high SBS threshold that enables high power delivery through this SMF.

Chapter 6

Mode stability enhancement in multimode fibres using doped strips

Multimode fibres (MMF) offer large effective mode areas (A_{eff}) and can be useful for high power lasers and amplifiers. However, a large mode area (LMA) results in an increased number of modes which can be more susceptible to mode coupling. This chapter discusses an innovative method to increase the modal spacing between higher order modes of a MMF such that the mode mixing due to external perturbations can be reduced.

6.1 Introduction

The performance of fibre lasers in terms of high beam quality, high efficiency and high average powers are directly linked with the characteristics of the rare-earth-doped fibre. One of the challenges in increasing the output power of fibre lasers especially for the pulsed fibre lasers is to mitigate non-linear effects such as Brillouin and Raman scattering, Four-wave mixing (FWM) and Self-phase modulation [129, 130]. The possible approaches to reduce the non-linear effects in fibre lasers is to reduce the fibre lengths or increase the effective mode field area. Optical fibres such as few-mode fibres or multimode fibres with larger core

size provide a higher effective area (A_{eff}) compared to smaller core fibres such as single mode fibres. Larger A_{eff} enables power scaling in fibre lasers as the non-linearity decreases with the increase in effective area. Therefore, much of the recent research focuses on large mode area fibres for the high-power fibre lasers [131]. However, there is a limit to increase the core radius while maintaining the single mode operation in LMA fibres. Figure 6.1 shows numerical aperture (NA) as a function of fibre core diameter for the wavelength of 1060 nm. The red line shows the regions for single mode or multimode operation with the change in core diameter. It can be observed that with the increase in the core radius, the NA value needs to be decreased in order to maintain single mode operation while achieving large mode area. However, due to fabrication limitations and increased bending loss, the value of NA is often restricted to 0.06 [132].

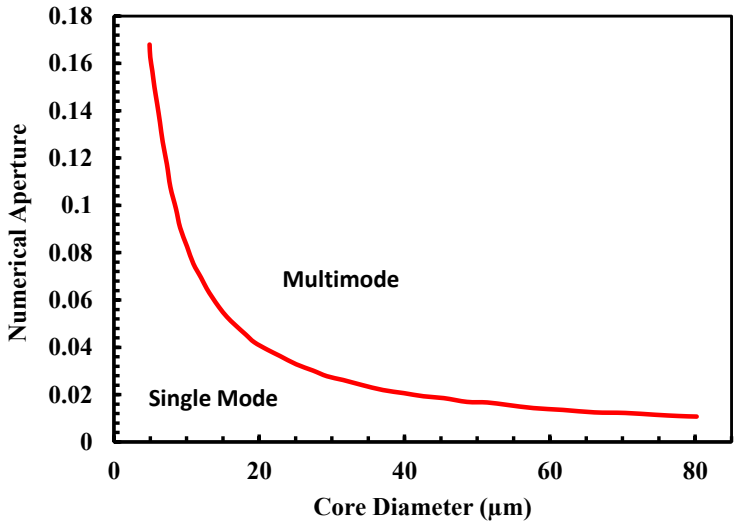

Fig. 6.1 Numerical aperture (NA) as a function of fibre core diameter for the cutoff wavelength of 1060 nm of step-index design [133].

Multimode fibres (MMF) offer large mode areas and high beam quality M^2 [134]. Zervas and Codemard have shown the variation in beam quality with a function of normalised frequency (V number) for different modes of a step-index fibre as shown in Fig. 6.2 [5]. It can be observed that the fundamental LP_{01} mode departs to higher value of $M^2 > 1$ as it approaches cutoff condition for $V < 1.5$. This is due to increased evanescent field extended

into the cladding which deviates from the ideal Gaussian profile. The similar behaviour is observed for other higher order modes as they approach cutoff condition and their field extends to the cladding. Higher order modes LP_{m1} with high orbital momentum, show considerably lower M^2 which grows at a much slower rate compared to other LP_{mn}.

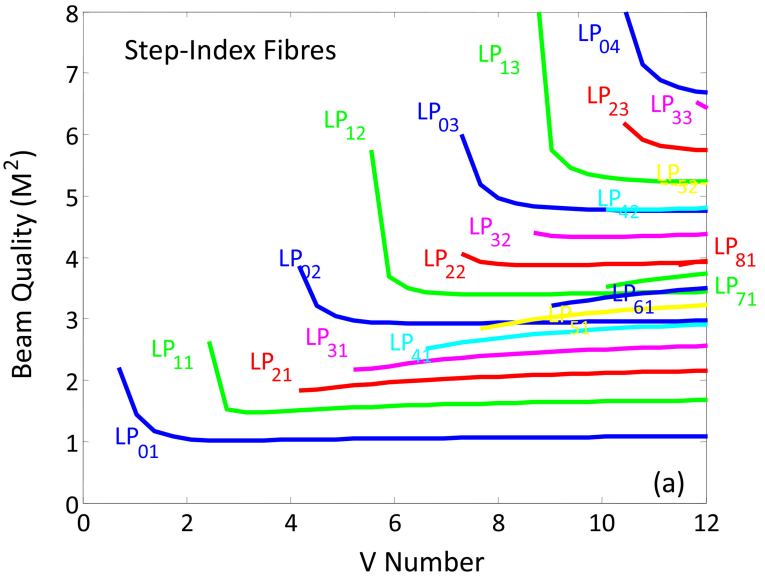

Fig. 6.2 Beam quality (M^2) as a function of V number for fundamental and higher order modes of step-index fibre [5].

A MMF with a larger core has a fundamental mode and multiple Higher order modes (HOM) depending on the core size and V number. Recent research shows that higher order modes (HOM) can provide more stable operation because the signal stability increases with an increase in the modal order [135, 136]. Several approaches have been presented in recent years to use HOM for high power fibre lasers and amplifiers. One of the methods involves the coupling of light from the fundamental mode to a single desired HOM using fibre Bragg gratings and then to propagate light in the higher order mode amplifying fibre [36]. These techniques provide considerably larger modal areas as well as more stable operation as described above. Moreover, for a given effective area, HOMs are also less sensitive to area reduction than the fundamental mode when bending [35, 137]. At the same time, compared to the fundamental mode, higher order modes are less prone to mode coupling as with the

increase in the modal order (m) the difference in effective index (Δn_{eff}) between a given higher mode $LP_{0,m}$ and its nearest antisymmetric mode $LP_{1,m+1}$ and $LP_{1,m-1}$ also increases [17].

In this chapter, a novel approach to increase the Δn_{eff} is discussed that result in resilience to mode-mixing and provides a more stable signal propagation with the advantage of significantly larger effective mode area (A_{eff}) by using HOMs. Annular rings with doping of increased or reduced refractive index are used at particular radial locations inside the core as shown in Fig. 6.3, such that the effective refractive index (n_{eff}) of a desired mode is increased or reduced [138]. To demonstrate the proposed concept, a MMF of numerical aperture (NA=0.22) with core radius (R_{core}=25 μm) and refractive index (n_{core}=1.457) is considered. Similarly, cladding radius and refractive index are taken as (R_{clad}=62.5 μm) and (n_{clad}=1.4403), respectively. For this study the central operating wavelength of (λ=1.05 μm) is chosen.

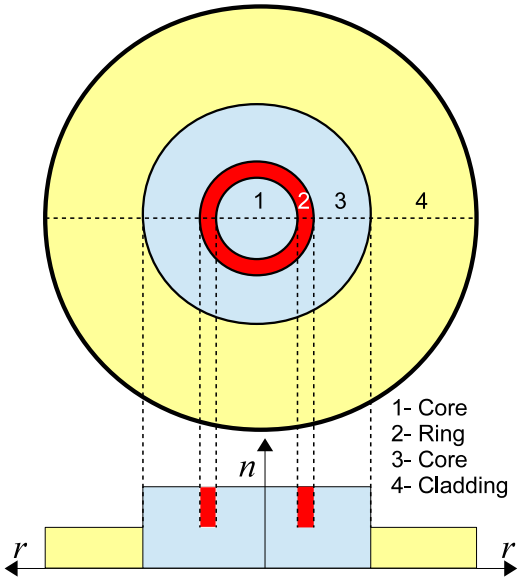

Fig. 6.3 Ring doping schematic of a MMF with the change in the refractive index along r-axis.

6.2 Theory

6.2.1 Modal solutions

Use of the higher order mode (HOM) of a multimode fibre (MMF) shows several advantages which includes mode area scaling to control laser high power and dispersion management for ultra-short pulses. Modal instabilities in HOMs are a common problem arising due to external perturbations, such as bending and fabrication imperfections. According to the symmetry rule, bend perturbation is odd in nature and direct coupling arises between even and odd order modes. Among the many modes guided by a MMF, sometimes a desired dominant mode (LP_{0m}) may transfer its energy to its nearest anti-symmetric ($LP_{1(m+1)}$ and $LP_{1(m-1)}$) modes [17]. A low effective index difference (Δn_{eff}) between adjacent modes enhances the modal energy transfer which results in actual modal energy loss along with the interference effects. This could result in inter-mode mixing in a MMF. Although a lower order (lower value of m) mode may be easier to excite, however, a higher value of m gives larger modal separation (Δn_{eff}) values, so a compromise is needed. However, for a given value of m, if the modal separation to the nearest anti-symmetric modes can be increased, this would be a more preferable design. Here, a novel MMF design with concentric material strips at strategically located positions is proposed to increase the Δn_{eff}=$(n_{eff}^{0m} - n_{eff}^{1m})$ in desired modes, such as, LP_{18}, LP_{09} and LP_{19} modes. Instead of using a perturbation approach, we have used a rigorous full vectorial **H**-field based finite element method (FEM) to find the modal solutions of our proposed MMF design. The FEM is one of the most numerically efficient and accurate approaches to obtain the modal solutions of an optical waveguide, to calculate the propagation constant (β), effective index (n_{eff}=β/k_o, where wavenumber k_o is given by $2\pi/\lambda$) and A_{eff}.

In order to increase the modal solution accuracy, the available two-fold symmetry of the fibre is exploited and only one-quarter of the structure is simulated [117, 118]. This allows

a more dense mesh distribution in the quarter structure of the fibre instead of distributing the same mesh over the whole structure. The polar mesh [139] discretisation is also used, which can accommodate the discretized elements more efficiently at the circular boundaries, which can provide more accurate results compared to the mesh distribution based on the Cartesian coordinate system [140]. It is well known that the simulation accuracy of the FEM is highly dependent on the number of discretized elements used. Variation of the effective index (n_{eff}) with the number of mesh elements (N) is shown in Fig. 6.4 by a solid black line for the higher order LP_{09} mode. It can be observed that initially as mesh density increases

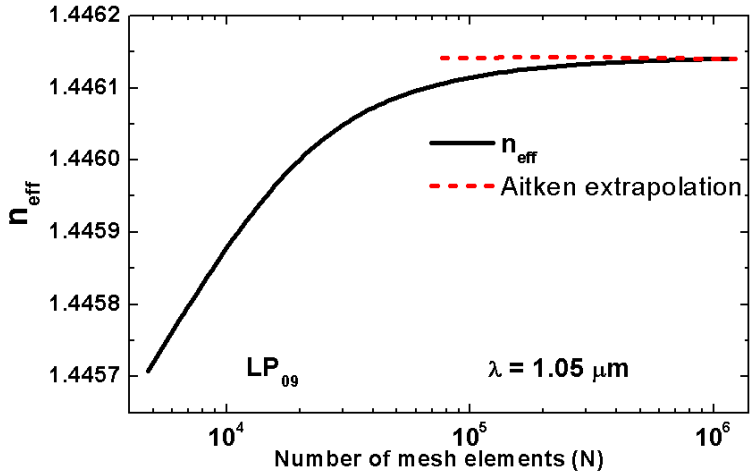

Fig. 6.4 Variation of $\mathbf{n}_{eff}$ of the LP_{09} mode with the mesh number (N) and convergence realised with the Aitken extrapolation technique.

the n_{eff} also increases rapidly and then asymptotically settles to a constant value. It should be noted that accuracy is up to the 3^{rd} decimal place when the number of elements used is, $N = 7 \times 10^4$ and it increases to the 5^{th} decimal place when $N = 5 \times 10^5$. Here N, is the number of triangular elements used to represent a quarter of the MMF. A powerful Aitken's extrapolation technique is used to test the convergence of the modal solutions [141, 142]. Three successive n_{eff} values for corresponding mesh divisions with a geometric ratio are

used in the Eq. (6.1).

$$n_{\text{eff}}^{\infty} = n_{\text{eff(r+1)}} - \frac{[n_{\text{eff(r+1)}} - n_{\text{eff(r)}}]^2}{n_{\text{eff(r+1)}} - 2n_{\text{eff(r)}} + n_{\text{eff(r-1)}}} \tag{6.1}$$

Using Eq. 6.1 the extrapolated values of n_{eff}^{∞} are shown in the Fig. 6.4 by the red-dashed line. Aitken's values are calculated for the mesh values $N = 7.66 \times 10^4$, 3.07×10^5, and 1.23×10^6 increased in fixed geometric ratio yielding the n_{eff} values 1.4460355, 1.4461157, and 1.4461358, respectively. It should be noted that in each solution the mesh density is two times (no. of the elements is four times) that of the previous and thus the geometrical mesh ratio is kept constant. From these values a more accurate extrapolated value of 1.4461398 is obtained. Similarly, Fig. 6.4 clearly shows the convergence of the extrapolated results and raw FEM results. As the trend of n_{eff} with increasing N for different modes is similar, so the accuracy of Δn_{eff} between two modes with increasing N is rather better.

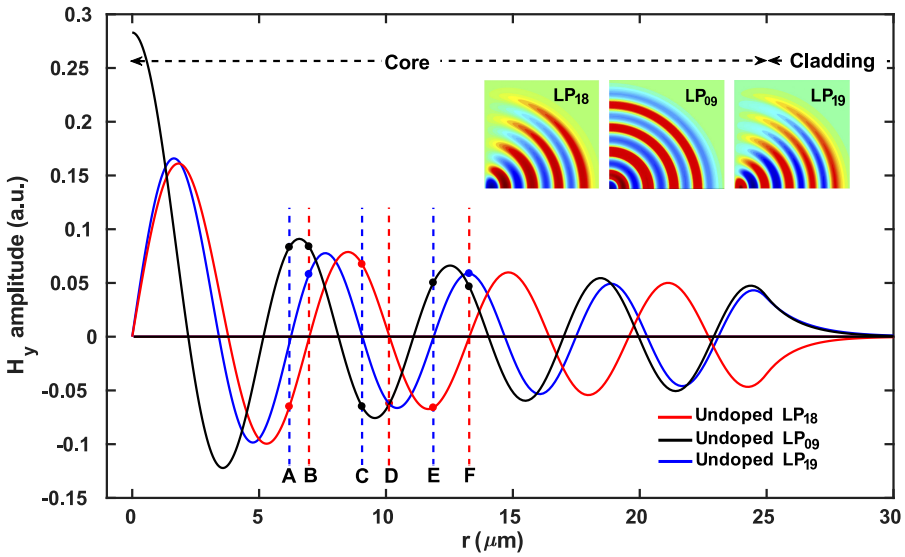

Fig. 6.5 Variations of H_y fields of the LP_{18}, LP_{09}, and LP_{19} modes along the r-axis of MMF, contour field profiles in inset and the key points of interest are also shown.

6.2.2 Mode stability

As previously discussed, higher order modes provide the unique benefit of increased stability due to a greater mode spacing (Δn_{eff}) compared with that of the fundamental modes (LP_{01}) [143]. The proposed technique can reduce mode mixing between the higher order LP_{18}, LP_{09} and LP_{19} modes, that could alternatively only be possible by considering a much higher modal order. For our design, we used LP_{09} as the central propagation mode and modified the refractive index profile of the fibre such that the mode stability between symmetric (LP_{09}) and the two nearest antisymmetric (LP_{18} and LP_{19}) modes is increased. A measure of the modal stability can be defined using the effective index differences as, S_1=$\Delta n_{eff}(LP_{18} - LP_{09})$ and S_2=$\Delta n_{eff}(LP_{09} - LP_{19})$. However, if required any other HOM of interest can also be selected and using the same concept its mode stability can be enhanced. For this structure, the effective indices of the LP_{18}, LP_{09}, and LP_{19} are calculated as 1.447317, 1.4461104, and 1.4448554, respectively, yielding S_1=0.0012066 and S_2=0.001255. The variation of the dominant H_y field profile of the LP_{18}, LP_{09} and LP_{19} modes is shown in Fig. 6.5 by red, black and blue lines, respectively. H_y field contours of the LP_{18}, LP_{09} and LP_{19} modes are also shown Fig. 6.5 as insets. It can be observed that the field profile of LP_{09} mode shown by a black line, has the highest magnitude at the centre (r=0) of the fibre and eight zero values along the radial direction. The antisymmetric LP_{18} and LP_{19} modes shown with red and blue lines, respectively, have zero field values at the centre ($r = 0$) of the fibre. The dominant H_y fields of the LP_{18} and LP_{19} modes have eight and nine zero field values along the radial direction, respectively. Table 6.1 shows all the radial locations where these modes have zero field values. For example, LP_{18} mode has its first three zero field locations at r=0, 3.78 and 6.966 μm. Using these zero crossings we have identified multiple locations that are suitable for doping such that the mode stability (S_1 and S_2) can be increased.

Some specific points, A, B, C, D, E and F are selected as shown in Fig. 6.5, where either LP_{18} or LP_{19} has zero crossing. The reason for choosing these points is that we want to have

Table 6.1 Zero crossing locations of field profiles of the LP_{18}, LP_{09} and LP_{19} modes along r-axis (μm).

Mode	**Location of zero crossings along r-axis (μm)**							
LP_{18}	0	3.78	6.966	10.138	13.279	16.315	19.557	22.684
LP_{09}	2.16	5.16	8.125	11.078	13.99	16.89	19.9	22.79
LP_{19}	0	3.36	6.193	9.058	11.867	14.577	17.472	20.252

less effect on one of the mode and have more effect on the other two modes using strips of different doping. The modal field values at these points are also given in Table 6.2. For

Table 6.2 Field values of LP_{18}, LP_{09} and LP_{19} at A, B, C, D, E and F points.

Mode	**A=6.193**	**B=6.966**	**C=9.058**	**D=10.138**	**E=11.867**	**F=13.279**
LP_{18}	0.06507	0	0.06741	0	0.6606	0
LP_{09}	0.08321	0.08328	0.06493	0.06218	0.05022	0.04658
LP_{19}	0	0.058	0	0.06267	0	0.05879

example at point A, the H_y field value of LP_{19} is zero, whereas, the field values of LP_{18} and LP_{09} modes are 0.06507 and 0.08321, respectively. As a result any change of refractive index doping at point A will have an almost negligible effect on the LP_{19} mode and comparatively more effect on the LP_{09} than the LP_{18} mode. However, at point F, where the H_y field value of LP_{18} mode is zero and these values for LP_{09} and LP_{19} modes are 0.04658 and 0.05879, respectively. Hence, at point F, doping will have no effect on the LP_{18} but will influence more effect on LP_{19} than the LP_{09} mode. This will result in an increase in the effective index of both modes while keeping the effective index of the LP_{18} mode unchanged, and a suitable selection can result in an increase in the modal stability. In order to increase the Δn_{eff} between these modes an annular strip of 0.3 μm wide is considered that can have an increased or reduced refractive index by Δn. Here, we have taken $\Delta n = 0.0167$, which is also the difference between the core and cladding refractive indices. However, different values of Δn in these strips can be chosen according to the required level of stability between modes.

6.3 Numerical results

Table 6.3 shows the effect of doping a single individual annular section at the above mentioned six positions along the r-axis. The second column of Table 6.3 shows the original Δn_{eff} between the modes without any doping. It can be noted that the Δn_{eff} between LP_{09} and LP_{19} modes is slightly higher than the Δn_{eff} between LP_{18} and LP_{09} modes. The values of $+\Delta n$ or $-\Delta n$ on particular points are chosen such that the effect on the central mode, in our case LP_{09} modes, is negligible or can be compensated with another doping layer where Δn is chosen with an opposite sign to the first point. For example, in layer A (at r=6.193 μm), $+\Delta n$ is chosen to increase the stability, S_1 between LP_{09} and LP_{19} modes, but unfortunately this reduces the stability, S_2 between LP_{18} and LP_{09} modes. On the other hand a reduction of refractive index in layer B increases modal separation S_2, but reduces that of S_1. However, an increase of refractive index in layer E and reduction in layer F enhances both the S_1 and S_2 modal stabilities. The same doping approach is considered at all six positions with either $+\Delta n$ or $-\Delta n$ as shown in Table 6.3. Here, two approaches can be considered;

1. Using a single layer doping to increase the stability between modes.

2. Using the combination of two or more layers to increase the stability.

Table 6.3 Individual strip doping effect on Δn_{eff} at points A, B, C, D, E, and F.

Δn_{eff}	**Without doping**	**A**	**B**	**C**	**D**	**E**	**F**
		+Δn	**-Δn**	**+Δn**	**-Δn**	**+Δn**	**-Δn**
$S_1 = LP_{18}$-LP_{09}	0.0012066	0.0010515	0.0015574	0.0012192	0.0014932	0.0013553	0.0014033
$S_2 = LP_{09}$-LP_{19}	0.001255	0.0015544	0.0010634	0.0015037	0.0012711	0.0014385	0.0014217

In Table 6.4 the above described approaches are shown with the percentage increase in Δn_{eff} (S_1 and S_2). The percentage increase is calculated with respect to the original Δn_{eff} between the modes as shown in column two. Here, three different options are suggested depending upon the required increase in the Δn_{eff}. It can be seen that with a single layer

of $-\Delta n$ doping at point F, S_1 and S_2 are increased by 16% and 14%, respectively. However, using two layers (at E & F points) the stabilities S_1 and S_2 between modes can be increased by 20% and 23%, respectively. It should be noted that the Δn doping at points E and F are taken as positive and negative, respectively. For further enhancement, three layers can be doped simultaneously at points C, D, and E which results in an increase of 35% and 38% for $\Delta n_{eff}(LP_{18} - LP_{09})$ and $\Delta n_{eff}(LP_{09} - LP_{19})$, respectively. Hence, our proposed design results in increased modal spacing between the higher order LP_{18}, LP_{09} and LP_{19} modes, thus providing more stable and mode-mixing resistant operation.

Table 6.4 Percentage increase in the Δn_{eff} using individual and combination approach.

Δn_{eff}	**Without doping**	**F only**		**E & F**		**C, D & E**	
		Δn_{eff}	**% Increase**	Δn_{eff}	**% Increase**	Δn_{eff}	**% Increase**
$S_1 = LP_{18}$-LP_{09}	0.0012066	0.0014033	16	0.0014551	20	0.0016254	35
$S_2 = LP_{09}$-LP_{19}	0.001255	0.0014217	14	0.0015318	23	0.0017357	38

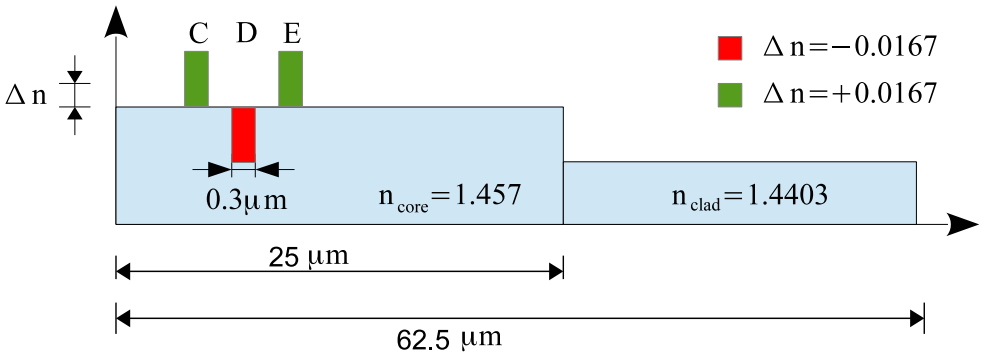

Fig. 6.6 Refractive index profile of the modified MMF along r-axis with $\pm\Delta n$ at C, D and E points.

Figure 6.6 shows the refractive index profile for three layer doping at C, D and E points. Here, Δn at points C and E are taken as positive such that it increases the local refractive index from 1.457 to 1.4737. Whereas, at point D, Δn is taken as negative resulting in the local refractive index being equal to that of the cladding. The combination is chosen such that $\Delta n_{eff}(LP_{18} - LP_{09})$ and $\Delta n_{eff}(LP_{09} - LP_{19})$ have an almost equal increase. Here, all

three annular strips are centred at points C, D and E and have an equal width of 0.3 μm. The LP_{09} mode is considered as a central propagation mode in our design. Hence next, the effect of three layers of doping at points C, D, and E points on the field profile of LP_{09} is studied. Figure 6.7 shows the H_y field profile of the LP_{09} mode before and after doping. The black line shows the undoped field profile whereas the dotted blue line represents the field profile of LP_{09} after doping these three layers at C, D, and E. It can be observed that until the appearance of the doped strips the field profile was almost unchanged, however beyond these strips, the field value is reduced compared to that of the original undoped fibre.

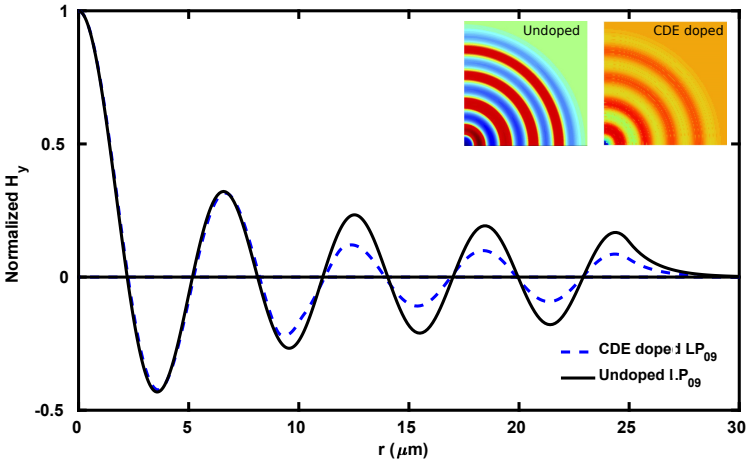

Fig. 6.7 Variations in the H_y fields of LP_{09} modes along the r-axis of the undoped fibre and the fibre with C, D, and E layers doped. The contour field profiles are also shown inset.

The Δn=0.0167 value used for the annular strips C, D, and E is equivalent to the refractive index difference between core and cladding of the fibre but if necessary other Δn values or even unequal values can be used for a particular design. To observe the effect of increased or reduced value of Δn, we have halved the refractive index difference as, $\pm\Delta n$=0.00835 and found that the modal stabilities S_1 and S_2 reduces to 18% and 19%, respectively. However, when refractive index difference is increased to double; as $\pm\Delta n$=0.0334, the modal stabilities S_2 increases to 74% but S_1 increased only slightly to 41%, as field profiles were distorted significantly. However, it can be stated that a significant enhancement in the modal stability can be achieved by this approach.

6.3.1 Scalability of proposed technique

Although in earlier section, we have focused on the enhancement of mode spacing between LP_{09} and its neighbouring antisymmetric LP_{18} and LP_{19} modes, however, the proposed technique is scalable and can be applied for other higher order modes. In order to show the scalability of proposed method, the enhancement of mode spacing of LP_{08} mode and its neighbouring antisymmetric LP_{17} and LP_{18} modes, we have carried out additional simulations after introducing the similar annular rings method. Six zero crossing points, $A^{'}$ to $F^{'}$ for LP_{17} or LP_{18} are identified as $A^{'}$=6.928, $B^{'}$=7.856, $C^{'}$=10.138, $D^{'}$=11.518, $E^{'}$=13.279, $F^{'}$=15.098 (in μm). Numerical simulations were carried out with 0.3 μm wide annular strips with $\pm\Delta n$=0.0167 introduced at these points. Table 6.5 shows the increase in $\Delta n_{eff}(LP_{17}-LP_{08})$ and $\Delta n_{eff}(LP_{08}-LP_{18})$ with single layer ($F^{'}$) or multiple layers ($E^{'},F^{'}$ and ($C^{'},D^{'},E^{'}$) with perturbed annular strips. It can be observed that the stability is increased to 46% for the LP_{08} mode when three annular layers at ($C^{'},D^{'},E^{'}$) points are used.

Table 6.5 Percentage increase in the Δn_{eff} of LP_{08} mode and its neighbouring antisymmetric modes using individual and combination of two or three strips doping.

Δn_{eff}	**Without doping**	$F^{'}$ **only**		$E^{'}$ & $F^{'}$		$C^{'},D^{'}$ & $E^{'}$	
		Δn_{eff}	**% Increase**	Δn_{eff}	**% Increase**	Δn_{eff}	**% Increase**
LP_{17}-LP_{08}	0.0010746	0.0012218	14	0.0013424	25	0.0015759	47
LP_{08}-LP_{18}	0.0011146	0.0013136	18	0.0015187	36	0.0016256	46

Similarly, the enhancement in the modal stability of a lower order LP_{05} mode is also achieved by increasing its effective index difference (Δn_{eff}) with its neighbouring antisymmetric LP_{14} and LP_{15} modes. As discussed earlier that the Δn_{eff} between the modes increases with the increase in the modal order (m), hence, change in the Δn_{eff} in lower order modes comparatively higher.

Figure 6.8 shows the variation of the dominant normalised H_y field profiles of the LP_{05} and two adjacent antisymmetric LP_{14} and LP_{15} modes. The H_y contour field profiles of these modes are also shown in Fig. 6.8 as insets. The LP_{05} mode has the peak value at $r=0$ and

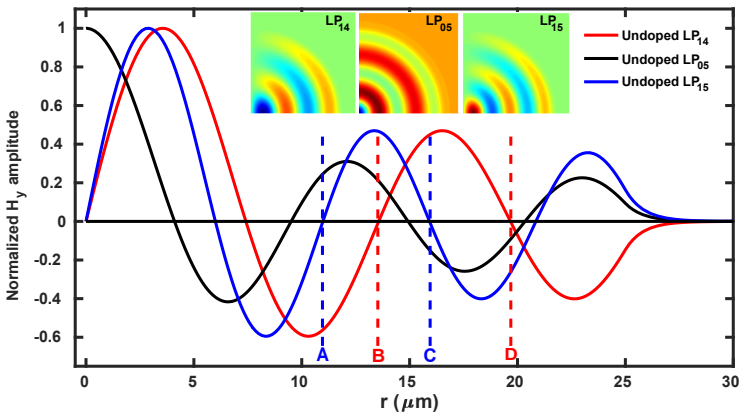

Fig. 6.8 Variations of H_y fields of the LP_{14}, LP_{05}, and LP_{15} modes along the r-axis of the MMF, contour field profiles are given as insets and the key locations of interest are also shown.

it crosses zero values at four different locations along the fibre radius. Similarly, the LP_{14} and LP_{15} modes have zero field values at the centre (r = 0) and have three and four zero crossings along the radius of the fibre as shown in Table 6.6, respectively. Four strategically located places (A, B, C and D) are chosen where either LP_{14} or LP_{15} mode has zero field values. An annular strip with width 0.4 μm and $\pm\Delta n = 0.0167$ is introduced at the above mentioned points and corresponding $S_1 = \Delta n_{eff}(LP_{14} - LP_{05})$ and $S_2 = \Delta n_{eff}(LP_{05} - LP_{15})$ are calculated. Here, for strip doping we have taken the $\Delta n = 0.0167$, equal to the difference between core and cladding refractive indices of the MMF. The effective indices of the modes increases or decreases for Δn positive or negative, respectively, and its value depends on the field value of the corresponding modes at that particular location.

Table 6.6 Zero crossing locations along the radius of multimode fibre where the H_y field values of LP_{14}, LP_{05} and LP_{15} modes are zero.

Higher order optical modes	**Effective index (n_{eff})**	**Zero crossing locations along r-axis** (μm)				
LP_{14}	1.45443491	0	7.357	13.525	19.60	31.529
LP_{05}	1.45378140	4.08	9.488	14.875	20.275	31.88
LP_{15}	1.45308231	0	5.94	10.916	15.839	20.757

Here, we report percentage increase in the modal stabilities using single or a combination of annular strips as shown in the Table 6.7. When a single strip of $-\Delta n = 0.0167$ is introduced at point $B = 13.252\ \mu m$ the modal stabilities S_1 and S_2 are increased by 38% and 34%, respectively. It should be noted here that at point B, the field value of LP_{14} mode is zero hence, any strip doping has very little effect on the effective index of the LP_{14} mode. However, the effective index of the LP_{05} and LP_{15} modes are reduced depending on their modal field values as shown in Fig. 6.8. Similar approach is conducted with two $-\Delta n$ doped strips at points B and D and the resultant modal stabilities increased to $S_1 = 45\%$ and $S_2 = 57\%$ as shown in Table 6.7. Moreover, with the combination of three strip dopings at points (A=$+\Delta n$), (B=$-\Delta n$) and (C=$+\Delta n$) the modal stabilities S_1 and S_2 are increased to 103% and 83%, respectively. This confirms that the concept presented here can be applied to any higher order modes, as required.

Table 6.7 Percentage increase in the $\Delta n_{eff}(LP_{14} - LP_{05})$ and $\Delta n_{eff}(LP_{05} - LP_{15})$ by individual and combination of doped strips.

Modal stability	**Without doping**	**B^- layer only**		**B^- & D^- layers**		**A^+, B^- & C^+ layers**	
		Δn_{eff}	**% Increase**	**Δn_{eff}**	**% Increase**	**Δn_{eff}**	**% Increase**
S_1 =LP_{14}-LP_{05}	0.00065351	0.00090188	38	0.00094974	45	0.00132629	103
S_2 =LP_{05}-LP_{15}	0.00069908	0.00093364	34	0.00109850	57	0.00127630	83

6.3.2 Fabrication tolerance of strip width

Here, we demonstrate the effect of possible variations in doped strips that can occur during the fabrication process. As for the LP_{09} mode, the combined doping of the three layers at points C, D, and E could be more sensitive to fabrication tolerances than the two or single layer doping so we will consider the three layers (C, D and E) case for further investigation.

The effect of a change in the layer width (w) from 0.3 μm to a higher or lower value is shown in Fig. 6.9. As discussed earlier, with w=0.3 μm the stabilities S_1 and S_2 between

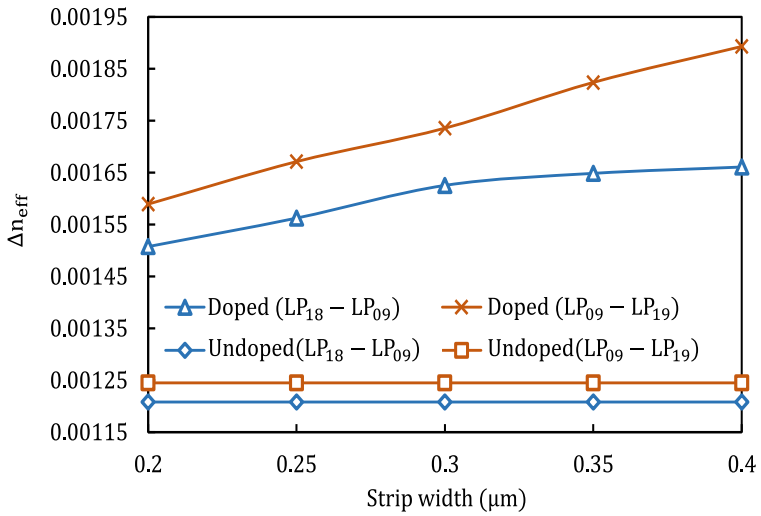

Fig. 6.9 Effect on Δn_{eff} of a change in width of doped layers at points C, D, and E for LP_{09} mode.

the modes are 35% and 38%, respectively. With an increase in the width from w=0.3 μm to w=0.4 μm, the stabilities S_1 and S_2 further increase to 38% and 51%, respectively. This is because the area of the doped layer is increased when the width is changed from 0.3 μm to 0.4 μm thus increasing its overall effect. However, as the width deceases to w=0.20 μm, the stability improvement reduces but still it remains above 25%.

Similarly, Fig. 6.10 shows the change in Δn_{eff} of LP_{05} mode with the variation in a single doped strip introduced at the position $B = 13.252\ \mu m$. Here, the doped strip width is varied from 0.20 μm to 0.60 μm and resultant Δn_{eff} is calculated. When the strip width is selected 0.20 μm the resultant modal stabilities S_1 and S_2 for LP_{05} mode are calculated as 0.00078596 and 0.00082062, and in terms of percentage 20% and 17%, respectively. Similarly, when the strip width is changed to 0.6 μm the resultant modal stabilities $S_1 = 0.000995229$ and $S_2 = 0.001038969$ and percentage improvements of $S_1 = 52\%$ and $S_1 = 49\%$ are calculated. This shows that wider strips increases the modal stability in this case.

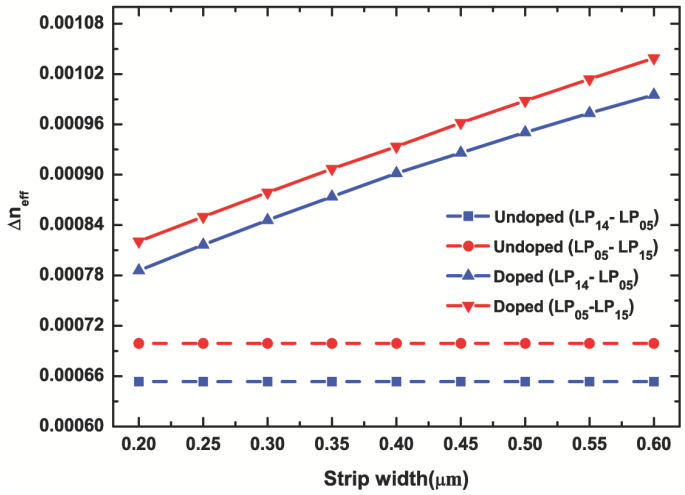

Fig. 6.10 Effect on Δn_{eff} of a change in width of single doped layer at position B for LP_{05} mode.

6.3.3 Fabrication tolerance of strips centre location

For the modal stability of LP_{09} mode, the proposed design with three layers are centred at positions C=9.058 μm, D=10.138 μm and E=11.867 μm and during fibre drawing these positions may change. Figure 6.11 shows the effect of a change in the location of the doped layer's centre points. It can be seen that the stability is highly dependent on the specified locations in Fig. 6.5.

When there is no shift in the location of the doped strips centres, the stability improvement is larger than 35%. With a tolerance of ± 0.05 μm the stability improvement still remains above 27% but as the shift is increased to 0.1 μm the S_1 improvement drops to 20% while S_2 improvement is increased to 51%. Moreover, when the annular strips shift is -0.1 μm, the modal stability S_1 improvement increases to 46% but that of S_2 decreases to 27%. For comparison the spacing between the modes before introduction of the C, D and E layers is also shown by two horizontal lines.

Similarly, Fig. 6.12 shows the change in the Δn_{eff} for LP_{05} mode when the location of doped strip introduced at position $B = 13.252$ μm is shifted ± 0.1 μm. It is noted that, for

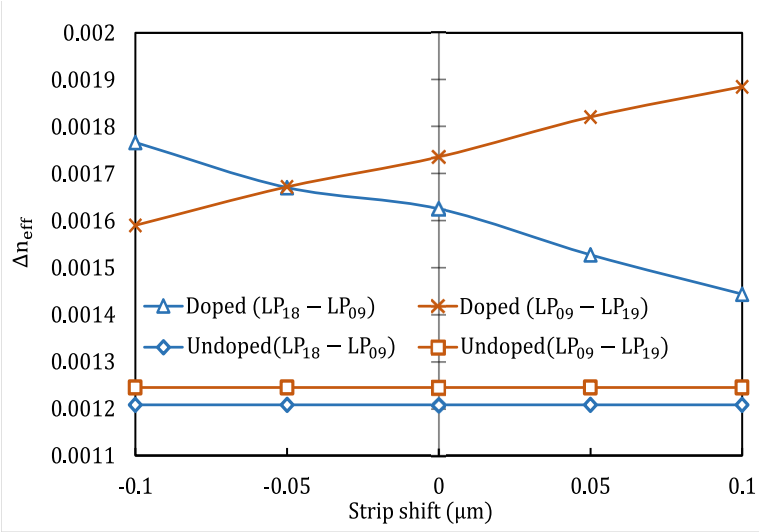

Fig. 6.11 Effect on the Δn_{eff} of a variation in the position of C, D, and E layers from centre location for LP_{09} mode.

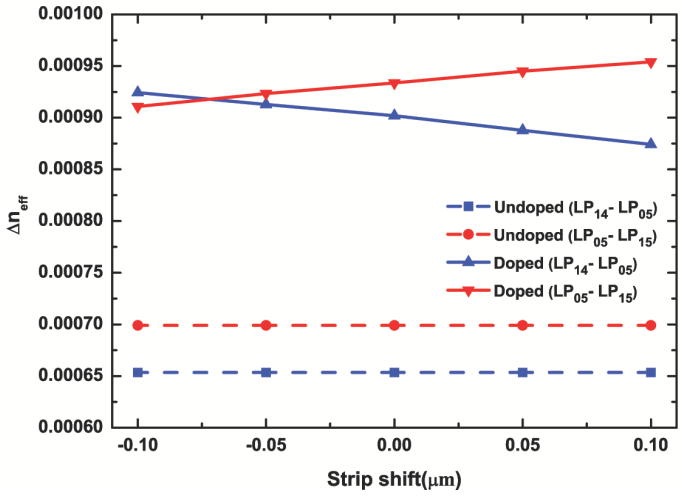

Fig. 6.12 Effect on the Δn_{eff} of a variation in the strip position from central point B for LP_{05} mode.

the strip shift of $\pm 0.1\ \mu m$ from centre point B the modal stability improvements for LP_{05} mode and its neighbouring antisymmetric LP_{14} and LP_{15} modes remains above 30%.

6.3.4 Fabrication tolerance of wavelength change

The above analysis is carried out at the centre wavelength of λ=1.05 μm. However, when the operating wavelength changes from this value the stability between modes can also change. To observe the impact of wavelength change on the stability between the modes, we varied the operating wavelengths and this is shown in Fig. 6.13. It can be observed that the stability between the LP_{18}, LP_{09} and LP_{19} modes increases with an increase in the wavelength. It should be noted that the refractive index of a material is also dependent on the wavelength. In our analyses we have used the core and clad refractive index values as n_{core}=1.457 and n_{clad}=1.4403 respectively at λ=1.05 μm. It should be noted that without doping at the C,

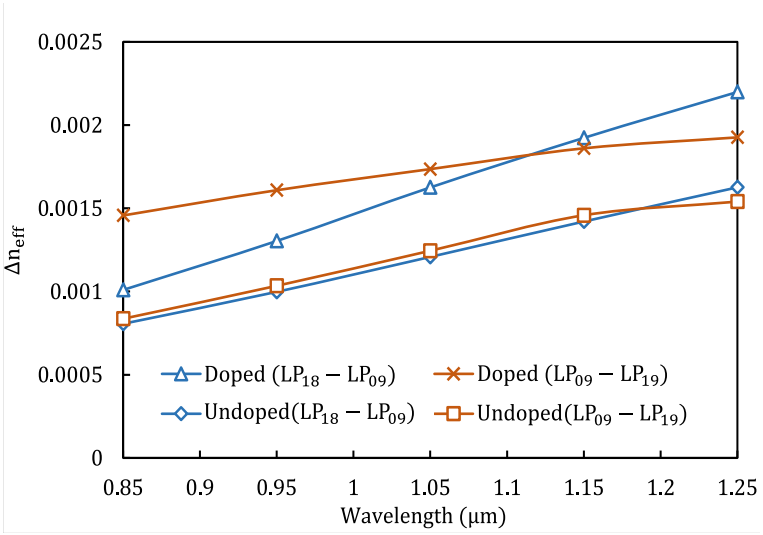

Fig. 6.13 Effect on the Δn_{eff} with the change in wavelength (λ) for LP_{09} mode and its neighbouring LP_{18} and LP_{19} modes

D, and E layers, the stability increases almost linearly with an increase in the wavelength. The increased wavelength reduces mode confinement and effective index values, and this also increases the separation between the modal index values. A similar effect is noticed

after the introduction of doping at layers C, D and E layers. When the centre wavelength is λ=1.05 μm, the modal stability values are S_1=0.0016254 and S_2=0.0017357, which are improvements of 35% and 38% from their undoped values, respectively. However, it can be noted that with a change in the wavelength from λ=1.05 μm to λ=0.85 μm the stability difference after doping shows a similar trend to the undoped case. The modal stability values at λ=0.85 μm reduced to S_1=0.0010095 and S_2=0.0014572, however this reflects a 25% and 74%, improvement from the standard fibre. Similar behaviour is observed when the centre wavelength is increased to λ=1.25 μm and modal stability increases to S_1=0.002199 and S_2=0.0019263, and these reflect improvements 35% and 25% increase from the standard fibre. The modal stability still remains 25% higher for the wavelength range from λ=0.85 μm to λ=1.25 μm, and hence the proposed design results in a sufficiently improved stability between the competing modes.

6.4 Summary

A novel design approach is discussed in chapter 6, which has been validated by rigorous numerical analysis, to improve the stability between the modes significantly. Increasing the Δn_{eff} between modes results in a more stable and mode-mixing resistant operation and thus allows scalability of power in laser applications. It is shown that using a single or combination of multiple doped strips having $\pm\Delta n$ refractive index the modal stability of LP_{09} mode and its neighbouring LP_{18} and LP_{19} mode can be increased more than 35 %. Moreover, it is shown that the proposed technique is scalable and can be applied to increase the modal stability of other higher order modes of a MMF. This is shown by increasing the modal stability of LP_{08} mode and its neighbouring antisymmetric LP_{17} and LP_{18} modes more than 46 %. Similarly, in the case of LP_{05} mode and it's neighbouring antisymmetric LP_{14} and LP_{15} mode, the modal stability is increased more than 83 %. It is also shown here that the design

is reasonably stable to possible fabrication tolerance such as the position and width of the doped annular strips.

Chapter 7

Mode stability enhancement in multimode and few-mode fibres using air-holes

As discussed in Chapter 6 that the modal stability or effective index difference (Δn_{eff}) between higher order modes of multimode fibres can be increased by introducing strategically located high, low or combination of both high and low index annular strips along the radius of MMF. In this chapter, we have proposed a novel approach to increase the Δn_{eff} between a higher order mode of a MMF and its neighbouring antisymmetric modes using air-holes. The second section of this chapter discusses similar technique applied to increase the Δn_{eff} between the modes of a few-mode fibre (FMF) to reduce the inter-modal coupling and interference for the mode division multiplexing.

7.1 Modal stability enhancement in MMF

7.1.1 Introduction

As discussed earlier that the multimode fibres (MMF) provides a large effective area that is useful for high power delivery but the existence of many modes may result in the random mode mixing and energy may transfer from a desired mode of propagation to its neighbouring modes. The identification and excitation of a selective mode are essential in multimode fibres for lasers and amplifiers related applications.

The larger fibre dimensions allow fundamental mode along with other higher order modes to propagate with different effective indices (n_{eff}). A lower value of Δn_{eff} between the adjacent modes may result in the inter-mode mixing and can cause interference effects. However, increasing the Δn_{eff} between these modes can significantly reduce this inter-mode mixing and any possible interference effects between them. In previous chapter, a combination of low and high index contrast doped strips is used to increase the Δn_{eff} values between LP_{09} mode and its neighbouring antisymmetric LP_{18} and LP_{19} modes [138]. These small sub-micron width strips can introduce a smaller change in the effective indices resulting in increased modal stability.

This section discusses the enhancement of Δn_{eff} between a higher order mode of MMF and its neighbouring antisymmetric modes. The proposed method uses strategically located small air-holes that can be easily fabricated by adopting a similar approach that is used for the fabrication of Photonic Crystal Fibres (PCF) [144, 145]. For our simulations, we have used a similar step-index multimode fibre with a core diameter of 50 μm as discussed in Chapter 6. The numerical aperture of the fibre is calculated as NA = 0.22 with the Ge-doped core and pure Silica cladding having refractive indices of n_{core}= 1.457 and n_{clad}= 1.4403, respectively. The operating wavelength of $\lambda = 1.05$ μm is considered for our simulations.

For a given MMF, the modal stability between higher order modes increases with the increase in modal order, m. This means that the Δn_{eff} of a higher order LP_{09} mode with its neighbouring antisymmetric LP_{18} and LP_{19} modes have a higher value compared to a lower order mode, say LP_{03} mode with its adjacent modes. However, exciting a higher order mode may involve more complexity as the power profile of the incident light is required to match the profile of a desired higher order mode to avoid any back reflection or coupling of other modes. Moreover, for given fibre dimensions the effective area of higher order modes also decreases with the increase in the mode order (m). So, it may be useful to enhance the modal stability for a specific higher order mode. Here, for our modal analyses, we have used LP_{06} mode and aimed to increase the effective index difference between LP_{15} and LP_{16} modes. Without any air-holes the effective indices of LP_{15}, LP_{06}, and LP_{16} modes are calculated as 1.4530823, 1.4522882 and 1.4514477, respectively. From these values, the resultant effective index differences S_1=$\Delta n_{eff}(LP_{15} - LP_{06})$ and S_2=$\Delta n_{eff}(LP_{06} - LP_{16})$ are calculated as 0.000794095 and 0.000840509, respectively.

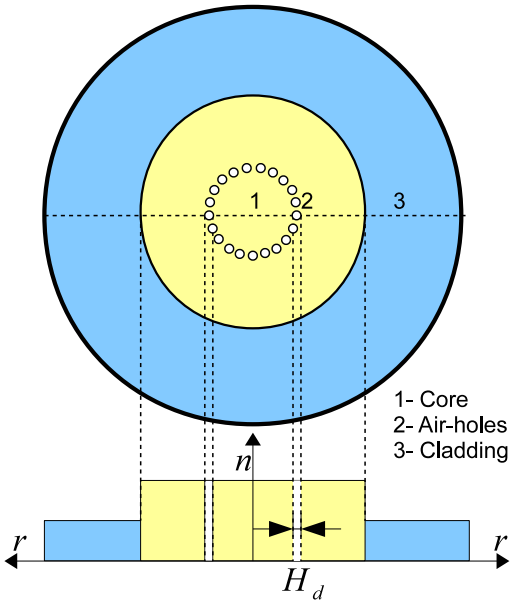

Fig. 7.1 Schematic cross-section design with annular air-holes array and refractive index profile along the radius of a MMF.

To increase the Δn_{eff} between LP_{06} mode and its neighbouring antisymmetric LP_{15} and LP_{16} modes, a circular array of air-holes is introduced along the circumference of a MMF. Figure 7.1 shows the schematic view of the proposed MMF design that includes a circular array of air-holes at a particular distance from the centre inside the core of MMF. The refractive index profile along the radius of the MMF is also shown in Fig. 7.1 where the refractive index of the holes having diameter H_d is considered as n_{hole}=1.0.

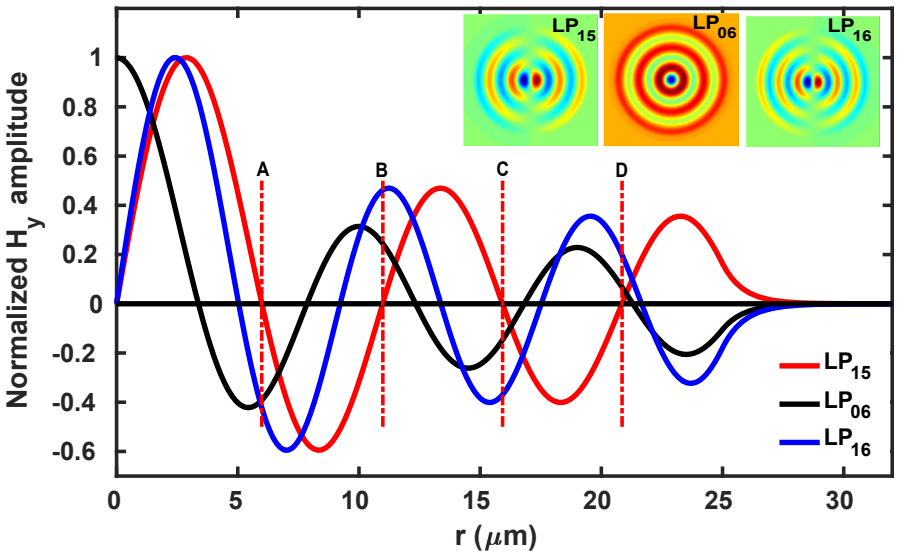

Fig. 7.2 Variations of H_y fields of the LP_{15}, LP_{06}, and LP_{16} modes along the r-axis of MMF, contour field profiles in inset and the key points of interest are also shown.

For a given mode, the reduction of its effective index depends on the magnitude of its modal field at the location of air-holes. Figure 7.2 shows the dominant H_y field variation of LP_{15}, LP_{06} and LP_{16} modes along the radius of given MMF. It can be observed that LP_{06} mode has a maximum amplitude at the centre of fibre core ($r = 0\ \mu m$), whereas, LP_{15} and LP_{16} modes have zero fields at the centre of the fibre core. The contour field profiles of these modes are also shown in Fig. 7.2 as insets. The zero crossing locations where the field value of these modes is zero are calculated and given in Table 7.1. Furthermore, zero crossing positions of LP_{15} mode are also highlighted with letters A, B, C, and D in Fig. 7.2 to assist further discussions.

Table 7.1 Zero crossing locations of field profiles of the LP_{15}, LP_{06} and LP_{16} modes along r-axis (μm).

Mode	**Zero crossing locations along r-axis (μm)**					
LP_{15}	0	5.999	10.985	15.925	20.855	-
LP_{06}	3.376	7.855	12.335	16.819	31.305	-
LP_{16}	0	5.041	9.225	13.38	17.523	21.66

7.1.2 Results and discussion

To increase the Δn_{eff} between the LP_{06} and its neighbouring antisymmetric LP_{15} and LP_{16} modes, one approach would be to increase the effective index of LP_{15} mode and reduce the effective index of LP_{16} mode while keeping the effective index of LP_{06} unchanged using high and low index doped strips proposed earlier [146]. The alternative technique proposed here is to include an array of air-holes that decreases the effective indices of LP_{06} and LP_{16} modes while keeping the LP_{15} mode effective index unchanged.

Table 7.2 Normalised field values of LP_{06} and LP_{16} modes at the zero crossings A, B, C and D points of LP_{15} mode.

Optical Modes	**A 5.999**	**B 10.985**	**C 15.925**	**D 20.855**
LP_{06}	0.3922	0.24435	0.147	0.067695
LP_{16}	0.4258	0.46145	0.3693	0.19815
Field values difference (LP_{16}-LP_{06})	0.0336	0.2171	0.2223	0.130455

Table 7.2 shows the normalised field values of LP_{06} and LP_{16} modes at different zero crossing location of the LP_{15} mode. An air-holes array introduced at the zero crossing locations of LP_{15} mode would decrease the effective indices of LP_{06} and LP_{16} modes, but this decrement will depend on the amplitude of their field values. For example, at the point, $A = 5.999\ \mu m$, the field value of LP_{15} mode is zero, but the normalised field values

of LP_{06} and LP_{16} modes are calculated as 0.3922 and 0.4258, respectively, resulting in a field difference of 0.0336. However, at point $B = 10.985\ \mu m$, the field value difference is calculated as 0.2171, which is higher than the value calculated at Point A. Similarly, at point C the field value difference is calculated as 0.2223. Depending on the field value difference, the position of air-holes array can be selected to achieve a comparable increase in Δn_{eff} between LP_{06} and its neighbouring LP_{15} and LP_{16} modes.

Here, an array of two hundred air-holes at the zero crossing positions A, B, C, and D of LP_{15} mode is introduced with each air-hole diameter taken as $H_d = 120\ nm$. Table 7.3 shows the absolute change and the percentage change in Δn_{eff}, which is calculated with respect to previous value as shown in Eq. 7.1.

$$\%\,Change = \frac{with\ holes\ \Delta n_{eff} - without\ holes\ \Delta n_{eff}}{without\ holes\ \Delta n_{eff}} * 100 \tag{7.1}$$

Table 7.3 Change in Δn_{eff} with the introduction of air-holes array at the zero crossings of LP_{15} mode.

■n_{eff}	Without holes	A=5.999 μm		B=10.985 μm		C=15.925 μm		D=20.855 μm	
		H_d=120nm	%change	H_d=120nm	%change	H_d=120nm	%change	H_d=120nm	%change
S_1=(LP_{15}-LP_{06})	0.00079409	0.001874673	136 ⇑	0.001471349	85 ⇑	0.00102064	29 ↑	0.000843914	6 ↑
S_2=(LP_{06}-LP_{16})	0.00084050	0.000163878	-81 ⇓	0.001003126	19 ↑	0.001187816	41 ⇑	0.00094461	12 ⇑

From Table 7.3, it can be observed that with the introduction of air-holes at A to D positions, the modal stability S_1 has increased. However, unfortunately, a noticeable reduction in the modal stability S_2 is observed because Δn_{eff} between LP_{06} and LP_{16} modes reduce when air-holes are introduced at position A. This significant reduction around 81% in the Δn_{eff} is due to small field value difference as the reduction in the effective index of LP_{06} mode is much higher as compared to the LP_{16} mode. However, at position B, the normalised field value difference between LP_{06} and LP_{16} modes is calculated as 0.2171 that resulted in 85% increase in S_1 and also 19% increase in S_2. Similarly, further away from the core centre

these modes have reduced field values and the normalised field difference at position C is calculated as 0.2223.

With the introduction of an array of 200 air-holes at C position the modal stabilities S_1 and S_2 increase to 29% and 41%, respectively. Similarly, at point D increase in modal stabilities are calculated as $S_1 = 6\%$ and $S_2 = 12\%$.

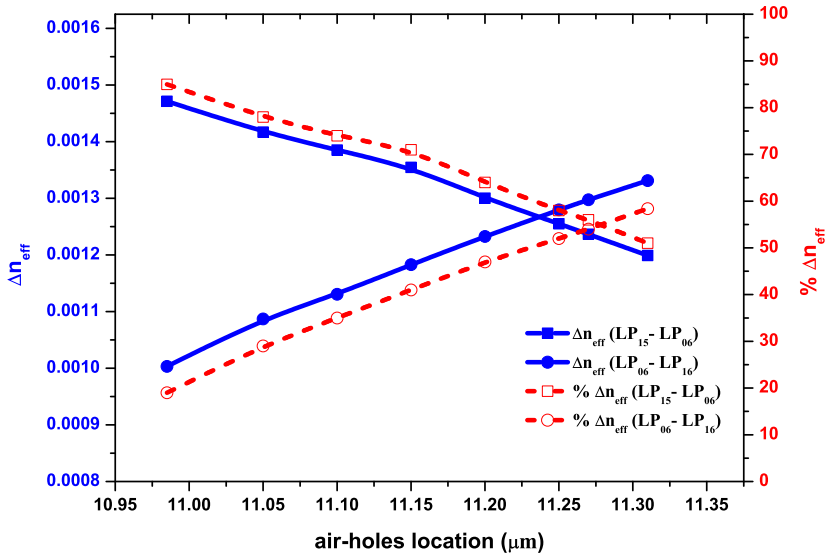

Fig. 7.3 Change in the Δn_{eff} with the location change of air-holes array along the radius of the fibre from point B and fixed 200 air-holes each having diameter of 120 *nm*.

The Δn_{eff} between the LP_{06} mode and its neighbouring antisymmetric LP_{15} and LP_{16} modes has increased significantly with the introduction of air-holes array at B and C positions. However, this increase in effective index difference S_1 and S_2 is not of similar magnitude as in case of position B this was calculated as 85% and 19%, respectively. To have a similar or comparable increase in the Δn_{eff}, the position of the air-holes array can be adjusted from its original location, $B = 10.985\ \mu m$. Variation in the Δn_{eff} and the percentage change in the Δn_{eff} is shown in Fig. 7.3 by solid blue and dashed red lines, respectively, when the air-holes array is shifted from position $B = 10.985\ \mu m$. As the air-holes array is moved towards the centre of the fibre core from position $B = 10.985\ \mu m$, the modal stability S_1 further increases and S_2 decreases, which may not be desirable. When the air-holes array is shifted 0.085

μm towards the core centre at 10.9 μm, the percentage increase in the modal stabilities S_1 and S_2 are calculated as 99.6% and 0.5%, respectively, but not shown here. However, when the air-holes array is moved away from the core centre towards fibre cladding, the percentage modal stability S_1 starts reducing but S_2 starts increasing. As shown in Fig. 7.3 the percentage increase in the effective index difference S_1 and S_2 are nearly equal at position $B^{'} = 11.27\ \mu m$. At position $B^{'}$, the Δn_{eff} between LP_{15} and LP_{06} modes is calculated as 0.00123656 and between LP_{06} and LP_{16} modes as 0.00129738. The percentage increase in S_1 and S_2 are calculated as 56% and 54%, respectively as shown in Fig. 7.3 with red dashed lines.

The same trend continues when the air-holes array is shifted further towards the cladding. It should be noted that as the location of air-holes is moved away from the exact zero crossings of the LP_{15} mode, its effective index will also reduce slightly, but a better control can be achieved by balancing S_1 and S_2. Hence, for our further analyses, we have used $B^{'} = 11.27$ μm as the new central position for the air-holes array.

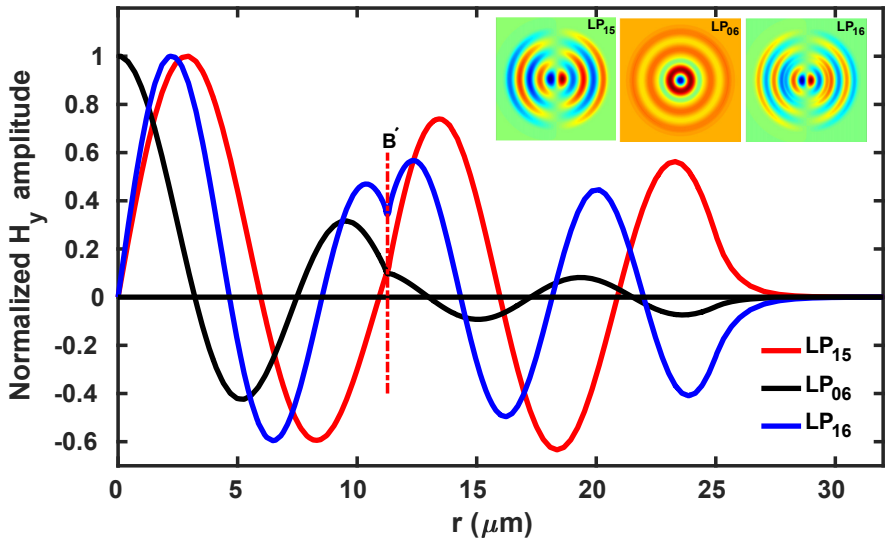

Fig. 7.4 Variations of H_y fields of the LP_{15}, LP_{06}, and LP_{16} modes along the r-axis of MMF with the introduction of 200 air-holes array each having $H_d = 120\ nm$, contour field profiles are also in inset.

Figure 7.4 shows the variation of H_y field profiles of LP_{15}, LP_{06} and LP_{16} modes along the radius of the MMF after the introduction of air-holes. Here, 200 hundred air-holes having $H_d = 120\ nm$ are introduced at $B^{'}$ position along the circumference of MMF. Following the introduction of air-holes, the effective indices of LP_{15}, LP_{06} and LP_{16} modes are reduced, and new values are calculated as 1.45303814, 1.451801579, and 1.45050419, respectively. Moreover, the normalised field values at position $B^{'}$ after the introduction of air-holes are also reduced, and these new values are calculated as 0.107, 0.098 and 0.3427 for the LP_{15}, LP_{06} and LP_{16} modes, respectively. From the H_y field variations of these modes shown in Fig. 7.4, it can be observed that the field profiles modify after the $B^{'}$ position due to the presence of these air-holes. The contour plots of LP_{15}, LP_{06} and LP_{16} modes after the introduction of air-holes are also shown in Fig. 7.4 as insets.

7.1.3 Fabrication tolerance

The drill-and-draw or extrusion technique can be used for the fabrication of such microstructured fibres consisting of air-holes [147]. However, for a large number of air-holes individual cylindrical glass rods, tubes, capillaries can be stacked according to predefined design. The resultant preform then drawn into optical fibres until the desired structure with required dimensions is not achieved [148]. However, with the smaller air-holes, the fabrication process can become more challenging as due to drilling in the preform or during the drawing process, air-holes diameter or their position can slightly change. To observe variation in the Δn_{eff} due to change in the air-holes diameter (from 120 nm) or change in the position, further numerical simulations were carried out.

Figure 7.5 shows the change in the effective index differences S_1 and S_2 with the change in the diameter of air-holes introduced at $B^{'}$ radial position. It can be observed that with the reduction in the air-holes diameter from 120 nm to a lower value, the effective index difference S_1 and S_2 also decrease linearly. When 200 air-holes having a diameter of 80 nm

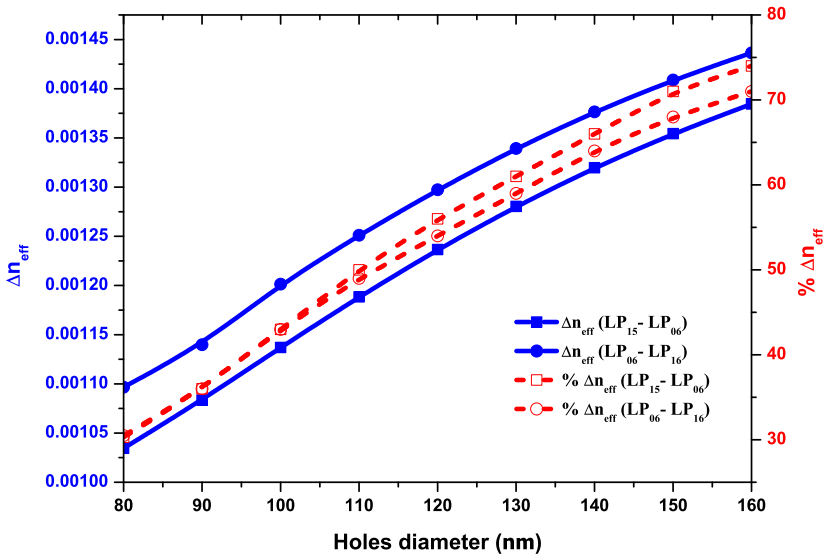

Fig. 7.5 Change in the absolute and percentage effective index difference S_1 and S_2 with the variation in the holes diameter with fixed 200 hundred holes.

are introduced at the $B^{'}$ position, the percentage increase in the effective index difference decreased and calculated as $S_1 = 30.3\%$ and $S_2 = 30.5\%$. The respective absolute Δn_{eff} values are also shown by blue lines in Fig. 7.5. However, when the air-holes diameter is increased to more than 120 nm, the percentage increase in the Δn_{eff} also increases, as shown by red dashed line and for a diameter of 160 nm the percentage increase in the effective index difference is calculated as $S_1 = 74\%$ and $S_2 = 71\%$. The above analysis also shows that even with the change of $\pm$ 40 nm in air-holes diameter, the percentage increase in modal stability remains above 30%.

One of the fabrication related issues may arise if the air-holes array is shifted from its central position, as for the above case, from $B^{'} = 11.27\ \mu m$. Figure 7.6 shows the change in the Δn_{eff} and percentage Δn_{eff} with the shift in the air-holes array position. When 200 air-holes having $H_d = 120$ nm are introduced at 11.15 μm (shift of -0.12 μm from $B^{'}$ position) the effective index difference S_1 and S_2 are calculated as 0.001343699 and 0.001182876, respectively yielding the percentage as 69.2% and 40.7% for S_1 and S_2, respectively. Similarly, when the air-holes array is shifted to 11.39 μm position which is

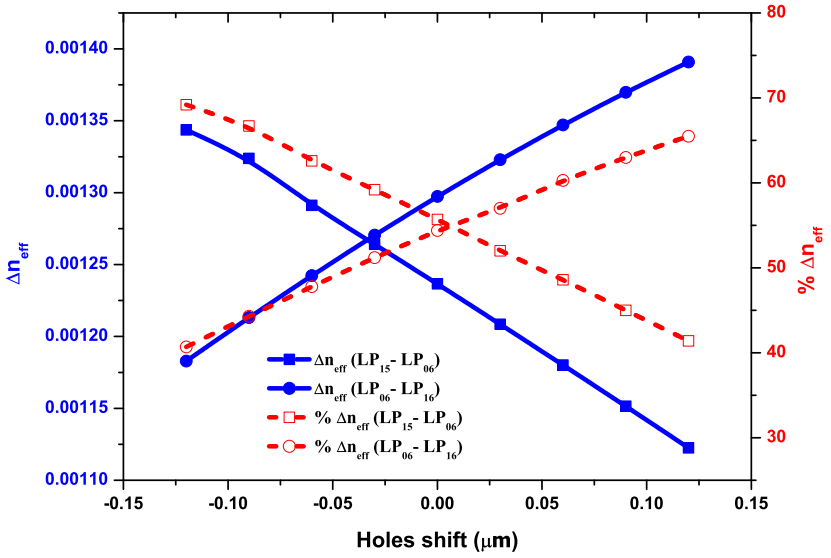

Fig. 7.6 Change in the real and percentage effective index difference S_1 and S_2 with the shift of air-holes array from central location H_{loc}=11.27 μm.

$+ 0.12\ \mu m$ shift from $B^{'}$ position, the resultant effective index differences of S_1 and S_2 are calculated as 0.001122553 and 0.001390885, respectively. Here, it should be noted that the percentage improvement in Δn_{eff} remains above 40% even with the shift of $\pm\ 0.12\ \mu m$ from the central $B^{'}$ position.

In Fig. 7.5, it was shown that the percentage of Δn_{eff} was increased up to 56% with 200 air-holes having 120 nm air-holes diameter. However, considering $B^{'}$ a central position for air-holes, we carried out further simulations to achieve similar effective index difference with less number of air-holes, which may be easier to fabricate.

Table 7.4 summarises different combinations of air-holes size and resulting increase in the Δn_{eff} between LP_{15}, LP_{06} and LP_{16} modes. When 100 air-holes with 176 nm diameter are introduced at $B^{'}$ position the resultant percentage increase in $S_1 = 57\%$ and $S_2 = 53\%$ are nearly equal to the initially proposed design with 200 air-holes having $H_d = 120$ nm. Similarly, when the number of air-holes is further reduced to 50 and air-holes diameter increased to $H_d = 286$ nm, the respective percentage increase in Δn_{eff} is calculated as $S_1 = 57\%$ and $S_2 = 53\%$. Moreover, the number of air-holes can be further reduced along

with the increased H_d (e.g. 25 air-holes having diameter $H_d = 580$ nm) to achieve a similar increase in the Δn_{eff}. This shows that the proposed technique is flexible in terms of the number of air-holes and also their dimensions that can be useful for a specific fabrication technique considered.

Table 7.4 Multiple combinations of air-holes diameter and their number to achieve similar increase in effective index difference.

Δn_{eff}	**Without air-holes**	**200 air-holes array**		**100 air-holes array**		**50 air-holes array**	
		H_d=120nm	**% Increase**	H_d=176nm	**% Increase**	H_d=286nm	**% Increase**
S_1=$LP_{15} - LP_{05}$	0.000794095	0.00123656	56	0.001246015	57	0.001243745	57
S_2=$LP_{05} - LP_{16}$	0.000840509	0.001297389	54	0.001286119	53	0.001287225	53

7.1.4 Scalability of proposed technique

Furthermore, we have used a similar approach to enhance the effective index difference between LP_{08} mode and its neighbouring antisymmetric LP_{17} and LP_{18} modes. Figure 7.7 shows the H_y field variation of LP_{17}, LP_{08}, and LP_{18} modes along the radius of the MMF. The contour field profiles of these modes are also shown in Fig. 7.7 as insets. Unlike LP_{15} mode, the LP_{17} mode has more zero crossing locations labelled as positions A to F in Fig. 7.7. These zero crossing positions of LP_{17}, LP_{08}, and LP_{18} modes are also given in Table 7.5. The effective indices of LP_{17} and LP_{08}, and LP_{18} modes are calculated as 1.4495339, 1.4484630, and 1.4473461, respectively. Without introduction of air-holes, the modal stabilities $S_1^{'} = \Delta n_{eff}(LP_{17} - LP_{08})$ and $S_2^{'} = \Delta n_{eff}(LP_{08} - LP_{18})$ between these modes are calculated as 0.001070831, and 0.001116877, respectively. As discussed in the introduction that the modal stability increases with the increase in the modal order (m), hence the original Δn_{eff} values for LP_{08} mode is higher than that of the LP_{06} mode.

Using the similar approach as discussed earlier, an array of 200 air-holes with diameter $H_d = 120$ nm are introduced at the zero crossing locations of LP_{17} mode and the resultant

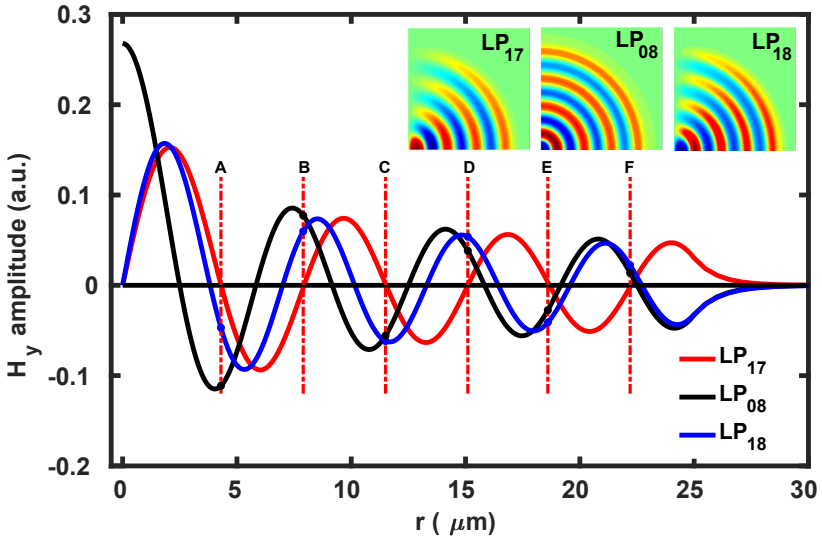

Fig. 7.7 Variations of H_y fields of the LP_{17}, LP_{08}, and LP_{18} modes along the r-axis of MMF, contour field profiles in inset and the key points of interest are also shown.

Table 7.5 Zero crossing locations of field profiles of the LP_{17}, LP_{08} and LP_{18} modes along r-axis (μm).

Mode	**Location of zero crossings along r-axis (μm)**						
LP_{17}	0	4.30	7.90	11.50	15.10	18.60	22.20
LP_{08}	2.40	5.80	9.10	12.40	15.80	19.10	22.40
LP_{18}	0	3.80	7.00	10.10	13.20	16.40	19.50

increase in the modal stabilities $S_1^{'}$ and $S_2^{'}$ are calculated. The effective index differences due to air-holes at point $D = 15.10\ \mu m$ are calculated as $S_1^{'} = 0.00137816$ and $S_2^{'} = 0.00154139$ which represents 29% and 38% increase in the percentage modal stabilities, respectively.

For an identical increase in the percentage modal stabilities $S_1^{'}$ and $S_2^{'}$, the location of air-holes array is adjusted from $D = 15.10\ \mu m$ to $D^{'} = 15.0\ \mu m$. The resultant increase in the modal stabilities with the combination of different air-holes size and quantity are given in Table 7.6. The percentage increase in the modal stability of $S_1^{'} = 34\%$ and $S_2^{'} = 36\%$ are achieved with the 200 air-holes with $H_d = 120\ nm$. A similar percentage increase is calculated when 100 air-holes with $H_d = 180\ nm$ and 50 air-holes with $H_d = 300\ nm$ are

introduced at the position $D^{'}$ along the radius of MMF, as given in Table 7.6. This shows that the proposed technique is scalable and can be used for a given higher order mode as required and its neighbouring modes in a MMF. Moreover, a different combination of air-holes numbers and their size can also be chosen depending on the fabrication facilities available to achieve a similar increase in the Δn_{eff}.

Table 7.6 Different combinations of air-holes diameter and quantity to increase the Δn_{eff} between LP_{08} mode and its neighbouring antisymmetric LP_{17} and LP_{18} modes.

Δn_{eff}	**Without air-holes**	**200 air-holes array**		**100 air-holes array**		**50 air-holes array**	
		H_d=120nm	**% Increase**	H_d=180nm	**% Increase**	H_d=300nm	**% Increase**
S_1=$LP_{17} - LP_{08}$	0.001070831	0.001437158	34	0.001437728	34	0.00143702	34
S_2=$LP_{08} - LP_{18}$	0.001116877	0.001515669	36	0.00151080	35	0.001504782	35

7.2 Modal stability enhancement in few-mode fibre

Recent studies show that the capacity limitation of a single mode optical fibre (SMF) is rapidly approaching the fundamental Shannon limit [149, 150]. Space division multiplexing (SDM) is considered to be an important approach to overcome the capacity limitation of single core based transmission systems. A multi-core fibre (MCF) or multimode fibre (MMF) has the advantage of boosting the transmission capacity without increasing the fibre count [151]. A few-mode fibre (FMF) has a core radius slightly larger than a conventional SMF, which not only enables more guided modes but also results in a larger effective area. This larger effective area of MMF or FMF enhances the power transmission capabilities that may result in long-distance communication and also less sensitive to area reduction due to the external perturbation like bending in fibre [35, 137]. However, an important issue arises in FMF transmission system that is the crosstalk or mode coupling between the modes of propagation [152, 153]. The mode division multiplexing in a three-mode fibre using multiple-input-multiple-output (MIMO) processing have shown significant transmission capacity improvements over the long distance communication [154]. MIMO based processing techniques are considered necessary to reduce the crosstalk and to reproduce the input signal. However, MIMO introduces latency in the system that further increases with the increased number of modes and also increases the overall complexity of the networks significantly [155, 156]. The cross-coupling between the modes is inversely proportional to the effective index difference between these modes and it is more severe between the neighbouring modes. A low effective index difference Δn_{eff} between the modes may result in energy transfer due to inter-mode mixing or energy loss because of the interference between the adjacent modes. An elliptical core-based MIMO free three-mode fibre design was also proposed to suppress the inter-modal coupling by increasing the effective index difference between LP_{01}, LP_{11a} and LP_{11b} modes [157]. Alexander and Michalis proposed a four-mode fibre with asymmetric refractive index profile that focuses on the enhancement of mode spacing between the LP_{21}

and LP_{02} modes, which resulted in a significant increase in mode spacing between LP_{21} and LP_{02} modes, however, the initial mode spacing between the LP_{01}, LP_{11} and LP_{21} modes was noticeably reduced [158].

In order to increase the effective index difference (Δn_{eff}) between the modes of FMF, a similar approach is used that is described in Section 7.1. An array of air-holes is introduced to increase the effective index difference between four guided LP_{01}, LP_{11}, LP_{21} and LP_{02} modes in two different few-mode fibre designs. We have shown significant improvement in the Δn_{eff} and the effect of any possible fabrication tolerances are also discussed. Furthermore, we have also shown that the proposed FMF designs are less susceptible to the bending loss compared to a standard SMF.

7.2.1 Stability enhancement in four-mode fibre

First, a four-mode fibre (FMF) design is considered with a core radius of 7.5 μm and cladding radius of 62.5 μm. The proposed FMF has a Germanium-doped Silica core and Silica cladding with refractive indices of $n_{core} = 1.450$ and $n_{clad} = 1.4403$, respectively. These fibre parameters are considered such that the FMF can allow only four guided modes. The V number using Eq. 2.3 is calculated as 5.1, where, a is the core radius and λ is the operating wavelength, taken here as 1.55 μm. The V number of 5.1 ensures robustness, good separation between the four modes, and cutting off the next higher order modes [159].

This fibre supports only four guided modes as expected and Fig. 7.8 shows the normalised dominant H_y field variation of these four LP_{01}, LP_{11}, LP_{21} and LP_{02} modes along the radial axis. For an accurate modal solution, the existing symmetry conditions of the fibre are exploited and only a quarter of the structure is simulated [117]. The complete H_y field contours of these modes are also shown as insets in Fig. 7.8. It can be observed that the field profiles of LP_{01} and LP_{02} shown by red and green lines, respectively, has a maximum amplitude at the centre ($r = 0$) of the fibre core. While, the LP_{11} and LP_{21} modes have zero

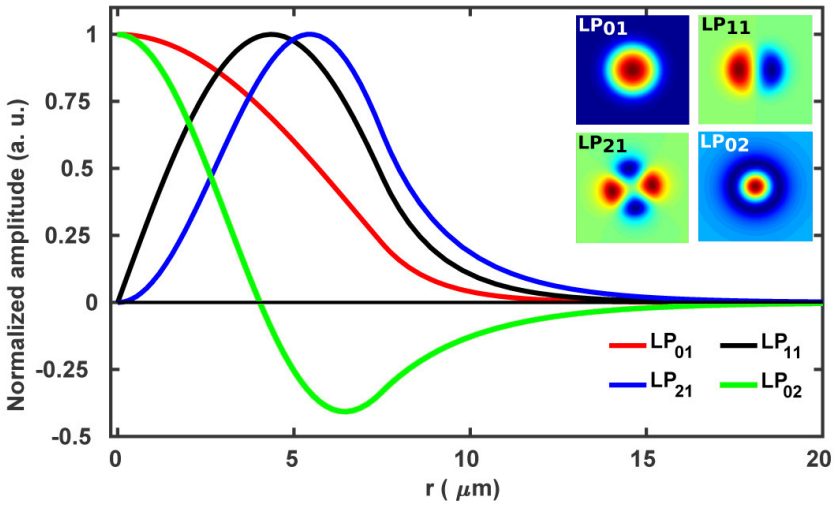

Fig. 7.8 Normalised H_y field variation of LP_{01}, LP_{11}, LP_{21} and LP_{02} modes along the radius of a step index few-mode fibre, contour field profiles are also shown as insets.

amplitude at the centre of the fibre core with peak amplitudes at 5.0 μm and 5.2 μm away from the centre, respectively.

The initial mode spacing or effective index differences (Δn_{eff}) between the modes are calculated as $S_1 = \Delta n_{eff}(LP_{01} - LP_{11}) = 2.253 \times 10^{-3}$, $S_2 = \Delta n_{eff}(LP_{11} - LP_{21}) = 2.850 \times 10^{-3}$ and $S_3 = \Delta n_{eff}(LP_{21} - LP_{02}) = 0.821 \times 10^{-3}$. It can be observed that Δn_{eff} between LP_{21} and LP_{02} modes is nearly 3.5 times smaller than the Δn_{eff} between LP_{11} and LP_{21} modes. This very low effective index difference makes these modes highly prone to mode coupling compared with the other modes with a larger effective index difference.

From Fig. 7.8, it can be observed that the normalised fields of all four modes beyond the core-clad interface decay exponentially. To increase the Δn_{eff} between these modes, we have proposed an array of air-holes along the circumference at a particular distance from the core centre. The location of the air-holes array is directly related to the relative amplitudes of these modes. For instance, the normalised amplitudes of the LP_{01}, LP_{11}, LP_{21} and LP_{02} modes at $r = 7.4$ μm are calculated as 0.235, 0.496, 0.664 and -0.344, respectively. Here, at location $r = 7.4$ μm, any positive or negative change in the refractive index would increase or decrease the effective index of these modes, however, the magnitude of change would

depend on their relative field values at this location. Figure 7.9 shows the schematic view of

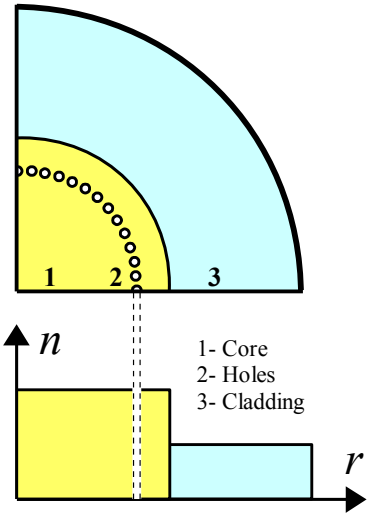

Fig. 7.9 A schematic illustration showing air-holes in FMF and change in the refractive index profile along the radius of fibre.

a quarter structure of a FMF with the introduction of air-holes array. The refractive index profile along the radius of fibre is also shown in Fig. 7.9.

Figure 7.10 shows that the Δn_{eff} between four modes increases with the increase in the size of 200 air-holes introduced at $r_{loc} = 7.4\ \mu m$ from the centre of the fibre. For better understanding, the percentage increase in the Δn_{eff} is also calculated with the change in the air-holes size and shown in Fig. 7.11. Here, the percentage increase in the stability related to the increase in the effective index difference is calculated by using in Eq. 7.1. It can be noted that with the increase in the size of air-holes, the Δn_{eff} increases nearly linearly. This is because following the introduction of the air-hole array, the effective indices of these modes decrease unequally depending on the relative amplitude of the field at $r = 7.4\ \mu m$. The modal stability improvement between the modes is observed to be around 26 %, when 200 air-holes each having 55 *nm* radius are introduced at $r = 7.4\ \mu m$ along the circumference of fibre. However, with the hole radius greater than 60 *nm*, the LP_{02} mode approaches its cut-off, resulting in the reduction in stability improvement for $\Delta n_{eff}(LP_{21} - LP_{02})$.

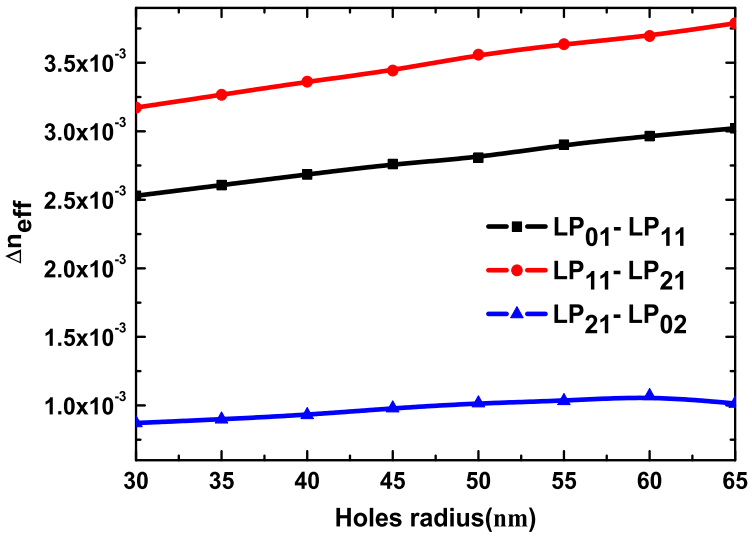

Fig. 7.10 Effect on the Δn_{eff} with a change in the air-holes radius at $H_{loc} = 7.4\ \mu m$ along the fibre radius.

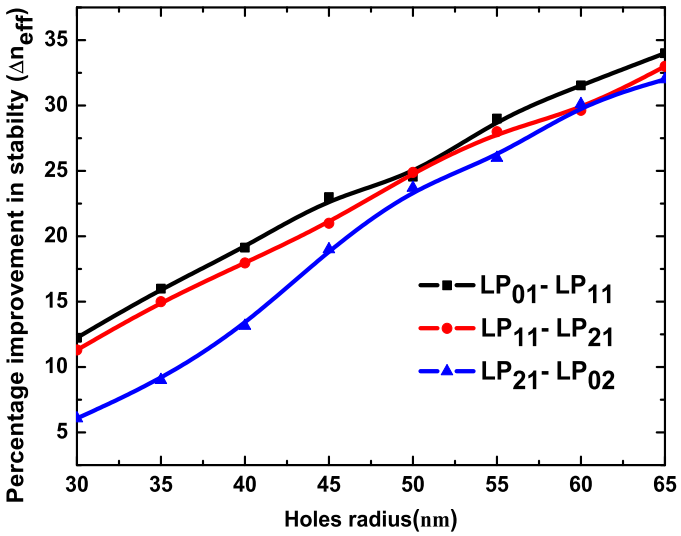

Fig. 7.11 Effect on the percentage Δn_{eff} with a change in the air-holes radius at $H_{loc} = 7.4$ μm along the fibre radius.

In case, a three-mode fibre design may be considered, the modal stabilities between the first three modes can be increased even more by increasing the radius of air-holes or increasing the number of holes. Moreover, to obtain similar Δn_{eff} one can also increase the air-holes diameter while reducing the number of air-holes in the array such that the resultant total air-holes area remains the same.

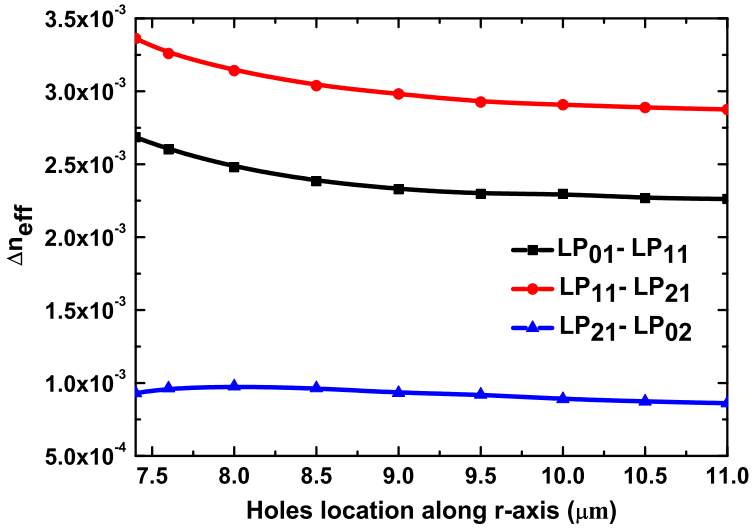

Fig. 7.12 Effect on Δn_{eff} with the change in the hole's array location along the radius of fibre. An array of two hundred air-holes with fixed radius of 40 *nm* is considered.

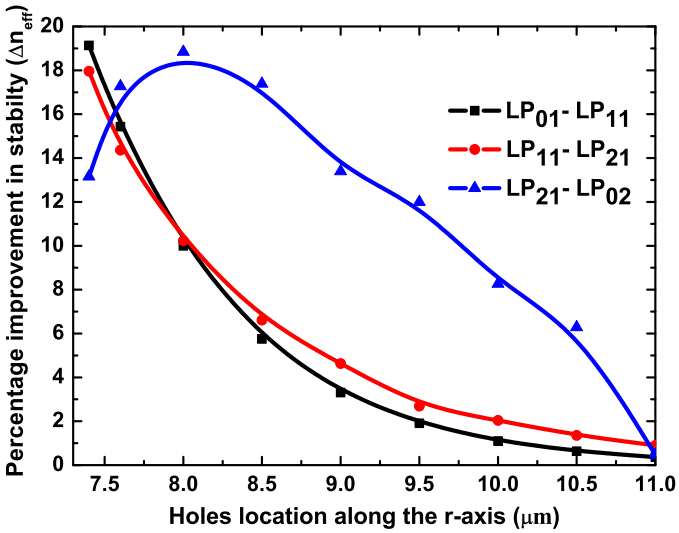

Fig. 7.13 Effect on the percentage Δn_{eff} with the change in the hole's array location along the radius of fibre. An array of two hundred air-holes with fixed radius of 40 *nm* is considered.

To select optimum position ($r = 7.4\ \mu m$ in the above case) we have introduced an array of the same number of holes with fixed radius but at the different locations along the fibre radii. Figure 7.12 shows that the modal stability improvement of the modes depends on the location of the introduced air-holes. It is observed that when the air-holes array is introduced near the boundary of core and cladding, the modal stability enhancement between four modes increases nearly equal. As the air hole's location is moved from 11 μm to 7.5 μm, the Δn_{eff} values increase continuously, except $\Delta n_{eff}(LP_{21} - LP_{02})$, which shows a saturation. This is due to LP_{02} mode approaching to cut-off, and its effective index change becomes small.

The percentage stability improvement for this study is shown in the Fig. 7.13. Here, two hundred air-holes with a fix radius of 40 *nm* are introduced at different locations along the radii of this four-mode fibre. The modal stability improvement increases as the holes array is moved from the $r_{loc} = 11.0\ \mu m$ towards the core radius $r = 7.5\ \mu m$. The percentage improvement in the modal stabilities $S_1 = 15\%$, $S_2 = 14\%$, $S_3 = 17\%$ can be noted when the hole's having radius of 40 *nm* are introduced at 7.6 μm. Here, the location and radius of the air-holes are optimised such that the percentage increase between the four modes remains similar. However, in order to achieve a different percentage improvement or to increase the Δn_{eff} between a particular set of modes a similar approach can be adopted.

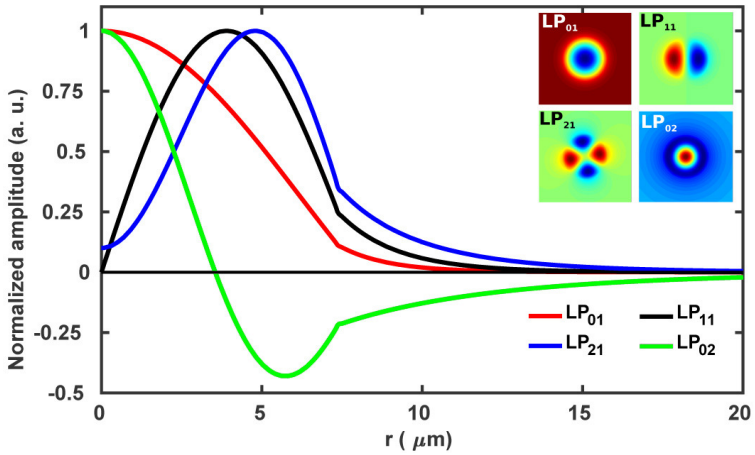

Fig. 7.14 Normalized H_y fields variations of LP_{01}, LP_{11}, LP_{21} and LP_{02} modes along the radius of modified four-mode fibre, field profile contours are also given as insets.

The introduction of the air-hole array also slightly changes the field profiles of these modes, as shown in Fig. 7.14. The contour field profiles of four modes are also shown as insets. This small field change can be observed at $r = 7.4\ \mu m$ along the radius of fibre when an array of two hundred air-holes each having radius of 40 *nm* is inserted in the fibre. The introduction of air-holes affects the magnitude of the field profiles and the normalised amplitudes of LP_{01}, LP_{11}, LP_{21} and LP_{02} modes at $r = 7.4\ \mu m$ are calculated as 0.107, 0.243, 0.338 and -0.216, respectively. The resultant mode spacing between these modes are calculated as $S_1 = 2.6851 \times 10^{-3}$, $S_2 = 3.362061 \times 10^{-3}$, $S_3 = 0.93006 \times 10^{-3}$ and these represent 19%, 18% and 13% increases, respectively. Additionally, an even higher percentage increase in the effective index difference can be achieved when the radius of holes is increased.

Figure 7.15 shows the changes in the effective mode areas of the first four modes with the change in the hole radius. Equation 7.2 is used to calculate the effective area optical modes of FMF [133].

$$A_{eff} = \frac{[\int |\overrightarrow{E}|^2 dxdy]^2}{\int |\overrightarrow{E}|^4 dxdy} \tag{7.2}$$

Here, $\overrightarrow{E}$ is the electric field of optical modes and without any air-holes the effective areas of the LP_{01}, LP_{11}, LP_{21} and LP_{02} modes are calculated as 124 μm^2, 177 μm^2, 199 μm^2 and 127 μm^2, respectively. However, the introduction of air-holes reduces the optical field near the air-holes due to the presence of low refractive index ($n_{air} = 1$) resulting in the reduction of effective mode area. However, it can be noted that the reduction of the mode area is less than the modal stability enhancement.

The introduction of air-holes also reduces the field intensity beyond the location of the air-holes array. With the fixed number of air-holes at $r = 7.4\ \mu m$, the effective area of the first three modes continue to decrease, but the effective area of LP_{02} increases when the air-hole size is increased more than 55 *nm* as this mode approaches its cut-off. However, with the small decrease in the effective area of these modes, the resultant modal stability

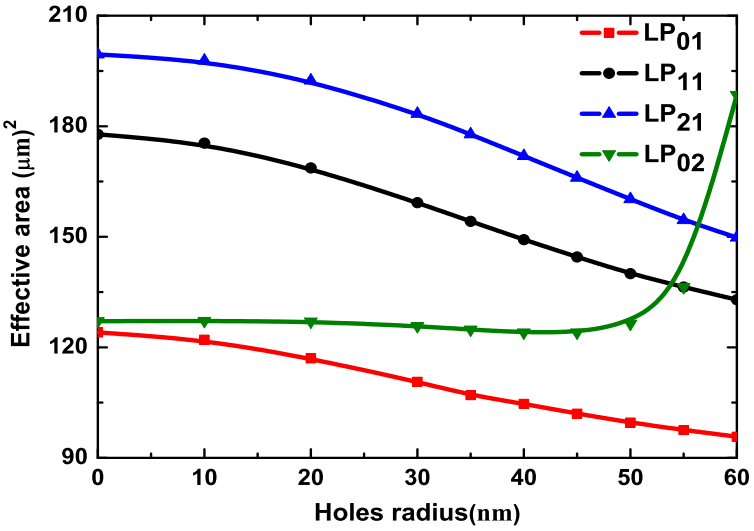

Fig. 7.15 Effect on the effective mode areas of a change in the hole's size introduced at $H_{loc} = 7.4\ \mu m$ along the radius of modified few-mode fibre.

improvement of more than 26% is achieved, and this can be increased further between the first three modes. The resultant effective areas of first three LP_{01}, LP_{11} and LP_{21} modes are calculated as 95.7 μm^2, 132.9 μm^2, and 149.7 μm^2, respectively. Moreover, as the LP_{02} mode approaches to cut-off condition for the air-hole size of 60 *nm* and its effective area is increased to 188.49 μm^2. Reduced mode area may limit the power handling capability but these mode area values are still significantly larger than that of a SMF along with the increased mode separation, which will reduce mode coupling appreciably.

7.2.2 Reduction of five modes to four modes for improved mode spacing

For the four-mode fibre design presented above, although it would have been possible to enhance further the Δn_{eff} between the first three modes, however, the $\Delta n_{eff}(LP_{21} - LP_{02})$ reaches to its saturation. In case we would like to enhance the Δn_{eff} between all the four modes further, a fibre which can guide five modes can be considered. In order to achieve higher mode effective index difference, next to a fibre with a larger core size is considered,

which can guide five modes. The core radius for the second fibre design is increased from 7.5 μm to 8.5 μm while keeping the core and cladding refractive indices same as the first fibre.

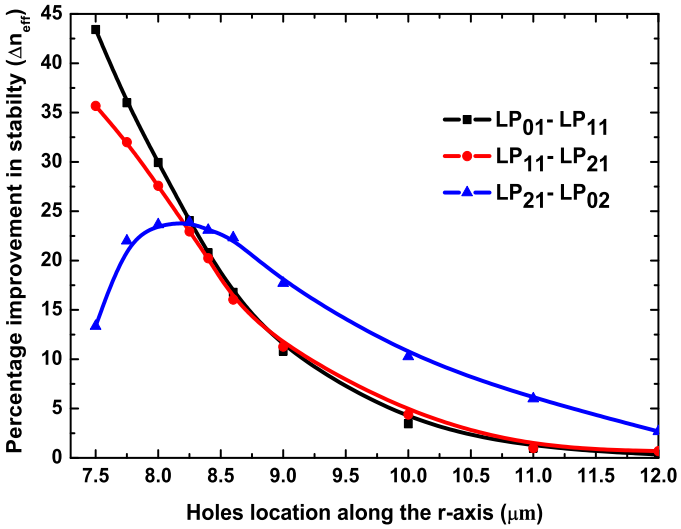

Fig. 7.16 Effect on the percentage stability improvement of a change in the location of air-holes array along the radius ($H_r = 50\ nm$) the second fibre design.

The V number for the second fibre is calculated as 5.77 at the same operating wavelength of 1.55 μm. This fibre guides five, LP_{01}, LP_{11}, LP_{21}, LP_{02} and LP_{31} modes. The Δn_{eff} between these modes are calculated as $\Delta n_{eff}(LP_{01} - LP_{11}) = 1.842 \times 10^{-3}$, $\Delta n_{eff}(LP_{11} - LP_{21}) = 2.360 \times 10^{-3}$, $\Delta n_{eff}(LP_{21} - LP_{02}) = 0.7396 \times 10^{-3}$, $\Delta n_{eff}(LP_{02} - LP_{31}) = 2.050 \times 10^{-3}$.

In order to increase the effective index difference between the first four modes, an array of two hundred air-holes ($r_{air} = 50\ nm$) is introduced at different locations along the radii of the second fibre. Figures 7.16 and 7.17 show the percentage increase in the modal stability between the first four modes as the air-hole array reaches to the core. The stability improvements between all four modes have similar increase near the core and cladding interface. However, when the air-holes array is moved further inside the core the stability between first three modes keep on increasing, but the fourth LP_{02} mode approaches to cut-off when $r < 8.0\ \mu m$. Similarly, as the array of air-hole is moved away from the core and towards cladding, the modal stability improvement reduces as a linear fashion. The

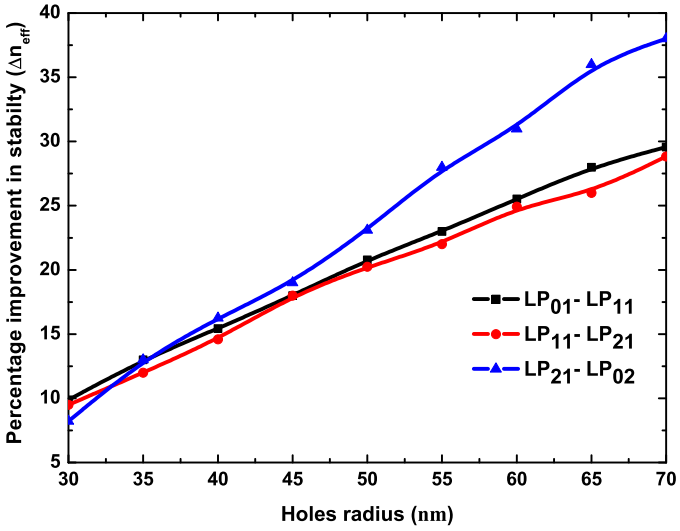

Fig. 7.17 Effect on the percentage stability improvement of a change in the air-holes size introduced at $H_{loc} = 8.4\ \mu m$ for the second fibre design.

increase in the effective index differences S_1, S_2 and S_3 is calculated as 2.225428×10^{-3}, 2.838742×10^{-3}, 0.91042×10^{-3}, respectively, for the second fibre when the two hundred air-holes each having 50 *nm* radius are introduced at a distance 8.4 μm from the centre. The resulting percentage increases are calculated as $S_1 = 21\%$, $S_2 = 20\%$ and $S_3 = 23\%$ as shown in Fig. 7.16. Moreover, percentage improvement in the Δn_{eff} between four modes improves with the increase in air-hole radius as shown in Fig. 7.17. As the air-holes size is increased the effective indices of these modes decreases depending on their relative field amplitudes near the air-holes. When the air-holes radius is increased to 70 *nm*, the modal stabilities S_1, S_2 and S_3 are calculated as 2.387×10^{-3}, 3.041×10^{-3} and 1.02×10^{-3}, respectively. Corresponding percentage increase are noted as $S_1 = 30\%$, $S_2 = 29\%$ and $S_3 = 38\%$, respectively.

The effective areas of the first four modes in the second fibre design also increase due to the larger core size compared to the first fibre design. The effective areas of LP_{01}, LP_{11}, LP_{21} and LP_{02} modes are calculated as 151.92 μm^2, 213.77 μm^2, 230.45 μm^2 and 137.00 μm^2 for the second fibre design, respectively. Figure 7.18 shows the effect on the effective area of the first four modes as the air-holes size is increased. It can be observed that as the air-holes

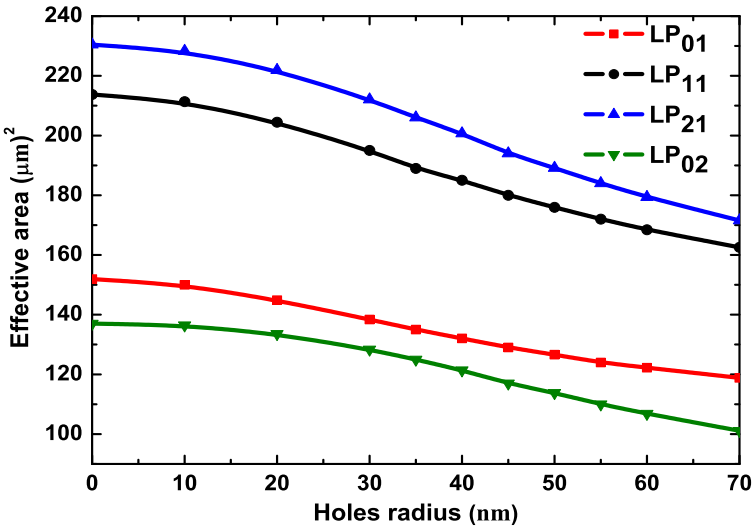

Fig. 7.18 Effect on the effective mode areas of a change in the hole's size at $H_{loc} = 8.4\ \mu m$ along the radius of second fibre design.

size is increased the effective areas of the modes reduces. When the radius of air-holes is increased to 70 *nm* the resultant effective area of LP_{01}, LP_{11}, LP_{21} and LP_{02} modes are calculated as 118.85 μm^2, 162.55 μm^2, 171.57 μm^2 and 101.09 μm^2, respectively. Table 7.7 summarizes the effective index differences between LP_{01}, LP_{11}, LP_{21} and LP_{02} modes and effective areas when 200 air-holes are introduced in our proposed designs.

For a four-mode fibre, the LP_{02} mode is closer to cut-off value (refractive index of cladding) as compared to five mode fibre design where the LP_{31} mode is near to the cut-off value. Hence, adding air-holes in a four modes fibre the effective area of LP_{02} mode start increasing due to approaching its cut-off as shown in Fig. 7.15. On the other hand, for a five-mode fibre, the effective area of LP_{02} mode shows a linear decrease as being further away from the cut-off and does not approach to cut-off value as shown in Fig. 7.18. Moreover, compared with the SMF transmission systems FMF design proposed here have significantly higher effective area and have the advantage of multiple modes to increase the transmission capacity.

Table 7.7 Summary of the effective index differences between LP_{01}, LP_{11}, LP_{21} and LP_{02} modes and their effective areas after the introduction of air-holes in the proposed fibre designs.

Fiber Design	200 air-holes radius (nm)	Effective index difference (Δn_{eff})						Effective area (um^2)			
		S_1	$\%S_1$	S_2	$\%S_2$	S_3	$\%S_3$	LP_{01}	LP_{11}	LP_{21}	LP_{02}
Four mode fibre	55	0.002902017	29	0.003634979	28	0.00103236	26	97.57	136.36	154.53	136
Five mode fibre	70	0.002387145	30	0.003041579	29	0.00102063	38	118.85	162.55	171.57	101.09

7.2.3 Bending effect

Further simulations are carried out to study the effect of bending in our proposed FMF and compare that with a standard SMF. Higher order modes of a FMF are more resilient to bend distortion because they have larger effective index difference as compared to a fundamental mode for a given fibre. Moreover, effective area reduction of the fundamental mode is significantly larger compared to other higher order modes of a FMF [35][160]. Hence, the bending loss and area reduction of only the fundamental mode in our proposed FMF is compared with a standard SMF. In order to compare these results, we considered a SMF with core radius 4.1 μm and cladding radius 35 μm. The refractive indices of core and cladding are taken as 1.44905 and 1.444, respectively.

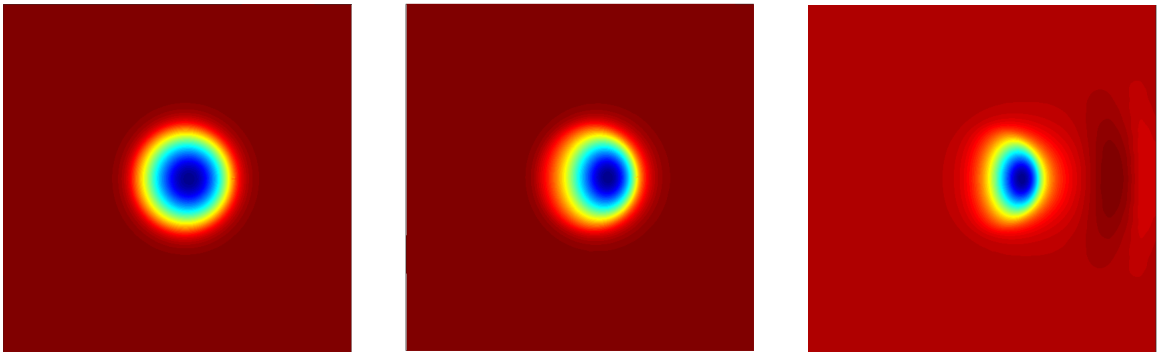

(a) (b) (c)

Fig. 7.19 Intensity profiles of LP_{01} mode without the introduction of air-holes along the circumference of second FMF with different bending (a) $R_{bend} = 30\ mm$, (b) $R_{bend} = 6\ mm$, (c) $R_{bend} = 2\ mm$ radii.

Figure 7.19 shows the intensity profiles of LP_{01} mode with three different bending radii (a) 30 mm (b) 6 mm and (c) 2 mm without any air-holes introduced in the FMF. It can be observed that with the decrease in the bending radius the mode intensity shifts outside the fibre core and the bending loss increases. The bending losses at $R_{bend} = 30\ mm$, $R_{bend} = 6\ mm$ and $R_{bend} = 2\ mm$ are calculated as 7.04×10^{-9}, 1.01×10^{-8} and 3.5×10^{-1}, dB/m respectively.

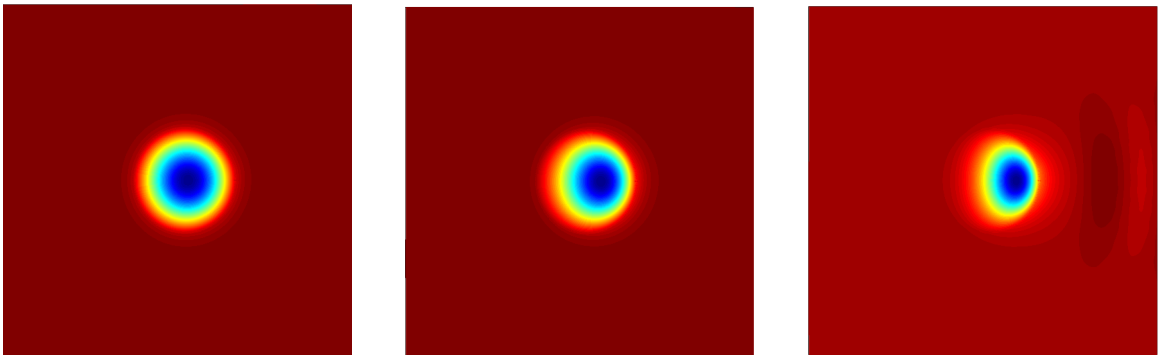

(a) (b) (c)

Fig. 7.20 Intensity profiles of LP_{01} mode with the introduction of 200 air-holes having 70 nm radius with different bending (a) $R_{bend} = 30\ mm$, (b) $R_{bend} = 6\ mm$, (c) $R_{bend} = 2\ mm$ radii.

With the introduction of 200 air-holes having radius of 70 nm, the bending loss of five mode fibre reduces as shown in Fig. 7.20. The bending loss after the introduction of air-holes

at different bending radii, $R_{bend} = 30\ mm$, $R_{bend} = 6\ mm$ and $R_{bend} = 2\ mm$ is calculated as 1.76×10^{-8}, 6.56×10^{-8} and $1.54 \times 10^{-1}\ dB/m$, respectively.

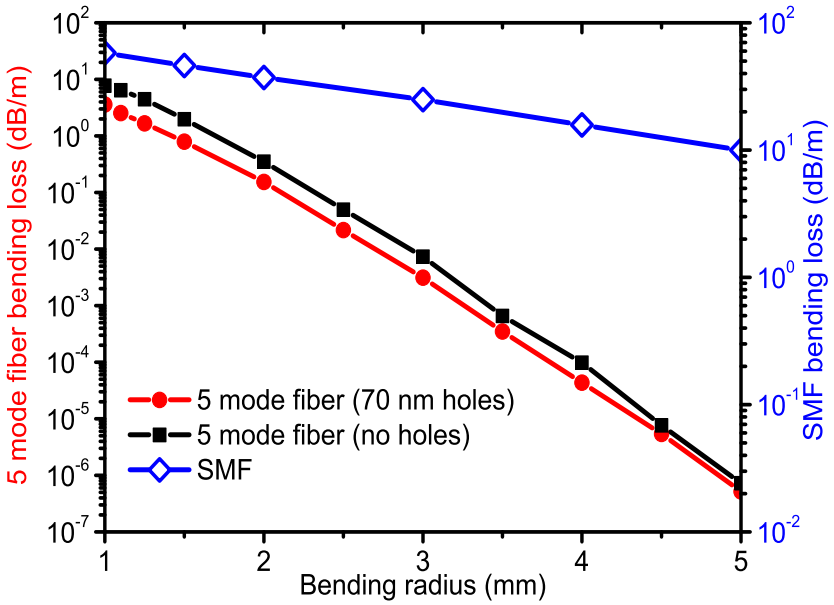

Fig. 7.21 Bending loss of the LP_{01} mode in a few-mode fibre without air-holes (black line) and with 200 air-holes (red line) with different bending radii. The bending loss of a SMF is also shown by blue line.

Figure 7.21 shows the variation of the bending loss with the bending radius (R_{bend}) for a standard SMF with a blue line. The bending losses of a five-mode fibre without air-holes and with air-holes are also shown in Fig. 7.21 by black and red lines, respectively. The bending loss of SMF at a R_{bend} of 5 mm is calculated as 9.97 dB/m and it increases as the bending radius is decreased. At $R_{bend} = 1\ mm$, the bending loss of SMF has increased to a significantly higher value and calculated as 57.97 dB/m. However, the bending loss of a five-mode fibre (without holes) at 5 mm and 1 mm are calculated as $7.28 \times 10^{-7}\ dB/m$ and 7.72 dB/m, respectively. This shows a significant reduction in the bending loss using a FMF compared to a standard SMF. Moreover, after introducing an array of 200 air-holes in our proposed FMF design, the bending loss reduces even further, as shown by a red line in Fig. 7.21. At $R_{bend} = 1\ mm$, the bending loss of five-mode fibre with air-holes is calculated as 3.59 dB/m which is nearly half of the value that was calculated without any air-holes. Figure

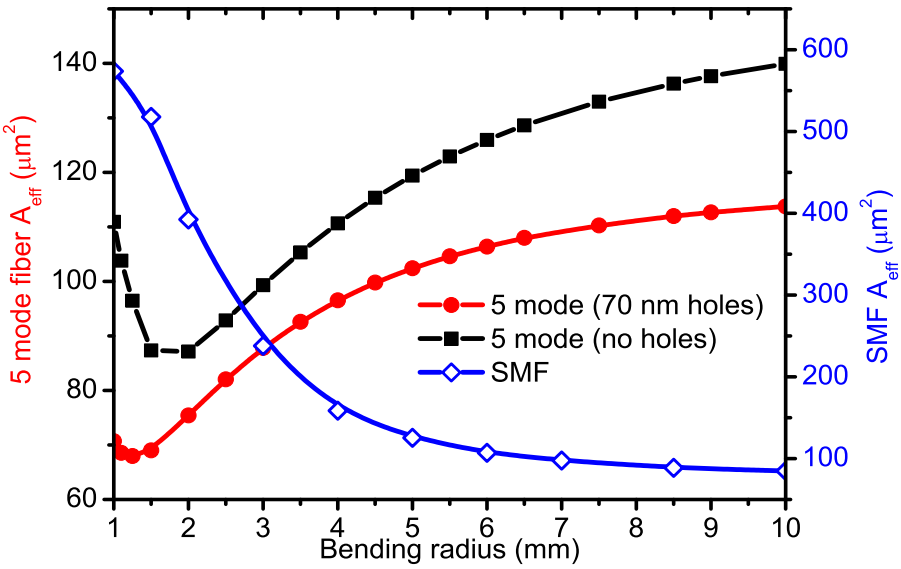

Fig. 7.22 Effective area of the LP_{01} mode as a function of bending radius for FMF without holes, with holes and a standard SMF.

7.22 shows the effect of bending on the effective area of a SMF and the fundamental mode of the FMF with and without air-holes. Due to the smaller core radius (4.1 μm), the effective area is calculated to be 78 μm^2 without any bending. This value is comparatively lower than the FMF with five modes, which is calculated as 151.92 μm^2 without any bending. Moreover, when the bending is introduced in SMF, the only guided mode quickly approaches to its cut-off value and the A_{eff} start increasing and calculated as 84.81 μm^2 at $R_{bend} = 10$ mm. As shown by a blue line in Fig. 7.22, the A_{eff} of SMF continues to increase as the bending radius is further decreased to 1 mm and calculated as 573.67 μm^2.

However, compared to the SMF, the A_{eff} of a FMF (no holes) reduces with the decrease in R_{bend} and calculated as 139.92 μm^2 at R_{bend} = 10 mm as shown by a black line in Fig. 7.22. When the R_{bend} approaches to 2 mm, the A_{eff} of FMF (no holes) approaches to its cut-off and with further decrease in R_{bend}, the effective area starts increasing. At $R_{bend} = 1$ mm, the A_{eff} increases to 110.94 μm^2. Similar trend is observed in our proposed FMF (70 nm holes) design where, the A_{eff} is calculated as 113.76 μm^2 at $R_{bend} = 10$ mm and it further reduces as the R_{bend} is decreased. As shown by the red line in Fig. 7.22, the FMF with holes

also approaches to its cut-off value at $R_{bend} = 1.25\ mm$ where the A_{eff} is calculated as 67.98 μm^2. This shows that our proposed FMF design with the air-holes suffers from significantly less bending loss and also provides more stable modal operation compared to a conventional SMF or a standard FMF.

7.3 Summary

A novel approach is proposed to increase the modal stability of higher order modes in a multimode fibre and few-mode fibre using air-holes. Multimode fibres provide higher effective area along with the increased modal stability in higher order modes. We have shown that the effective index difference between LP_{06} mode and its neighbouring antisymmetric LP_{15} and LP_{16} modes can be increased more than 54% by introducing air-holes along the circumference of multimode fibre. The increased modal stability reduces the modal cross talk and interference between HOMs of MMF and can improve the power capability of fibre lasers. The proposed technique is also scalable, and we have shown that the percentage Δn_{eff} between LP_{08} mode and its neighbouring LP_{17} and LP_{18} modes can also be increased to more than 34% by using the proposed method.

A similar technique is used to increase the modal spacing or effective index difference between the different modes of a few-mode fibre. FMF not only provides a significantly larger effective area compared to SMF, but they are also capable of transmitting more optical power and can result in longer communication lengths. Our proposed technique involves the use of uniform air-holes array along the radius of the fibre such that the effective indices of the modes are decreased depending on their field profile at that particular location. We have shown that for a four-mode fibre design, the modal stability between the modes can be increased more than 26% without a significant reduction in the mode quality. Moreover, we have also proposed another technique where a five-mode fibre is reduced to four modes and results in even higher (above 30%) effective index difference and also larger mode

area compared to the first design. It is also shown here that the bending loss of FMFs with air-holes is the significantly smaller and modal area is more stable with the bending.

Chapter 8

Conclusions and future work

As a conclusive chapter, the strength of improved full-vectorial finite element method based computer simulation code to analyse the acoustic wave propagation in the optical waveguide is summarised here. The proposed penalty method eliminates the spurious modes in acoustic modal solution resulting in improved and more accurate acoustic modes. The power limiting effect of non-linearity in optical fibres and ways to reduce this effect by reducing stimulated Brillouin scattering overlap between optical and acoustic modes and by using large mode area fibres are also explained. Moreover, this chapter also paves the platform for future research on stimulated Brillouin scattering and large mode area fibres.

8.1 Conclusions

The aim of the thesis was to study nonlinear effects in optical fibres. To mitigate these nonlinear effects, two approaches are explored in the thesis. One of the approaches was to study the stimulated Brillouin scattering (SBS) using a full-vectorial finite element method based in-house code. The computer simulation code performs rigorous characterisation of the acoustic wave in both low and high index contrast waveguides. The phase-matched acoustic-optic interaction due to the SBS process was studied. A penalty term was introduced

in the acoustic modal solution to remove the non-physical spurious modes and improve the quality of the acoustic modes. The achievements of this approach are stepwise mentioned below:

- An improved full-vectorial FEM based computer code is developed that uses eigenvalue solver to find the acoustic modes in both low and high index contrast waveguides.
- The use of full-vectorial FEM increases the accuracy of the modal solution, but the existence of spurious modes is often considered as an important challenge. An updated acoustic modal solution is presented where a penalty term is introduced to eliminate these spurious modes.
- The program can also exploit the symmetry boundary conditions of the waveguide and only half or quarter of the structure can be simulated, enabling higher mesh distribution for a more accurate solution.
- In order to study acoustic-optic overlap, two designs of SMF are proposed, where, light-sound interactions is either increased or reduced for fibre optic sensing or high power transmission applications, respectively. By lowering the SBS overlap, the SBS threshold level increases that allows high power transmission.

The second approach to reducing the non-linearity in optical fibre was the use of large mode area fibres. Due to lower optical intensities, large mode area fibres such as few mode fibres and multimode fibres have effectively lower non-linearities. However, with the increase in the core diameter, optical fibres become multimode and more than one mode exist, which can be more susceptible to mode coupling. With the increase in the modal order, the effective index difference (Δn_{eff}) between the modes also increases, and these higher order modes can be used for high power transmission applications such as fibre lasers and amplifiers. To increase the modal stability between higher order modes, two proposed methods were considered and that are listed below:

- A novel design validated by rigorous numerical analysis was proposed, where, a single or multiple annular strip(s) of low and high index contrast refractive index are introduced at particular radial locations inside the core of MMF. According to symmetry rule, bend perturbations is odd in nature, and direct coupling arises between even and odd higher order modes. Annular strips were introduced at particular locations along the fibre radius such that the effective index difference between a desired mode of propagation remains unchanged but the effective indices of nearest antisymmetric modes changes that result in the increased modal stability.

- In the second method, the air-holes array was used to increase the modal stability of a desired mode of propagation. The introduction of air-holes at particular location reduces the effective index of the modes. The radial location along the radius of the fibre is chosen such that the effective index of desired ($LP_{0,n}$) mode and its neighbouring higher order antisymmetric $LP_{1,n+1}$ mode reduces relative to their field intensities at that location. The effective index change in a given lower order $LP_{1,n-1}$ was negligible when the air-holes array was introduced at the zero crossing location of this mode. Hence, the strategic location of air-holes reduces the effective index of $LP_{1,n+1}$ mode more than the $LP_{0,n}$ mode while keeping the effective index of $LP_{1,n-1}$ mode unchanged. A similar method was used to increase the modal stability of few-mode fibre. Here, the effective index difference between first four LP_{01}, LP_{11}, LP_{21} and LP_{02} modes of FMF is increased more than 26% by using air-holes along the radius of the fibre. Moreover, in a second design, the modal stability is increased above 30 % where a five-mode fibre was reduced to a four-mode fibre. It was also shown here that the bending loss of proposed FMF designs with air-holes is comparatively lower and modal area is more stable with the bending.

Overall, the thesis discusses the non-linearity as a power limiting effect in optical fibres and two possible ways to reduce its effect are discussed. The acoustic modal solution to

study light-sound interaction is discussed where a penalty term is introduced to remove the spurious modes to facilitate acoustic simulations. In one case, fibre geometry is modified such that the overlap between optical and acoustic modes is reduced which would increase the SBS threshold. In another approach, the large mode area fibres that provide a larger effective area where light is distributed over a larger area were used to reduce the nonlinear effects. However, the existence of more than one mode in large mode area fibres may result in the inter-modal interference and energy can be transferred to a mode of propagation to the nearest mode. Two techniques are proposed to increase the modal stability of a higher order mode and its neighbouring antisymmetric modes. One of the methods involves the use of low and high index doped annular strips along the circumference of fibre. The second proposed technique involves the use of air-holes to increase modal stability. Both methods have shown a significant increase in the effective index difference between the higher order modes and thus reduces the modal coupling.

8.2 Future work

It is hard to explore and investigate all areas of nonlinear effects in optical waveguides in such a short time. All results presented in this thesis are considered as a small contribution of the on-going global research to minimise the nonlinear effects for high power transmission or exploit these effects for fibre optic based sensing applications. The improved in-house code to study light-sound interaction can be considered as a foundation and can be used for further analysis of higher Brillouin gain using a different combination of materials and for the study of stimulated Brillouin scattering in complex structures. SBS overlap is a necessary parameter to calculate the SBS gain and SBS threshold and similarly for Brillouin gain spectrum. In this thesis, we have shown the acoustic-optic overlap of the fundamental and higher order acoustic modes with the fundamental optical mode. However, SBS spectrum can be calculated by considering some other parameters such as Brillouin gain linewidth and

elasto-optic coefficients etc. in the SBS gain formulations. In addition to above mentioned future aspects, some other doped materials can be used to analyse stimulated Brillouin scattering. In telecommunication fibres, where Fluorine is used to decrease the optical refractive index of cladding, the SBS may play an important role. In contrast to B_2O_3 used to increase the acoustic optic overlap other materials such as P_2O_5 in combination with Fluorine can also be used to study the acoustic optic overlap. The refractive index profile of step index fibre is considered smooth in our simulations. Real telecommunication step-index fibres have a small variation in the core and cladding refractive indices during fabrication process. Although there is very slight differences expected in the modal solution results. However, a comparative study between real refractive index profile and ideal step index profile can be considered as future work.

The acoustic-optic overlap in multimode fibres (MMF) can also be very useful for the applications that required a large effective mode area. Mode spacing between higher order modes of a MMF increases with the modal order, hence resulting in increased stability. These higher order modes with more stability, higher effective area and a low SBS overlap can be a good option for the high power fibre lasers. This gives a high SBS threshold and less interference with the neighbouring modes. Similarly, the mode spacing with the neighbouring anti-symmetric modes can also be increased by doping the core of the MMF on certain locations such that it affects only antisymmetric modes while keeping the central propagation mode unaffected. Moreover, the material density and radiation pressure variations were neglected in the acoustic modal solution discussed in the thesis. These density and pressure variations can also be accommodated in the code as future work, particularly for very small waveguides. This addition will not only make the modal solution more realistic but also make it useful for the analysis of nanoscale devices.

References

[1] Cisco, "White paper: Cisco VNI forecast and methodology, 2015–2020," 2016. [Online]. Available: http://www.cisco.com/c/en/us/solutions/collateral/service-provider/visual-networking-index-vni/complete-white-paper-c11-481360.html

[2] R. W. Tkach, "Scaling optical communications for the next decade and beyond," *Bell Syst. Tech. J.,* vol. **14**, no. 4, pp. 3–9, 2010.

[3] A. D. Ellis, N. M. Suibhne, D. Saad, and D. N. Payne, "Communication networks beyond the capacity crunch," *Philosophical Transactions of the Royal Society A: Mathematical, Physical and Engineering Sciences*, vol. **374**, no. 2062, 2016.

[4] C. J. Koester and E. Snitzer, "Amplification in a fiber laser," *Appl. Opt.*, vol. **3**, pp. 1182-1186, 1964.

[5] M. N. Zervas and C. A. Codemard, "High power fiber lasers: A review," *IEEE J. Sel. Top. Quantum Electron.*, vol. **20**, no. 5, pp. 219–241, 2014.

[6] C. Jauregui, J. Limpert, and A. Tunnermann, "High-power fibre lasers," *Nat. Photonics*, vol. **7**, no. 11, pp. 861, 2013.

[7] E. Zucker, D. Zou, L. Zavala, H. Yu, P. Yalamanchili, L. Xu, H. Xu, D. Venables, J. Skidmore, V. Rossin, and R. Raju, "Advancements in laser diode chip and packaging technologies for application in kW-class fiber laser pumping", *High-Power Diode Laser Technology and Applications XII*, SPIE proceedings, vol. **8965**, 2014.

[8] I. Savelii, L. Bigot, B. Capoen, C. Gonnet, C. Chanéac, E. Burova, A. Pastouret, H. El-Hamzaoui, and M. Bouazaoui, "Benefit of Rare-Earth "Smart Doping" and Material Nanostructuring for the Next Generation of Er-Doped Fibers", *Nanoscale Res. Lett.*, vol. **12**, no. 1, pp. 206, 2017.

[9] S. Fu, W. Shi, Y. Feng, L. Zhang, Z. Yang, S. Xu, X. Zhu, R. A. Norwood, and N. Peyghambarian, "Review of recent progress on single-frequency fiber lasers", *J. Opt. Soc. Am. B*, vol. **34** no. 3, pp. A49–A62, 2017.

[10] H. Fu, D. Chen, and Z. Cai, "Fiber sensor systems based on fiber laser and microwave photonic technologies," *Sensors*, vol. **12**, no. 5, pp. 5395–5419, 2012.

[11] A. Tunnermann, T. Schreiber and J. Limpert, "Fiber lasers and amplifiers: an ultrafast performance evolution", *Appl. Opt.*, vol. **49**, no. 25, pp. F71–F78, 2010.

[12] W. S. Wong, X. Peng, J. M. McLaughlin, and L. Dong, "Breaking the limit of maximum effective area for robust single-mode propagation in optical fibers", *Opt. Lett.*, vol. **30**, no. 21, pp. 2855–2857, 2005.

[13] J. Limpert, F. Roser, D. N. Schimpf, E. Seise, T. Eidam, S. Hadrich, J. Rothhardt, C. J. Misas, and A Tunnermann, "High repetition rate gigawatt peak power fiber laser systems: Challenges, Design, and Experiment", *IEEE J. Sel. Top. Quantum Electron*, vol. **15**, no. 1, pp. 159–169, 2009.

[14] D. J. Richardson, J. Nilsson, and W. A. Clarkson, "High power fiber lasers: current status and future perspectives," *J. Opt. Soc. Am. B*, vol. **27**, pp. B63-B92, 2010.

[15] J. Limpert, F. Roser, S. Klingebiel, T. Schreiber, C. Wirth, T. Peschel, R. Eberhardt, and A. Tünnermann, "The rising power of fiber lasers and amplifiers," *IEEE J. Sel. Top. Quantum Electron*. vol. 13, pp. 537–545, 2007.

[16] M-J. Li, X. Chen, J. Wang, A. B. Ruffin, D. T. Walton, S. Li, D. A. Nolan, S. Gray, and L. A. Zenteno, "Fiber designs for reducing stimulated Brillouin scattering," *Optical Fiber Communication Conference*. Optical Society of America, p. OTuA4, (2006).

[17] S. Ramachandran, J. M. Fini, M. Mermelstein, J. W. Nicholson, S. Ghalmi, and M. F. Yan, "Ultra large effective area, higher order mode fibers: a new strategy for high power lasers," *Laser Photonics Rev.* vol. **2**, no. 6, pp. 429–448, 2008.

[18] M. D. Mermelstein, S. Ramachandran, J. M. Fini, and S. Ghalmi, "SBS gain efficiency measurements and modeling in a 1714 μm^2 effective area LP_{08} higher-order mode optical fiber," *Opt. Express* vol. **15**, pp. 15952–15963, 2007.

[19] S. Gray, D. T. Walton, X. Chen, J. Wang, M-J. Li, A. Liu, A. B. Ruffin, J. A. Demeritt, and L. A. Zenteno, "Optical fibers with tailored acoustic speed profiles for suppressing stimulated Brillouin scattering in high-power, single-frequency sources." *IEEE J. Sel. Top. Quantum Electron.*, vol. **15**, no. 1, pp. 37–46, 2009.

[20] M. A. Soto, G. Bolognini and F. Di Pasquale, "Enhanced simultaneous distributed strain and temperature fiber sensor employing spontaneous Brillouin scattering and optical pulse coding," *IEEE Photon. Technol. Lett.*, vol. **21**, pp. 450–452, 2009.

[21] L. Thevenaz, M. Nikles, A. Fellay, M. Facchini and P. Robert, "Truly distributed strain and temperature sensing using embedded optical fibers," *Proc. SPIE*, vol. **3330**, pp. 301–314, 1998.

[22] K. Y. Song, K. S. Abedin, K. Hotate, M. G. Herraez, and L. Thevenaz, "Highly efficient Brillouin slow and fast light using As_2Se_3 chalcogenide fiber," *Opt. Express*, vol. **14**, no. 13, pp. 5860–5865, 2006.

[23] T. Schneider, "Time delay limits of stimulated-Brillouin-scattering-based slow light systems," *Opt. Lett.* vol. **33**, no. 13, pp. 1398–1400, 2008.

[24] G. Bahl, M. Tomes, F. Marquardt, and T. Carmon, "Observation of spontaneous Brillouin cooling," *Nat. Phys.*, vol. **8**, no. 3, pp. 203–207, 2012.

[25] V. Scarnera, F. Ghiringhelli, A. Malinowski, C. A. Codemard, M. K. Durkin, and M. N. Zervas, "Modal instabilities in high power fiber laser oscillators," *Opt. Express*, **27**, 4386-4403, 2019.

[26] D. Taverner, D. J. Richardson, L. Dong, J. E. Caplen, K. Williams, and R. V Penty, "158 μJ pulses from a single-transverse-mode, large-mode-area erbium-doped fiber amplifier," *Opt. Lett.* vol. **22**, 378–380, 1997.

[27] D. Jain, Y. Jung, P. Barua, S. Alam, and J. K. Sahu, "Demonstration of ultra-low NA rare-earth doped step index fiber for applications in high power fiber lasers," *Opt. Express* vol. **23**, 5200–5203, 2015.

[28] W. Xu, Z. Lin, M. Wang, S. Feng, L. Zhang, Q. Zhou, D. Chen, L. Zhang, S. Wang, C. Yu, and L. Hu, "50 μm core diameter $Yb^{3+}/Al^{3+}/F^{-}$ codoped silica fiber with $M^2 < 1.1$ beam quality," Opt. Lett., vol. **41**, 504, 2016.

[29] V. Khitrov, J. D. Minelly, R. Tumminelli, V. Petit, and E. S. Pooler, "3kW singlemode direct diode-pumped fiber laser," in SPIE LASE (2014), p. 89610V–89610V.

[30] P. S. J. Russell, "Photonic-crystal fibers," *J. Light. Technol.* vol. **24**, 4729–4749, 2006.

[31] W. J. Wadsworth, R. M. Percival, G. Bouwmans, J. C. Knight, and P. S. J. Russel, "High power air-clad photonic crystal fibre laser," *Opt. Express* vol. **11**, 48–53, 2003.

[32] X. Zhu, A. Schülzgen, H. Li, L. Li, Q. Wang, S. Suzuki, V. L. Temyanko, J. V. Moloney, and N. Peyghambarian, "Single-transverse-mode output from a fiber laser based on multimode interference", *Opt. Lett.*, vol. **33**, no. 9, pp. 908–910, 2008.

[33] B. M. Trabold, D. Novoa, A. Abdolvand, and P. S. J. Russell, "Selective excitation of higher order modes in hollow-core PCF via prism-coupling", *Opt. Lett*. vol. **39**, no. 13, pp. 3736–3739, 2014.

[34] N. Bhatia, K. C. Rustagi, and J. John, "Single $LP_{0,n}$ mode excitation in multimode fibers", *Opt. Express* vol. **22**, no. 14, pp. 16847–16862, 2014.

[35] J. M. Fini and S. Ramachandran, "Natural bend-distortion immunity of higher-order-mode large-mode-area fibers", *Opt. Lett.*, vol. **32**, no. 7, pp. 748–750, 2007.

[36] S. Ramachandran, J. W. Nicholson, S. Ghalmi, M. F. Yan, P. Wisk, E. Monberg, and F. V. Dimarcello, "Light propagation with ultralarge modal areas in optical fibers", *Opt. Lett.*, vol. **31**, no. 12, pp. 1797–1799, 2006.

[37] K. C. Kao and G. A. Hocham, "Dielectric fiber surface waveguides for optical frequencies," *In proceedings of the Institution of Electrical Engineers*, vol. **113**, pp. 1151–1158, July, 1966.

[38] F. P. Kapron, D. B. Keck, and R. D. Maurer, "Radiation losses in glass optical waveguides," *Appl. Phys. Lett.*, vol. **17**, no. 10, pp. 423–425, 1970.

[39] T. Miya, Y. Terunuma, T. Hosaka, and T. Miyashita, "Ultimate low-loss singlemode fiber at 1.55 micron," *Electron. Lett.*, vol. **15**, no. 4, pp. 106–108, 1979.

[40] S. Personick, "Fiber optic communication - A technology coming of age," *IEEE Commun. Soc. Mag.* vol. **16**, pp. 12–20, 1978.

[41] S. Saint-Jaml, "Soliton-based fiber light sources for nonlinear spectroscopy and microscopy" PhD dissertation, Aix Marseille University, 2014.

[42] K. Morita, Y. Yamamoto, T. Hasegawa, Y. Honma, K. Sohma, & T. Fujii, "Ultralow-loss large-core fiber for submarine cables," *SEI Technical Review,* **85**, 15-18, 2017.

[43] D. Marcuse, "Cutoff condition of optical fibers," *J. Opt. Soc. Am.*, vol. **63**, pp. 1369–1371, 1973.

[44] G. P. Agrawal, *Nonlinear Fiber Optics*, 3rd Edition, Academic Press, San Diego, CA, 2001.

[45] J. M. Senior, and M. Y. Jamro, *Optical fiber communications: principles and practice.* Pearson Education, 2009.

[46] J. A. Mores, G. N. Malheiros-Silveira, H. L. Fragnito, and H. E. Hernandez-Figueroa, "Efficient calculation of higher-order optical waveguide dispersion," *Opt. Express*, vol. **18**, pp. 19522–19531, 2010.

[47] N. Kikuchi, K. Sekine, and S. Saski, "Analysis of XPM effect on WDM transmission performance," *Electron. Lett.*, Vol. **33**, 653–654, 1997.

[48] S. P. Singh, and N. Singh, "Nonlinear effects in optical fibers: origin, management and applications," *Progress In Electromagnetics Research*, vol. **73**, 249–275, 2007.

[49] Y. T. Cho and T. P. Newson, "Brillouin-based distributed fibre temperature sensors at 1.53 μm using Raman amplification", 15th International conference on optical fiber sensors technical digest (OFS), pp. 305–309, May 2002.

[50] D. W. Shipp, F. Sinjab, and I. Notingher, "Raman spectroscopy: techniques and applications in the life sciences," *Adv. Opt. Photon.* vol. **9**, pp. 315–428, 2017.

[51] M. N. Alahbabi, Y. T. Cho and T. P. Newson, "Simultaneous temperature and strain measurement with combined spontaneous Raman and Brillouin scattering", *Opt. Lett.*, vol. **30**, no. 11, pp. 1276–1278, 2005.

[52] J. Toulouse, "Optical nonlinearities in fibers: review, recent examples, and systems application", *J. Light. Tech.,* vol. **23**, no. 11, pp. 3625–3641, 2005.

[53] G. P. Agrawal, Nonlinear Fiber Optics, *5th Edition, Academic Press*, 2013.

[54] S. Dasgupta, F. Poletti, S. Liu, P. Petropoulos, D. J. Richardson, L. Gruner-Nielsen, and S. Herstrom, "Modeling Brillouin gain spectrum of solid and microstructured optical fibers using a finite element method," *J. Light. Technol.*, vol. **29**, no. 1, 22–30, 2011.

[55] L. Brillouin, "Diffusion de la lumiere et des rayons X par un corps transparent homogene: Influence de l'agitation thermique." Ann. Phys.(Paris), vol. **9**, no. 17, pp. 88–122, 1922.

[56] A. Yeniay, J. M. Delavaux, and J. Toulouse, "Spontaneous and stimulated Brillouin scattering gain spectra in optical fibers," *J. Light. Technol.*, vol. **20**, no. 8, 2002.

[57] J. G. Dil and H. Blok. "Propagation of electromagnetic surface waves in a radially inhomogeneous optical waveguide," *Opt. Quant. Electron.,* vol. **5**, pp. 415–428, 1973.

[58] M. O. Vassell, "Calculation of propagating modes in a graded-index optical fibre," *Opt. Quant. Electron.*, vol. **6**, no. 4, pp. 271–286, 1974.

[59] S. S. Rao, *The Finite Element Method in Engineering*. Amsterdam : Elsevier Butterworth Heinemann, 4 edition, 2005.

[60] E. Schweig and W. B. Bridges, "Computer analysis of dielectric waveguides: A finite-difference method", *IEEE Trans. Microwave Theory Tech.*, vol. **32**, no. 5, pp. 531–541, 1984.

[61] A. Taflove, and S. C. Hagness, "Computational electrodynamics: the finite-difference time-domain method". Artech House, 2005.

[62] I. L. Fabelinskii, "Molecular scattering of light", *Springer Science & Business Media*, (2012).

[63] V. Laude, and J. C. Beugnot, "Spontaneous Brillouin scattering spectrum and coherent Brillouin gain in optical fibers" *Applied Sciences*, vol. **8**, no. 6, pp. 907, 2018.

[64] H. A. Al-Asadi, A. A. A. Bakar, F. M. Adikan, and M. A. Mahdi, "Analytical study of nonlinear phase shift through stimulated Brillouin scattering in single mode fiber with the pump power recycling technique," *Journal of Optics*, vol. **13**, no. 10, pp. 105701, 2011.

[65] R. W. Boyd, "*Nonlinear Optics*", 3rd ed. New York, USA: Academic Press, 2008.

[66] A. Kobyakov, M. Sauer, and D. Chowdhury, "Stimulated Brillouin scattering in optical fibers," *Adv. Opt. Photon.*, vol. **2**, no. 1, pp. 1-59, 2010.

[67] M. J. Damzen, V. I. Vlad, V. Babin and A. Mocofanescu, "*Stimulated Brillouin Scattering: Fundamentals and Applications,*" Temple Back, Bristol, UK: Institute of Physics, 2003.

[68] V. I. Kovalev and R. G. Harrison, "Suppression of stimulated Brillouin scattering in high-power single-frequency fiber amplifiers," *Opt. Lett.*, vol. **31**, no. 2, pp. 161–163, 2006.

[69] A. Gulistan and S. Ghafoor, "Self-phase modulation-based multiple carrier generation for radio over fiber duplex baseband communication", *Photonic Network Communications*, vol. **29**, no. 2, pp. 133–137, 2015.

[70] R. B. Ellis, F. Weiss and O. M. Anton, "HFC and PON-FTTH networks using higher SBS threshold singlemode optical fibre," *Electron. Lett.,* vol. **43**, no. 7, pp. 405–407, 2007.

[71] M. D. Vaughn, A. B. Ruffin, A. Kobyakov, A. Woodfin, C. Mazzali, R. Whitman, A.Boskovic, R. E. Wagner, D. Kozischek, and D. Meis, "Techno-economic study of the value of high stimulated Brillouin scattering threshold single-mode fiber utilization in fiber-to-the-home access networks," *J. Opt. Netw.*, vol. **5**, no. 1, pp. 40-57, 2006.

[72] X. Bao, "Optical Fiber Sensors Based on Brillouin Scattering," *Optics & Photonics News*, vol. **20**, no. 9, pp. 40-45, 2009.

[73] J. Wang, "Distributed pressure and temperature sensing based on stimulated Brillouin scattering", *Master of Science thesis, Virginia Polytechnic Institute*, 2013.

[74] L. Thevenaz, M. Facchini, A. Fellay, P. Robert, D. Inaudi and B. Dardel, "Monitoring of large structure using distributed Brillouin fibre sensing", *13th International Conference on Optical Fiber Sensors*, vol. **3746**, no. THEVE-CONF-1999-006, pp. 345–348, 1999.

[75] M. N. Islam, "Raman amplifiers for telecommunications," *IEEE J. Sel. Top. Quantum Electron*, vol. **8**, no. 3, pp. 548–559, 2002.

[76] B. Foley, M. L. Dakss, R. W. Davies and P. Melman, "Gain saturation in fiber Raman amplifiers due to stimulated Brillouin scattering," *J. Light. Technol*, vol. **7**, no. 12, pp. 2024–2032, 1989.

[77] Y. Aoki, S. Kishida, and K. Washio, "Stable cw backward Raman amplification in optical fibers by stimulated Brillouin scattering suppression," *Appl. Opt.*, vol. **25**, no. 7, pp. 1056–1060, 1986.

[78] L. Thevenaz, "Slow and fast light in optical fibres," *Nat. Photonics*, vol. **2**, no. 8, pp. 474–481, 2008.

[79] Z. Zhu, D. J. Gauthier, and R. W. Boyd, "Stored light in an optical fiber via stimulated brillouin scattering" *Science*, vol. **318**, no. 5857, pp. 1748–1750, 2007.

[80] M.G Herraez, K. Y.Song, and L. Thevenaz, "Arbitrary-bandwidth Brillouin slow light in optical fibers," *Optics Express*, vol. **14**, no. 4, pp. 1395–1400, 2006.

[81] Z. Zhu, A. M. Dawes, D. J. Gauthier, L. Zhang, A. E. Willner, "Broadband SBS slow light in an optical fiber," *J. Light. Technol*, vol. **25**, no. 1, pp. 201-206, 2007.

[82] R. N. Thurston, "Elastic waves in rods and clad rods," *J. Acoust. Soc. Am.*, vol. **64**, no. 1, pp. 1-37, 1978.

[83] B. A. Auld, "*Acoustic fields and waves in solids*," 1973.

[84] C. K. Jen, , J. E. B. Oliveira, N. Goto, and K. Abe, "Role of guided acoustic wave properties in single-mode optical fibre design," *Electron. Lett.*, vol. **24**, no. 23 pp. 1419-1420, 1988.

[85] M. M. Rahman, "Full-vectorial study of light and sound interactions in low and high index contrast silica waveguides" PhD dissertation, City University London, 2016.

[86] S. Sriratanavaree, "Characterisation of acoustic waves in optical waveguides," PhD dissertation, City University London, 2014.

[87] F. Mouhat and F. X. Coudert, "Necessary and sufficient elastic stability conditions in various crystal systems," *Phys. Rev. B*, vol. **90**, no. 22, pp. 224104, 2014.

[88] D. Royer and E. Dieulesaint, "Elastic Waves in Solids I: Free and Guided Propagation, translated by DP Morgan," *Springer Science & Business Media New York*, 2000.

[89] NDT course material (Ultrasound), available at:[https://www.nde - ed.org/EducationResources/CommunityCollege/Ultrasonics/Physics/modepropagation.htm]

[90] P. E. Lagasse, "Higher-order finite-element analysis of topographic guides supporting elastic surface waves," *J. Acoust. Soc. Am.*, vol. **53** no. 4, pp. 1116-1122, 1973.

[91] S. Sriratanavaree, B. M. A. Rahman, D. M. H. Leung, N. Kejalakshmy, and K. T. V. Grattan, "Rigorous characterization of acoustic-optical interactions in silicon slot waveguides by full-vectorial finite element method," *Opt. Express*, vol. **22**, no. 8, pp. 9528–9537, 2014.

[92] O. C. Zienkiewicz, R. L. Taylor, and J. Z. Zhu, "*The Finite Element Method: Its Basis and Fundamentals,*" 7th ed. Waltham, MA, USA: Butterworth-Heinemann, 2013.

[93] K. S. Chiang, "Review of numerical and approximate methods for the modal analysis of general optical dielectric waveguides," *Optical and Quantum Electronics*, vol. **26**, no. 3, pp. S113-S13, 1994.

[94] N. Nguyen-Thanh, T. Rabczuk, H. Nguyen-Xuan, and S. P. A. Bordas, "A smoothed finite element method for shell analysis," *Computer Methods in Applied Mechanics and Engineering*, vol. **198**, no. 2, pp. 165–177, 2008.

[95] B. M. A. Rahman and A. Agrawal, "*Finite Element Modeling Methods for Photonics*," Artech House, 2013.

[96] P. P. Silvester, and R. L. Ferrari, "*Finite Elements for Electrical Engineers*," Cambridge University Press, UK, 1996.

[97] J. M. Jin, "The finite element method in electromagnetics," *John Wiley & Sons*, 2015.

[98] N. Mabaya and P. E. Lagasse, "Finite element analysis of optical waveguides," *In 1980 IEEE MTT-S International Microwave symposium Digest*, pp. 329–331, (1980).

[99] B. M. A. Rahman, F. A. Fernandez, and J. B. Davies, "Review of finite element methods for microwave and optical waveguides," *Proceedings of the IEEE*, vol. **79**, no. 10, pp.1442–1448, 1991.

[100] A. Berk, "Variational principles for electromagnetic resonators and waveguides", *IRE Transactions on Antennas and Propagation*, vol. **4**, no. 2, pp. 104–111, 1956.

[101] B. M. A. Rahman and J. B. Davies, "Penalty function improvement of waveguide solution by finite elements." *IEEE Trans. Microw. Theory Tech,*, vol. **32**, no. 8, pp. 922–928, 1984.

[102] J. R. Winkler and J. B. Davies. "Elimination of spurious modes in finite element analysis." *J. Comput. Phys.*, vol. **56**, no. 1, pp 1–14, 1984.

[103] A. H. McCurdy, "Modeling of stimulated Brillouin scattering in optical fibers with arbitrary radial index profile." *J. Light. Technol.*, vol. **23**, no. 11, pp. 3509, 2005.

[104] J. C. Beugnot, S. Lebrun, G. Pauliat, H. Maillotte, V. Laude, and T. Sylvestre, "Brillouin light scattering from surface acoustic waves in a subwavelength-diameter optical fiber." *Nat. Commun.* vol. **5**, pp. 5242, 2014.

[105] A. R. Chraplyvy, "Limitations on lightwave communications imposed by optical-fiber nonlinearities." *J. Light. Technol.*, vol. **8**, no. 10, pp. 1548–1557, 1990.

[106] N. Shibata, A. Yuji, T. Horiguchi, and M. Tateda, "Identification of longitudinal acoustic modes guided in the core region of a single-mode optical fiber by Brillouin gain spectra measurements." *Opt. Lett.* vol. **13**, no. 7, 595–597, 1988.

[107] P. D. Dragic, C. H. Liu, G. C. Papen, and A. Galvanauskas, "Optical fiber with an acoustic guiding layer for stimulated Brillouin scattering suppression," I*n Conference on Lasers and Electro-Optics*, Optical Society of America, p. CThZ3, 2005.

[108] V. L. Iezzi, S. Loranger, A. Harhira, R. Kashyap, M. Saad, A. Gomes, and S. Rehman, "Stimulated Brillouin scattering in multi-mode fiber for sensing applications." *In fiber and optical passive components (WFOPC)*, 7^{th} IEEE proceeding, Montreal, QC, Canada, pp. 1–4, 2011.

[109] S. Selleri, L. Vincetti, A. Cucinotta, and M. Zoboli, "Complex FEM modal solver of optical waveguides with PML boundary conditions," *Opt. Quantum Electron*, vol. **33**, no. 4, pp. 359–371, 2001.

[110] W. W. Zou, Z. Y. He, and K. Hotate,"Two-dimensional finite element modal analysis of Brillouin gain spectra in optical fibers," *IEEE Photon. Technol. Lett.*, vol. **18**, no. 21–24, pp. 2487–2489, 2006.

[111] D. Sun, J. Manges, X. Yuan and Z. Cendes, "Spurious modes in finite-element methods," in *IEEE Antennas Propag. Mag.*, vol. **37**, no. 5, pp. 12–24, 1995.

[112] A. Konrad, "Vector variational formulation of electromagnetic fields in anisotropic media," *IEEE Trans. Microwave Theory Tech.*, vol. **24**, pp. 55–559, 1976.

[113] I. C. M. Littler, L. B. Fu, E. C. Magi, D. Pudo and B. J. Eggleton, "Widely tunable, acousto-optic resonances in chalcogenide As_2Se_3 fiber," *Opt. Express*, vol. **14**, no. 18, pp. 8088–8095, 2006.

[114] Y. S. Mamdem, X. Pheron, F. Taillade, Y. Jaouen, R. Gabet, V. Lanticq, G. Moreau, A. Boukenter, Y. Ouerdane, S. Lesoille, and J. Bertrand, "Two-dimensional FEM analysis of Brillouin gain spectra in acoustic guiding and antiguiding single mode optical fibers," In COMSOL Conference, 2010.

[115] K. Ogusu and H. Li, "Brillouin-gain coefficient of chalcogenide glasses," *J. Opt. Soc. Am. B*, vol. **21**, no. 7, pp. 1302-1304, 2004.

[116] L. Tartara, C. Codemard, J. N. Maran, R. Cherif, and M. Zghal, "Full modal analysis of the Brillouin gain spectrum of an optical fiber," *Optics Communications* vol. **282**, no. 12, pp. 2431–2436, 2009.

[117] S. Virally, N. Godbout, S. Lacroix, and L. Labonte, “Two-fold symmetric geometries for tailored phasematching in birefringent solid-core air-silica microstructured fibers,” *Opt. Express* vol. **18**, pp. 10731-10741, 2010.

[118] M. Koshiba and K. Inoue, “Simple and efficient finite–element analysis of microwave and optical waveguides,” *IEEE Trans. Microwave Theory Tech.*, vol. **40**, no. 2, pp. 371–377, 1992.

[119] A. C. Bedoya, B. Morrison, M. Pagani, D. Marpaung, and B. J. Eggleton, “Tunable narrowband microwave photonic filter created by stimulated Brillouin scattering from a silicon nanowire,” *Opt. Lett.* vol. **40**, no. 17, pp. 4154-4157, 2015.

[120] R. Zhang, J. Sun, G. Chen, M. Cheng, and J. Jiang, “Demonstration of highly efficient forward stimulated Brillouin scattering in partly suspended silicon nanowire racetrack resonators,” *Appl. Phys. Lett.*, vol. **111**, no. 3, pp. 031102, 2017.

[121] R. Pant, C. G. Poulton, D. Y. Choi, H. Mcfarlane, S. Hile, E. Li, L. Thevenaz, B. L. Davies, S. J. Madden, and B. J. Eggleton, “On-chip stimulated Brillouin scattering,” *Opt. Express*, vol. **19**, no. 9, pp. 8285–8290, 2011.

[122] M. S. Kang, A. Butsch, and P. S. J. Russell, “Reconfigurable light-driven opto-acoustic isolators in photonic crystal fiber," *Nat. Photonics*, vol. **5**, pp. 549–553, 2011.

[123] B. M. A. Rahman, and M. M. Rahman, “Interactions of acoustic and optical waves in Ge-doped silica planar optical waveguide,” *Opto-Electronics and Applied Optics (IEM OPTRONIX)*, 2nd International Conference on, pp. 1–4. IEEE, 2015.

[124] C. K. Jen, C. Neron, A. Shang, K. Abe, L. Bonnell, and J. Kushibiki, “Acoustic characterization of silica glasses,” *J. Am. Ceram. Soc.*, vol. **76**, no. 3, pp. 712–716, 1993.

[125] M. J. Li, X. Chen, J. Wang, S. Gray, A. Liu, J. A. Demeritt, A. B. Ruffin, A. M. Crowley, D. T. Walton, and L. A. Zenteno, “Al/Ge co-doped large mode area fiber with high SBS threshold,” *Opt. Express*, vol. **15**, no. 13, pp. 8290–8299, 2007.

[126] F. A. Hatim, F. N. Hasoon, and S. Shaari, “Effects of nonlinear Stimulated Brillouin Scattering on performance analysis of an optical CDMA transmission system,” *Journal of Optical Communications*, vol. **30**, no. 2, pp. 104–108, 2009.

[127] J. Nagel, V. Temyanko, M. E. Likhachev, J. Dobler, A. N. Guryanov, M. Y. Salganskii, D. S. Lipatov, M. M. Bubnov, E. M. Dianov, and N. Peyghambarian, “Experimental investigation of silicate-glass-based Raman gain fibers with enhanced SBS suppression by selective transverse doping,” *J. Light. Technol.* vol. **34**, no. 3, pp. 928–942, 2016.

[128] M. D. Mermelstein, M. J. Andrejco, J. Fini, C. Headley, and D. J. DiGiovanni, “SBS suppression and acoustic management for high-power narrow-linewidth fiber lasers and amplifiers,” *Proceedings of SPIE*, vol. **7580**, pp. 75801G-1, 2010.

[129] J. W. Nicholson, J. M. Fini, A. M. DeSantolo, E. Monberg, F. DiMarcello, J. Fleming, C. Headley, D. J. DiGiovanni, S. Ghalmi, and S. Ramachandran, “A higher-order-mode Erbium-doped-fiber amplifier,” *Opt. Express*, vol. **18**, no. 17, pp. 17651–17657, 2010.

[130] J. S. Wong, W. Wong, S. Peng, J. McLaughlin, and L. Dong, "Robust single-mode propagation in optical fibers with record effective areas," *Conference on Lasers and Electro-Optics*, p. CPDB10, 2005.

[131] J. W. Nicholson, J. M. Fini, A. M. DeSantolo, X. Liu, K. Feder, P. S. Westbrook, V. R. Supradeepa, E. Monberg, F. DiMarcello, R. Ortiz, C. Headley, and D. J. DiGiovanni, "Scaling the effective area of higher-order-mode erbium-doped fiber amplifiers," *Opt. Express*, vol. **20**, no. 22, pp. 24575–24584, 2012.

[132] F. Kong, C. Dunn, J. Parsons, M.T. Kalichevsky-Dong, T. W. Hawkins, M. Jones, and L. Dong, "Large-mode-area fibers operating near single-mode regime," *Opt. Express*, vol. **24**, no. 10, pp. 10295–10301, 2016.

[133] M. Li, X. Chen, A. Liu, S. Gray, J. Wang, D. T. Walton, and L. A. Zenteno, "Limit of effective area for single-mode operation in step-index large mode area laser fibers," *J. Light. Technol.*, vol. **27**, no. 15, pp. 3010–3016, 2009.

[134] S. Wielandy, "Implications of higher-order mode content in large mode area fibers with good beam quality," *Opt. Express*, vol. **15**, no. 23, pp. 15402–15409, 2007.

[135] F. Stutzki, F. Jansen, H. J. Otto, C. Jauregui, J. Limpert, and A. Tunnermann, "Designing advanced very-large-mode-area fibers for power scaling of fiber-laser systems," *Optica*, vol. **1**, no. 4, pp. 233–242, 2014.

[136] K. Rottwitt, S. M. M. Friis, M. A. U. Castaneda, E. N. Christensen and J. G. Koefoed, "Higher order mode optical fiber Raman amplifiers," 18^{th} *International Conference on Transparent Optical Networks*, 2016.

[137] A. Argyros, R. Lwin, and M. C. J. Large, "Bend loss in highly multimode fibres," *Opt. Express*, vol. **16**, no, 23, pp. 18590–18598, 2008.

[138] A. Gulistan, S. Ghosh, S. Ramachandran, and B. M. A. Rahman, "Efficient strategy to increase higher order inter-modal stability of a step index multimode fiber," *Opt. Express*, vol. **25**, no. 24, pp. 29714–29723, 2017.

[139] V. Rastogi and K. S. Chiang, "Analysis of segmented-cladding fiber by the radial-effective-index method," *J. Opt. Soc. Am. B*, vol. **21**, no. 2, pp. 258–265, 2004.

[140] A. Kumar, V. Rastogi, A. Agrawal, and B. M. A. Rahman, "Birefringence analysis of segmented cladding fiber," *Appl. Opt.,* vol. **51**, no. 15, pp. 3104–3108, 2012.

[141] B. M. A. Rahman and J. B. Davies, "Vector–H finite element soluion of GaAs/GaAlAs rib waveguides," *IEE Proceedings J-Optoelectronics*, vol. **132**, no. 6, pp. 349–353, 1985.

[142] M. R. Karim, B. M. A. Rahman, and G. P. Agrawal, "Dispersion engineered $Ge_{11.5}As_{24}Se_{64.5}$ nanowire for supercontinuum generation: A parametric study," *Opt. Express*, vol. **22**, no. 25, pp. 31029–31040, 2014.

[143] N. Lindlein, G. Leuchs, and S. Ramachandran, "Achieving Gaussian outputs from large-mode-area higher-order-mode fibers," *Appl. Opt.*, vol. **46**, no. 22, pp. 5147–5157, 2007.

[144] C. M. Rollinson, S. T. Huntington, B. C. Gibson, S. Rubanov, and J. Canning, "Characterization of nanoscale features in tapered fractal and photonic crystal fibers", *Opt. Express*, vol. **19**, no. 3, pp. 1860–1865, 2011.

[145] Y. Ruan, H. Ebendorff-Heidepriem, S. Afshar, and T. M. Monro, "Light confinement within nanoholes in nanostructured optical fibers", *Opt. Express*, vol. **18**, no. 25, pp. 26018-26026, 2010.

[146] A. Gulistan, S. Ghosh, S. Ramachandran, and B. M. A. Rahman. "Enhancing mode stability of higher order modes in a multimode fiber." *In Specialty Optical Fibers*, pp. SoW2H-7. Optical Society of America, 2018.

[147] R. S. Windeler, "Microstructure Fibers", *Encyclopedia of Modern Optics*, Academic Press 195, 2018.

[148] D. Pysz, I. Kujawa, R. Stepien, M. Klimczak, A. Filipkowski, M. Franczyk, L. Kociszewski, J. Buzniak, K. Harasny, and R. Buczyński, "Stack and draw fabrication of soft glass microstructured fiber optics." *Bulletin of the Polish Academy of Sciences Technical Sciences*, vol. **62**, no. 4, pp. 667-682, 2014.

[149] R. J. Essiambre, G. Kramer, P. J. Winzer, G. J. Foschini and B. Goebel, "Capacity limits of optical fiber networks," *J. Light. Technol.*, vol. **28**, no. 4, pp. 662–701 2010.

[150] M. Secondini and E. Forestieri, "Scope and Limitations of the Nonlinear Shannon Limit," *J. Light. Technol.*, vol. **35**, no. 4, pp. 893–902, 2017.

[151] B. Franz, and H. Bulow, "Mode group division multiplexing in graded–index multimode fibers," *Bell Labs Tech. J.* vol. **18**, no. 3, pp. 153–172, 2013.

[152] R. Maruyama, N. Kuwaki, S. Matsuo and M. Ohashi, "Relationship between modecrosstalk and fiber characteristics in few mode fibers," *Optical Fiber Communications Conference and Exhibition (OFC), Anaheim*, CA 1–3, 2016.

[153] F. Yaman, E. Mateo, and T. Wang, "Impact of modal crosstalk and multi-path interference on few-mode fiber transmission," *Optical Fiber Communication Conference (OFC)*, p. OTu1D.2, 2012.

[154] R. Ryf, S. Randel, A. H. Gnauck, C. Bolle, A. Sierra, S. Mumtaz, M. Esmaeelpour, E. C. Burrows, R. J. Essiambre, P. J. Winzer, and D. W. Peckham, "Mode-Division Multiplexing over 96 km of few-mode fiber using coherent 6×6 MIMO processing," *J. Light. Technol.*, vol. **30**, no. 4, pp. 521–531, 2012.

[155] Y. Kokubun, T. Watanabe, S. Miura, and R.Kawata, "What is a mode in few mode fibers?: Proposal of MIMO-free mode division multiplexing using true eigenmodes," *IEICE Electronics Express*, vol. **13**, no. 18, 2016.

[156] T. Mori, T. Sakamoto, M. Wada, T. Yamamoto, and F. Yamamoto, "Few-Mode fibers supporting more than two LP modes for Mode-Division-Multiplexed transmission with MIMO DSP," *J. Light. Technol.*, vol. **32**, no. 14, pp. 2468–2479, 2014.

[157] J. Liang, Q. Mo, S. Fu, M. Tang, P. Shum, and D. Liu, "Design and fabrication of elliptical-core few-mode fiber for MIMO-less data transmission," *Opt. Lett.*, vol. **41**, no. 13, pp. 3058–3061, 2016.

[158] R. A. May, and M. N. Zervas, "Few-mode fibers with improved mode spacing," *IEEE Optical Communication (ECOC)*, pp. 1–3, 2015.

[159] P. Sillard, M. Astruc, D. Boivin, H. Maerten, and L. Provost, "Few-Mode Fiber for uncoupled Mode-Division Multiplexing transmissions," *37th European Conference and Exposition on Optical Communications, OSA Technical Digest (CD)*, p. Tu.5.LeCervin.7, 2011.

[160] J. W. Nicholson, J. M. Fini, A. D. Yablon, P. S. Westbrook, K. Feder, and C. Headley, "Demonstration of bend-induced nonlinearities in large-mode-area fibers," *Opt. Lett.*, vol. **32**, no. 17, pp. 2562–2564, 2007.

[161] S. Ghosh, "Design and Optimisation of Integrated Photonic Waveguides and Sensors," PhD dissertation, City, University of London, 2018.

Appendix A

2D FV-FEM: calculations of matrix elements [161]

A.1 Evaluation of $[Q]$ Matrix

Equation 4.19 shows that the $[Q]$ is a product of $[\vec{\nabla}\times]$ and the shape function $[N]$. Hence,

$$[Q] = \begin{bmatrix} 0 & -\frac{\partial}{\partial z} & \frac{\partial}{\partial y} \\ \frac{\partial}{\partial z} & 0 & -\frac{\partial}{\partial x} \\ -\frac{\partial}{\partial y} & \frac{\partial}{\partial x} & 0 \end{bmatrix} [N] \tag{A.1}$$

where

$$[\vec{\nabla}\times] = \begin{bmatrix} 0 & -\frac{\partial}{\partial z} & \frac{\partial}{\partial y} \\ \frac{\partial}{\partial z} & 0 & -\frac{\partial}{\partial x} \\ -\frac{\partial}{\partial y} & \frac{\partial}{\partial x} & 0 \end{bmatrix} \tag{A.2}$$

and, the shape function is

$$[N] = \begin{bmatrix} N_1 & N_2 & N_3 & 0 & 0 & 0 & 0 & 0 & 0 \\ 0 & 0 & 0 & N_1 & N_2 & N_3 & 0 & 0 & 0 \\ 0 & 0 & 0 & 0 & 0 & 0 & jN_1 & jN_2 & jN_3 \end{bmatrix} \tag{A.3}$$

The j term in the shape function matrix is introduced for lossless cases where the H_z component is 90° out of phase with the transverse components. Equation A.1 then becomes

$$[Q] = \begin{bmatrix} 0 & -\frac{\partial}{\partial z} & \frac{\partial}{\partial y} \\ \frac{\partial}{\partial z} & 0 & -\frac{\partial}{\partial x} \\ -\frac{\partial}{\partial y} & \frac{\partial}{\partial x} & 0 \end{bmatrix}_{3\times3} \begin{bmatrix} N_1 & N_2 & N_3 & 0 & 0 & 0 & 0 & 0 & 0 \\ 0 & 0 & 0 & N_1 & N_2 & N_3 & 0 & 0 & 0 \\ 0 & 0 & 0 & 0 & 0 & 0 & jN_1 & jN_2 & jN_3 \end{bmatrix}_{3\times9} \tag{A.4}$$

or,

$$[Q] = \begin{bmatrix} 0 & 0 & 0 & -\frac{\partial N_1}{\partial z} & -\frac{\partial N_2}{\partial z} & -\frac{\partial N_3}{\partial z} & j\frac{\partial N_1}{\partial y} & j\frac{\partial N_2}{\partial y} & j\frac{\partial N_3}{\partial y} \\ \frac{\partial N_1}{\partial z} & \frac{\partial N_2}{\partial z} & \frac{\partial N_3}{\partial z} & 0 & 0 & 0 & -j\frac{\partial N_1}{\partial x} & -j\frac{\partial N_2}{\partial x} & -j\frac{\partial N_3}{\partial x} \\ -\frac{\partial N_1}{\partial y} & -\frac{\partial N_2}{\partial y} & -\frac{\partial N_3}{\partial y} & \frac{\partial N_1}{\partial x} & \frac{\partial N_2}{\partial x} & \frac{\partial N_3}{\partial x} & 0 & 0 & 0 \end{bmatrix}_{3\times9} \tag{A.5}$$

Assuming the wave propagation in z-direction, the operator $\frac{\partial}{\partial z}$ can be replaced by $-j\beta$ in Eq. A.5. Thus, the coefficients of $[Q]$ matrix can be obtained as follows

$$[Q] = \begin{bmatrix} 0 & 0 & 0 & j\beta N_1 & j\beta N_2 & j\beta N_3 & j\frac{\partial N_1}{\partial y} & j\frac{\partial N_2}{\partial y} & j\frac{\partial N_3}{\partial y} \\ -j\beta N_1 & -j\beta N_2 & -j\beta N_3 & 0 & 0 & 0 & -j\frac{\partial N_1}{\partial x} & -j\frac{\partial N_2}{\partial x} & -j\frac{\partial N_3}{\partial x} \\ -\frac{\partial N_1}{\partial y} & -\frac{\partial N_2}{\partial y} & -\frac{\partial N_3}{\partial y} & \frac{\partial N_1}{\partial x} & \frac{\partial N_2}{\partial x} & \frac{\partial N_3}{\partial x} & 0 & 0 & 0 \end{bmatrix}_{3\times9} \tag{A.6}$$

Similarly, $[Q]^*$ can be obtained as:

$$[Q]^* = \begin{bmatrix} 0 & j\beta N_1 & -\frac{\partial N_1}{\partial y} \\ 0 & j\beta N_2 & -\frac{\partial N_2}{\partial y} \\ 0 & j\beta N_3 & -\frac{\partial N_3}{\partial y} \\ -j\beta N_1 & 0 & \frac{\partial N_1}{\partial x} \\ -j\beta N_2 & 0 & \frac{\partial N_2}{\partial x} \\ -j\beta N_3 & 0 & \frac{\partial N_3}{\partial x} \\ -j\frac{\partial N_1}{\partial y} & j\frac{\partial N_1}{\partial x} & 0 \\ -j\frac{\partial N_2}{\partial y} & j\frac{\partial N_2}{\partial x} & 0 \\ -j\frac{\partial N_3}{\partial y} & j\frac{\partial N_3}{\partial x} & 0 \end{bmatrix}_{9\times 3} \tag{A.7}$$

where

$$\frac{\partial [N]}{\partial x} = \begin{bmatrix} b_1 & b_2 & b_3 \end{bmatrix} \tag{A.8}$$

and

$$\frac{\partial [N]}{\partial y} = \begin{bmatrix} c_1 & c_2 & c_3 \end{bmatrix} \tag{A.9}$$

These partial differentiations have been evaluated from Eqs. 4.3 and 4.6.

A.2 Evaluation of $[A]_e$ and $[B]_e$ Matrix

$[A]_e$ element matrix from Eq. 4.28 can be evaluated based on $[Q]$ and $[Q]_e$ as

$$[A]_e = \hat{\varepsilon}_r^{-1} \int_A [Q]^* \cdot [Q] \, dA \tag{A.10}$$

$$= \hat{\varepsilon}_r^{-1} \int_A \begin{bmatrix} \beta^2 [N]^T [N] + \frac{\partial [N]^T}{\partial y} \frac{\partial [N]}{\partial y} & -\frac{\partial [N]^T}{\partial y} \frac{\partial [N]}{\partial x} & \beta [N]^T \frac{\partial [N]}{\partial x} \\ -\frac{\partial [N]^T}{\partial x} \frac{\partial [N]}{\partial y} & \beta^2 [N]^T [N] + \frac{\partial [N]^T}{\partial x} \frac{\partial [N]}{\partial x} & \beta [N]^T \frac{\partial [N]}{\partial y} \\ \beta [N] \frac{\partial [N]^T}{\partial x} & \beta [N] \frac{\partial [N]^T}{\partial y} & \frac{\partial [N]^T}{\partial y} \frac{\partial [N]}{\partial y} + \frac{\partial [N]^T}{\partial x} \frac{\partial [N]}{\partial x} \end{bmatrix} dA \tag{A.11}$$

here $dA = dxdy$ defines the area integration over the surface.

$[B]_e$ element matrix based on $[N]$ and $[N]^T$ (Eq. 4.29) can be obtained as

$$[B]_e = \hat{\mu}_r \int_A [N]^T \cdot [N] \, dA \tag{A.12}$$

$$= \hat{\mu}_r \int_A \begin{bmatrix} [N]^T [N] & [0] & [0] \\ [0] & [N]^T [N] & [0] \\ [0] & [0] & [N]^T [N] \end{bmatrix} dA \tag{A.13}$$

(A.14)

or,

$$[B]_e = \hat{\mu}_r \int_A \begin{bmatrix} N_1^2 & N_1N_2 & N_1N_3 & 0 & 0 & 0 & 0 & 0 & 0 \\ N_2N_1 & N_2^2 & N_2N_3 & 0 & 0 & 0 & 0 & 0 & 0 \\ N_3N_1 & N_3N_2 & N_3^2 & 0 & 0 & 0 & 0 & 0 & 0 \\ 0 & 0 & 0 & N_1^2 & N_1N_2 & N_1N_3 & 0 & 0 & 0 \\ 0 & 0 & 0 & N_2N_1 & N_2^2 & N_2N_3 & 0 & 0 & 0 \\ 0 & 0 & 0 & N_3N_1 & N_3N_2 & N_3^2 & 0 & 0 & 0 \\ 0 & 0 & 0 & 0 & 0 & 0 & N_1^2 & N_1N_2 & N_1N_3 \\ 0 & 0 & 0 & 0 & 0 & 0 & N_2N_1 & N_2^2 & N_2N_3 \\ 0 & 0 & 0 & 0 & 0 & 0 & N_3N_1 & N_3N_2 & N_3^2 \end{bmatrix} dA \tag{A.15}$$

As the linear triangular element has straight sides, a constant Jacobian, we can apply the numerical Gaussian quadrature integration. The exact expression of numerical integration for linear triangular element is

$$\int_A N_1^i N_2^j N_3^k \, dA = \frac{i!\,j!\,k!\,2!}{(i+j+k+2)!} A_e \tag{A.16}$$

here A_e signifies the area of the triangular element.

Therefore, the numerical integration of different forms can be obtained as

$$\int_A N_1^2 \, dA = \int_A N_2^2 \, dA = \int_A N_3^2 \, dA = \frac{A_e}{6} \tag{A.17}$$

$$\int_A N_1N_2 \, dA = \int_A N_2N_3 \, dA = \int_A N_1N_3 \, dA = \frac{A_e}{12} \tag{A.18}$$

and

$$\int_A dA \;=\; A_e \tag{A.19}$$

Therefore, with the help of Eqs. A.8 and A.9, some of the matrix elements of $[A]_e$ (Eq. A.11) matrix can be obtained as

$$[A_{1,1}]_e \;=\; \hat{\varepsilon}^{-1}\int_A \left(\beta^2 N_1^2 + \left(\frac{\partial N_1}{\partial y}\right)^2\right) dA \;=\; \frac{1}{\varepsilon}\left[\frac{\beta^2 A_e}{6} + c_1^2 A_e\right] \tag{A.20}$$

$$[A_{1,2}]_e \;=\; \hat{\varepsilon}^{-1}\int_A \left(\beta^2 N_1 N_2 + \frac{\partial N_1}{\partial y}\frac{\partial N_2}{\partial y}\right) dA \;=\; \frac{1}{\varepsilon}\left[\frac{\beta^2 A_e}{12} + c_1 c_2 A_e\right] \tag{A.21}$$

$$[A_{1,3}]_e \;=\; \hat{\varepsilon}^{-1}\int_A \left(\beta^2 N_1 N_3 + \frac{\partial N_1}{\partial y}\frac{\partial N_3}{\partial y}\right) dA \;=\; \frac{1}{\varepsilon}\left[\frac{\beta^2 A_e}{12} + c_1 c_3 A_e\right] \tag{A.22}$$

$$[A_{1,4}]_e \;=\; -\hat{\varepsilon}^{-1}\int_A \left(\frac{\partial N_1}{\partial x}\frac{\partial N_1}{\partial y}\right) dA \;=\; -\frac{1}{\varepsilon} b_1 c_1 A_e \tag{A.23}$$

$$[A_{1,5}]_e \;=\; -\hat{\varepsilon}^{-1}\int_A \left(\frac{\partial N_2}{\partial x}\frac{\partial N_1}{\partial y}\right) dA \;=\; -\frac{1}{\varepsilon} b_2 c_1 A_e \tag{A.24}$$

$$[A_{1,6}]_e \;=\; -\hat{\varepsilon}^{-1}\int_A \left(\frac{\partial N_3}{\partial x}\frac{\partial N_1}{\partial y}\right) dA \;=\; -\frac{1}{\varepsilon} b_3 c_1 A_e \tag{A.25}$$

and so on.

In a similar fashion, the $[B]_e$ matrix shown in Eq. A.15 can be written as

$$[B]_e = \hat{\mu}_r \begin{bmatrix} \frac{A_e}{6} & \frac{A_e}{12} & \frac{A_e}{12} & 0 & 0 & 0 & 0 & 0 & 0 \\ \frac{A_e}{12} & \frac{A_e}{6} & \frac{A_e}{12} & 0 & 0 & 0 & 0 & 0 & 0 \\ \frac{A_e}{12} & \frac{A_e}{12} & \frac{A_e}{6} & 0 & 0 & 0 & 0 & 0 & 0 \\ 0 & 0 & 0 & \frac{A_e}{6} & \frac{A_e}{12} & \frac{A_e}{12} & 0 & 0 & 0 \\ 0 & 0 & 0 & \frac{A_e}{12} & \frac{A_e}{6} & \frac{A_e}{12} & 0 & 0 & 0 \\ 0 & 0 & 0 & \frac{A_e}{12} & \frac{A_e}{12} & \frac{A_e}{6} & 0 & 0 & 0 \\ 0 & 0 & 0 & 0 & 0 & 0 & \frac{A_e}{6} & \frac{A_e}{12} & \frac{A_e}{12} \\ 0 & 0 & 0 & 0 & 0 & 0 & \frac{A_e}{12} & \frac{A_e}{6} & \frac{A_e}{12} \\ 0 & 0 & 0 & 0 & 0 & 0 & \frac{A_e}{12} & \frac{A_e}{12} & \frac{A_e}{6} \end{bmatrix} \tag{A.26}$$

Appendix B

Calculations for penalty term in acoustic modal solution

$$PenaltyTerm = \alpha \int (\nabla \times U)^* \cdot (\nabla \times U) dA \tag{B.1}$$

$$\vec{U} = [N]\{U\}_e$$

$$\vec{U} = \begin{bmatrix} N_1 & 0 & 0 & N_2 & 0 & 0 & N_3 & 0 & 0 \\ 0 & N_1 & 0 & 0 & N_2 & 0 & 0 & N_3 & 0 \\ 0 & 0 & N_3 & 0 & 0 & N_2 & 0 & 0 & N_3 \end{bmatrix} \begin{bmatrix} U_{x1} \\ U_{y1} \\ U_{z1} \\ U_{x2} \\ U_{y2} \\ U_{z2} \\ U_{x3} \\ U_{y3} \\ U_{z3} \end{bmatrix}$$

$$(\vec{\nabla} \times \vec{U}) = \vec{\nabla} \times [N]\{U\}_e \tag{B.2}$$

$$(\vec{\nabla} \times \vec{U}) = \begin{bmatrix} 0 & -\frac{\partial}{\partial z} & \frac{\partial}{\partial y} \\ \frac{\partial}{\partial z} & 0 & -\frac{\partial}{\partial x} \\ -\frac{\partial}{\partial y} & \frac{\partial}{\partial x} & 0 \end{bmatrix} [N]\{U\}_e$$

or

$$M = \begin{bmatrix} 0 & -\frac{\partial}{\partial z} & \frac{\partial}{\partial y} \\ \frac{\partial}{\partial z} & 0 & -\frac{\partial}{\partial x} \\ -\frac{\partial}{\partial y} & \frac{\partial}{\partial x} & 0 \end{bmatrix}$$

and equation B.2 can be written as

$$(\vec{\nabla} \times \vec{U}) = [M][N]\{U\}_e \tag{B.3}$$

Now

$$[P] = [M][N]$$

$$[P] = \begin{bmatrix} 0 & -\frac{\partial}{\partial z} & \frac{\partial}{\partial y} \\ \frac{\partial}{\partial z} & 0 & -\frac{\partial}{\partial x} \\ -\frac{\partial}{\partial y} & \frac{\partial}{\partial x} & 0 \end{bmatrix} \begin{bmatrix} N_1 & 0 & 0 & N_2 & 0 & 0 & N_3 & 0 & 0 \\ 0 & N_1 & 0 & 0 & N_2 & 0 & 0 & N_3 & 0 \\ 0 & 0 & N_3 & 0 & 0 & N_2 & 0 & 0 & N_3 \end{bmatrix}$$

$$[P] = \begin{bmatrix} 0 & -\frac{\partial N_1}{\partial z} & \frac{\partial N_1}{\partial y} & 0 & -\frac{\partial N_2}{\partial z} & \frac{\partial N_2}{\partial y} & 0 & -\frac{\partial N_3}{\partial z} & \frac{\partial N_3}{\partial y} \\ \frac{\partial N_1}{\partial z} & 0 & -\frac{\partial N_1}{\partial x} & \frac{\partial N_2}{\partial z} & 0 & -\frac{\partial N_2}{\partial x} & \frac{\partial N_3}{\partial z} & 0 & -\frac{\partial N_3}{\partial x} \\ -\frac{\partial N_1}{\partial y} & \frac{\partial N_1}{\partial x} & 0 & -\frac{\partial N_2}{\partial y} & \frac{\partial N_2}{\partial x} & 0 & -\frac{\partial N_3}{\partial y} & \frac{\partial N_3}{\partial x} & 0 \end{bmatrix}$$

Updated equation B.3 can be written as

$$(\vec{\nabla} \times \vec{U}) = [P]\{U\}_e \tag{B.4}$$

Now taking transpose of equation B.4

$$(\vec{\nabla} \times \vec{U})^T = ([P]\{U\}_e)^T$$

$$(\vec{\nabla} \times \vec{U})^T = ([P]\{U\}_e)^T = \{U\}_e^T [P]^T \tag{B.5}$$

Now the main equation (B.1) can be written as,

$$\int_A (\vec{\nabla} \times \vec{U})^T . (\vec{\nabla} \times \vec{U}) dA = \int_A \{u\}_e^T [P]^T [P]\{u\}_e dA \tag{B.6}$$

here, for simplicity, $[R] = [P]^T [P]$ is considered

$$[R] = [P]^T [P]$$

$$[R] = \begin{bmatrix} 0 & \frac{\partial N_1}{\partial z} & -\frac{\partial N_1}{\partial y} \\ -\frac{\partial N_1}{\partial z} & 0 & \frac{\partial N_1}{\partial x} \\ \frac{\partial N_1}{\partial y} & -\frac{\partial N_1}{\partial x} & 0 \\ 0 & \frac{\partial N_2}{\partial z} & -\frac{\partial N_2}{\partial y} \\ -\frac{\partial N_2}{\partial z} & 0 & \frac{\partial N_2}{\partial x} \\ \frac{\partial N_2}{\partial y} & -\frac{\partial N_2}{\partial x} & 0 \\ 0 & \frac{\partial N_3}{\partial z} & -\frac{\partial N_3}{\partial y} \\ -\frac{\partial N_3}{\partial z} & 0 & \frac{\partial N_3}{\partial x} \\ \frac{\partial N_3}{\partial y} & -\frac{\partial N_3}{\partial x} & 0 \end{bmatrix} \begin{bmatrix} 0 & -\frac{\partial N_1}{\partial z} & \frac{\partial N_1}{\partial y} & 0 & -\frac{\partial N_2}{\partial z} & \frac{\partial N_2}{\partial y} & 0 & -\frac{\partial N_3}{\partial z} & \frac{\partial N_3}{\partial y} \\ \frac{\partial N_1}{\partial z} & 0 & -\frac{\partial N_1}{\partial x} & \frac{\partial N_2}{\partial z} & 0 & -\frac{\partial N_2}{\partial x} & \frac{\partial N_3}{\partial z} & 0 & -\frac{\partial N_3}{\partial x} \\ -\frac{\partial N_1}{\partial y} & \frac{\partial N_1}{\partial x} & 0 & -\frac{\partial N_2}{\partial y} & \frac{\partial N_2}{\partial x} & 0 & -\frac{\partial N_3}{\partial y} & \frac{\partial N_3}{\partial x} & 0 \end{bmatrix}$$

$$
\begin{bmatrix}
(\frac{\partial N_1}{\partial z})^2+(\frac{\partial N_1}{\partial y})^2 & (-\frac{\partial N_1}{\partial x}\frac{\partial N1}{\partial y}) & (-\frac{\partial N_1}{\partial z}\frac{\partial N_1}{\partial x}) & (\frac{\partial N_1}{\partial z}\frac{\partial N_2}{\partial z}+\frac{\partial N_1}{\partial y}\frac{\partial N_2}{\partial y}) & (-\frac{\partial N_1}{\partial y}\frac{\partial N_2}{\partial x}) & (-\frac{\partial N_1}{\partial z}\frac{\partial N_2}{\partial x}) & (\frac{\partial N_1}{\partial z}\frac{\partial N_3}{\partial z}+\frac{\partial N_1}{\partial y}\frac{\partial N_3}{\partial y}) & (-\frac{\partial N_1}{\partial y}\frac{\partial N_3}{\partial x}) & (-\frac{\partial N_1}{\partial z}\frac{\partial N_3}{\partial x}) \\
(-\frac{\partial N_1}{\partial x}\frac{\partial N_1}{\partial y}) & (\frac{\partial N_1}{\partial z})^2+(\frac{\partial N_1}{\partial x})^2 & (-\frac{\partial N_1}{\partial z}\frac{\partial N_1}{\partial y}) & (-\frac{\partial N_1}{\partial x}\frac{\partial N_2}{\partial y}) & (\frac{\partial N_1}{\partial z}\frac{\partial N_2}{\partial z}+\frac{\partial N_1}{\partial x}\frac{\partial N_2}{\partial x}) & (-\frac{\partial N_1}{\partial y}\frac{\partial N_2}{\partial z}) & (-\frac{\partial N_1}{\partial x}\frac{\partial N_3}{\partial y}) & (\frac{\partial N_1}{\partial z}\frac{\partial N_3}{\partial z}+\frac{\partial N_1}{\partial x}\frac{\partial N_3}{\partial x}) & (-\frac{\partial N_1}{\partial y}\frac{\partial N_3}{\partial z}) \\
(-\frac{\partial N_1}{\partial x}\frac{\partial N_1}{\partial z}) & (-\frac{\partial N_1}{\partial y}\frac{\partial N_1}{\partial z}) & (\frac{\partial N_1}{\partial y})^2+(\frac{\partial N_1}{\partial y})^2 & (-\frac{\partial N_1}{\partial x}\frac{\partial N_2}{\partial z}) & (-\frac{\partial N_1}{\partial y}\frac{\partial N_2}{\partial z}) & (\frac{\partial N_1}{\partial y}\frac{\partial N_2}{\partial y}+\frac{\partial N_1}{\partial x}\frac{\partial N_2}{\partial x}) & (-\frac{\partial N_1}{\partial x}\frac{\partial N_3}{\partial z}) & (-\frac{\partial N_1}{\partial y}\frac{\partial N_3}{\partial z}) & (\frac{\partial N_1}{\partial y}\frac{\partial N_3}{\partial y}+\frac{\partial N_1}{\partial x}\frac{\partial N_3}{\partial x}) \\
(\frac{\partial N_1}{\partial z}\frac{\partial N_2}{\partial z}+\frac{\partial N_1}{\partial y}\frac{\partial N_2}{\partial y}) & (-\frac{\partial N_1}{\partial x}\frac{\partial N_2}{\partial y}) & (-\frac{\partial N_1}{\partial x}\frac{\partial N_2}{\partial z}) & (\frac{\partial N_2}{\partial z})^2+(\frac{\partial N_2}{\partial y})^2 & (-\frac{\partial N_2}{\partial y}\frac{\partial N_2}{\partial x}) & (-\frac{\partial N_2}{\partial z}\frac{\partial N_2}{\partial x}) & (\frac{\partial N_2}{\partial z}\frac{\partial N_3}{\partial z}+\frac{\partial N_2}{\partial y}\frac{\partial N_3}{\partial y}) & (-\frac{\partial N_2}{\partial x}\frac{\partial N_3}{\partial y}) & (-\frac{\partial N_2}{\partial x}\frac{\partial N_3}{\partial x}) \\
(-\frac{\partial N_1}{\partial y}\frac{\partial N_2}{\partial x}) & (\frac{\partial N_1}{\partial z}\frac{\partial N_2}{\partial z}+\frac{\partial N_1}{\partial x}\frac{\partial N_2}{\partial x}) & (-\frac{\partial N_1}{\partial y}\frac{\partial N_2}{\partial z}) & (-\frac{\partial N_2}{\partial y}\frac{\partial N_2}{\partial x}) & (\frac{\partial N_2}{\partial z})^2+(\frac{\partial N_2}{\partial x})^2 & (-\frac{\partial N_2}{\partial z}\frac{\partial N_2}{\partial y}) & (-\frac{\partial N_2}{\partial y}\frac{\partial N_3}{\partial x}) & (\frac{\partial N_2}{\partial z}\frac{\partial N_3}{\partial z}+\frac{\partial N_2}{\partial x}\frac{\partial N_3}{\partial x}) & (-\frac{\partial N_2}{\partial z}\frac{\partial N_3}{\partial y}) \\
(-\frac{\partial N_1}{\partial z}\frac{\partial N_2}{\partial x}) & (-\frac{\partial N_1}{\partial z}\frac{\partial N_2}{\partial y}) & (\frac{\partial N_1}{\partial y}\frac{\partial N_2}{\partial z}+\frac{\partial N_1}{\partial x}\frac{\partial N_2}{\partial x}) & (-\frac{\partial N_2}{\partial z}\frac{\partial N_2}{\partial y}) & (-\frac{\partial N_2}{\partial z}\frac{\partial N_2}{\partial x}) & (\frac{\partial N_2}{\partial y})^2+(\frac{\partial N_2}{\partial x})^2 & (-\frac{\partial N_2}{\partial z}\frac{\partial N_3}{\partial y}) & (-\frac{\partial N_2}{\partial z}\frac{\partial N_3}{\partial x}) & (\frac{\partial N_2}{\partial y}\frac{\partial N_3}{\partial y}+\frac{\partial N_2}{\partial x}\frac{\partial N_3}{\partial x}) \\
(\frac{\partial N_1}{\partial z}\frac{\partial N_3}{\partial z}+\frac{\partial N_1}{\partial y}\frac{\partial N_3}{\partial y}) & (-\frac{\partial N_1}{\partial x}\frac{\partial N_3}{\partial y}) & (-\frac{\partial N_1}{\partial x}\frac{\partial N_3}{\partial z}) & (\frac{\partial N_2}{\partial z}\frac{\partial N_3}{\partial z}+\frac{\partial N_2}{\partial y}\frac{\partial N_3}{\partial y}) & (-\frac{\partial N_2}{\partial x}\frac{\partial N_3}{\partial y}) & (-\frac{\partial N_2}{\partial x}\frac{\partial N_3}{\partial z}) & (\frac{\partial N_3}{\partial z})^2+(\frac{\partial N_3}{\partial y})^2 & (-\frac{\partial N_3}{\partial y}\frac{\partial N_3}{\partial x}) & (-\frac{\partial N_3}{\partial z}\frac{\partial N_3}{\partial x}) \\
(-\frac{\partial N_1}{\partial y}\frac{\partial N_3}{\partial x}) & (\frac{\partial N_1}{\partial z}\frac{\partial N_3}{\partial z}+\frac{\partial N_1}{\partial x}\frac{\partial N_3}{\partial x}) & (-\frac{\partial N_1}{\partial y}\frac{\partial N_3}{\partial z}) & (-\frac{\partial N_2}{\partial y}\frac{\partial N_3}{\partial x}) & (\frac{\partial N_2}{\partial z}\frac{\partial N_3}{\partial z}+\frac{\partial N_2}{\partial x}\frac{\partial N_3}{\partial x}) & (-\frac{\partial N_2}{\partial z}\frac{\partial N_3}{\partial y}) & (-\frac{\partial N_3}{\partial y}\frac{\partial N_3}{\partial x}) & (\frac{\partial N_3}{\partial z}\frac{\partial N_3}{\partial z}+\frac{\partial N_3}{\partial x}\frac{\partial N_3}{\partial x}) & (-\frac{\partial N_3}{\partial z}\frac{\partial N_3}{\partial y}) \\
(-\frac{\partial N_1}{\partial z}\frac{\partial N_3}{\partial x}) & (-\frac{\partial N_1}{\partial z}\frac{\partial N_3}{\partial y}) & (\frac{\partial N_1}{\partial y}\frac{\partial N_3}{\partial z}+\frac{\partial N_1}{\partial x}\frac{\partial N_3}{\partial x}) & (-\frac{\partial N_2}{\partial z}\frac{\partial N_3}{\partial x}) & (-\frac{\partial N_2}{\partial z}\frac{\partial N_3}{\partial y}) & (\frac{\partial N_2}{\partial y}\frac{\partial N_3}{\partial y}+\frac{\partial N_2}{\partial x}\frac{\partial N_3}{\partial x}) & (-\frac{\partial N_3}{\partial z}\frac{\partial N_3}{\partial x}) & (-\frac{\partial N_3}{\partial z}\frac{\partial N_3}{\partial y}) & (\frac{\partial N_3}{\partial y})^2+(\frac{\partial N_3}{\partial x})^2
\end{bmatrix}
\tag{B.7}
$$

Equation B.6 can be written as

$$\int_A (\vec{\nabla} \times \vec{U})^T . (\vec{\nabla} \times \vec{U}) dA = \int_A \{U\}_e^T [R] \{U\}_e dA \tag{B.8}$$

N matrix equations

$$\begin{aligned} N_1 &= a_1 + b_1 x + c_1 y \\ N_2 &= a_2 + b_2 x + c_2 y \\ N_3 &= a_3 + b_3 x + c_3 y \end{aligned} \tag{B.9}$$

$$\frac{\partial}{\partial z}(e^{-ikz}) = ik \tag{B.10}$$

Now solving the derivatives in [R] matrix by using equations (B.9) and (B.10)

$$[R] = \begin{bmatrix} (-k^2N_1^2 + c_1^2) & (-b_1c_1) & (ikN_1b_1) & (-k^2N_2N_1 + c_1c_2) & (-c_1b_2) & (ikN_1b_2) & (-k^2N_1N_3 + c_1c_3) & (-c_1b_3) & (ikN_1b_3) \\ (-b_1c_1) & (-k^2N_1^2 + b_1^2) & (ikN_1c_1) & (-b_1c_2) & (-k^2N_1N_2 + b_1b_2) & (ikN_1c_2) & (-b_1c_3) & (-k^2N_1N_3 + b_1b_3) & (ikN_1c_3) \\ (ikN_1b_1) & (ikN_1c_1) & (c_1^2 + b_1^2) & (ikb_1N_2) & (ikc_1N_2) & (c_1c_2 + b_1b_2) & (ikb_1N_3) & (ikc_2N_3) & (c_1c_3 + b_1b_3) \\ (-k^2N_2N_1 + c_1c_2) & (-b_1c_2) & (ikb_1N_2) & (-k^2N_2^2 + c_2^2) & (-c_2b_2) & (ikN_2b_2) & (-k^2N_2N_3 + c_2c_3) & (-c_2b_3) & (ikb_3N_2) \\ (-c_1b_2) & (-k^2N_1N_2 + b_1b_2) & (ikN_2c_1) & (-c_2b_2) & (-k^2N_2^2 + b_2^2) & (ikN_2c_2) & (-b_2c_3) & (-k^2N_2N_3 + b_2b_3) & (ikN_2c_3) \\ (ikN_1b_2) & (ikN_1c_2) & (c_1c_2 + b_1b_2) & (ikN_2b_2) & (ikN_2c_2) & (c_2^2 + b_2^2) & (ikN_3b_2) & (ikN_3c_2) & (c_2c_3 + b_1b_3) \\ (-k^2N_1N_3 + c_1c_3) & (-b_1c_3) & (ikN_3b_1) & (-k^2N_2N_3 + c_2c_3) & (-b_2c_3) & (ikN_3b_2) & (-k^2N_3^2 + c_3^2) & (-c_3b_3) & (-ikN_3b_3) \\ (-c_1b_3) & (-k^2N_1N_3 + b_1b_3) & (ikN_3c_2) & (-c_2b_3) & (-k^2N_2N_3 + b_2b_3) & (ikN_3c_2) & (-c_3b_3) & (-k^2N_3^2 + b_3^2) & (ikN_3c_3) \\ (ikN_1b_3) & (ikN_1c_3) & (c_1c_3 + b_1b_3) & (ikN_2b_3) & (ikN_2c_3) & (c_2c_3 + b_1b_3) & (-ikN_3b_3) & (ikN_3c_3) & (c_3^2 + b_3^2) \end{bmatrix} \tag{B.11}$$

Now, [R] matrix need to be converted into real matrix

$$[R]_F = [L]^* [R] [L] \tag{B.12}$$

Where $[L]$ and $[L]^*$ are given bellow,

$$[L] = \begin{bmatrix} 1 & 0 & 0 & 0 & 0 & 0 & 0 & 0 & 0 \\ 0 & 1 & 0 & 0 & 0 & 0 & 0 & 0 & 0 \\ 0 & 0 & -i & 0 & 0 & 0 & 0 & 0 & 0 \\ 0 & 0 & 0 & 1 & 0 & 0 & 0 & 0 & 0 \\ 0 & 0 & 0 & 0 & 1 & 0 & 0 & 0 & 0 \\ 0 & 0 & 0 & 0 & 0 & -i & 0 & 0 & 0 \\ 0 & 0 & 0 & 0 & 0 & 0 & 1 & 0 & 0 \\ 0 & 0 & 0 & 0 & 0 & 0 & 0 & 1 & 0 \\ 0 & 0 & 0 & 0 & 0 & 0 & 0 & 0 & -i \end{bmatrix} \quad [L]^* = \begin{bmatrix} 1 & 0 & 0 & 0 & 0 & 0 & 0 & 0 & 0 \\ 0 & 1 & 0 & 0 & 0 & 0 & 0 & 0 & 0 \\ 0 & 0 & i & 0 & 0 & 0 & 0 & 0 & 0 \\ 0 & 0 & 0 & 1 & 0 & 0 & 0 & 0 & 0 \\ 0 & 0 & 0 & 0 & 1 & 0 & 0 & 0 & 0 \\ 0 & 0 & 0 & 0 & 0 & i & 0 & 0 & 0 \\ 0 & 0 & 0 & 0 & 0 & 0 & 1 & 0 & 0 \\ 0 & 0 & 0 & 0 & 0 & 0 & 0 & 1 & 0 \\ 0 & 0 & 0 & 0 & 0 & 0 & 0 & 0 & i \end{bmatrix}$$

From (B.12) we will can find $[R]_1$ which is $[R]_1 = [R][L]$

$$[R]_1 = \begin{bmatrix} (-k^2N_1^2+c_1^2) & (-b_1c_1) & (kN_1b_1) & (-k^2N_2N_1+c_1c_2) & (-c_1b_2) & (kN_1b_2) & (-k^2N_1N_3+c_1c_3) & (-c_1b_3) & (kN_1b_3) \\ (-b_1c_1) & (-k^2N_1^2+b_1^2) & (kN_1c_1) & (-b_1c_2) & (-k^2N_1N_2+b_1b_2) & (kN_1c_2) & (-b_1c_3) & (-k^2N_1N_3+b_1b_3) & (kN_1c_3) \\ (ikN_1b_1) & (ikN_1c_1) & -i(c_1^2+b_1^2) & (ikN_2b_1) & (ikN_2c_1) & -i(c_1c_2+b_1b_2) & (ikN_3b_1) & (ikN_3c_2) & -i(c_1c_3+b_1b_3) \\ (-k^2N_1N_2+c_1c_2) & (-b_1c_2) & (kN_2b_1) & (-k^2N_2^2+c_2^2) & (-c_2b_2) & (kN_2b_2) & (-k^2N_2N_3+c_2c_3) & (-c_2b_3) & (kN_2b_3) \\ (-c_1b_2) & (-k^2N_1N_2+b_1b_2) & (kN_2c_1) & (-c_2b_2) & (-k^2N_2^2+b_2^2) & (kN_2c_2) & (-b_2c_3) & (-k^2N_2N_3+b_2b_3) & (kN_2c_3) \\ (ikN_1b_2) & (ikN_1c_2) & -i(c_1c_2+b_1b_2) & (ikN_2b_2) & (ikN_2c_2) & -i(c_2^2+b_2^2) & (ikN_3b_2) & (ikN_3c_2) & -i(c_2c_3+b_1b_3) \\ (-k^2N_1N_3+c_1c_3) & (-b_1c_3) & (kN_3b_1) & (-k^2N_2N_3+c_2c_3) & (-b_2c_3) & (kN_3b_2) & (-k^2N_3^2+c_3^2) & (-c_3b_3) & (kN_3b3) \\ (-c_1b_3) & (-k^2N_1N_3+b_1b_3) & (kN_3c_2) & (-c_2b_3) & (-k^2N_2N_3+b_2b_3) & (kN_3c_2) & (-c_3b_2) & (-k^2N_3^2+b_3^2) & (kN_3c_3) \\ (ikN_1b_3) & (ikN_1c_3) & -i(c_1c_3+b_1b_3) & (ikN_2b_3) & (ikN_2c_3) & -i(c_2c_3+b_1b_3) & (-ikN_3b_3) & (ikN_3c_3) & -i(c_3^2+b_3^2) \end{bmatrix}$$

Now equation (B.12) can be written as

$$[R]_F = [L]^*[R]_1 \tag{B.13}$$

$$[R]_F = \begin{bmatrix}
(-k^2N_1^2+c_1^2) & (-b_1c_1) & (kN_1b_1) & (-k^2N_2N_1+c_1c_2) & (-c_1b_2) & (kN_1b_2) & (-k^2N_1N_3+c_1c_3) & (-c_1b_3) & (kN_1b_3) \\
(-b_1c_1) & (-k^2N_1^2+b_1^2) & (kN_1c_1) & (-b_1c_2) & (-k^2N_1N_2+b_1b_2) & (kN_1c_2) & (-b_1c_3) & (-k^2N_1N_3+b_1b_3) & (kN_1c_3) \\
(kN_1b_1) & (-kN_1c_1) & (c_1^2+b_1^2) & (-kN_2b_1) & (-kN_2c_1) & (c_1c_2+b_1b_2) & (-kN_3b_1) & (-kN_3c_2) & (c_1c_3+b_1b_3) \\
(-k^2N_1N_2+c_1c_2) & (-b_1c_2) & (kN_2b_1) & (-k^2N_2^2+c_2^2) & (-c_2b_2) & (kN_2b_2) & (-k^2N_2N_3+c_2c_3) & (-c_2b_3) & (kN_2b_3) \\
(-c_1b_2) & (-k^2N_1N_2+b_1b_2) & (kN_2c_1) & (-c_2b_2) & (-k^2N_2^2+b_2^2) & (kN_2c_2) & (-b_2c_3) & (-k^2N_2N_3+b_2b_3) & (kN_2c_3) \\
(kN_1b_2) & (-kN_1c_2) & (c_1c_2+b_1b_2) & (-kN_2b_2) & (-kN_2c_2) & (c_2^2+b_2^2) & (-kN_3b_2) & (-kN_3c_2) & (c_2c_3+b_1b_3) \\
(-k^2N_1N_3+c_1c_3) & (-b_1c_3) & (kN_3b_1) & (-k^2N_2N_3+c_2c_3) & (-b_2c_3) & (kN_3b_2) & (-k^2N_3^2+c_3^2) & (-c_3b_3) & (kN_3b3) \\
(-c_1b_3) & (-k^2N_1N_3+b_1b_3) & (kN_3c_2) & (-c_2b_3) & (-k^2N_2N_3+b_2b_3) & (kN_3c_2) & (-c_3b_2) & (-k^2N_3^2+b_3^2) & (kN_3c_3) \\
(kN_1b_3) & (-kN_1c_3) & (c_1c_3+b_1b_3) & (-kN_2b_3) & (-kN_2c_3) & -(c_2c_3+b_1b_3) & (kN_3b_3) & (-kN_3c_3) & (c_3^2+b_3^2)
\end{bmatrix} \tag{B.14}$$

Now to obtain the integration following equation is used

$$\int\int_e N_1^m N_2^n N_3^p dA = 2A_e \frac{m!n!p!}{(m+n+p+2)!} \tag{B.15}$$

this gives following results of $[R]_F$ elements

$$\int_A N_1^2 dA = \frac{2!}{(2+2)!}2A = \frac{A}{6}$$
$$\int_A N_1N_2 dA = \frac{1!1!}{(1+1+2)!}2A = \frac{A}{12}$$
$$\int_A N_1 dA = \frac{1!}{(1+2)!}2A = \frac{A}{3}$$